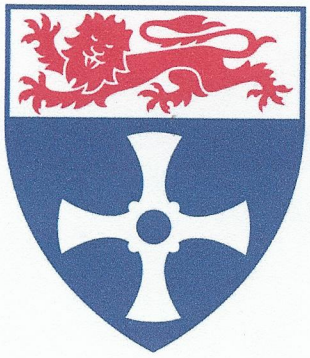

Newcastle University

FUNDAMENTAL AND APPLIED STUDIES ON THE DEVELOPMENT OF AN ALKALINE ANION EXCHANGE MEMBRANE-BASED DIRECT ALCOHOL FUEL CELL.

Thesis submitted by:

DOUGLAS LINARES MOYA

For the degree of Doctor of Philosophy

Newcastle University
School of Chemical Engineering and Advanced Materials

August 2011

Declaration

I hereby declare that the work embodies in this thesis entitled "Fundamental and applied studies on the development of an alkaline anion exchange membrane-based direct alcohol fuel cell" is the result of investigations carried out in the School of Chemical Engineering and Advanced Materials at Newcastle University.

Douglas Linares Moya
August 2011
Newcastle upon Tyne
United Kingdom

Acknowledgements

Many thanks to the Universidad del Zulia for sponsorship and Newcastle University for hospitality too. Thank you very much to my supervisor Prof. Paul. A. Christensen for his time and advice, and for not killing me in a horrible and slow way, as he ever warned me. To Dr. Wenfeng Ling for his advices, to Professor Keith Scott for his support, to professor David Woods and Dr. Mark Rosamond in Durham University for their collaboration and to Henriette, Charlotte and Lyria Christensen, because they do the hardest work, making Paul a happy man. Thank you to all my past and present lab-mates, to Ajchara for offering me a sincere and selfless friendship, to Fei, Gouhua, Shuihua, Xiaoyi, and Rui for trying to teach me some Chinese too (谢谢 thank you), to Renato and Ricardo for giving me back some "Latin-American warm", to my pal David for endless patience in proof-reading, to the gang: Khalid, Nutchapon, Panos, Danny, Taner, Xiaoteng. What shall I do without you? (and vice versa), you all have made my days a little happier.

Thank you to three very special ladies: Pauline (SEM), Tracy (TEM) and Maggie (XRD), all professional in their fields; thanks to James and Helen at the PhysChem lab and to Rob at the Millennium lab, they were always willing to help. Thank you to all university administrative/clerical staff in the Bedson Building and Merz Court: to Isobel, Margaret, Janny, Susan and Claire in Chemistry and Justine in CEAM for doing the hideous paper work; to Robin, Kay and Craig for buying goods for us (with our money of course). Thank you to John Marshall a true artist in glassblowing; to Gary, John and Neville, because mechanical details counts. Thank you to all my fellow expats Beatriz, Jorge, Nathalie, Suher and Yadira, only we know how hard this is, and thanks you to the people who support us at home, Professors Jorge, Matilde, Miguel, and Oladis, to the ladies at the CEC lab, Lesdy, Liliana, Lisseth, Marianela, Mariela, Mariana, Moraima, and Nathalie, and the gentlemen Orlando and William. Thanks to that very special person (十二), thinking of you helps me to go on. Thank you to my flatmates Ed, EJ and Dimi, their friendship has stood an acid test. Thank you to my family and friends, I miss you so much. If your names are not here that does not mean I forgot about you all.

Finally, and the most important thanks of all: thank you God! I owe you another one.

Abstract.

This thesis reports fundamental and applied studies on fuel cell electrocatalysis, primarily of relevance to direct alcohol alkaline fuel cells, as well as work on a novel, composite anode with potential application to fuel cell-on-a-chip technology. The fundamental work on anode electrocatalysis employed *in-situ* Fourier Transform Infra-Red (FTIR) spectroscopy to study the electro-oxidation of small organic molecules at polycrystalline Pt anodes. The original aim of this work was to produce a spectroscopic database of intermediates and products which would be directly relevant to the next stage of the project, which was the study of small organic fuel molecules at Pt-free anodes. However, the data from the Pt studies proved extremely interesting as it suggested that the oxidation of organic molecules in alkaline solution takes place *via* the formation of metal-oxygen bonds, with no attendant cleavage of the C-C bond in > C_2 molecules, in contrast to the generally accepted mechanism in acid solution where metal-carbon bond formation dominates. In addition, the presence of oxygen was found to have a significant effect upon methanol and formate oxidation. Novel synthetic routes were devised for $Ru_{72}Ni_{28}$, $Co_{50}Ni_{50}$ and $Pd_{40}Ni_{60}$ nanoparticles, and the electroactivity of these materials with respect to methanol and ethanol electro-oxidation was investigated using standard IVt techniques. Fuel cell studies were conducted using $Pd_{40}Ni_{60}$/C and $Pt_{40}Ru_{20}$/C for comparison. Nafion (in its K^+ exchanged form) was employed as the polymer electrolyte membrane, as well as a novel, in-house alkaline anion exchange membrane. A maximum power density of 1.3 mW cm^{-2} was obtained using $Pd_{40}Ni_{60}$/C anode and Pt/C cathode with the novel membrane. Finally, results are presented on a novel composite anode which was found to exhibit an electrochemical response hitherto not reported in the literature.

Table of Content

List of Figures

List of Tables

List of Publications

Journal publications

1. P. A. Christensen and **D. Linares-Moya**. "The role of adsorbed formate and oxygen in the oxidation of methanol at a polycrystalline Pt electrode in 0.1 M KOH: An *in-situ* Fourier Transform Infrared study. J. Phys. Chem. C, 2010, 114 (2), pp 1094-1101. DOI: 10.1021/jp908726f

2. P. A. Christensen, A. Hamnett and **D. Linares-Moya**. Oxygen reduction and fuel oxidation in alkaline solution. Phys. Chem. Chem. Phys., 2011, 13, 5206- 5214. DOI: 10.1039/C0CP02365E.

3. P. A. Christensen, M. A. Carroll, **D. Linares-Moya**, D. Molyneux, M. C. Rosamond, and D. Wood. A Novel Composite Anode: The Electrooxidation of Organic Molecules via Formation of Highly Energetic Holes. J. Phys. Chem. C, 2011, 115 (21), pp 10777-10783. DOI: 10.1021/jp202325m

4. P. A. Christensen, A. Hamnett and **D. Linares-Moya**. The electro-oxidation of formate ions at a polycrystalline Pt electrode in alkaline solution: an *in-situ* FTIR study. Phys. Chem. Chem. Phys., 2011, 13, 11739-11747. DOI: 10.1039/C1CP20166B

5. P. A. Christensen, A. Hamnett and **D. Linares-Moya**. *In-situ* FTIR Studies of Ethanol Oxidation at Polycrystalline Pt in Alkaline Solution. Submitted to The Journal of Physical Chemistry, July 2011.

Conference publications

1. Electrochem 2008 (Poster presentation), "Ru-Ni anode catalyst for direct alcohol alkaline anion exchange membrane fuel cell", 15 – 17 September 2008, Department of Chemistry, The University of Liverpool, Liverpool, United Kingdom.

2. The 2009 CEAM Post Graduate Student Research Conference (Oral presentation), "The oxidation of methanol at a polycrystalline Pt electrode in alkaline solution:

an *in-situ* FTIR spectroscopy study", 16 – 17 April 2009, School of Chemical Engineering and Advanced Materials, Newcastle University, Newcastle upon Tyne, United kingdom.

3. Electrochem 2009 (Oral presentation), "The oxidation of methanol at a polycrystalline Pt electrode in alkaline solution: an *in-situ* FTIR spectroscopy study", 16 – 17 September 2009, School of Chemistry, The University of Manchester, Manchester, United Kingdom.

4. The 2009 CEAM Post Graduate Student Research Conference (Oral presentation), "The role of adsorbed formate in the oxidation of methanol at a polycrystalline Platinum electrode in 0.1 M KOH. An *in-situ* FTIR study", 14 – 15 April 2010, School of Chemical Engineering and Advanced Materials, Newcastle University, Newcastle upon Tyne, United Kingdom.

List of Abbreviations

Nomenclature

a	Diffusion length of the OFI radicals at the composite anodes /μm
B_θ	Full width of the peak corresponding to 26 at the half height (or integral breadth), in Scherrer's equation /radian
d	Composite anode grid thickness /μm
d	Macroparticle diameter /μm
e^-	Electron
e^-_{CB}	Electrons in the conduction band
E	Electrode potential /V
E°	Standard electrode potential /V
E*a*	Anodic potential limit
$E_{a,act}$	Actual anodic limit as function of V_b/V
$E_{a,m}$	Anodic limit imposed by the potentiostat over the composite anode
E*c*	Cathodic potential limit
E_F	Fermi's level
E_g	Energy band gap /eV
E_r	Reversible thermodynamic potential /V
F	Faraday constant (96485) /s A mol^{-1}
ΔG	Gibb's free energy /J
h^+	Electronic hole
h^+_{VB}	Holes in the valence band
hv	Plank constant times frequency (energy measurement) /eV
$HO^\bullet$	Hydroxyl radical
I_b	Bias current /mA
$I_{p,a}$	Anodic current peak in a CV /mA
$I_{p,c}$	Cathodic current peak in a CV /mA
j	Current density /mA cm^{-2}
j_0	Exchange current density /mA cm^{-2}
k	Absorption index
l	Composite anode grid separation /μm
L	Distance between voltage measurement /0.5 cm (cell's design)
Lp	Minority carrier length /m
n	Refractive index
n-	Negative doped semiconductor
Ox	Oxide state species in a redox couple
Rd	Reduced state species in a redox couple
R	Electrical resistance / Ω (or Ω cm^{-2})
ΔR/R	Common FTIR data manipulation normalization
$R(E_S)$	Response signal in FTIR experiments at sample potential (E_S)
$R(E_R)$	Response signal in FTIR experiments at reference potential (E_R)
T	Membrane sample thickness /cm
V_b	Bias voltage /V
W_d	Depletion layer width /m
W	Electrical work at constant temperature and pressure /J
W_S	Membrane sample width /cm
z	Number of moles of electrons transferred in the reaction (Nernst equation)

Greek symbols

α	Light absorption coefficient /m^{-1}
β	Tafel slope /V dec^{-1}
δ	Asymmetric stretch in organic molecules spectra
λ	Wavelength (light, infrared radiation, X-ray, etc.) /nm
2θ	Angle of maximum reflection in XRD diffractograms /radian
η	Efficiency
ν	Symmetric stretch in organic molecules spectra
ν_s	Common literature nomenclature for symmetric stretch bonds
ν_{as}	Common literature nomenclature for asymmetric stretch bonds
σ	In-plane conductivity /S cm^{-1}
σ-	Electron acceptor/donor in σ orbital
ρ	In-plane resistivity / Ω cm

Acronyms

AAEM	Alkaline Anion Exchange Membrane
AFC	Alkaline Fuel Cell
AIRE	Abnormal Infrared Effects
ATR	Attenuated Total Reflectance
CE	Counter electrode
CIGARS	Current Induced Generation of Adsorbed Reactive Species
COE	Chloroform/methanol solution of cyclooctene
CV	Cyclic Voltammetry/Voltammogram
DAAFC	Direct Alcohol Alkaline Fuel Cell
DC	Direct Current
DCPD	Dicyclopentadiene
DMFC	Direct Methanol Fuel Cell
DOE	US Department Of Energy
DVM	Digital Voltmeter
E. coli	Escherichia coli (bacteria)
ECF	Electrochemical fluorination
ED	Electro Deposited
EDX	Energy-Dispersive X-ray spectroscopy
EFE	Electric Field Enhancement
ESEM	Environmental Scanning Electron Microscopy
ETFE	poly-(ethylene-co-tetrafluoroethylene)
ETSU	Energy Technology Support Unit (The National Archives)
FEG	Field Emission Gun
FEMS	Federation of European Microbiological Societies
FEP	Poly-(tetrafluoroethylene-co-hexafluoropropylene)
FTIR	Fourier Transform Infrared
I/C	Ionomer to Carbon ratio
ICDD	International Centre for Diffraction Data
IEC	Ion Exchange Capacity /mmol OH^- g^{-1}
IR	Infrared
IUPAC	International Union of Pure and Applied Chemistry
JCPDS	Joint Committee on Powder Diffraction Standards
LED	Light Emitting Diode

MCT	Mercury-Cadmium-Telluride (infrared detector)
MEA	Membrane Electrode Assembly
MMO	Mercury-Mercury Oxide (reference electrode)
MOR	Methanol Oxidation Reaction
NASA	National Aeronautics and Space Administration
NCIMB	National Collection of Industrial Food and Marine Bacteria
ORR	Oxygen Reduction Reaction
PAC	Professor Paul A. Christensen research group in Newcastle University
PEM	Polymer Electrolyte Membrane
PEMFC	Polymer Electrolyte Membrane Fuel Cell
PET	Positron Emission Tomography
PL-L	Plug in - Light bulbs lamp type
PTFE	Polytetrafluoroethylene
PVBC	Poly-vinylbenzyl chloride
PVBTMAOH	Poly-(vinylbenzyl-trimethylammonium hydroxide)
R&D	Research and development
RE	Reference electroe.
RG	Radiation-Grafted
RHE	Reversible Hydrogen Electrode
SCE	Saturated Calomel Electrode
SD1	The Doherty's group nomenclature for their AAEM.
SEIRAS	Surface Enhanced Infrared Absorption Spectroscopy
SEM	Scanning Electron Microscopy
SHE	Standard Hydrogen Electrode
SLA	Sealed Lead Acid (battery)
SME	Society of Mining Engineers
S_N2	Nucleophilic Substitution (bimolecular)
SNIFTIRS	Subtractively Normalized *In-situ* Fourier Transform Infra-Red Spectroscopy
SR	Scan rate
TEM	Transmission Electron Microscopy
TGPH	Toray™ carbon paper type
UV	Ultraviolet light
WE	Working electrode
XPS	X-ray photoelectron spectroscopy
XRD	X-Ray Diffraction/Difractogram

1. Introduction

This thesis concern primarily work on the electro-oxidation of small organic molecules under conditions of relevance to the alkaline fuel cell. Hence this chapter introduces the fuel cell concept, describes alkaline fuel cell technology in detail and puts it in historical and scientific context.

1.1. The fuel cell concept

A fuel cell is an example of a galvanic electrochemical cell where a fuel is in contact with the anode and an oxidant (typically oxygen in air) in contact with the cathode, the anode and cathode compartment separated by an ionically conducting (electronically insulating) membrane. If the electrodes are connected together by a wire, the chemical components in the two electrode compartments react spontaneously, exchanging electrons at the electrodes and then causing a current to flow through the wire, electrons moving from anode to cathode. The basic components of a fuel cell are shown in figure 1.1

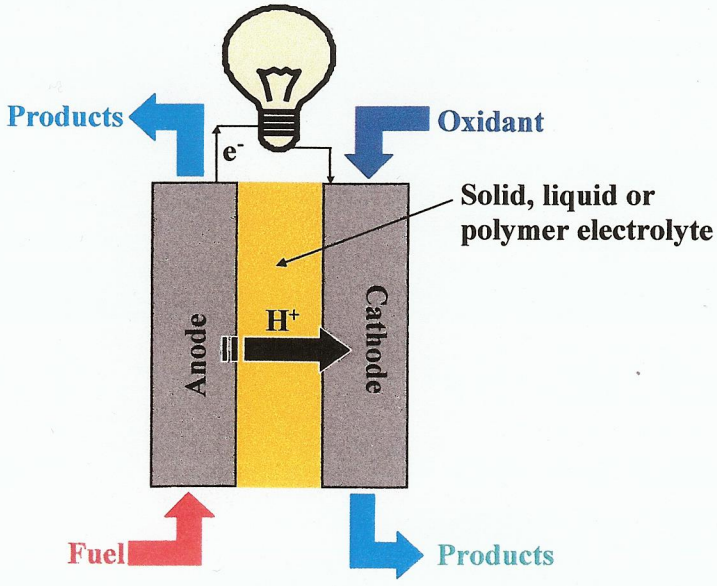

Figure 1.1. The fuel cell concept.

As an example, the simplest fuel cell uses hydrogen as fuel and oxygen as oxidant:

At the anode:

$$2H_2O + H_2(g) \rightarrow 2H_3O^+ + 2e^- \quad (1.1)$$

At the cathode:

$$O_2 + 4H^+ + 4e^- \rightarrow 2H_2O \quad (1.2)$$

Overall cell reaction:

$$2H_2 + O_2 \rightarrow 2H_2O \quad (1.3)$$

In essence, a fuel cell converts chemical energy into electrical energy or work; the maximum electrical work at constant temperature and pressure is:

$$W_{e,max} = \Delta G \quad (1.4)$$

Where ΔG is the Gibbs free energy change of the cell reaction (e.g. (1.3)), and is negative for a spontaneous reaction; the variation in ΔG as the reaction proceeds may be represented as in fig. 1.2 [1]:

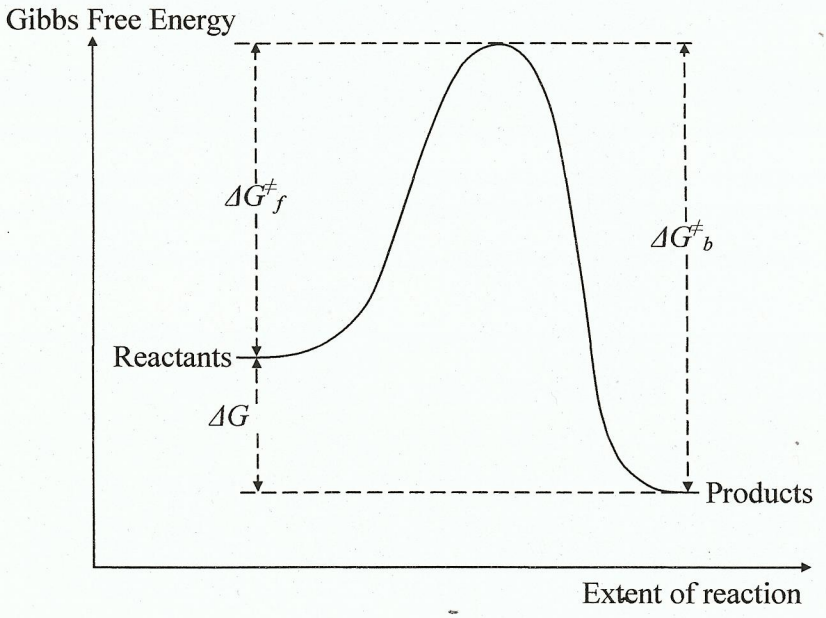

Figure 1.2. The variation in Gibbs Free Energy during a spontaneous chemical reaction. $\Delta G^{\neq}_f$ and $\Delta G^{\neq}_b$ are the Gibbs Free Energies of activation for the forward and reverse reactions, respectively.

Fuel is fed to the anode where, in the case of hydrogen, it is oxidised to protons which pass through the Polymer Electrolyte Membrane (PEM, if protons are the mobile species; e.g. Nafion) and electrons move around the external circuit to the cathode where they combine with protons and oxygen to produce water. As current scales with surface area, fuel cell electrodes typically comprise small particles of electrocatalyst supported on very high surface area, porous carbon substrates (in the low temperature, < 100 °C, fuel cells relevant to this thesis). The electrolyte separates the fuel and oxidant, facilitates the ion transport between anode and cathode and prevents electrical short circuit between electrodes.

1.2. The advantages of alkaline fuel cells (AFC)

It is generally accepted that the oxygen reduction reaction (ORR) is more facile under alkaline conditions than in acid solution [2], and that the electro-oxidation of methanol under such conditions is structure insensitive [3]; further, electrocatalytic processes in general are facilitated due to the significantly weaker specific adsorption of anions and hence decreased inhibition [4]. The improved kinetics and less corrosive nature of alkaline electrolytes compared to acid also allows the use of non-noble metals as electrocatalysts. Thus, a large range of potential cathode catalysts have been investigated including: carbon [5-7], transition metals [8-10], metal oxides [11-13], metalloporphyrins [14, 15] and metallophthalocyanines [16, 17]. For in-depth reviews of the ORR see references [4] and [18].

To gain some insight into the relative importance of the losses in a fuel cell we may use the treatment of Blomen and Mugerwa [19, 20] and McLean et al. [2]. Thus, a typical polarization plot for a H_2/O_2 Polymer Electrolyte Membrane (PEM e.g. Nafion) fuel cell is shown in fig 1.3

As may be seen, the majority of the losses are associated with the ORR as hydrogen oxidation is facile (see fig. 1.3). Region (i) is the activation overpotential region, dominated by kinetic loss (poor kinetics) at the cathode. Region (ii) is due to resistive losses across the fuel cell and (iii) to mass transport loss. According to Barendrecht [19], where mass transport is not a problem (regions (i) & (ii) in fig. 1.3) the cell voltage E_{cell} is related to current density j by:

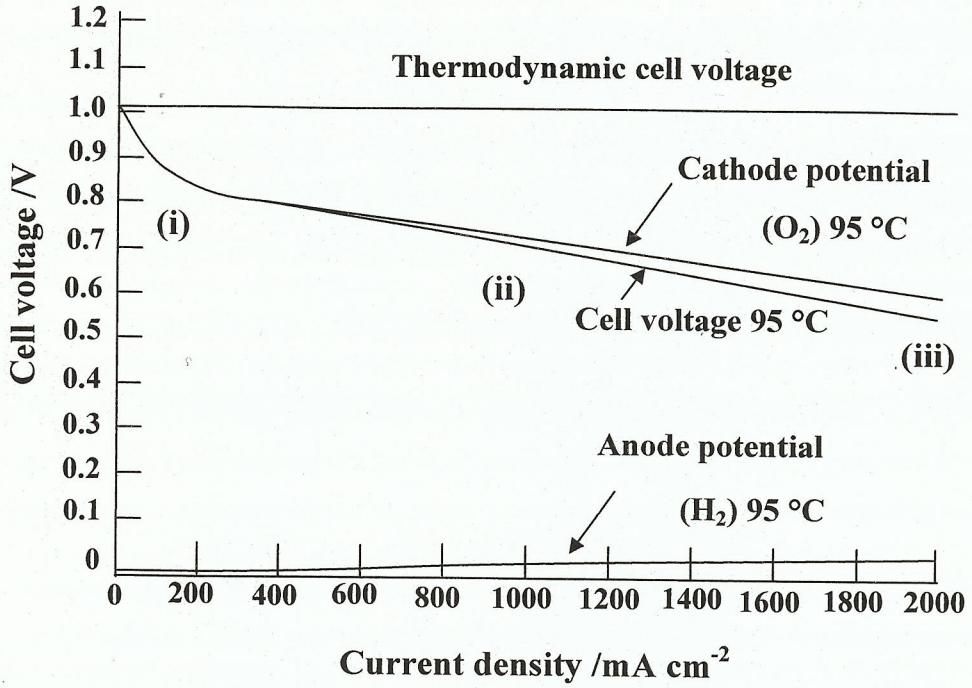

Figure 1.3. The variation of the cell voltage of a H_2/O_2 PEM fuel cell as a function of current density. From ref [2].

$$E = E^\circ - \beta \log j - R j \tag{1.5}$$

$$E^\circ = E_r + \beta \log j_0 \tag{1.6}$$

Where E_r is the reversible thermodynamic potential for the overall cell reaction (1.3), β is the Tafel slope [22] and j_0 is the exchange current density. R is the electrical resistance in Ω cm^{-2}. Differentiating (1.5):

$$\frac{\partial E}{\partial j} = -\frac{\beta}{j} - R \tag{1.7}$$

At low current densities the β/j term is dominant and gives rise to the steep fall in j in the initial part of region (i) in fig. 1.3. At higher j_0, R » β and the electrical resistance dominates, resulting in the essentially linear fall in E_{cell} in region (ii). Thus, the optimum performance of a fuel cell results from minimizing β and R, and maximizing j_0. In general, the more facile ORR kinetics under alkaline conditions results in β values ca. 30% lower than in the H_2/O_2 PEMFC when Pt is the cathode and anode catalyst [2, 23]. With respect to R, the primary contribution to the resistance of a fuel

cell is, in general, the electrolyte or polymer electrolyte membrane. Comparing a liquid (e.g. typically concentrated 30 – 50 wt. % KOH [24, 25], 50 wt. % = 9 M KOH) with a PEM is, perhaps, not ideal as the resistance of both depends upon electrolyte thickness, but McLean et al. [2] made the statement that the resistance of a typical PEM (presumably Nafion) is 0.08 Ω cm^{-2} compared to 0.05 Ω cm^{-2} for KOH.

Alkaline fuel cells are a relatively straightforward technology [26] and, coupled with the production of heat and pure water as side products, proved ideal for use in space, where they had a long and successful history [27, 28]. Table 1.1 summarizes the performance of AFC's in space applications; given the fact that the data in the table were obtained in the early 1970's or using 1970's technology, the results are impressive, even by the standards of today.

Operating point		Power ($W\ cm^{-2}$)	Press. (psig)	Temp. (°C)	Ref
mV	$mA\ cm^{-2}$				
950	140	0.133	29	98	[29]
950	220	0.209	58	98	[29]
950	310	0.2945	116	98	[29]
950	150	0.1425	58	65	[29]
950	280	0.266	58	96	[29]
950	440	0.418	58	130	[29]
600	3200	1.92	58	98	[29]
600	4200	2.52	58	121	[29]
800	6730	5.384	299	149	[25]
740	1000	0.74	29	80	[30]
900	320	0.288	29	80	[30]
900	1000	0.9	60	80	[30]

Table 1.1 Summary of the performance of H_2/O_2 alkaline fuel cells in space [2].

1.3. The rise of H_2/O_2 AFC's.

An early pioneer in AFC technology was Sir Francis Bacon, see fig. 1.4(a), who started his research in Cambridge in the late 1930's and produced the first viable power unit in the 1950's (see fig. 1.4(b)), which was a 5kW stack (i.e. a number of

individual cells connected in series to increase the output voltage) utilising pure H_2 and O_2 as fuel and oxidant, respectively.

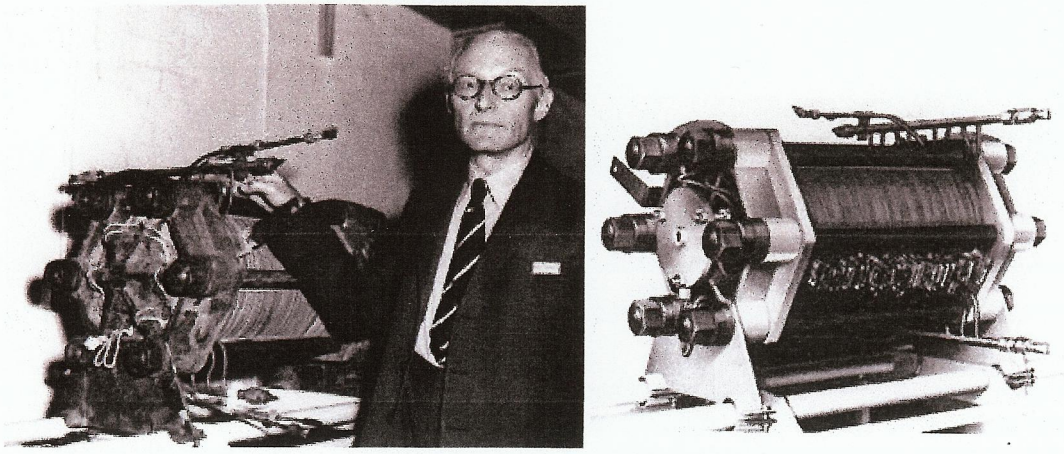

a) b)

Figure 1.4. a) Francis Thomas Bacon (1904 - 1992), b) Bacon 5kW AFC (from IEEE global history network [31]).

Bacon's AFC employed 30 wt. % KOH as the circulating electrolyte, operating at 200 °C and 5 MPa to prevent the electrolyte from boiling. The technology was bought by NASA and featured extensively in its space programme [32], see fig. 1.5.

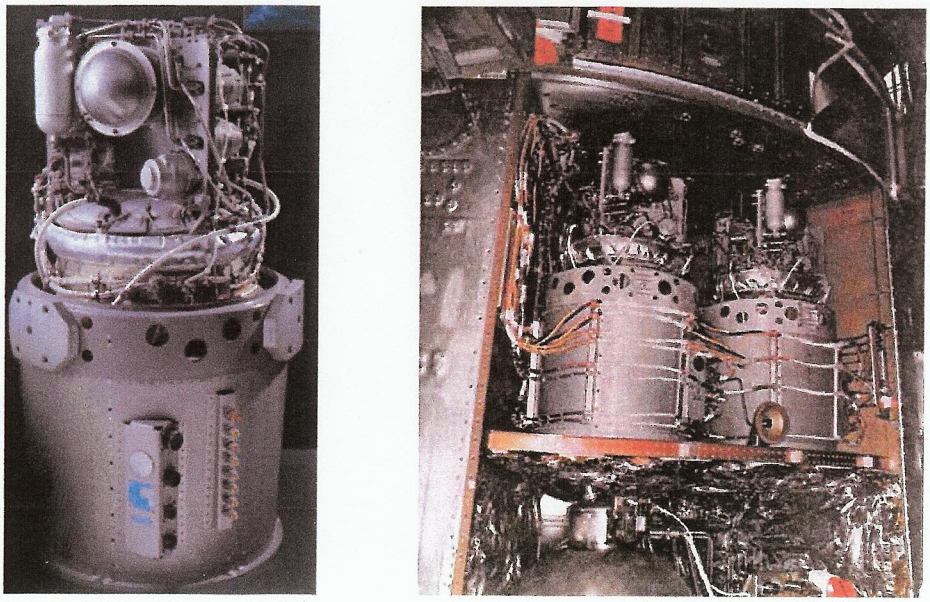

a) b)

Figure 1.5. a) Pratt & Whitney fuel cell power plant used in NASA's Apollo program: 31 cells, 100 mA cm^{-2}, 1.12 kW at 28 V, 110 kg. b) The fuel cell bay in Apollo IV. [32]

AFC's found wider applications than just in space, being used as the power source in a range of vehicles. Thus in the 1960's, Allis-Chalmers built the first large vehicle powered by a fuel cell [33], which was a farm tractor using a 15 kW stack of over 1000 cells, able to pull ca. 1.5 tons, see fig. 1.6.

A strong supporter of AFC technology, K.V. Kordesch, drove an Austin A40 battery/fuel cell hybrid car with a 6 kW H_2-air fuel cell system for many years in the 1960's [21, 34], fig. 1.7

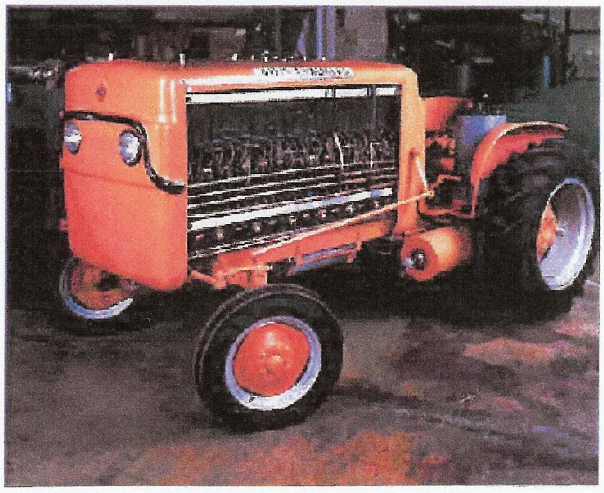

Figure 1.6. The Allis-Chalmers 1.5 kW AFC tractor in the Smithsonian museum (from Smithsonian institutions [33])

Figure 1.7. The Austin A-40 hybrid car of K. V. Kordesch. Six hydrogen bottles were mounted on the roof, the 6 kW H_2-Air fuel cell system was in the rear, lead-acid batteries were under the bonnet [21].

Nowadays environmental policies around the world have boosted the attempts to construct an electric vehicle, fully operational with zero or low emissions, and with performance comparable to those of internal combustion engines, but the results of using fuel cells or batteries have been modest; and the combinations of technologies have given birth to so-called hybrid cars (see fig. 1.8).

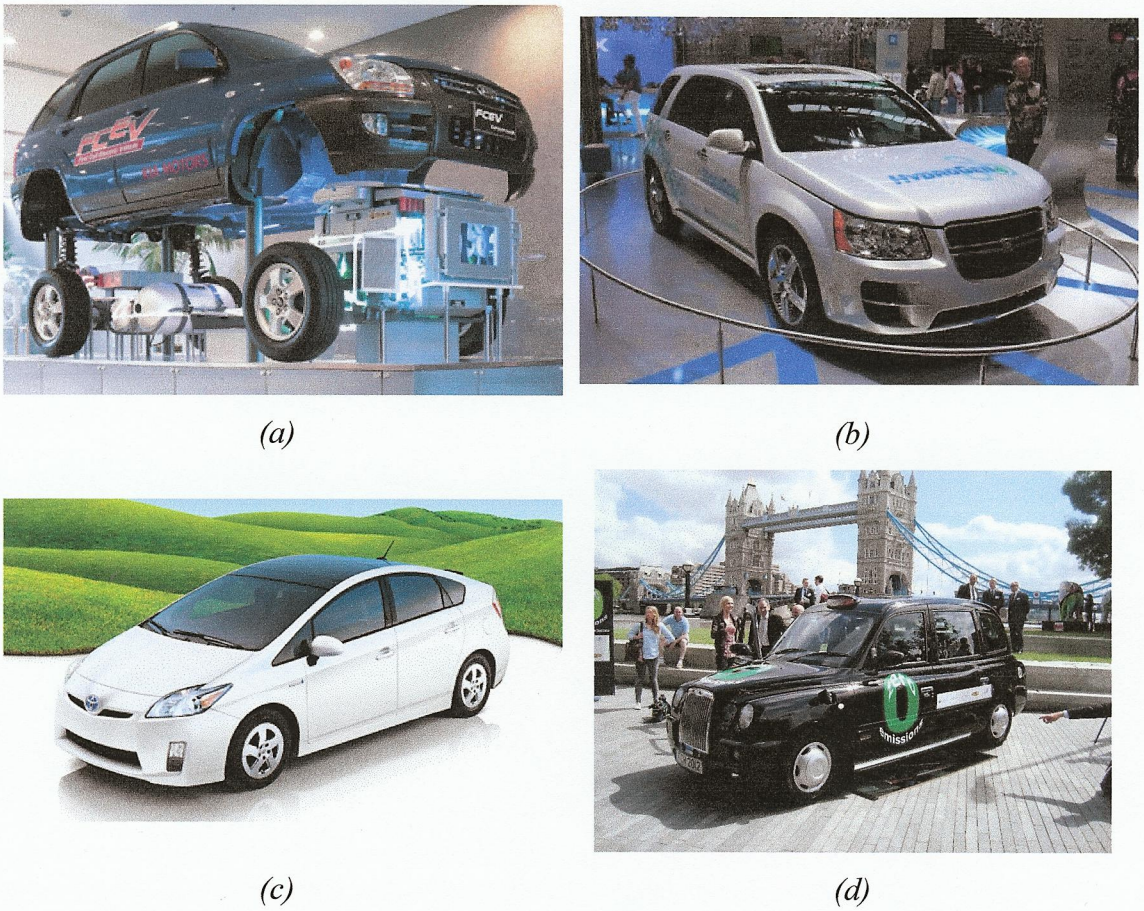

Figure 1.8. Fuel cell concept vehicles (a) Hyudai Tucson II 2007, (b) GM Hydrogen4 2007; vehicles in the market (c) Toyota Prius 2010 (d) Fuel cell hybrid London taxi 2011

A growing list of manufacturers committed in the task can be found elsewhere [35]. The use of AFC still remains as one of the most promising technologies.

1.4. Direct alcohol alkaline fuel cells.

In contrast to the pressurized H_2/O_2 systems employed in space, of more relevance to terrestrial applications are systems operating under atmospheric pressure and preferably utilizing air. Table 1.2 summarizes the performance of such fuel cells up to the time of the review by McLean et al. [2].

Current density at 0.7 V (mA cm^{-2})	Power at 0.7 V (W cm^{-2})	Point 2 (W cm^{-2})		Power at Point 2 (W cm^{-2})	Press, (psig) & gases	Temp (°C)	Ref
		mV	mA cm^{-2}				
290	0.203	800	260	0.208	atm H_2-air	75	[36]
450	0.315	800	280	0.224	atm H_2-air	75	[36]
N=A	N=A	670	100	0.067	atm	N=A	[37]
90	0.063	800	35	0.028	(44) H_2-air	40	[38]
108	0.076	800	102	0.082	(44) H_2-air	40	[38]
115	0.081	570	225	0.128	atm H_2-air	40	[39]
125	0.088	700	125	0.088	atm H_2-O_2	40	[39]
88	0.062	700	88	0.062	atm H_2-air	40	[39]
N=A	N=A	750	186	0.140	atm H_2-O_2	40	[39]
157	0.110	700	157	0.110	atm H_2-air	40	[39]
N=A	N=A	850	100	0.085	atm H_2-air	65	[40]
N=A	N=A	900	100	0.090	atm H_2-O_2	65	[40]
87	0.061	670	100	0.067	atm H_2-air	70	[41]
40	0.028	N=A	N=A	N=A	atm H_2-air	60	[42]

Table 1.2 Summary of terrestrial AFC performance [2],

More recent performance data for H_2/air AFC's may be found in the work of Schulze and Gülzow [43] who described in detail important operational limitations, as well as the paper by Nijmeijer et al. [44], an updated review.

From the literature [45, 46] there can be no doubt that the H_2/O_2 alkaline fuel cell (AFC) is the best performing of all fuel cells, due to their capabilities: > 300 mW cm^{-2} at 75 °C and using air as the oxidant, and 80 mW cm^{-2} at 40 °C under the same conditions [46]; even at room temperature, it performs well [34]. Lifetimes of 15000 hours have been demonstrated [34, 43, 46]. However, the possibility of developing a direct alcohol fuel cell and, in particular, a direct methanol AFC, has long been of interest to the scientific community, for a variety of technical and scientific reasons. Thus, methanol has a higher volumetric energy density than liquid hydrogen (see table 1.3), methanol is easier to store and transport than gas or liquid H_2, and the current

liquid fuel distribution network is amenable to straightforward conversion to methanol, whereas a new and costly distribution structure will be required for H_2 [47-49].

Fuel	E°/V	We /kWh kg^{-1} (kWh dm^{-3})	η_{rev}
Hydrogen (H_2)	1.23	39.0 (2.6 liquid H_2)	0.83
Methanol (CH_3OH)	1.21	6.1 (4.8)	0.97
Ethanol (C_2H_5OH)	1.15	8.0 (6.3)	0.97
Propanol (C_3H_7OH)	1.07	8.6 (6.8*)	0.93
Ethylene glycol (HOC_2H_4OH)	1.22	5.3 (5.9)	0.99

*Table 1.3. The standard thermodynamic voltages (E°), energy densities (We), and maximum reversible efficiencies (η_{rev}) of hydrogen and selected pure alcohols *2-propanol [47].*

In addition, direct methanol fuel cells (i.e. that use the alcohol directly as a fuel rather that reforming it first to H_2 and then using this as the fuel) were perceived as an alternative technology to replace batteries in portable electronic devices such as laptops, mobiles phones, etc. [47, 50, 51]; however, this perception has since been disputed as fuel cell technology becomes more generally applicable (i.e. toys, tools, military devices, etc.), and as the number of applications of fuel cells increases exponentially [52, 53] e.g. rather than powering mobile phones, fuel cells have been developed to charge the batteries of mobiles phones [54]. Since these fuel cells are actually larger than the plug transformers (and batteries) normally supplied with the phones, size appears to be a recurrent problem [34, 49, 55]. It would be advantageous to produce cost effective fuel cells of a comparable size to batteries; however, reduction in the size of fuel cells has proved difficult due to the necessity for high surface area electrodes [56].

Despite current concerns over the volumetric density of direct alcohol alkaline fuel cell systems (DAAFC's), their potential use in a wide range of applications remains of very significant interest. Direct alcohol alkaline fuel cells have a number of advantages over their acidic counterparts. Thus, as was mentioned above, it is generally accepted that methanol oxidation at Pt-based anode catalysts is not structure sensitive, and is more facile, in alkaline than acid electrolytes [57-59].

One reason for this may be that at least in the case of Pt-based materials, the anode catalysts do not suffer from the poisoning seen in acid solution due to strongly adsorbed CO [60] see fig. 1.9.

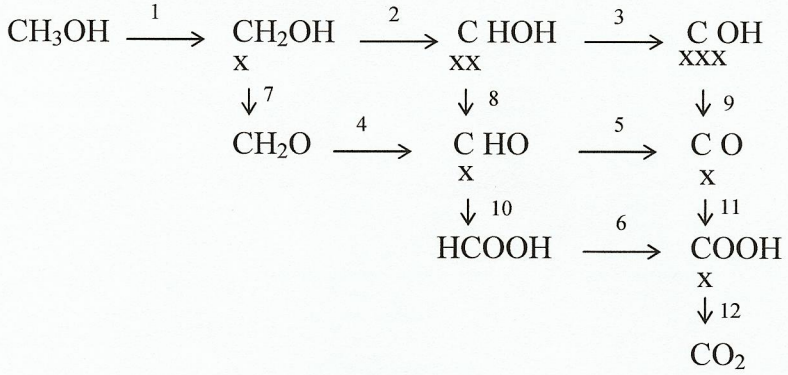

Figure 1.9. The "scheme of squares" mechanism for the oxidation of methanol at Pt in acid solution, from [60].

In addition, in acid solution, it is believed that a key step is the oxidation of adsorbed CO by adsorbed OH "active oxygen", according to the Langmuir - Hinshelwood mechanism first proposed in this context by Watanabe and Motoo [61].

$$Pt\text{-}OH + Pt\text{-}C{\equiv}O \rightarrow 2Pt + CO_2 + H^+ + e^- \qquad (1.8)$$

In alkaline solution, adsorbed OH forms at Pt a relatively cathodic potentials [62] hence providing 'active oxygen' for the oxidation of active species at relatively lower potentials than in acid.

The desirability of a direct alcohol alkaline fuel cell may be seen from the fact that one of the first direct methanol fuel cells, developed in 1955 [63] employed an alkaline electrolyte with a porous Ni anode and porous Ni/Ag cathode.

The enhanced activity of Pt towards methanol in alkaline, as opposed to acid, electrolyte is show in fig. 1.10. As may be seen from the figure, the oxidative current observed at the Pt electrode in alkaline electrolyte is significantly larger than that observed in acid, reflecting the more facile process in the former electrolyte.

Koscher and Kordesch [64], have reviewed work on direct alcohol fuel cells and include one particular piece of work that illustrates the potential of direct methanol AFC's. Thus, Vielstich and Vogel [65] reported in 1969 a D-size (i.e. torch battery) methanol fuel cell utilizing a sintered Ni foil/Pt-Pd anode and carbon cathode.

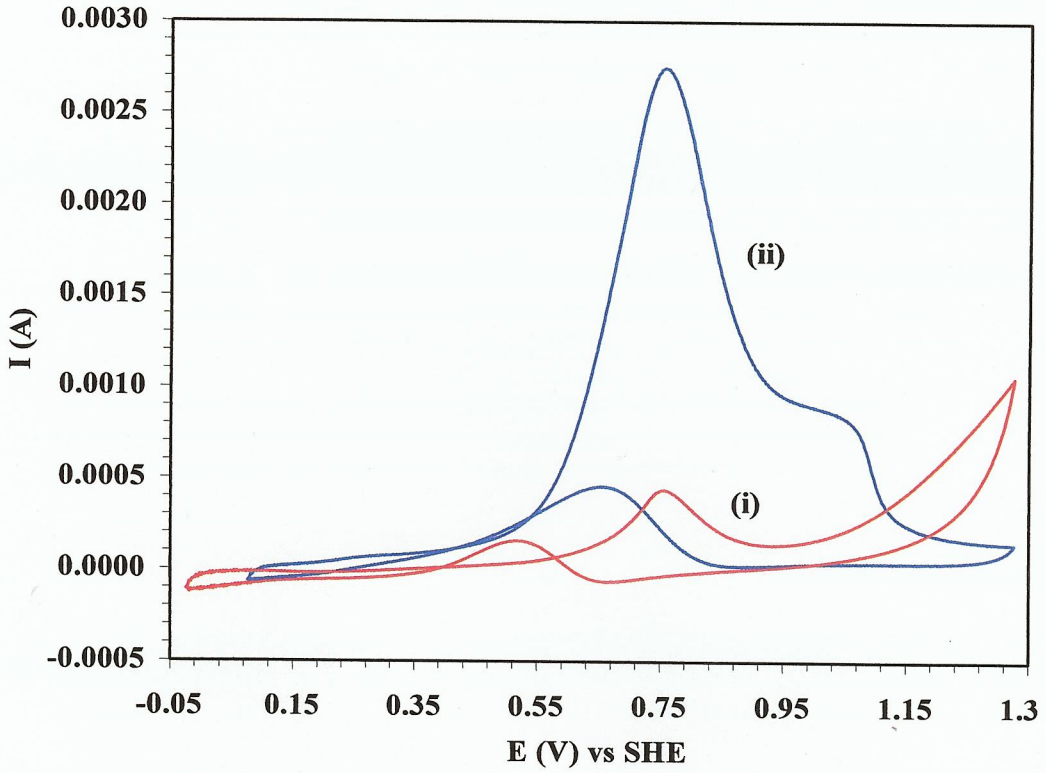

Figure 1.10. Cyclic voltammograms of a polycrystalline Pt electrode immersed in (i) 1 M CH_3OH + 1 M H_2SO_4 and (ii) 1 M CH_3OH +1 M KOH.

The capacity of the fuel cell was 20 - 23 Ah at 0.7 – 0.5 V, which was far superior to the Leclanché dry cell of the time at 3.5 Ah and 1.5 – 0.7 V. Even when compared to the current state-of-the-art Duracell Procell at 1.5 V and 18 Ah, the Vielstich and Vogel cell still compares favourably, given the 41 additional years of development the Duracell battery has benefitted from.

1.5. The disadvantages of alkaline fuel cells

Despite the significant (and highly visible) success of AFC's in the 1960's, interest and research in AFC technology until the 2000's was extremely limited, and totally eclipsed by research into polymer electrolyte membrane (PEM)-based fuel cells using Nafion [46, 66].

PEM fuel cells most commonly employ H_2 (the H_2 can be supplied from compressed gas cylinders or by reforming organics such as methanol, which gives a mixture of H_2, CO and CO_2) or methanol (Direct Methanol Fuel Cells, or DMFC's) as fuel, and O_2 or air as oxidant. The decline of AFC's was due to 4 key factors [21]:

1. The use of flowing electrolyte. The problems experienced during the attempted development of the analogous anionic membranes to PEM's (see below) have precluded any significant advances to date in their application in AFC's or Direct Alcohol AFC's, and no serious stack research has been undertaken. The majority of research and development (driven by extra-terrestrial applications) has focussed on static or, more usually, flowing alkaline (KOH) electrolyte systems. To minimise the attendant cost and complexity, an AFC stack must utilise a flowing, common electrolyte, leading to parasitic current leakage and hence power loss.

2. The formation of carbonate. By far the most serious and limiting problem with AFC developments is caused by carbonate precipitation when using air at the cathode (and reformate gas or alcohols to the anode):

$$2K^+ + 2OH^- + CO_2 \rightarrow K_2CO_3 \downarrow + H_2O \qquad (1.9)$$

Reaction (1.9) dilutes the electrolyte and removes hydroxide anions, causing conductivity to decrease, and the precipitate blocks catalysts sites & pores and can lead to physical damage. This problem demands the replacement of both static (not possible in some, e.g. extra-terrestrial, applications) and flowing electrolytes (as scrubbing is not sufficiently effective), as well as completely precluding the use of reformate or alcohol (methanol, ethanol) anode feeds.

3. Liquid electrolyte both lowers the gravimetric power density and increases system complexity markedly with respect to a polymer electrolyte membrane-based system.

4. KOH is an extremely effective wetting agent, causing both a major susceptibility to leaks in the peripheral system and steady wetting of the electrode

pores (weeping), removing the 3-phase regions essential for operation with gaseous (i.e. H_2 and O_2) feeds. This requires that a Teflon coating is applied to the gas sides of the anode and cathode and hence that electrical connection can only be made at the edges. In addition, when the fuel cell is shutdown, the electrolyte has to be drained to prevent seepage across the membranes.

All the above challenges would be addressed if an effective Alkaline Anion Exchange Membrane (AAEM) could be developed. AAEM's are the alkaline analogue to PEM's such as Nafion and utilise cationic head groups such as $-NR_3^+$ immobilised within a polymeric framework, the AAEM being ion-exchanged with OH^- ions before use to provide the mobile, conducting species. The absence of any free metal cations precludes precipitation of carbonate, and it is clear from the literature that such ion exchange membranes function in the presence of carbonate at neutral and alkaline pH [34, 46]. Ion exchange membranes have been employed to convert $NaHCO_3$ to NaOH and CO_2 [46], and for the electro-transport of CO_3^{2-} and HCO_3^- with no loss of conductivity or fouling of the membranes employed [67], The use of an AAEM replaces liquid electrolyte and hence removes challenges 1 & 3 – 4 and, as stated above, also removes the carbonate problem. In addition, OH^- ions are consumed at the anode and produced at the cathode in alkaline fuel cells and hence electro-osmotic drag opposes [21] methanol crossover, a major problem with DMFC's [45].

The most promising AAEM's researched to date have been predominantly based upon the use of tertiary ammonium headgroups, $-NR_3^+$, and the development of an effective AAEM has been prevented by three principle problems which have previously proved extremely challenging:

1. Conductivity. The ionic conductivities of AAEM's reported in the literature are typically an order of magnitude lower than that of Nafion (0.1 S cm^{-1}) [21, 68].

2. Stability. $-NR_3^+$ is a good leaving group, and C atoms adjacent to the N atom are prone to nucleophilic attack by OH^-; in addition, the presence of C-H bonds β- to the N atom renders the polymer susceptible to the Hoffman Elimination [47, 69], see fig. 1.11. The widely-accepted stability limit for AAEM's is 60 °C, above which these processes become a serious problem.

3. The ionomer problem. The electrodes of PEMFC-based fuel cells are formulated with the addition of soluble ionomeric Nafion which ensures good ionic contact between the catalyst particles and the membrane. It has not proved possible to date to synthesis analogous ionomeric solutions for AAEM's [21, 66] leading to significant resistive losses in AAEM-based fuel cells [70-72]. Attempts to employ 'interfacial solutions' using KOH and e.g. a polymer such as polyacrylic acid [68] or by including KOH in the anode stream [73] provide a short term answer, but are doomed to fail in terms of durability due to the carbonate problem detailed above.

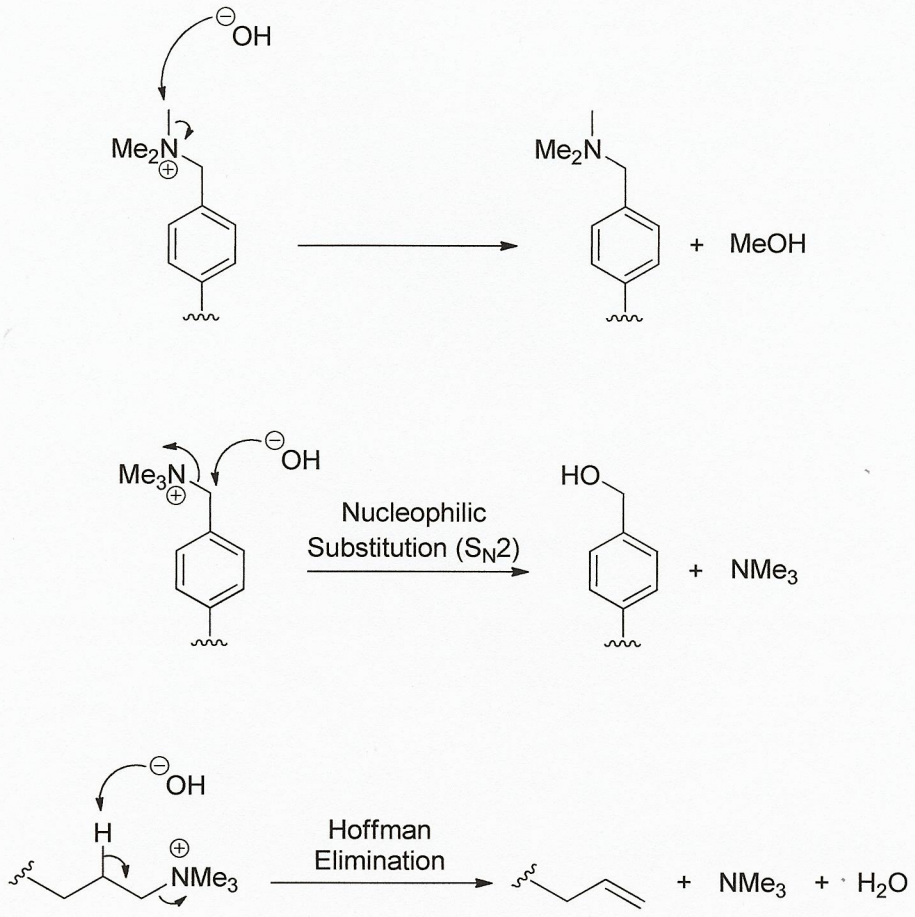

Figure 1.11. Hydroxide ion-induced nucleophilic substitution (S_N2) attack and Hoffman elimination in $-NR_3^+$ based Alkaline Anion Exchange Membranes, (redrawn from [47]).

As a result of the above problems, R&D investment in AFC's and Direct Alcohol AAEM-based fuel cells has been a very small fraction of that in PEMFC and DMFC

development. However, recent advances could be set to change this situation dramatically.

1.6. Recent research on the development of AAEM's.

Varcoe and Slade [74] initially worked on the development of an AAEM formed by radiation-grafting of vinylbenzyl chloride onto poly-(tetrafluoroethylene-co-hexafluoropropylene), FEP, see fig. 1.12.

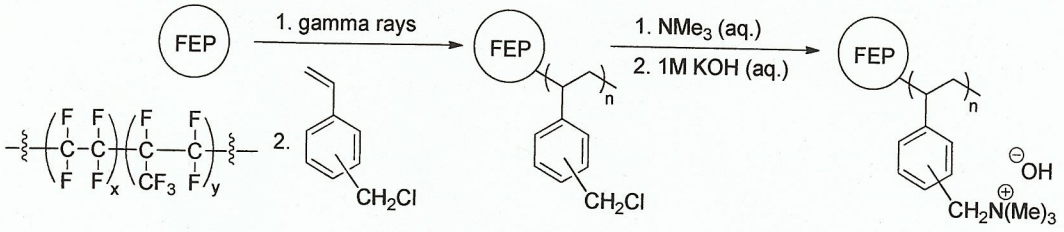

Figure 1.12. Preparation of FEP-g-PVBC radiation-grafted membranes from FEP and vinylbenzyl chloride. Subsequent amination and ion-exchange yields FEP-grafted-poly(vinylbenzyltrimethlammonium hydroxide) alkaline anion-exchange membranes (FEP-g-PVBTMAOHRG-AAEMs) [74].

The polymer exhibited conductivities between 0.010 and 0.035 S cm^{-1} over the temperature range 20 °C – 80 °C, which compared favourably with that of Nafion, 0.100 S cm^{-1} [74, 75]. However, the AAEM lacked sufficient physical strength for use in a fuel cell, and the Surrey group focussed on an AAEM where the FEP was replaced by poly-(ethylene-co-tetrafluoroethylene), ETFE, see fig. 1.13 [69].

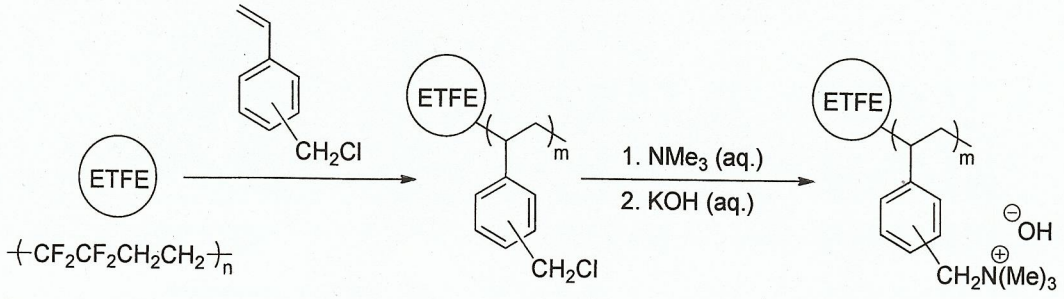

Figure 1.13. The synthesis of radiation-grafted ETFE alkaline anion exchange membrane (AAEM) [69].

As with the FEP-based AAEM, ETFE-VBC offers no beta-hydrogen atoms for Hoffman elimination [47].

Initial studies of the ETFE polymer were extremely promising; the polymer showed an Ion Exchange Capacity (IEC) of 1.42 x 10^{-3} mol(OH^-) g^{-1} (dry polymer) compared to 0.92 x 10^{-3} (H^+) g^{-1} (dry polymer) for Nafion [76], and a thickness when fully hydrated of 153 ± 3 μm (Nafion 117 = 183 μm, 115 = 127 μm [77]).

The Surrey group sought to address the "ionomer problem" by employing an "interfacial polymer" [69, 78], The carbon-supported Pt electrodes were sprayed with poly-vinyl benzyl chloride dissolved in ethyl acetate, after which they were immersed in N,N,N',N'-tetramethylhexane-1,6-diamine to effect crosslinking, see fig. 1.14.

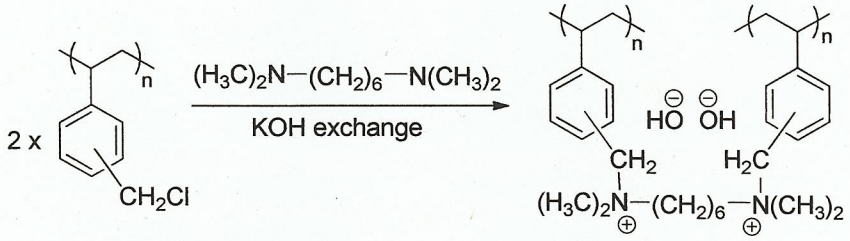

Figure 1.14. The synthesis of the alkaline polymer electrochemical interface [69].

The performance of the ETFE-based AFC was promising: using H_2 and O_2 at a flow rate of 2 dm^3 min^{-1} and 100% relative humidity, a peak power density of 130 mW cm^{-2} was obtained, which compared favourably with 480 mW cm^{-2} obtained with Nafion 115 under the same conditions [69], see fig. 1.15.

The initial data obtained by the Surrey group using methanol as fuel was poor and has remained poor since; Varcoe and Slade [69] observed a maximum power density of 1.5 – 8.5 mW cm^{-2} at 50 – 80 °C compared to 30 – 80 mW cm^{-2} for Nafion based DMFC's under similar conditions. However, the data did compare favourably to literature values [71, 79] obtained using commercial AAEM's and employing NaOH added to the fuel stream. Adding base to the alcohol feed facilitates the delivery of OH^- to catalyst sites (necessary in the absence of ionomer) and prevents the build-up of CO_3^{2-}/HCO_3^- (see below) [47]. The Surrey group did not follow this approach as, in their view, it adds engineering complexity and reduces energy density [47], and hence negates one of the key advantages of employing AAEM's. Furthermore, durability

studies using methanol and air showed a very low performance loss [78]. On the basis of their data, they suggested that base was not required in the fuel feed of direct alcohol AFC's utilising on their AAEM.

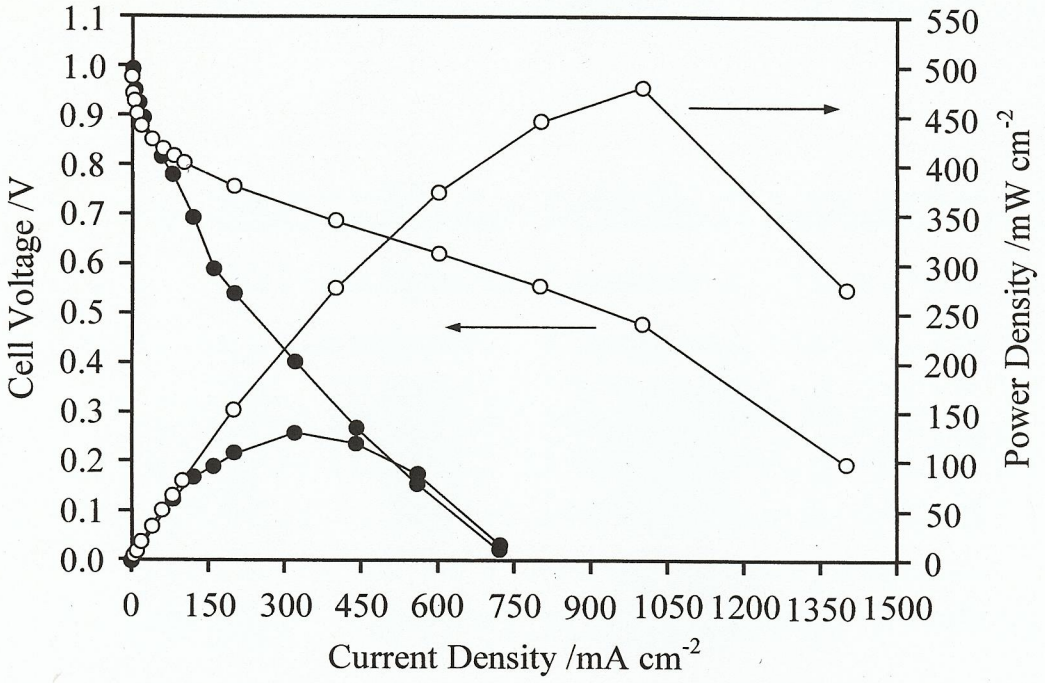

Figure 1.15. The H_2/O_2 fuel cell performance obtained by Varcoe and Slade at 50 °C (no back-pressure) of the 4 mg cm^{-2} catalysed AAEM-MEA (•) compared to an analogous Nafion115-MEA (○, the same electrodes but coated with 0.8 mg cm^{-2} Nafion dispersion and pressed at 120 kgf cm^{-2} at 135 °C for 3 min) [69].

The initial papers on the ETFE based AAEM's were submitted by Varcoe and Slade in early 2006 [69, 78]. By summer of the same year, they had come to realize that the performance of the ETFE-based AFC's (H_2/O_2) seemed to be incapable of improvement beyond a fraction of that observed with PEMFC's [80]; e.g. the highest obtained to date being 230 mW cm^{-2} at 50 °C [81], compared to 770 mW cm^{-2} at 65 °C [82] or 1070 mW cm^{-2} at 80 °C [83] for Nafion-based PEMFC's.

With respect to methanol, the performance of the ETFE membrane was significantly worse, with peak power densities remaining $\prec$ 10 mW cm^{-2} [84], Varcoe and Slade postulated the existence of a general problem at the cathode for their ETFE-based fuel cells, due to the lack of sufficient water reaching actives sites on the cathode catalyst [80, 84], see equation (1.10).

$$H_2O + \tfrac{1}{2}O_2 + 2e^- \rightarrow 2OH^- \quad (1.10)$$

A significant source of water is back transport from the anode where it is produced from the oxidation of methanol, see equation (1.11).

$$CH_3OH + 6OH^- \rightarrow CO_2 + 6e^- + 5H_2O \quad (1.11)$$

This back transport is opposed to the transport of OH^- from cathode to anode. At high current densities, high flow rates are required, which lower the relative humidity at the anode and hence, reduce the back transport. This postulate does not, however, explain the extremely poor performance generally observed with direct alcohol alkaline fuel cells employing AAEM's [18, 47, 85].

In order to explain the generally poor performance of direct alcohol AAEM AFC's, some workers, including the Surrey group [86] and Johnson Matthey [87] have looked back to the work of Zhuang and co-workers in 2003 [88], which has not been fully regarded until recently.

Zhuang and co-workers employed model calculations to show that, at 20 °C, a pH difference of 6.1 would exist across the AAEM of direct alcohol AFC due to CO_2 produced at the anode forming HCO_3^-/CO_3^{2-} lowering the pH there compared to the high pH maintained at the cathode by the continuous production of OH^- ions according to equation (1.10). This pH difference equated to a potential drop of 360 mV at 20 °C, falling to 290 mV at 80 °C. If realized in practice, this would lower the cell voltage to unacceptable levels, and would lead to unsustainable incorporation of carbonate into the membrane with a steady decline in performance. However, Zhuang et al.'s calculations employed the aqueous solution thermodynamic values of the various species (HCO_3^-, CO_3^{2-}, etc.) and assumed a CO_2 pressure at the anode of 1 atmosphere, which will clearly differ from the actual values in the membrane. Furthermore, Zhuang et al. demonstrated that the thermodynamic potential losses associated with the pH difference would be cancel out by kinetics gains associated with operation at higher temperatures and current densities (due to improved electrode kinetics), as well as expected gains due to reduced alcohol crossover.

It is difficult to analyse the performance of direct alcohol fuel cells due to the controversy surrounding the inclusion of KOH into the fuel feed [18, 89], and the lack of long term performance data. However, where KOH is not added to the fuel feed, the performance is poor, but relatively stable [71, 78], Where CO_2 is a minor product, e.g. direct ethanol fuel cells, there is little evidence of carbonate incorporation into the membrane nor of performance degradation over time [90]. The development of AAEM's is relative to PEM's, still in its infancy, and hence the data remains encouraging and new materials continue to be reported [18, 44, 85]; thus Coates et al. [91, 92] recently reported AAEM's based on the copolymerization of compound 1 (see fig. 1.16) with cyclo-octene:

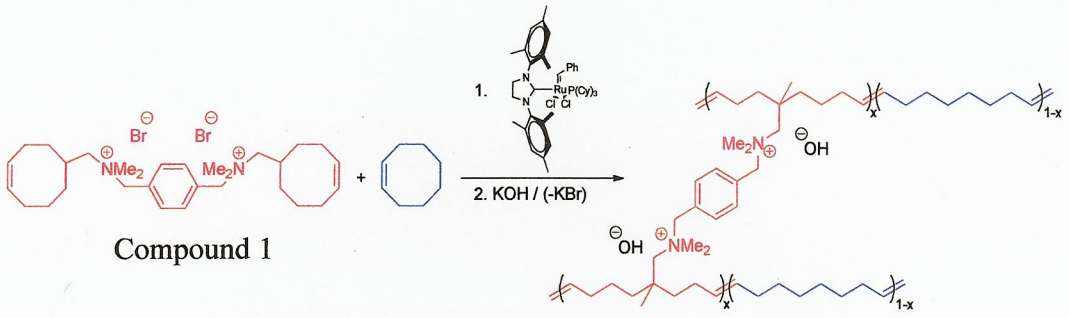

Figure 1.16. The general AAEM synthesis of Coates et al. includes combining compound 1 and COE in a chloroform/methanol cosolvent; addition of the Grubbs second generation catalyst, followed by transfer to a metal dish at 35 °C and subsequent hydroxide ion exchange furnishes the desired AAEM [92].

These AAEM's gave optimum ionic conductivities identical to Nafion at $T \geq 50$ °C (e.g. 0.111 S cm^{-1} at 50 °C) and IEC's of 2.3 ± 0.2 mmoles OH^- g^{-1}. The authors have also reported the synthesis of ionomers [92].

1.7. Composite anodes.

A detailed introduction to the work on composite anodes is given in Chapter 7. Briefly, it was found that a thin (120 nm) layer of TiO_2 deposited on a Si wafer gave significant photocurrent when irradiated with UV light, and that this photocurrent resulted in the production of OH radicals at the TiO_2/aqueous interface. By depositing a gold grid onto the TiO_2, and biasing the grid negative with respect to the Si, OH radicals were produced in the dark [22]. Preliminary experiments carried out prior to

the work reported in this thesis suggested that such composite anodes may have application in fuel cell technology [25].

1.8. Research objectives.

The work reported in this thesis seeks to investigate the electro-oxidation of methanol and ethanol at polycrystalline Pt electrodes in aqueous KOH using *in-situ* Fourier Transform Infrared (FTIR) spectroscopy in order to provide a theoretical basis (and a spectral database of intermediates and products) to extend the work to the study of novel, non-noble metal compounds (i.e. Ni/Ni alloys as first approach) and hence identify potential anode catalysts for use in direct alcohol alkaline fuel cells, DAAFC's. Once identified, the active metals will then be evaluated as anode catalyst in a small scale (9 cm^2) DAAFC. As part of the later aspect of the research, a novel, alkaline anion exchange membrane, and an ionomeric form of the membrane, developed in Newcastle will be evaluated.

In addition to the above, the electrochemistry of $Si/TiO_2/Au$ composite anodes will be evaluated, initially in acidic electrolyte (to follow on from the preliminary studies) in order to elucidate the mechanism by which charge transport takes place through the anode, and how this influences electrochemistry at the gold grid. The potential application of these novel materials in fuel cell technology will then be evaluated.

1.9. References

1. Levine I.N., (2002). *Physical chemistry international edition*, 5 ed. New York: McGraw-Hill Science Engineering.
2. McLean G.F., Niet T., Prince-Richard S., and Djilali N., (2002). International Journal of Hydrogen Energy, 27, 5, pp. 507-526.
3. Adzic R.R., Avramov-Ivic M.I., and Tripkovic A.V., (1984). Electrochimica Acta, 29, 10, pp. 1353-1357.
4. Spendelow J.S. and Wieckowski A., (2007). Physical Chemistry Chemical Physics, 9, 21, pp. 2654-2675.
5. Brito P.S.D. and Sequeira C.A.C., (1994). Journal of Power Sources, 52, 1, pp. 1-16.
6. Xu J., Huang W., and McCreery R.L., (1996). Journal of Electroanalytical Chemistry, 410, 2, pp. 235-242.
7. Morcos I. and Yeager E., (1970). Electrochimica Acta, 15, 6, pp. 953-975.
8. Bagotzky V.S., Shumilova N.A., Samoilov G.P., and Khrushcheva E.I., (1972). Electrochimica Acta, 17, 9, pp. 1625-1635.
9. Sepa D.B., Vojnovic M.V., and Damjanovic A., (1980). Electrochimica Acta, 25, 11, pp. 1491-1496.

10. Schmidt T.J., Stamenkovic V., Arenz M., Markovic N.M., and Ross P.N., (2002). Electrochimica Acta, 47, 22-23, pp. 3765-3776.
11. Jörissen L., (2006). Journal of Power Sources, 155, 1, pp. 23-32.
12. Lima F.H.B., Calegaro M.L., and Ticianelli E.A., (2006). Journal of Electroanalytical Chemistry, 590, 2, pp. 152-160.
13. Mao L., Sotomura T., Nakatsu K., Koshiba N., Zhang D., and Ohsaka T., (2002). Journal of The Electrochemical Society, 149, 4, pp. A504-A507.
14. Gojkovic S.L., Gupta S., and Savinell R.F., (1999). Journal of Electroanalytical Chemistry, 462, 1, pp. 63-72.
15. Bettelheim A., White B.A., and Murray R.W., (1987). Journal of Electroanalytical Chemistry and Interfacial Electrochemistry, 217, 2, pp. 271-286.
16. Zagal J., Páez M., Tanaka A.A., dos Santos Jr J.R., and Linkous C.A., (1992). Journal of Electroanalytical Chemistry, 339, 1-2, pp. 13-30.
17. Song C., Zhang L., and Zhang J., (2006). Journal of Electroanalytical Chemistry, 587, 2, pp. 293-298.
18. Antolini E. and Gonzalez E.R., (2010). Journal of Power Sources, 195, 11, pp. 3431-3450.
19. Barendrecht E., (1993). *Electrochemistry of fuel cells*, in: Fuel Cell Systems, J.M.J. Blomen and M.N. Mugerwa Editors, Plenum Press, New York. p. 73-120.
20. Appleby A.J., (1993). *Characteristics of fuel cell systems*, in: Fuel Cell Systems, J.M.J. Blomen and M.N. Mugerwa Editors, Plenum Press, New York, p. 157-200.
21. Hamnett A., (2003). *Introduction to fuel-cell types*, in: Handbook of Fuel Cells Fundamental Technology and Applications, W. Vielstich, A. Lamm, and H.A. Gasteiger Editors, John Wiley & sons Ltd. p. 36 - 43.
22. Christensen P.A. and Hamnett A., (1994). *Techniques and Mechanisms in Electrochemistry*, 1 ed. Oxford: Blackie Academic & Professional, an imprint of Chapman & Hall. 396.
23. Srinivasan S., Davé B.B., Murugesamoorthi K.A., Parthasarathy A., and Appleby A.J., (1993). *Overview of fuel cell technology*, in: Fuel Cell Systems, J.M.J. Blomen and M.N. Mugerwa Editors, Plenum Press, New York. p. 37 - 72.
24. Gtilzow E., (1996). Journal of Power Sources, 61, 1-2, pp. 99-104.
25. Martin R.E. and Manzo M.A. (1988). in 23rd Intersociety Energy Conversion Engineering Conference. Denver CO. 301 - 304.
26. Cifrain M. and Kordesch K.V., (2004). Journal of Power Sources, 127, 1-2, pp. 234-242.
27. Scott J.H., (2009). Journal of Fuel Cell Science and Technology, 6, 2, pp. 021011-7.
28. Wagner H.A., (2003). *Space-shuttle fuel cell*, in: Handbook of Fuel Cells Fundamental Technology and Applications, W. Vielstich, A. Lamm, and H.A. Gasteiger Editors, John Wiley & sons Ltd. p. 1224 - 1230.
29. Matryonin V.I., Ovchinikov A.T., and Tzedilkin A.P. International Journal of Hydrogen Energy, 22, 10-11, pp. 1047-1052.
30. Jo J.-H. and Yi S.-C., (1999). Journal of Power Sources, 84, 1, pp. 87-106.
31. IEEE. Bacon's fuel cell. [Web page] (2010) [cited 2011 26/07/2011]; Available from: http://www.ieeeghn.org/wiki/index.php/Bacon%27s fuel cell.
32. NASA. Fast facts: Apollo fuel cells. (2010) [cited 2011 26/07/2011]; Available from: http://galaxywire.net/tag/fuel-cell/.

33. Smithsonian. Fuel cells: Allis-Chalmers fuel-cell tractor. (1998) [cited 2011 26/07/2011]; Available from: http://historvwired.si.edu/detail.cfm?ID=223.
34. Kordesch K., Hacker V., Gsellmann J., Cifrain M., Faleschini G., Enzinger P., Fankhauser R., Ortner M., Muhr M., and Aronson R.R., (2000). Journal of Power Sources, 86, 1-2, pp. 162-165.
35. Fuelcells.org. Fuel cell vehicles. (2011) [cited 2011 26/07/2011]; Available from: http://www.fuelcells.org/info/charts/carchart.pdf.
36. Kordesch K., Gsellmann J., and Cifrain M. (1998). in Proceeding Fuel Cell Seminar. Palm Springs.
37. De Geeter E., Mangan M., Spaepen S., Stinissen W., and Vennekens G., (1999). Journal of Power Sources, 80, 1-2, pp. 207-212.
38. Swette L., Kosek J.A., Cropley C.C., and LaConti A.B. (1993). in Proceedings of the Intersociety Energy Conversion Engineering Conference. 1227-1232.
39. Kiros Y., Myrén C., Schwartz S., Sampathrajan A., and Ramanathan M., (1999). International Journal of Hydrogen Energy, 24, 6, pp. 549-564.
40. Tomantschger K., McClusky F., Oporto L., Reid A., and Kordesch K., (1986). Journal of Power Sources, 18, 4, pp. 317-335.
41. Michael P., (2000). *An assessment of the prospects for fuel cell powered cars*. ETSU, R-126 GB_ 2000:12033, 43.
42. Vegas A., Garcia C., and Gonzalez A. (1998). in Proceeding Hydrogen Energy Progress XII. Buenos Aires. 1621 - 1628.
43. Schulze M. and Gülzow E., (2009). *FUEL CELLS - ALKALINE FUEL CELLS. Overview Performance and Operational Conditions*, in: Encyclopedia of Electrochemical Power Sources, Elsevier, Amsterdam, p. 353-361.
44. Merle G., Wessling M., and Nijmeijer K., (2011). Journal of Membrane Science, 377, 1-2, pp. 1-35.
45. USDOE, (2004). *Fuel Cell Handbook*. U.S.D.o. Energy, DE-AM26-99FT40575.
46. Carrette L., Friedrich K.A., and Stimming U., (2001). Fuel Cells, 1, 1, pp. 5- 39.
47. Varcoe J.R. and Slade R.C.T., (2005). Fuel Cells, 5, 2, pp. 187-200.
48. Dunn S., (2002). International Journal of Hydrogen Energy, 27, 3, pp. 235-264.
49. Stone C. and Morrison A.E., (2002). Solid State Ionics, 152-153, pp. 1-13.
50. Cohen D., (2002). NewScientist, 2365, pp. 40 - 44.
51. Ren X., Zelenay P., Thomas S., Davey J., and Gottesfeld S., (2000). Journal of Power Sources, 86, 1-2, pp. 111-116.
52. fiveIPoffices. Patents & IP register office. (2011) [cited 2011 27/07/2011]; Available from: www.fiveipoffices.org/.
53. FuelCellToday, (Accessed 27/07/2011). http://www.fuelcelltodav.com/media/pdf/surveys/2011-Fuel-Cell-Patent-Review.pdf.
54. Horizon F.C.T., (Accessed 27/07/2011). http://www.horizonfuelcell.com/electronics.htm.
55. Stone C,, (2007). Fuel Cells Bulletin, 2007, 10, pp. 12-15.
56. Achmad F., Kamarudin S.K., Daud W.R.W., and Majlan E.H. Applied Energy, 88, 5, pp. 1681-1689.
57. Lamy C., Belgsir E.M., and Léger J.M., (2001). Journal of Applied Electrochemistry, 31,7, pp. 799-809.
58. Tripkovic A.V., Popovic K.D., Grgur B.N., Blizanac B., Ross P.N., and Markovic N.M., (2002). Electrochimica Acta, 47, 22-23, pp. 3707-3714.

59. Yu E.H., Scott K., and Reeve R.W., (2003). Journal of Electroanalytical Chemistry, 547, 1, pp. 17-24.
60. Hamnett A., (1997). Catalysis Today, 38, 4, pp. 445-457.
61. Watanabe M. and Motoo S., (1975). Journal of Electroanalytical Chemistry, 60, 3, pp. 275-283.
62. Chen Q.-S., Sun S.-G., Zhou Z.-Y., Chen Y.-X., and Deng S.-B., (2008). Physical Chemistry Chemical Physics, 10, 25, pp. 3645-3654.
63. Bockris J.O., Conway B.E., and White R.E., (2001). *Modem Aspects of Electrochemistry*. Vol. 34. New York: Plenum Press. 200.
64. Koscher G.A. and Kordesch K., (2003). Journal of Solid State Electrochemistry, 7, 9, pp. 632-636.
65. Vielstich W. and Vogel U. (1967). in 5th Biennial Fuel Cell Symposium. Chicago: American Chemical Society. 341.
66. Dickinson A.J., (2000). *Development of a Direct Methanol Fuel Cell System*. PhD Thesis. Newcastle upon Tyne: Newcastle University.
67. Costamagna P. and Srinivasan S., (2001). Journal of Power Sources, 102, 1-2, pp. 242-252.
68. Hamnett A., (2003). *Direct methanol fuel cells (DMFC)*, in: Handbook of Fuel Cells Fundamental Technology and Applications, W. Vielstich, A. Lamm, and H.A. Gasteiger Editors, John Wiley & sons Ltd. p. 305 - 322.
69. Varcoe J.R. and Slade R.C.T., (2006). Electrochemistry Communications, 8, 5, pp. 839-843.
70. Carrette L., Friedrich K.A., and Stimming U., (2000). ChemPhysChem, 1, 4, pp. 162-193.
71. Yu E.H. and Scott K., (2004). Journal of Power Sources, 137, 2, pp. 248-256.
72. Yu E.H. and Scott K., (2005). Journal of Applied Electrochemistry, 35, 1, pp. 91-96.
73. Larmine J. and Dicks A., (2003). *Fuel cell systems explained*, 2 ed: John Wiley & Sons Ltd. 406.
74. Slade R.C.T. and Varcoe J.R., (2005). Solid State Ionics, 176, 5-6, pp. 585- 597.
75. Silva R.F., De Francesco M., and Pozio A., (2004). Journal of Power Sources, 134, 1, pp. 18-26.
76. Hubner G. and Roduner E., (1999). Journal of Materials Chemistry, 9, 2, pp. 409-418.
77. DuPont, (Accessed 27/07/2011). http://www2.dupont.com/FuelCells/en US/assets/downloads/dfcl01.pdf.
78. Varcoe J.R., Slade R.C.T., and Lam How Yee E., (2006). Chemical Communications, 13, pp. 1428-1429.
79. Coutanceau C., Demarconnay L., Lamy C., and Léger J.M., (2006). Journal of Power Sources, 156, 1, pp. 14-19.
80. Varcoe J.R., Slade R.C.T., Wright G.L., and Chen Y., (2006). The Journal of Physical Chemistry B, 110, 42, pp. 21041-21049.
81. Poynton S.D., Kizewski J.P., Slade R.C.T., and Varcoe J.R., (2010). Solid State Ionics, 181, 3-4, pp. 219-222.
82. Soehn M., S.Zils, Nicoloso N., and Roth C., (2011). Journal of Power Sources, 196, 15, pp. 6079-6084.
83. Liu X., Villacorta R., Adame A., and Kannan A.M., (2011). International Journal of Hydrogen Energy, In Press, Corrected Proof, doi:10.1016/j.ijhydene.2011.05.141.

84. Varcoe J.R., Slade R.C.T., Lam How Yee E., Poynton S.D., Driscoll D.J., and Apperley D.C., (2007). Chemistry of Materials, 19, 10, pp. 2686-2693.
85. Yu E.H., Krewer U., and Scott K., (2010). Energies, 3, 8, pp. 1499-1528.
86. Varcoe J.R., (2010). *Performance of AAEM AFC's (Private communication)*. Christensen, [Recip],
87. Hogarth M., (2010). *(Private communication)*. Christensen, [Recip],
88. Wang Y., Li L., Hu L., Zhuang L., Lu J., and Xu B., (2003). Electrochemistry Communications, 5, 8, pp. 662-666.
89. Yu E.H., Scott K., Reeve R.W., Yang L., and Allen R.G., (2004). Electrochimica Acta, 49, 15, pp. 2443-2452.
90. Bianchini C., Bambagioni V., Filippi J., Marchionni A., Vizza F., Bert P., and Tampucci A., (2009). Electrochemistry Communications, 11, 5, pp. 1077- 1080.
91. Robertson N.J., Kostalik H.A., Clark T.J., Mutolo P.F., Abruna H.D., and Coates G.W., (2010). Journal of the American Chemical Society, 132, 10, pp. 3400-3404.
92. Kostalik H.A., Clark T.J., Robertson N.J., Mutolo P.F., Longo J.M., Abruna H.D., and Coates G.W., (2010). Macromolecules, 43, 17, pp. 7147-7150.

2. Experimental

2.1. List of reagents

Reagent / Material	Analysis	Supplier
Acetic acid, ReagentPlus® (CH_3COOH)	≥ 99 %	Sigma-Aldrich Cat No A6283
Ammonium hydroxide solution 28% in H_2O	99.99+ %	Sigma-Aldrich Cat No 338818
Carbon paper (Toray TGPH-60)	—	E-Tek inc.
Cobalt (II) nitrate hexahydrated, Puriss p.a. ($Co(NO_3)_2.6H_2O$)	ACS reagent Ni ≤ 0.001%.	Sigma-Aldrich Cat No 60832
Ethanol absolute (C_2H_5OH)	> 99.5 % ACS	Sigma-Aldrich Cat No 459844
Ethylene glycol ($HOCH_2CH_2OH$)	99+ %	Sigma-Aldrich Cat No 10,246-6
Gold (Au)	99.99 %	Goodfellow Ltd. Au005137/2
Hydrogen mix (H_2 35%, Ar)	35 % H_2	BOC Gases
Hydrogen peroxide solution, stabilized (H_2O_2)	35 wt.% Puriss	Riedel-de Haën Cat No 18304
Methanol (CH_3OH)	> 99.9 % ACS	Sigma-Aldrich Cat No 154903
Millipore water (H_2O)	(18.2 MΩ.cm)	Millipore
Nafion® perfluorinated ion-exchange resin, 5wt % in a mixture of lower aliphatic alcohols & H_2O	5 wt.%	Sigma-Aldrich Cat No 510211
Nafion 117® perfluorinated membrane.	—	DuPont
Nickel (II) Chloride hexahydrated ($NiCl_2.6H_2O$)	Reagent plus	Sigma-Aldrich Cat No 22,338-7
Oxalic acid (HOOCCOOH)	98%	Sigma-Aldrich Cat No 194131
Oxygen (O_2)	> 95 %	BOC gases
Palladium dichloride ($PdCl_2$)	99.9 %	Sigma-Aldrich Cat No 520659
PolyTetraFluoroEthylene preparation 60 wt. % dispersion in H_2O (PTFE)	60 % wt	Sigma-Aldrich Cat No 665800
Potassium chloride (KC1)	> 99.0 %	Sigma-Aldrich Cat No P9333

Potassium ferrocyanide trihydrate ($K_3Fe(CN)_6.3H_2O$)	ACS reagent	Analar Analytical Cat No 6986
Potassium fluoride (KF)	≥ 99.99 %	Sigma-Aldrich Cat No 449148
Potassium hydroxide (KOH)	>85 %	Sigma-Aldrich Cat No P1767
Potassium Iodide (KI)	≥ 99.0 %	Sigma-Aldrich Cat No P2963
Potassium Nitrate (KNO_3)	99.999 %	Sigma-Aldrich Cat No 542049
Potassium phosphate, monobasic (KH_2PO_4)	99%	Sigma-Aldrich Cat No P0662
Platinum 10% on activated carbon (Pt/carbon)	10%	Sigma-Aldrich Cat No 205958
Platinum 20% wt. on carbon, HiSpec (Pt-nom. 20% /C)	20%	Alfa Aesar Cat No 035849
Platinum Ruthenium on carbon, HiSpec (Pt-nom. 40 % Ru-nom. 20 % / C)	—	Alfa Aesar Item 44172
2-Propanol $(CH_3)_2CHOH$	99.5 %	Sigma-Aldrich Cat No 278475
Ruthenium(III) chloride hydrated ($RuCl_3.XH_2O$)	40% (minimum Ru)	Alfa Aesar Item 011043
Sodium bicarbonate ($NaHCO_3$)	> 99.5 %	Sigma-Aldrich Cat No S6297
Sodium borohydride ($NaBH_4$)	> 98.5 %	Sigma-Aldrich Cat No 45,288-2
Sodium carbonate (Na_2CO_3)	> 99.0 %	Sigma-Aldrich Cat No S7795
Sodium formate, puriss (HCOONa)	99+ % ACS reagent	Sigma-Aldrich Cat No 71541
Sodium hydroxide (NaOH)	> 98 %	Sigma-Aldrich Cat No S8045
Sodium sulphate (Na_2SO_4)	> 99.0 %	Sigma-Aldrich Cat No 23931-3
Sulfuric acid (H_2SO_4)	95.0 – 98.0 %	Sigma-Aldrich Cat No 258105
Vulcan carbon black XC-72	—	Cabot corp.

Table 2.1 List of chemicals employed in the work reported in this thesis.

2.2. Synthesis of catalyst macroparticles

The catalyst synthesis was based on the work reported by Tarasevich et al. [1, 2], Macroparticles are defined as having diameters *d*, 0.1 μm < d < 100 μm. Taking the procedure for Ru:Ni 60:40 as typical: 0.2527 g of $RuCl_3.xH_2O$ and 0.1585 g $NiCl_2.6H_2O$ were dissolved in 100 cm^3 of H_2O + methanol 1:1 (v/v), and stirred for 5 minutes to give a black solution with concentrations of Ru^{3+} and Ni^{2+} of 10 mM and 6.67 mM respectively, such that the Ru:Ni atomic ratio was 60:40 and the final mass of metal (Ru+Ni) was 0.1402 g. The same general procedure was employed to prepare all the catalysts, i.e. nominally Ru:Ni 72:28 and Ru:Ni 84:16.

0.7945 g of Carbon black XC-72 was added to the Ru + Ni solution with vigorous stirring for 10 minutes in order to assure a final metal content of 15 wt. %. The suspension was then sonicated for 30 minutes in order to ensure impregnation of the metals ions into the porous carbon support, followed by a period of slow stirring for 2 hours. The suspension was then evaporated until dry, ground mechanically, sifted and finally subjected to 400 – 420 °C in an H_2-rich atmosphere (i.e. 35 wt. % H_2 in argon flowing at 20 cm^3 min^{-1}) for 2 hours, in order to reduce the metals and eliminate all chloride ions *via* the formation of HCl gas. Finally, the catalyst powder was left to cool down to room temperature in the same atmosphere overnight.

According to Tarasevich et al. [1, 2], the above procedure produces particles of catalyst mixed as Ru, Ni, Ru-Ni alloys and oxides of both metals (i.e. RuO_x, NiO_y) in non stoichiometric quantities and in proportions that have yet to be clearly defined, since they depend on the materials used and the processing employed.

2.3. Syntheses of catalyst nanoparticles

2.3.1. Ruthenium-nickel

A number of syntheses of nanoparticles have been reported in the literature as catalyst for fuel cells, mainly Pt and Pt-Ru for anode [1], but there are no literature precedents for the synthesis of Ru:Ni nanoparticles. Hence a polyol procedure developed by Dr. H. Christensen (unpublished results) was employed, which was based on a synthesis of Pt:Ru nanoparticles reported elsewhere [2-7]. In the polyol process the metal precursor(s) are suspended or dissolved in a polyol such as ethylene glycol; the resultant glycol-metal precursor mixture is then heated to reflux and the metallic

particles (micron and submicron in size) precipitated out of solution. Targeting a catalyst composition of Ru:Ni 72:28 (at. %), 0.5019 g $RuCl_3$ (48.7 % Ru) and 0.2237 g $NiCl_2.6H_2O$ were dissolved separately in 10 cm^3 ethylene glycol (EG), stirred until dissolved ($t \geq 30$ min). Once dissolved, the solutions were added to form 20 cm^3 of a single dark brown solution containing 0.2446 g Ru and 0.0552 g Ni (i.e. 72:28 molar ratio). The pH of the solution was adjusted to 13, using EG + saturated NaOH solution, to a final volume of 30 cm^3. The solution was heated to 170 °C, and kept at this temperature for 3 hours. 1.2 g of carbon powder (XC-72) was then added and stirred for further 30 minutes, giving a metal content of 20 wt. % on carbon. The solution was allowed cool to 80 °C and stirred for 12 hours to settle the particles; it was then filtered, washed and dried under vacuum at 80 °C.

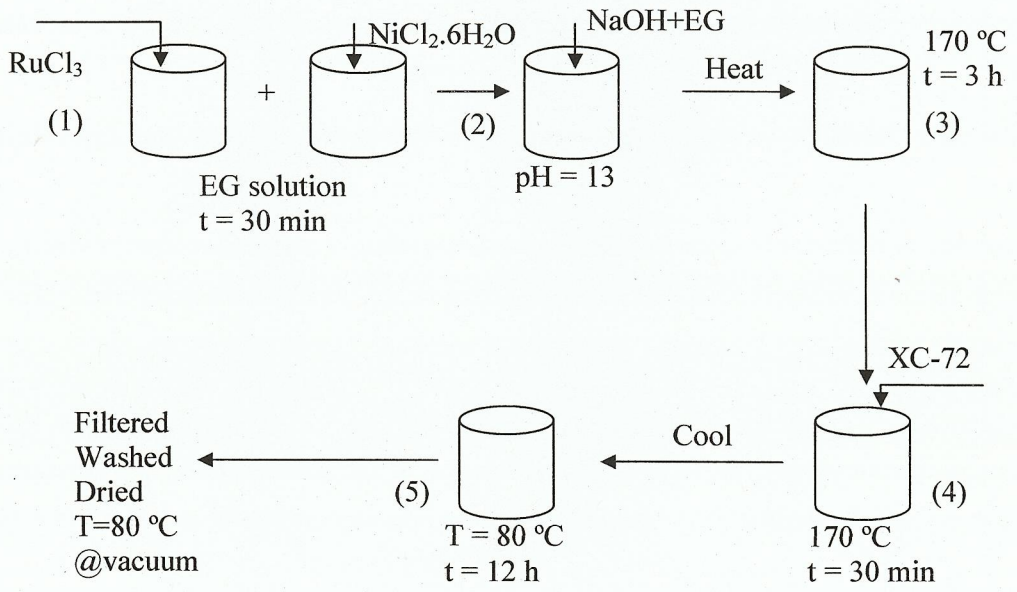

Figure 2.1. Synthesis of Ru:Ni nanoparticles on porous carbon (XC-72).

2.3.2. Palladium-nickel

On the basis of the work of Zhao et al. [8] and Sung et al [9], the target composition of the Pd:Ni catalyst was 40:60 (at. %); they found this to be the most active anode catalyst with respect to ethanol oxidation. The synthetic procedure employed by Zhao et al. [8] was as follows (see fig. 2.2):

0.2736 g $PdCl_2$ and 0.3034 g $NiCl_2.6H_2O$ were dissolved in two aliquots of 25 cm^3 of Millipore water, stirred for 10 min and, once dissolved, mixed together to form a 50 cm^3 brown/terracotta-coloured solution containing 0.1642 g Pd and 0.1358 g Ni (2:3 molar ratio). 1.2 g of carbon powder (XC-72) was added to the combined solution and stirred for a further 30 minutes, giving 20 wt. % (Pd + Ni) on carbon. Finally, 0.030 g $NaBH_4$ was added and stirred for further 10 min, the final decanted solution was filtered, washed and dried under vacuum at 80 °C.

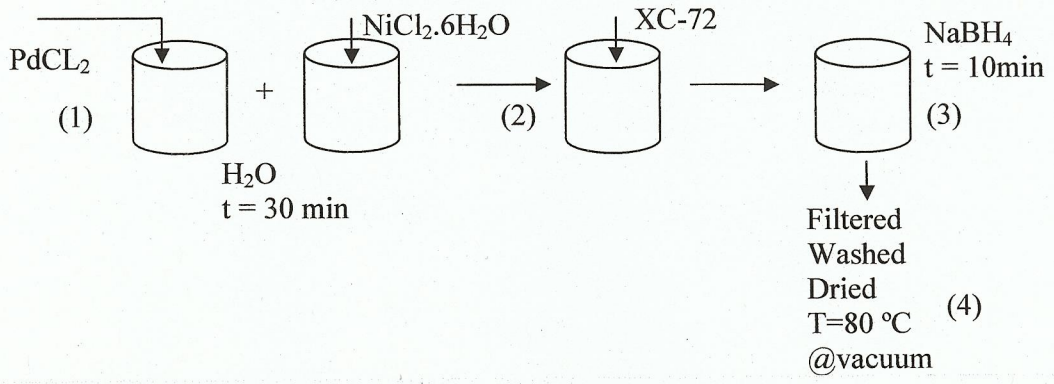

Figure 2.2. Synthesis of Pd:Ni nanoparticles on porous carbon (XC-72).

2.3.3. Cobalt-Nickel:

On the basis of the work of Luna et al. [10], Fernandes et al. [11] and Ferrando et al. [7], the target composition of the Co:Ni catalyst was 50:50 (at. %), the procedure employed was as follows (see fig. 2.3):

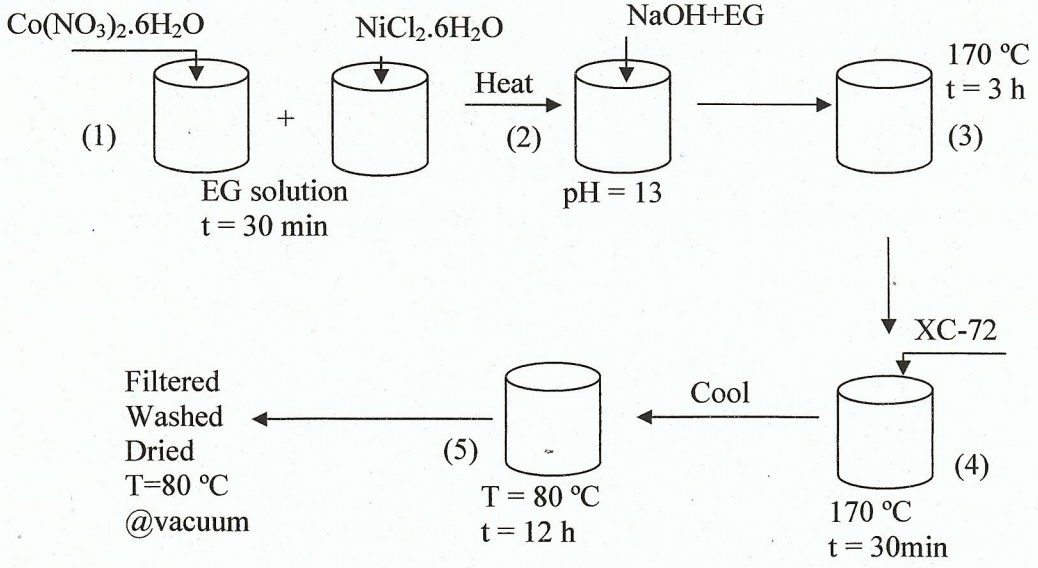

Figure 2.3. Synthesis of Co:Ni nanoparticles on porous carbon (XC-72).

0.74227 g $Co(N0_3)_2.6H_2O$ and 0.60375 g $NiCl_2.6H_2O$ were dissolved in two aliquots of 10 cm^3 EG, stirred for 30 min and, once dissolved, mixed together to form a purple solution containing 0.1503 g Co and 0.1497 g Ni. The pH of the solution was adjusted to 13 using EG + NaOH saturated solution, reaching a final volume of 30 cm^3. The solution was heated to 170 °C and kept at this temperature for 3 hours, after which 1.2 g of carbon powder (XC-72) was added and stirred for a further 30 minutes, giving a final metal content of 20 wt. % (Co + Ni) on carbon. The solution was then cooled to 80 °C and stirred for 12 hours to settle the particles after which it was filtered, washed and dried under vacuum at 80 °C.

2.4. Catalyst ink preparation.

50 mg of catalysed carbon powder was added to 40 µl Millipore water, after which 1 cm^3 of ethanol was added and stirred for 1 minute, sonicated for 5 minutes, and then stirred for another minute. The stir/sonicate/stir steps were repeated 3 times. If the ink was too viscous, i.e. lumps formed on the walls of the container or on the stirrer bar, 0.1 cm^3 of ethanol were added with sonication (and more added as necessary).

Ionomeric Nafion® (5 wt. % in isopropanol) was employed as binder added to the solution just before application to make electrodes; the required quantity of commercial 5 wt.% Nafion solution was used (as received) in order to obtain the required loading of Nafion (i.e. Nafion dry/total mass of catalyst + carbon) and the solution was sonicated for 30 minutes.

2.5. The electrochemical cell

The glass cell used for the electrochemical IVt measurements was designed and built in-house, and was fabricated in two halves, see figs. 2.4(a) and (b). The lower part of the cell comprised a 50 cm^3 receptacle equipped with a jacket for temperature control, constructed from a Quickfit B40 socket; the top part was constructed from a B40 cone. The bottom of the cell was provided with two SQ13 screw-threaded joints to house a counter electrode (Pt or Pt/Ti mesh) and the luggin capillary of the reference electrode. The top (B40 cone) was fitted with a B14 socket, to allow the solution to be sparged with N_2 gas, the sparge inlet being retracted during measurements to allow a N_2 blanket to be maintained above the electrolyte. The top half of the cell also had two

SQ13 screw-threaded joints, one for admitting the working electrode and the other to allow a thermometer to be positioned in the electrolyte before measurements were taken and to house a bubbler, to maintain a positive N_2 pressure within the cell, preventing oxygen entry during measurements.

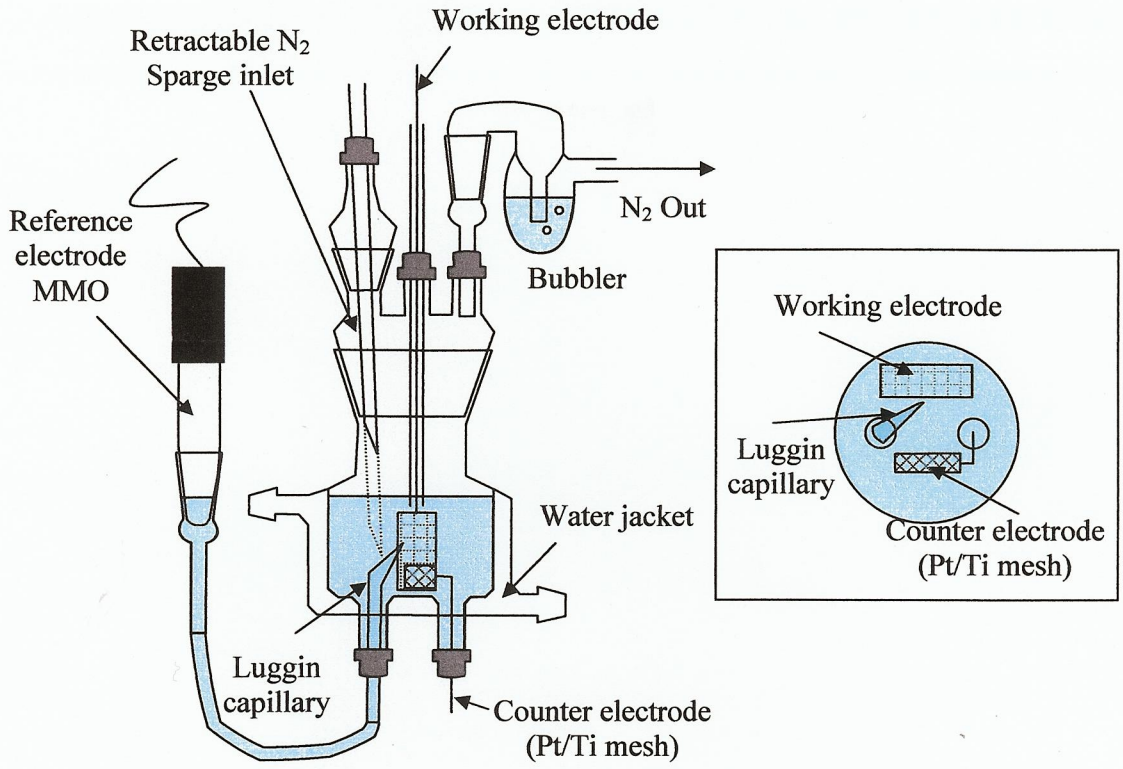

(a)

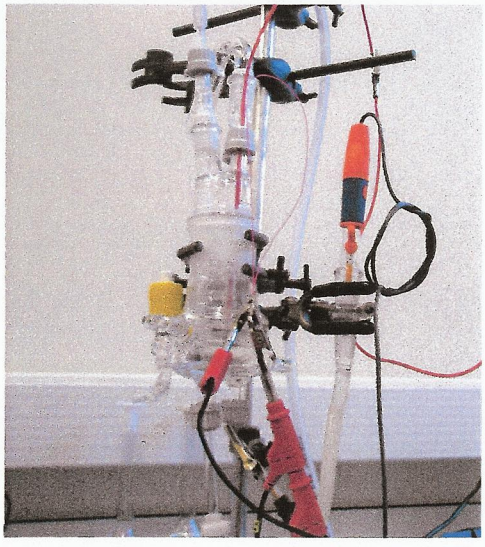

(b)

Figure 2.4. (a) Schematic of the electrochemical cell with top view in inset, (b) Photograph of cell.

Electrochemical experiments were carried out at 25 °C and 60 °C. A Platinized Titanium (Pt/Ti) mesh was used as counter electrode, and a mercury/mercury oxide (MMO) as reference (E°= +0.850V vs. SHE). Before commencing experiments, the cell was allowed to reach the required temperature, after which it was sparged with N_2 gas for 10 minutes, maintaining a blanket of N_2 above the electrolyte with a reduced gas flow.

2.6. In-situ FTIR equipment

2.6.1. The Spectrometer

The FTIR spectrometer was a Varian FTS-7000 equipped with a globar source and a narrow band, liquid N_2-cooled mercury cadmium telluride (MCT) detector.

2.6.2. Optical bench

The optical bench was designed and fabricated in-house and is shown in fig. 2.5.

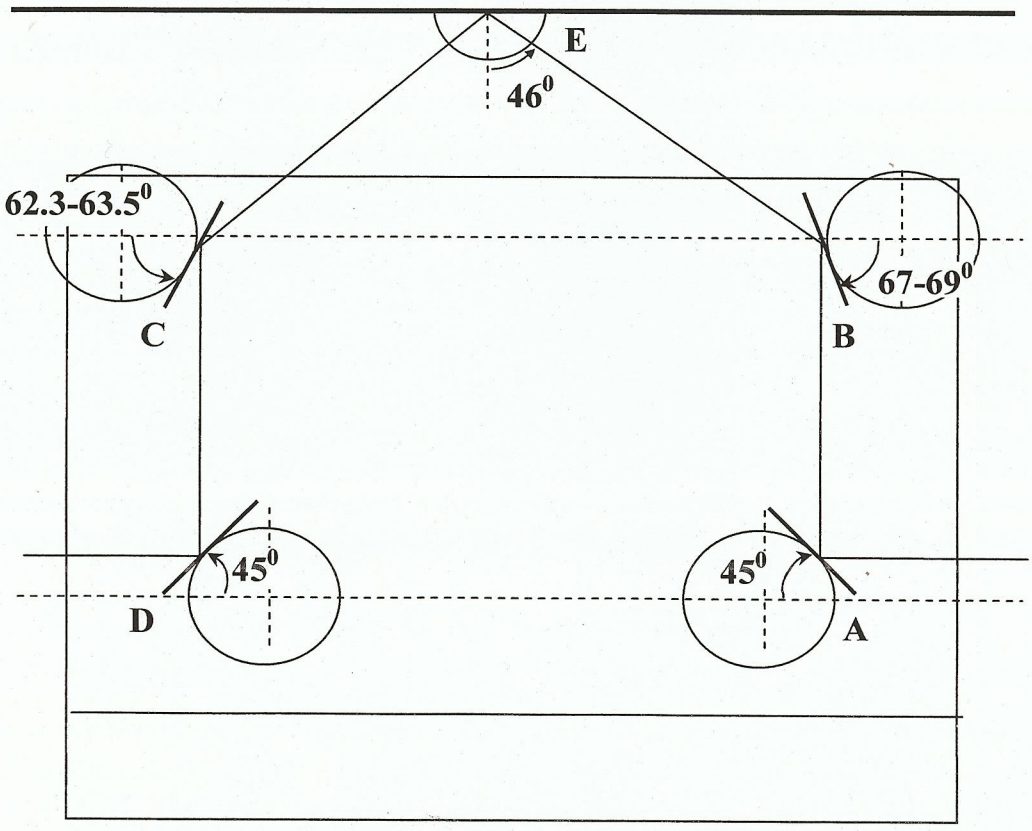

Figure 2.5. Schematic of the optical bench employed in the in situ FTIR experiments. A and D are fixed mirrors, whilst mirrors B and C are adjustable to optimize signal at the detector, E) CaF_2 prism.

The base plate of the bench was designed to fit snugly onto the floor of the sample compartment *via* positioning pins. Two mirrors (A, B) were located in order to direct the IR beam onto the hemispherical cell window (E) and two mirrors (C, D) to direct the beam to the MCT detector of the FT1R spectrometer.

The angle of incidence of the IR beam (assuming 0° beam divergence) on the CaF_2 (n = 1.41, k = 0^{25})/electrolyte interface was 46° (see fig. 2.6, normal incidence at CaF_2/air interface) giving an angle of incidence at the platinum electrode (assuming n = 1.33 and approximating k to 0 for water) of 50°. Even allowing for ± 6° beam spread, the incidence on the inner side of the CaF_2/electrolyte interface is well below the critical angle, hence precluding any enhancement effects due to total internal reflectance [12].

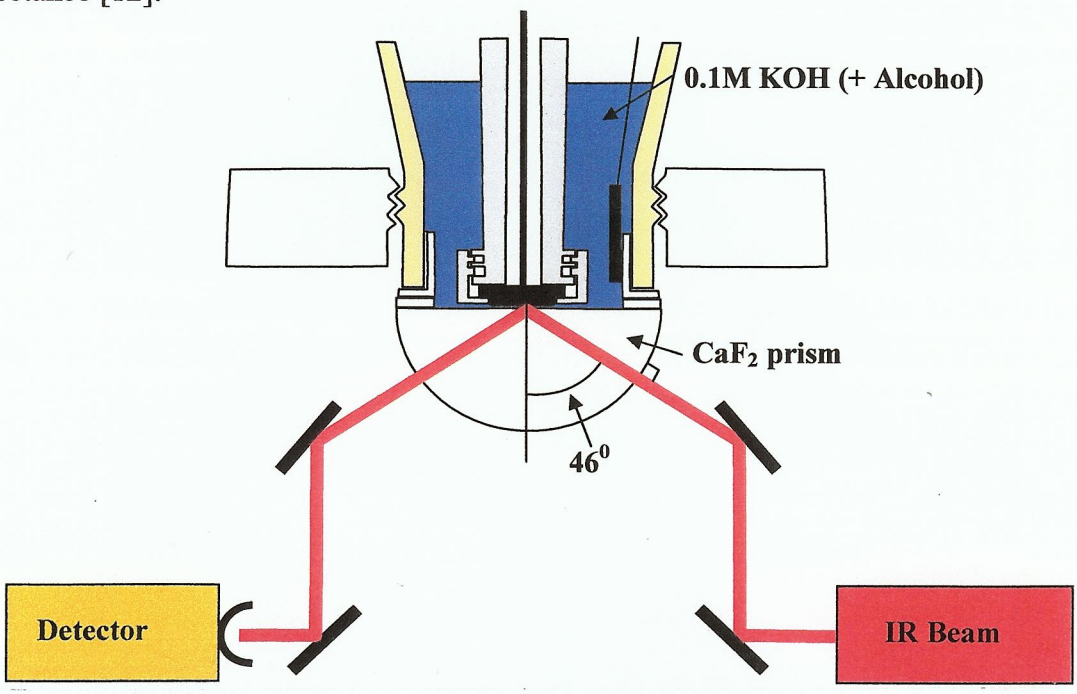

Figure 2.6. Schematic of the spectroelectrochemical system used in in-situ FTIR experiments.

2.6.3. Spectroelectrochemical cell

The spectroelectrochemical cell was home-built and fitted with a hemispherical CaF_2 window (Medway Optics Ltd.) [13, 14], The cell was mounted vertically on the lid of the sample compartment of the spectrometer, see figs. 2.7(a) and (b), and was designed to allow electrolyte exchange under potential control. The cell was jacketed to allow careful control of temperature of the electrolyte in the body of the cell. The plate employed to mount the cell on the sample compartment was hollow to allow the

passage of heating/cooling liquid. The counter electrode was a ca.1.7 cm^2 Pt mesh. A MMO reference electrode was mounted on the top of the cell as can be seen in figs. 2.7(a) and (b). Experiments were carried out at 25 °C. A photograph of the spectrometer with the spectroelectrochemical cell *in-situ* is shown in fig. 2.8.

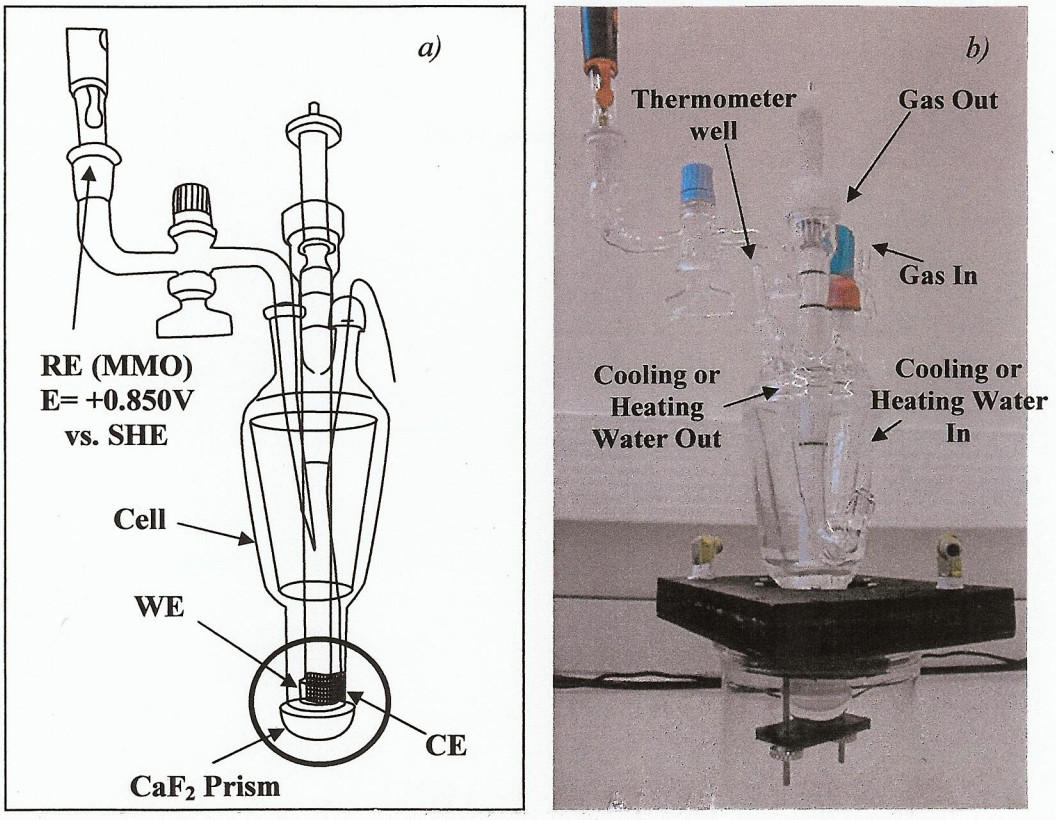

Figure 2.7. Spectroelectrochemical cell a) schematic, b) photograph.

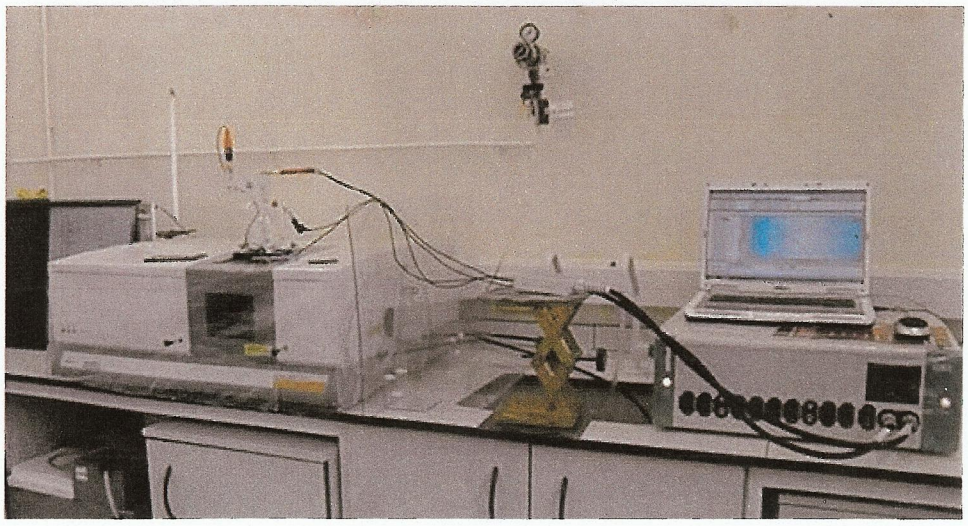

Figure 2.8. Photograph of spectrometer, cell and potentiostat employed in in-situ FTIR experiments.

2.6.4. The reflective working electrode:

The working electrodes employed in the *in-situ* FTIR experiments were platinum and glassy carbon, in the form of a "top hat", see fig. 2.9, having an area of 0.64 cm^2 exposed to the electrolyte. The electrode was mounted on a PTFE body via a nylon screw cap, (see fig. 2.10) and good electrical contact was maintained by a screw and pushrod arrangement which also ensured good optical contact between electrode and window. The electrodes were polished using a Buehler polishing cloth (microcloth) and 0.05 μm Al_2O_3.

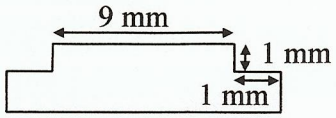

Figure 2.9. The "top hat "-shaped FTIR electrodes.

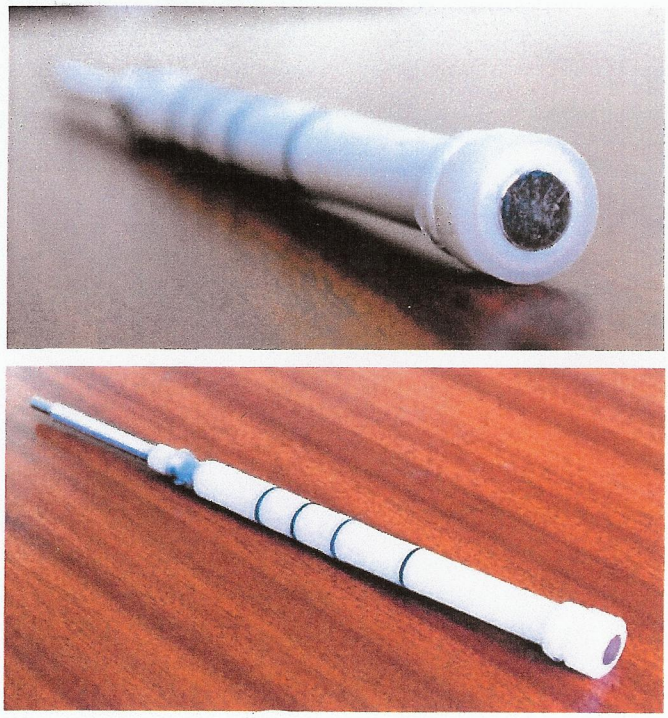

Figure 2.10. Electrode in PTFE body.

2.6.5. Data manipulation

A typical *in-situ* FTIR experiment would be carried out as follows: after collecting cyclic voltammograms (CV) in the absence of methanol, the potential was held at -0.85 V vs. MMO, and methanol was added to a final concentration of 1.0 M, after which the electrode was pressed against the CaF_2 cell window and the spectrometer

was allowed to purge free of CO_2 and water vapour (ca. 30 – 60 min). The reference spectrum (S_R, 100 coadded and averaged scans at 8 cm^{-1} resolution, ca. 35 s per scanset) was collected, and a second spectrum taken at the same potential (to check for electrode movement, etc.), after which spectra (S_S) were collected at -0.8 V and then every 100 mV up to 0.4 V vs. MMO. The spectra in this thesis are presented as:

$$\text{Absorbance} = -\log_{10}(S_S/S_R) \qquad (2.1)$$

This data manipulation results in difference spectra in which peaks pointing up, to +(Absorbance), arise from the gain of absorbing species in S_S with respect to S_R, and peaks pointing down, to -(Absorbance), are due to the loss of absorbing species.

2.7. Cyclic voltammetry

Cyclic voltammetry (CV) is the basic tool of the electrochemist, and is generally the first technique applied to investigate a new electrochemical system or to assess the cleanliness of a system under study. Cyclic voltammetry is most usually employed with small ($\leq$ 1 cm^2) working electrodes (WE) in a three-electrode cell comprising WE, counter electrode (CE) and reference electrode (RE). The WE and CE are held cofacial to each other in electrochemical cell, such as that described in section 2.5 above, which allows the electrolyte to be sparged with gas. In a CV experiment, the potential of the WE with respect to the RE is cycled repeatedly between two preset (anodic and cathodic) limits, see fig. 2.11, at a fixed scan rate (V s^{-1} or mV s^{-1}) and the current recorded as a function of the WE potential.

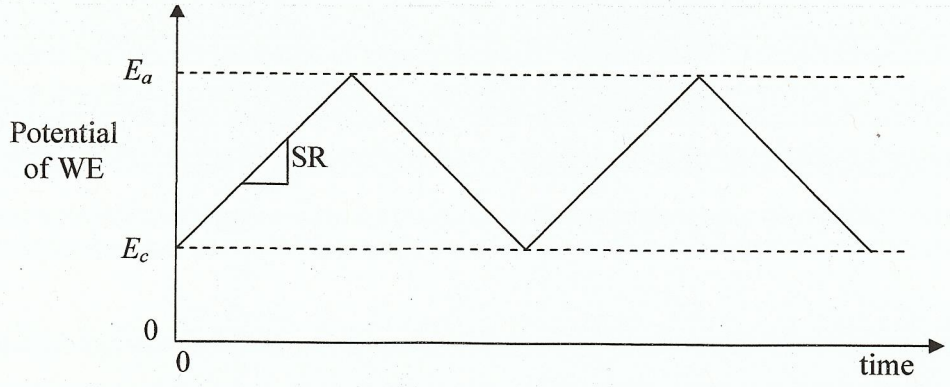

Figure 2.11. The potential profile employed in a cyclic voltammetry experiment. E_c and E_a are the cathodic and anodic potential limits, respectively, and SR *is the scan rate in V or mV s^{-1}.*

In essence, a CV simply shows current peaks and/or exponential increases (anodic) or decreases (cathodic) in current, and is generally employed to (1) show at what potentials Faradaic processes happen and/or (2) whether the electrochemical system is clean. In the latter case, expected current peaks such as those arising from the adsorption and desorption of hydrogen in the CV of Pt in aqueous acid are suppressed by adventitious impurities (as the adsorbed H is a monolayer thick, extremely small concentrations of impurities can render the system "dirty"), and this suppression is a clear indication of contamination. Some quantitative information can be determined from CV's, such as diffusion coefficients, and a full discussion of the application of cyclic voltammetry may be found elsewhere [15, 16].

In broad terms, three types of electrochemical systems are observed in cyclic voltammetry, reversible, quasi-reversible, and irreversible. Taking the two extremes, fig. 2.12 shows a cyclic voltammogram of 2 mM $K_3Fe(CN)_6$, at a 1.6 mm diameter Pt electrode in 1 M KNO_3 at a scan rate of 20 mV s^{-1} [17].

$$Fe(CN)_6^{3-} + e^- \leftrightarrow Fe(CN)_6^{4-} \qquad (2.2)$$

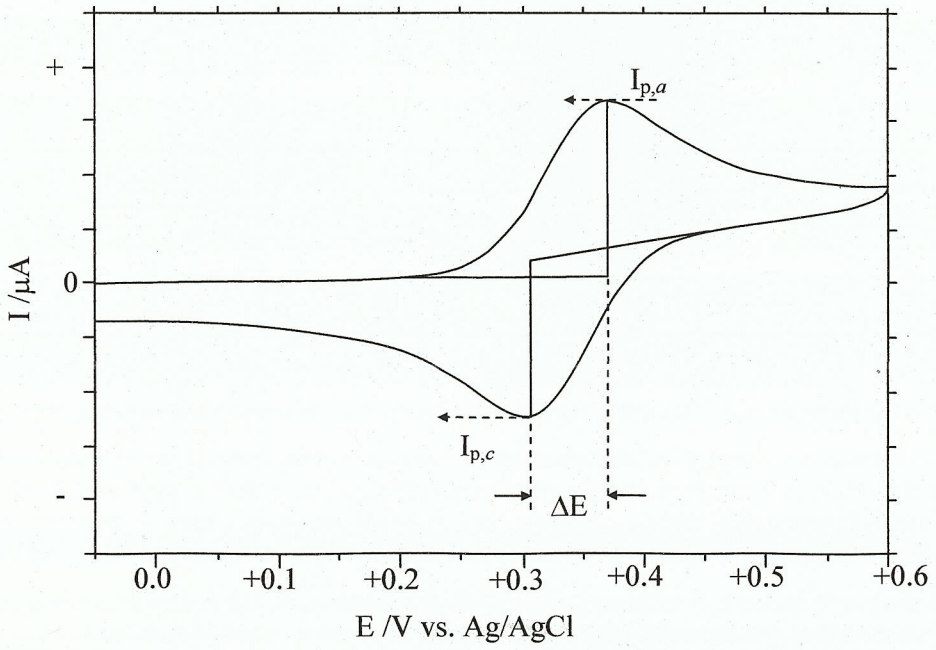

Figure 2.12. Reversible cyclic voltammogram of 2 mM $K_3Fe(CN)_6$ in 1 M KNO_3, scan rate 20 mV s^{-1} [17].

The figure is typical of a reversible electrochemical system. In general for a redox couple:

$$Ox + e^- \rightarrow Rd \qquad (2.3)$$

The shape of the voltammogram can be explained as follows: on increasing the potential from the region where Rd is stable, anodic current starts to flow as the potential approaches the equilibrium (E°) for the Ox/Rd couple. The current continues to increase with increasing potential until the rate of consumption of Rd at the electrode becomes such that transport from the bulk of the solution is not fast enough to maintain constant the concentration of Rd in the near electrode region, therefore it drops in order to enhance the flux of Rd to the surface. As the potential moves past E°, the near-electrode concentration of Rd falls almost to zero, the mass transfer of Rd reaches a maximum rate (in unstirred solutions) this rate then declines as depletion of Rd further and further from the electrode takes place. Thus, the current passes through a maximum ($I_{p,a}$) before dropping again.

On reversing the potential scan, the above sequence of event is repeated for the reduction of the electrochemically generated Ox that now predominate in the near-electrode region [16].

Figure 2.13 shows a CV of an Au wire immerse in KCl. The exponential increase in current with an onset near 0.86 V vs. SCE is due to the irreversible oxidation of Cl^-

$$Cl^- \rightarrow \tfrac{1}{2} Cl_2 + e^- \qquad (2.4)$$

The small cathodic return wave near 0.63 V vs. SCE is due to the reduction of trace Cl_2 near the electrode, i.e. the reverse of reaction 2.4.

2.8. Alkaline Anion Exchange Membranes (AAEM)

The synthesis of the AAEM (SD1) was carried out by the Doherty group in Newcastle University as part of a newly initiated project to develop the applications of imidazolium based materials, and explores their potential as alkaline anion exchange membranes for use in fuel cells.

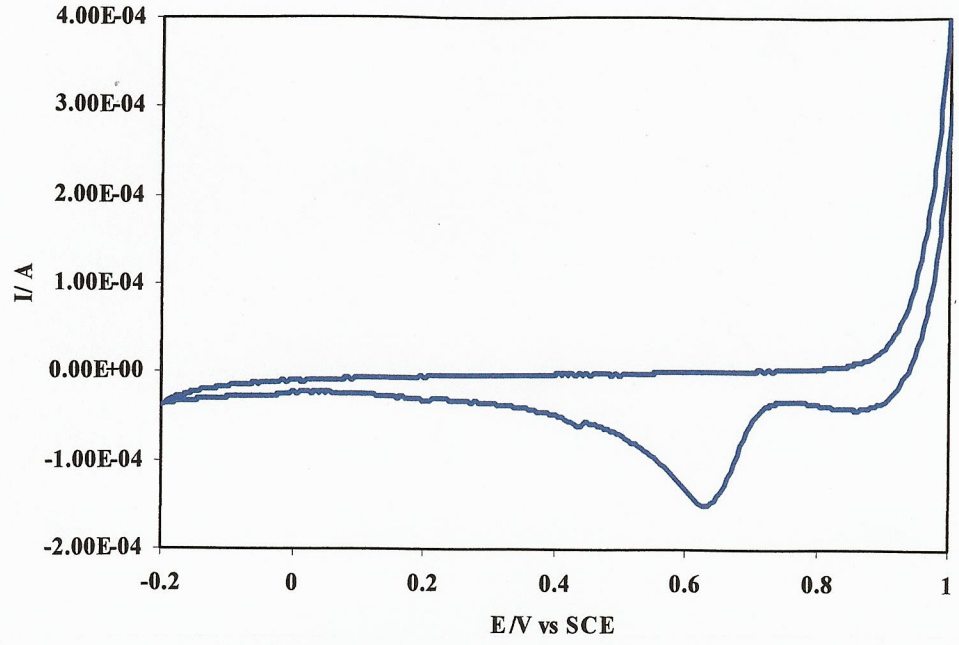

Figure 2.13. CV of a, 0.020 cm diameter, 1 cm^2 area, Au wire immersed in 0.5 M H_2S0_4 + 0.1 M KCl. Scan rate 0.1 $V.s^{-1}$.

In preliminary studies that paralleled an earlier study by Coates and co-workers [18, 19], the pyrrolidinium functionalised norbornene based monomer (1) was prepared as depicted in fig. 2.14, and shown to undergo ring opening metathesis polymerisation in the presence of dicyclopentadiene (DCPD) to afford robust cross linked membrane materials of varying thickness depending on the (1):DCPD ratio.

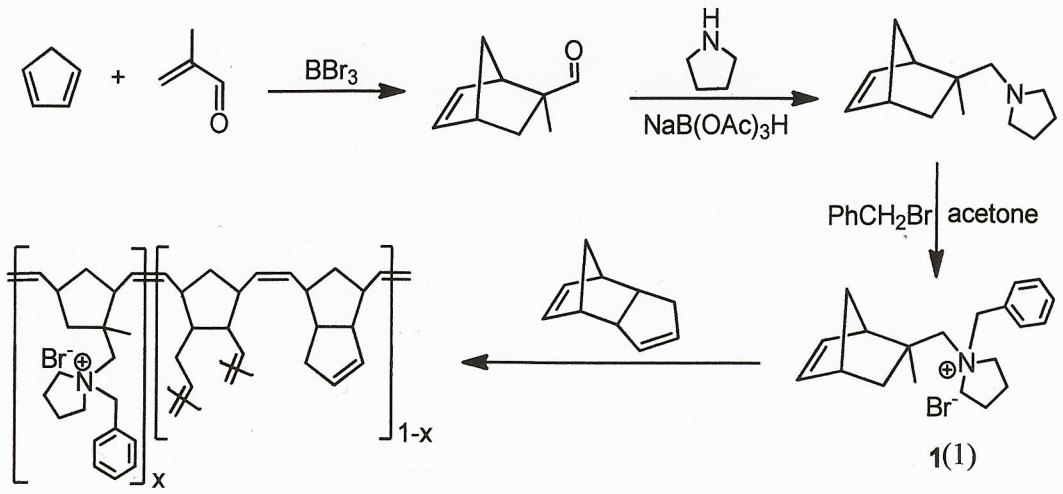

Figure 2.14. Pyrrolidinium functionalised norborene polymerization in the presence of dicyclopentadiene (DCPD).

The resulting AAEM's were converted to the hydroxide form by immersion in 1 M KOH at 60 °C for 30 minutes, washing and immersion in Millipore water for 24 hours. The conductivity was determined as described in section 2.9.

2.9. Conductivity test

The conductivity test was based on a US Department of Energy (DOE) procedure [20], Following synthesis, the membrane was immerse in water for 24 hours to ensure full hydration, and then converted to the OH^--conducting form [21] by immersion for a further 24 hours in 1 M KOH at room temperature, followed by thorough washing with Millipore water.

A Mitutoyo model 2736 digital thickness gauge (± 0.010 mm) was employed for thickness measurements; the thicknesses of the membrane reported below are averages of at least 5 measurements across each membrane. Membranes were cut into 1 cm x 2.5 cm strips in order to fit the conductivity cell membrane sample holder in the cell shown in fig. 2.15(a), which comprises four Pt electrodes embedded in a PTFE body. Tweezers were used to gently insert the membrane sample under the platinum wires as shown in fig. 2.15(b); the top membrane clamp was placed onto the top surface of the membrane sample, and gently secured the membrane clamp using the four fastener bolts.

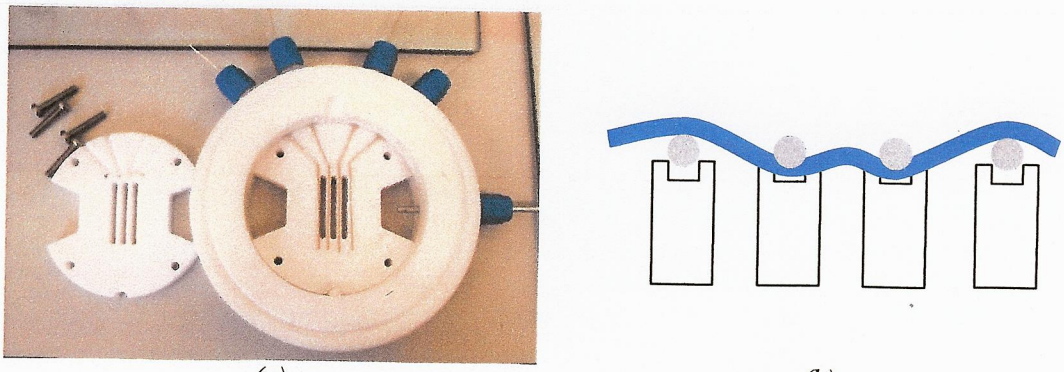

(a) *(b)*

Figure 2.15. (a) Membrane sampler holder, (b) schematic of the membrane placed under the Pt wires.

The assembly of the conductivity cell is show in fig. 2.16. Four long bolts were used to secure the half cell/conductivity/half cell sandwich. The cell's PTFE body will

expand upon heating, so if the sandwich is bolted too tightly, the Teflon will deform between the plates and begin to "flow out" the sides. Millipore water was then pumped into the cell chamber by a Watson Marlow 101U/R pump at a flow rate of 10 cm^3 min^{-1}. The conductivity cell was then connected to a temperature control and allowed reach equilibrium for 10 to 15 minutes before each test.

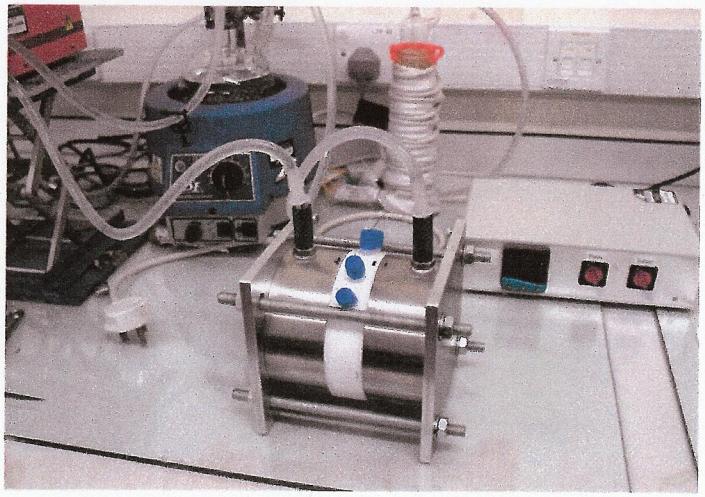

Figure 2.16. The conductivity cell.

The electrical connection to the potentiostat was as depicted in fig. 2.17. The software employed was Voltalab Voltamaster 4, and cyclic voltammograms were obtained over the range -0.30 V to +0.20 V at a scan rate of 10 mV s^{-1}.

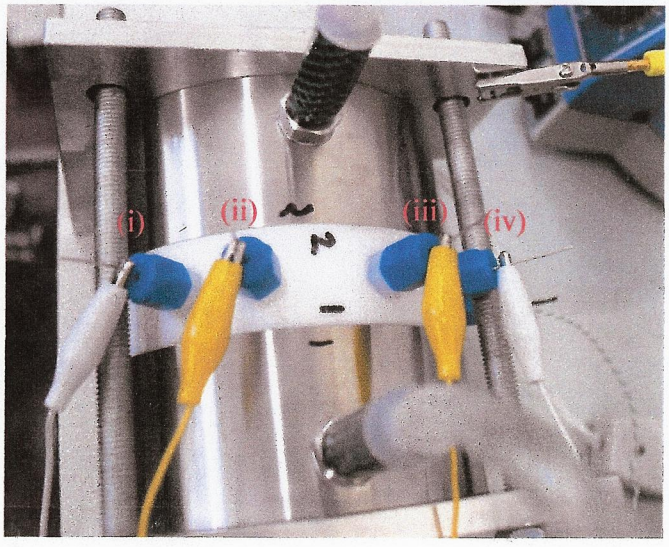

Figure 2.17. Wiring of the conductivity cell (i) working, (ii) working sense, (iii) reference, (iv) counter electrodes.

The resistance of the cell was calculated as 1/slope (in the linear region) from the plot I /Amps vs. E /V. The in-plane conductivity was obtained using the information provided in figs. 2.18 and equations 2.5 & 2.6.

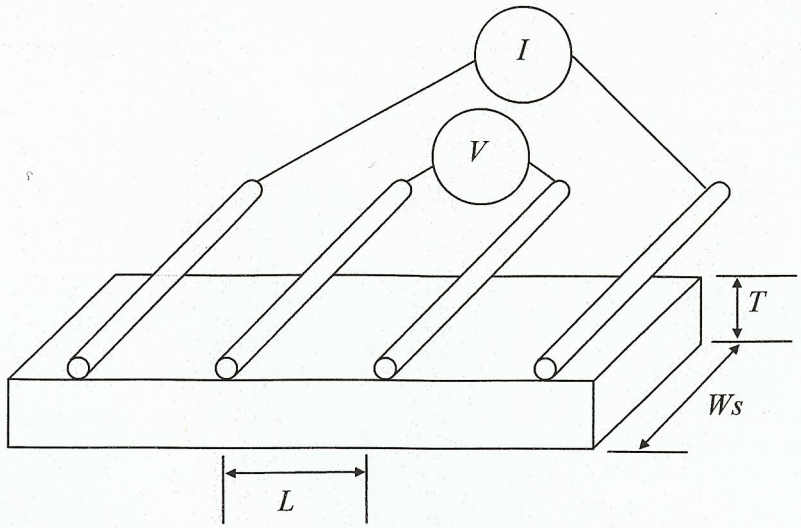

Figure 2.18. In-plane conductivity cell parameters: (I) current /A, (V) voltage /V, (T) sample thickness /cm, (Ws) sample width /cm, (L) distance between voltage measurement/0.5 cm (cell's design).

$$R(\Omega) = \frac{\Delta E(V)}{\Delta I(A)} \tag{2.5}$$

$$\sigma(S\,cm^{-1}) = \frac{1}{\rho(\Omega\,\mathrm{cm})} = \frac{L(\mathrm{cm})}{R(\Omega)Ws(\mathrm{cm})T(\mathrm{cm})} \tag{2.6}$$

2.10. Fuel cell test set up.

Fuel cell tests were carried out with advice from Prof. Scott's group in Newcastle University. The membranes were either: 1) Nafion 117 (K^+ form) [21] or 2) SD1 membrane (section 2.8); after being cut 5 cm x 5 cm, both were converted to the alkaline form (or cation conducting form) by immersion in 1 M KOH at 60 °C for 30 min after 24 hours of immersion in Millipore water. The membrane was stored in Millipore water prior to use.

The anode comprised 3 cm x 3 cm Toray TGPH-060 non-teflonised carbon paper (ca. 100 μm diffusion layer), the catalyst layer was made of either: 1) commercially available Pt(40%)Ru(20%)/C catalyst with a loading of 0.5 mg metal cm^{-2} or 2)

$Pd_{40}Ni_{60}$/C catalyst 1.0 mg metal cm^{-2}; the binder was: 1) Nafion ionomer solution when using Nafion membrane, with a dry ionomer to carbon ratio (I/C) of 0.3 (ca. 24 wt. % ionomer dry mass) or 2) SD1 ionomer form (as described by Coates et al. [22]) when using SD1 membrane with the same load, i.e. 24 wt. %. The cathode was a 3 cm x 3 cm Toray TGPH-060 teflonised carbon paper, with a catalyst layer of Pt black (20%) on carbon, with a load of 0.40 mg Pt cm^{-2} and the same ionomer as the anode. Regardless of the membrane, cold pressing was used to make the MEA, applying 1.5 Nm torque, in order to been able to compare directly the performance of SD1 and Nafion (SD1 membrane can not be hot pressed).

The fuel cell system was tested using a 5 cm x 5 cm graphite bipolar plate, as depicted in fig. 2.19. Four long bolts were used to secure the MEA assembly, using a RS torque wrench to apply 1.5 Nm to each bolt (previous work had shown this pressure to be enough to assure ionic contact and avoid fluids leaks and/or piercing of the membrane).

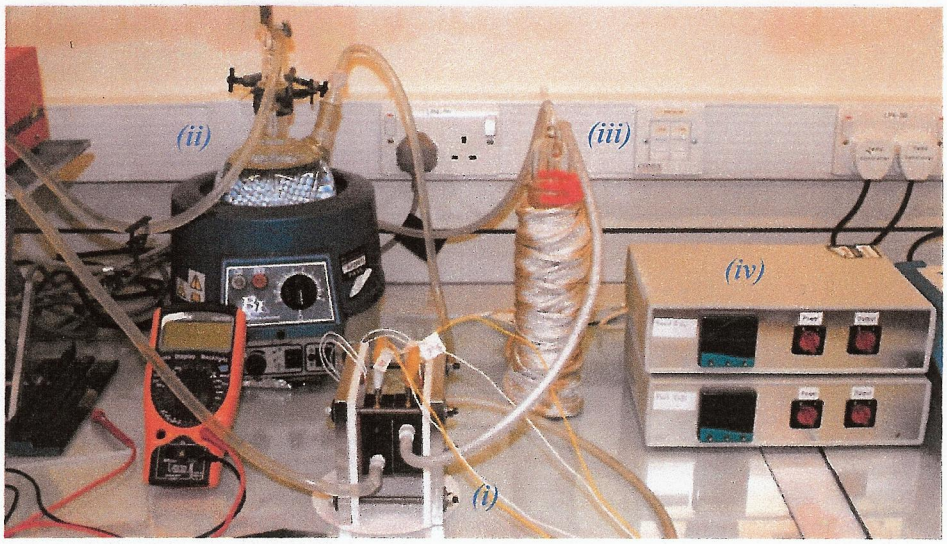

Figure 2.19. Fuel cell system set up (i) bipolar plate, (ii) fuel tank (i.e. either 1 M methanol or ethanol), (iii) humidifier and (iv) temperature controler for (i) and (iii).

Fuel solution (either 1 M methanol or 1 M ethanol) was pumped into the anode using a Watson Marlow 101U/R pump at a flow rate of 10 cm^3 min^{-1}, and oxygen from a pressurised cylinder pumped through a humidifier (iii in fig. 2.19) into the cathode at 150 cm^3 min^{-1} and 1.5 bar.

The system was kept at constant temperature using a CAL 9400 control equipment, and the open circuit voltage measured using a digital voltmeter (DVM) until stabilization before the test.

2.11. The composite anodes

The $Si/TiO_2/Au$ composite anodes discussed in this thesis comprised a TiO_2 layer deposited on a 50.8 mm diameter Si wafer (n-type phosphorus doped, 10-30 Ω.cm, (100) orientation, 300 ± 10 μm thick). A gold grid was deposited on the TiO_2 (see figs. 2.20(a) and (b)). The TiO_2 was deposited via magnetron sputtering of a compound target in argon, and the Au similarly deposited using a gold target.

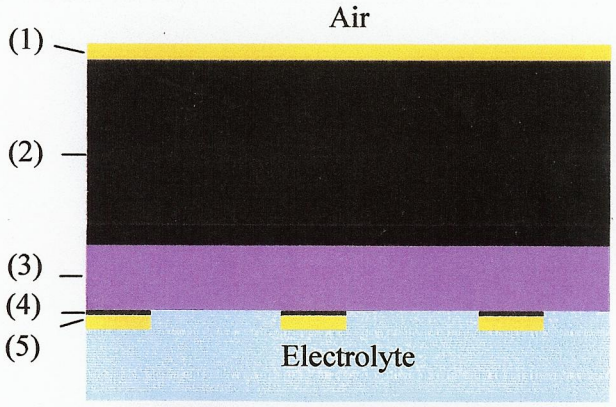

(a)

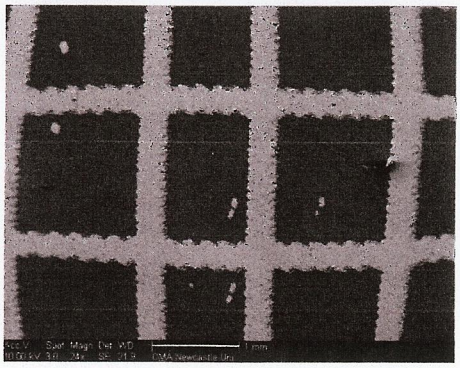

(b)

Figure 2.20. (a) Schematic of the composite anode: (1) 100 nm Au Ohmic contact; (2) 300 μm Si wafer; (3) 120 nm TiO_2 layer; (4) 10 nm Ti wetting layer and (5) 120 nm Au grid, (b) SEM of the $Si/TiO_2/Au$ device; bar 5 1 mm. The light areas represent the Au grid deposited on the TiO_2 overlayer on Si.

An Ohmic contact to the back of the wafer was formed via an electron beam evaporated 100 nm 99% Au:l% Sb layer, annealed at 400 °C under nitrogen for 15

minutes, followed by a 80 nm Au layer. The wafer was then cleaned in dilute hydrofluoric acid before a 120 ± 7 nm TiO_2 layer was sputtered on the front.

The Ti target employed (Kurt J. Lesker Co. Ltd) was 99.9% TiO_2 with As (0.001 wt. %), Fe (0.002 wt. %) and Zn (0.001 wt. %) as the main impurities. The TiO_2 layer so formed may be considered to be a disordered dielectric. Finally, a square Au grid was patterned on top of the TiO_2 layer by lift-off.

The Au was 120 nm thick and the grid was 375 μm wide with 1 mm^2 open area. A 10 nm Ti layer of the same dimensions as the grid was used to ensure strong adhesion of the Au to the TiO_2. Once deposition was complete, the electrodes were cut into four segments. Two contacts were made to the Au grid, and one to the centre of the Si, using silver araldite (RS™ silver loaded epoxy adhesive/hardener system) covered with Araldite Rapid™ resin to provide support for the contacts and protect them from electrolyte. The geometric area of the Au grid was 2.1 cm^2.

The Au grid was biased relative to the Au Ohmic contact on the reverse of the Si wafer via a AM 6-12 (Maplin) 6 V-12Ah SLA battery using the circuit shown in fig. 2.21; a battery was chosen as a DC power supply to avoid complications due to earth loops. The grid was also employed as the working electrode in a standard, 3-electrode cell.

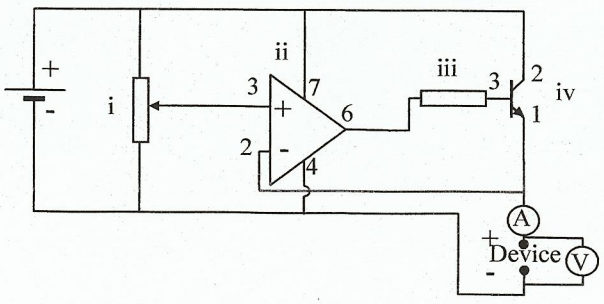

Figure 2.21. Circuit used for bias experiments. i) 1 kΩ potentiometer (WR40T), ii) CA3140 op-amp (N35CH), iii) 470 ohm resistor (D470R), iv) NPN transistor (QF70H).

The composite electrode was mounted on the end of a glass rod and held inverted *via* a thermometer joint in the glass electrochemical cell shown in figure 2.4(a) & (b). The

Au grid of the composite electrode was held ca. 1 cm from, and cofacial with, a 4 cm^2 Pt/Ti mesh counter electrode, see figs. 2.22(a) – (c). The Au Ohmic layer on the Si was not immersed in the 0.5 M H_2SO_4 electrolyte in the cell.

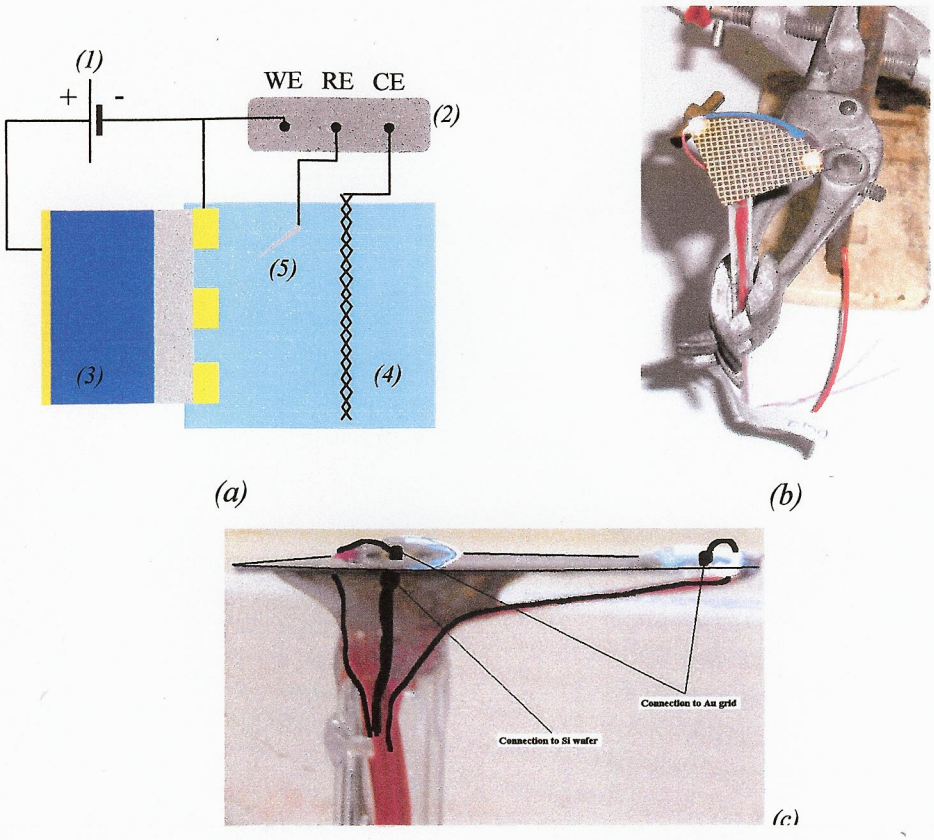

Figure 2.22. (a) Schematic of the composite electrode experimental set up. (1) Battery, (2) potentiostat, (3) composite electrode, (4) Pt/Ti mesh counter electrode, (5) Saturated Calomel Electrode (SCE). (b) A Si/TiO_2/Au electrode, (c) Photograph of a composite electrode showing its electrical contact.

A Saturated Calomel reference electrode (SCE, Sentek) was in ionic contact with the cell electrolyte via a Luggin capillary. The potential of the Au grid was controlled with respect to the reference electrode using an Autolab PGStat 12 potentiostat. The 'bias voltage' V_b between Au grid and Si (grid negative with respect to Si) results in a bias current I_b. These parameters distinguish the current through, and voltage across, the composite anode from the electrochemical potential on the Au grid and electrochemical current between the grid and counter electrode.

2.12. X-ray diffraction

X-ray data were obtained using a PANalytical X'Pert Pro Diffractometer, fitted with an X'Celerator and secondary monochromator employing CuKα radiation (λ =

1.54180 Å). For each catalyst ($Ru_{72}Ni_{28}$, $Co_{50}Ni_{50}$ and $Pd_{40}Ni_{60}$) 50 mg of powder was place in a holder and flattened before the test, no other sample preparation was required.

2.13. SEM/EDX

Micrographs were obtained using an Environmental Scanning Electron Microscope (ESEM) FEI XL30 High vacuum, equipped with a Field Emission Gun (FEG), and a source of 20 KeV, which allowed small spot size and high magnification, typically from 80,000x to 100,000x. EDAX analyses were carried out using a Röntec equipment cooled by liquid nitrogen and running Quantax (version 1.2) software. For these tests, the samples were mounted on a special kind of support disk, having carbon based cement in order to glue the catalyst on top, and no other preparation was required.

2.14. References

1. Yoon S.B., Fang B., Kim M,, Kim J.H., Yu J.-S., and Gerhard W., (2009). Nanostructured Supported Catalysts for Low-Temperature Fuel Cells, in: Frontiers of Nanoscience, R.E. Palmer [Editor], Elsevier. p. 173-231.
2. Kurihara L.K., Chow G.M., and Schoen P.E., (1995). Nanostructured Materials, 5, 6, pp. 607-613.
3. Kim J.-Y., Kim K.-H., Park S.-H., and Kim K.-B., (2010). Electrochimica Acta, 55, 27, pp. 8056-8061.
4. Liu Z., Ling X.Y., Guo B., Hong L., and Lee J.Y., (2007). Journal of Power Sources, 167, 2, pp. 272-280.
5. You D.J., Kwon K., Pak C., and Chang H., (2009). Catalysis Today, 146, 1-2, pp. 15-19.
6. Lin Z., Ji L., Krause W.E., and Zhang X., (2010). Journal of Power Sources, 195, 17, pp. 5520-5526.
7. Ferrando R., Jellinek J., and Johnston R.L., (2008). Chemical Reviews, 108, 3, pp. 845-910.
8. Shen S.Y., Zhao T.S., Xu J.B., and Li Y.S., (2010). Journal of Power Sources, 195,4, pp. 1001-1006.
9. Li H., Sun G., Jiang Q., Zhu M., Sun S., and Xin Q., (2007). Journal of Power Sources, 172, 2, pp. 641-649.
10. Luna C., Morales M.d.P., Serna C.J., and Vazquez M., (2004). Nanotechnology, 15, 4, pp. S293-S297.
11. Fernandes R., Patel N., and Miotello A., (2009). International Journal of Hydrogen Energy, 34, 7, pp. 2893-2900.
12. Faguy P.W. and Fawcett W.R., (1990). Appl. Spectrosc., 44, 8, pp. 1309-1316.
13. Lin W.F., Christensen P.A., Hamnett A., Zei M.S., and Ertl G., (2000). The Journal of Physical Chemistry B, 104, 28, pp. 6642-6652.
14. Lin W.-F., Christensen P.A., Jin J.-M., and Hamnett A., (2007). *In-situ FTIR Spectroscopic Studies of the Adsorption and Oxidation of Small Organic*

Molecules at the Ru(0001) Electrode Under Various Conditions, in: In-situ Spectroscopic Studies of Adsorption at the Electrode and Electrocatalysis, S.-G. Sun, P.A. Christensen, and A. Wieckowski Editors, Elsevier Science B.V., Amsterdam, p. 99-138.

15. Bard A.J. and Faulkner L.R., (2001). *Electrochemical methods : fundamentals and applications*, 2 ed. New York: John Wiley & Sons, INC. 833.
16. Christensen P.A. and Hamnett A., (1994). *Techniques and Mechanisms in Electrochemistry*, 1 ed. Oxford: Blackie Academic & Professional, an imprint of Chapman & Hall. 396.
17. Bott A.W. and Jackson B.P., (1996). Current Separations, 15, 1, pp. 25-30.
18. Clark T.J., Robertson N.J., Kostalik Iv H.A., Lobkovsky E.B., Mutolo P.F., Abruna H.D., and Coates G.W., (2009). Journal of the American Chemical Society, 131, 36, pp. 12888-12889.
19. Robertson N.J., Kostalik H.A., Clark T.J., Mutolo P.F., Abruña H.D., and Coates G.W., (2010). Journal of the American Chemical Society, 132, 10, pp. 3400-3404.
20. FSEC, (2008). *Procedure for performing in-plane membrane conductivity testing*. USDOE, DE-FC36-06G016028, 19.
21. Yu E., Scott K, and Reeve R., (2006). Journal of Applied Electrochemistry, 36, 1, pp. 25-32.
22. Kostalik H.A., Clark T.J., Robertson N.J., Mutolo P.F., Longo J.M., Abruña H. D., and Coates G.W., (2010). Macromolecules, 43, 17, pp. 7147-7150.

3. *In-situ* FTIR studies on the oxidation of methanol at polycrystalline Pt in aqueous 0.1 M KOH

3.1. Introduction.

An important aspect of the work reported in this thesis was to research the potential application of novel, non-noble metals as catalysts for the anode of direct alcohol fuel cells. With respect to this, *in-situ* Fourier Transform Infra-Red spectroscopy (FTIR) has proved to be invaluable in studies of the oxidation of small organic molecules in acid solution at noble metal anodes, (see for example [1-10], and references therein). Beden et al. [10] published the seminal work on the oxidation of methanol at Pt in 1982 which concluded that adsorbed CO was an intermediate (rather than poison) and that the mechanism involved the reaction of chemisorbed CH_3OH fragments with adsorbed OH. However, studies of organic electro-oxidation in alkaline solution are far less numerous.

In a series of papers, on methanol oxidation at Pt electrode in alkaline solution, Tripković et al. [11-13], have developed the concept of the "dual path" mechanism involving two parallel routes: *via* a poisoning intermediate (CO_L and CO_B, the indirect path) and *via* a reactive intermedia (the direct path). The former leads to CO_3^{2-} as the soluble product, the latter to formate. The authors postulated that the distribution (CO_L vs. CO_B) and the amount of the adsorbed CO poison both depend strongly on the Pt facet, and that the adsorbed CO is removed at higher potentials. The model also included two types of adsorbed oxygen species: Pt-OH or $Pt(OH)_{ads}$, which is reversibly adsorbed, and Pt-O^-, which is strongly adsorbed. The former is an active intermediate whereby methanol oxidation is initiated at the onset of Pt-OH formation, and that the activity of various Pt facets reflects their ability to adsorb OH, presumably in competition with the adsorption of the CO poison.

It was decide to investigate the oxidation of methanol, formate (Chapter 4) and ethanol (Chapter 5) at polycrystalline Pt electrode in aqueous KOH in order to build up a database of *in-situ* FTIR spectra of potential intermediates and products. This would then be employed to interpret IR spectra obtained from the oxidation of methanol and ethanol at the non-noble metal-based anodes. Further, it was decided to

investigate the effect of the presence of oxygen as studies by the Christensen group [14-16] on CO electro-oxidation at Ru(0001) and Ru-polycrystalline Pt electrodes have shown clearly that oxygen can have a very significant effect upon the oxidation of adsorbed CO. Moreover, it has been known since the work of Gottesfeld and Pafford [17] that CO and CO_2 poisoning of Pt-based PEMFC anodes can be ameliorated by introducing a small amount of air into the fuel stream, i.e. an "air bleed". This approach remains controversial in terms of the reduction in poisoning being offset by reduced durability due to the attack of H_2O_2 on the catalyst layer, carbon support, and PEM [18, 19], and fundamental studies remain relatively sparse. To my knowledge, the effect of oxygen on the oxidation of methanol at polycrystalline Pt in alkaline solution has not been investigated with *in situ* FTIR spectroscopy.

In the work discussed in this chapter, a high concentration of methanol was chosen, as initial experiments using 0.1 M CH_3OH showed clear indication that the methanol in the thin layer was consumed relatively quickly, and hence that the current subsequently observed was due to methanol diffusing from the bulk of the solution and reacting at the edge of the Pt electrode.

3.2. Current-Voltage-time (IVt) data.

Figure 3.1 shows CVs (scan rate = 100 mV s^{-1}) of the Pt electrode in N_2- and O_2-saturated 0.1 M KOH, respectively. As may be seen from the figure, compared to acid solution, there is an additional anodic wave between the hydride stripping features in the anodic scan and the formation of oxide; this wave has an onset near -0.5 V and may be attributed to the reversible formation of OH_{ads} [9]. In O_2-saturated solution, as well as the downward movement of the voltammograms due to oxygen reduction, the hydride region is suppressed by ca. 22%, the oxide stripping peak is significantly enhanced, and the peak current due to OH_{ads} is increased by a factor of ca. 2.5.

In alkaline solution, the oxidation of methanol at Pt is suppressed at potentials in the Pt oxide region when low concentrations of methanol are employed [20], In contrast to the behaviour generally observed at lower methanol concentrations, methanol oxidation is not suppressed by the formation of the oxide at high methanol concentrations [21, 22].

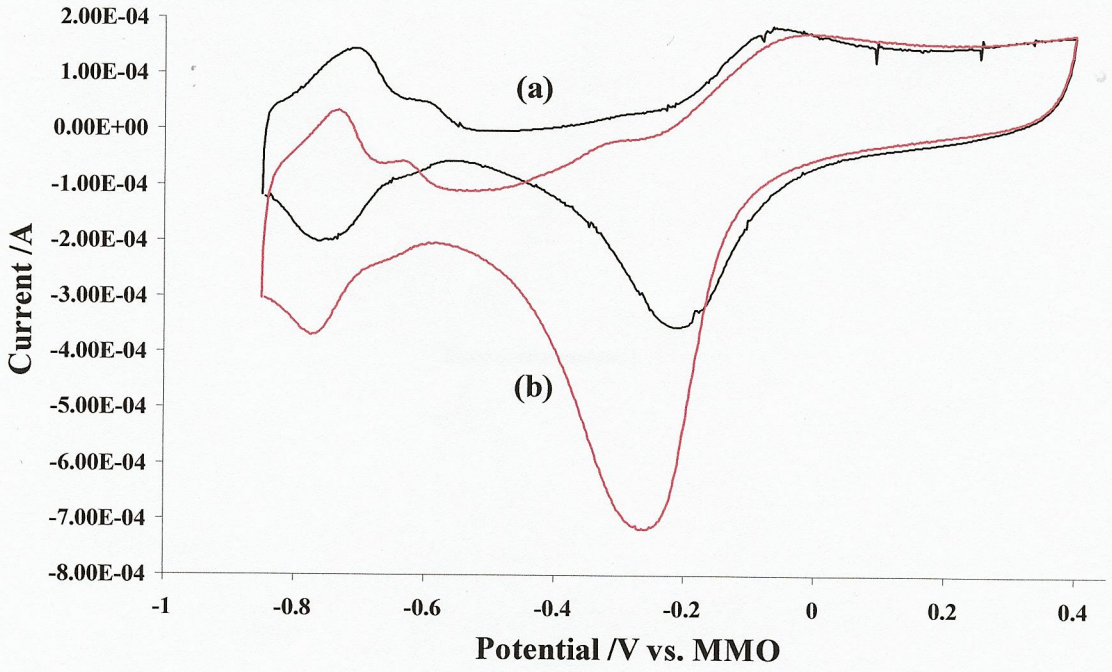

Figure 3.1. CV of a 0.64 cm^2 polycrystalline Pt electrode in (a) N_2- and (b) O_2-saturated 0.1 M KOH. Scan rate = 100 mVs^{-1}.

Thus, fig. 3.2 shows voltammograms analogous to those in fig. 3.1 in the presence of 5 M methanol carried out in the spectro-electrochemical cell with the Pt electrode pulled back from the cell window. In fig. 3.2, there is very little hysteresis from -0.85 V up to -0.05 V on the anodic sweep of the CV of the Pt in N_2-saturated KOH and -0.05 V to -0.85 V on the cathodic sweep.

Methanol oxidation seems to be maintained at the oxide on the anodic sweep (or the preferential oxidation of methanol inhibits oxide formation); however, the electrode is clearly poisoned by the time the return (cathodic sweep) commences as the current drops dramatically until -0.05 V, the onset of oxide stripping, when it recovers. In O_2-saturated solution, there is very little poisoning, as shown by the small hysteresis across the full voltammogram.

Interestingly, the CV in O_2-saturated solution does not exhibit an autocatalytic peak in the cathodic sweep, and the onset of anodic current due to methanol oxidation is somewhat delayed in the O_2-saturated electrolyte.

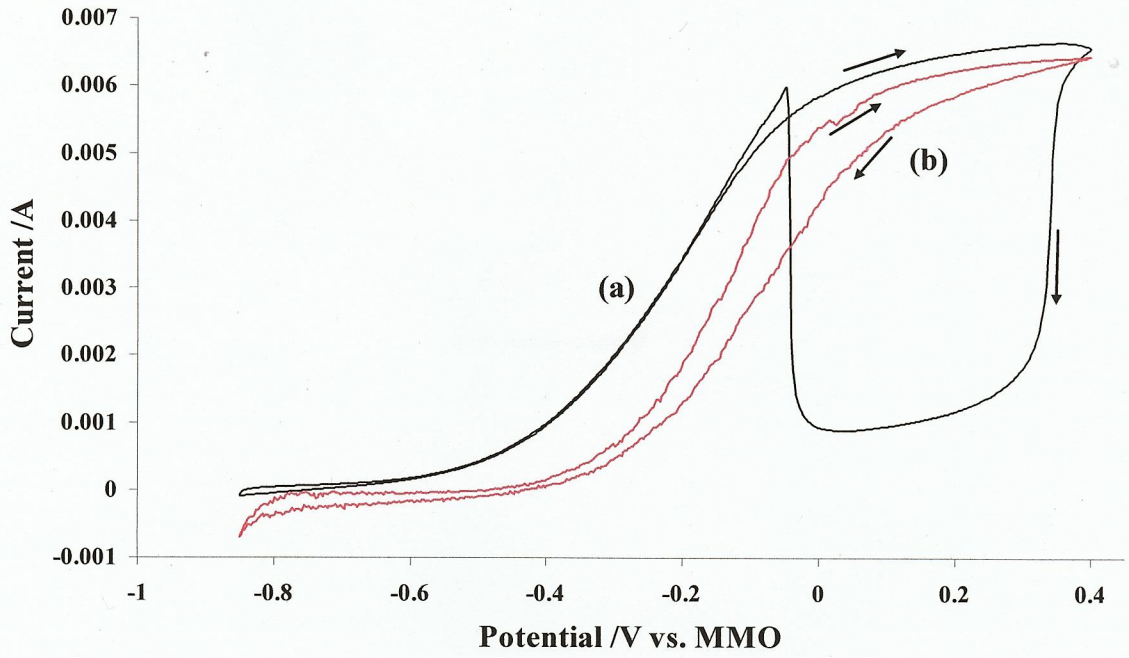

Figure 3.2. CVs of the electrode in Figure 3.1 immersed in (a) N_2- and (b) O_2-saturated 0.1 M KOH + 5M CH_3OH. Scan rate = 100 mVs^{-1}.

3.3. In-situ FTIR data in N_2-saturated solution

Figure 3.3(a) shows spectra collected between -0.85V and -0.5V. The spectra up to -0.6 V show the gain of a broad O-H feature centered near 3289 cm^{-1}, which appears at -0.8V, and features near 1581, 1383, and 1351 cm^{-1}, which appear at -0.6 V (in agreement with the onset of anodic current in fig. 3.2) and may be attributed to solution formate [8] possibly complexed with methanol (see below).

In addition, a sharp feature near 1317 cm^{-1} also appears at -0.6 V; on the basis of the literature [9, 23-32], (including a study by Sun and co-workers [9] on methanol oxidation in 0.1 M NaOH) this band is assigned to the symmetric O-C-O stretch of formate adsorbed through both O-atoms with the C_2 axis of the molecule perpendicular to the surface.

Figure 3.3(b) shows a spectrum collected during an experiment in which an aqueous solution of 0.1 M NaOOCH/0.1 M KOH was admitted into the spectroelectrochemical cell with the electrode held at -0.85V and pressed against the CaF_2 window and trapping aqueous 0.1 M KOH. The spectrum was collected at the end of the

experiment (ca. 30 min) and shows simply aqueous $HCOO^-$. As may be seen, the band frequencies are in reasonable agreement with those in fig. 3.3(a); however, the ratios of the various features differ quite markedly, as may be seen in table 3.1.

Peak /cm^{-1}	**1581**	**1383**	**1351**
Assignment	ν(COO)	δ(CH) or ν(COO)	ν(COO)
$HCOO^-$ peaks in figure 3.3(a) /cm^{-1}	1581	1383	1351
Relative intensities	3.7	1.0	1.2
$HCOO^-$ peaks in figure 3.3(b) /cm^{-1}	1580	1382	1351
Relative intensities	1.6	1.0	1.0
$HCOO^-$ peaks in figure 3.3(c)/cm^{-1}	1580	1382	1351
Relative intensities	2.3	1.0	1.3

Table 3.1. A comparison of the relative intensities of the formate bands observed in the spectra in figs. 3.3(a) – (c) [33].

Figure 3.3(b) also shows spectra of 0.1 M $NaHCO_3$ in water and 0.1 M Na_2CO_3 in 0.1 M KOH obtained in the same way. Figure 3.3(c) compares the NaOOCH spectrum in fig. 3.3(b) to that of a solution of 5 M CH_3OH + 1 M NaOOCH obtained in the same way; the NaOOCH plot was increased by a factor of 4, for clarity. The relative intensities of the formate bands are closer to those observed in fig. 3.3(a), although not identical. Thus, it is possible that the peak intensities in fig. 3.3(a) have been distorted by the formation of a complex, possibly hydrogen bonded, between the methanol and formate. However, while there are clear differences in the relative intensities of the formate in solution with and without added methanol, the fact that there are no concomitant differences in the frequencies of the three bands mitigates against this explanation.

The 1581 cm^{-1} feature appears to have a broad band growing beneath it, which is responsible for enhancing its intensity relative to the two lower frequency features; both HCO_3^- and CO_3^{2-} show weaker, very broad features near 1650 cm^{-1}, but the relative intensity of the 1400 cm^{-1} and 1650 cm^{-1} bands are such that it is unlikely that the former could sufficiently enhance the 1581 cm^{-1} band.

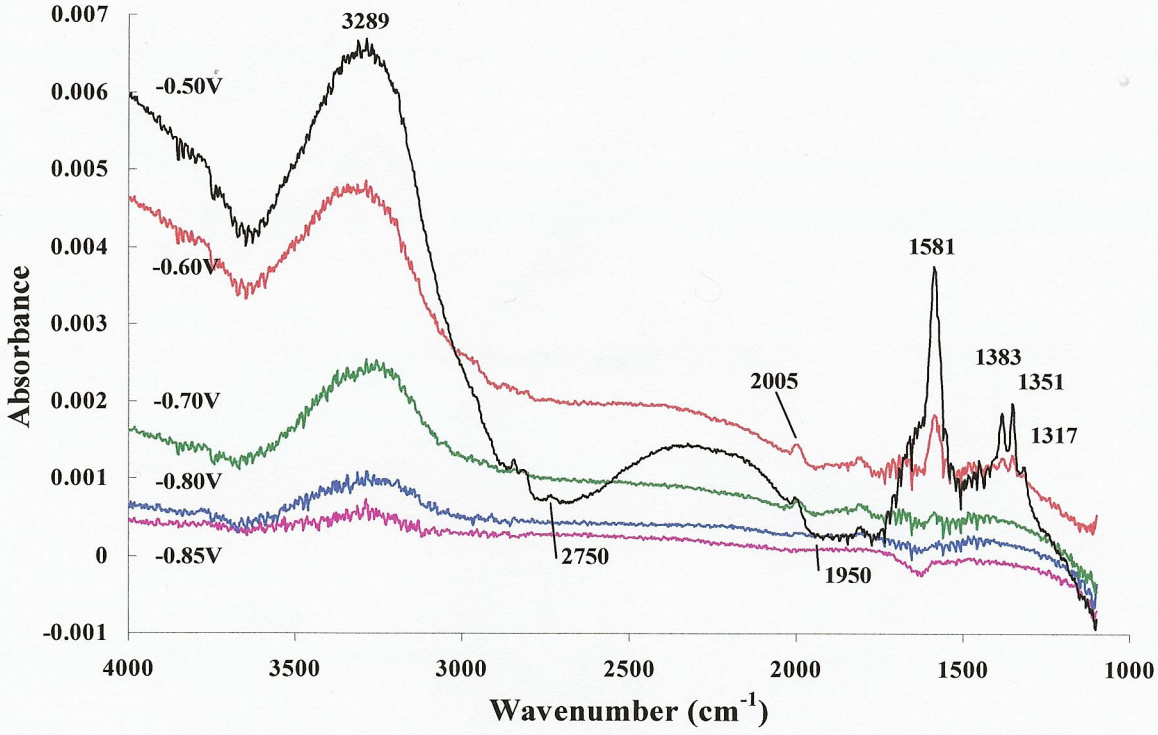
0.007
0.006
0.005
0.004
0.003
0.002
0.001
0
-0.001
Absorbance
3289
-0.50V
-0.60V
-0.70V
-0.80V
-0.85V
1581
1383
1351
1317
2005
2750
1950
4000
3500
3000
2500
2000
1500
1000
Wavenumber (cm-1)

(a)

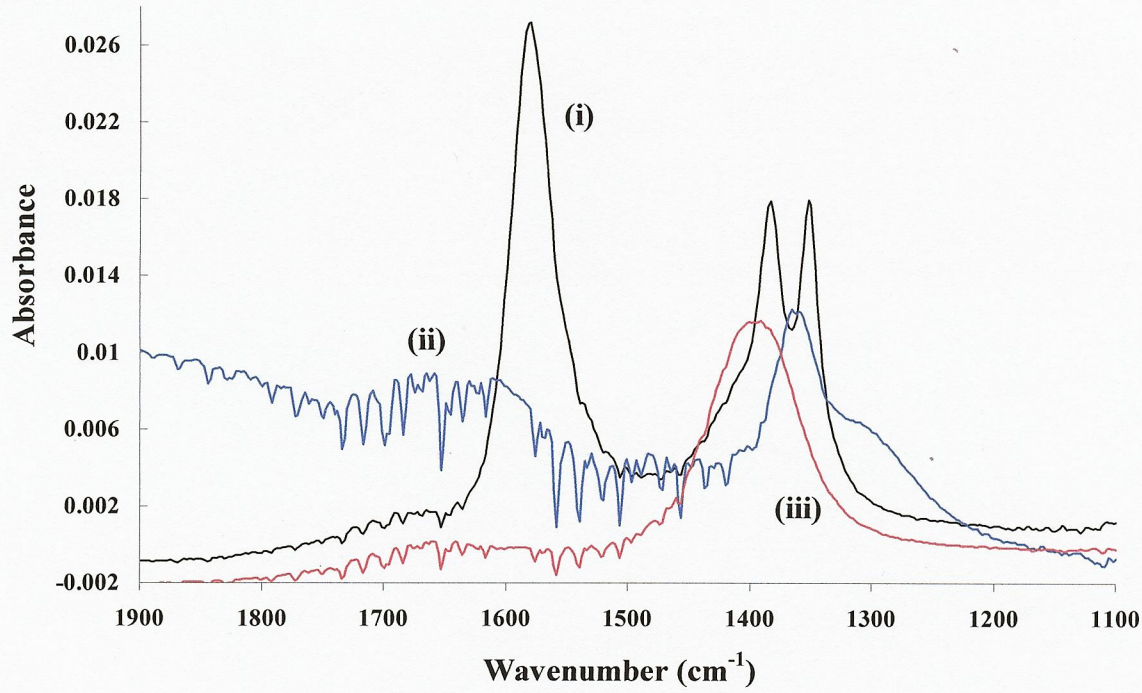
0.026
0.022
0.018
0.014
0.01
0.006
0.002
-0.002
Absorbance
(i)
(ii)
(iii)
1900
1800
1700
1600
1500
1400
1300
1200
1100
Wavenumber (cm-1)

(b)

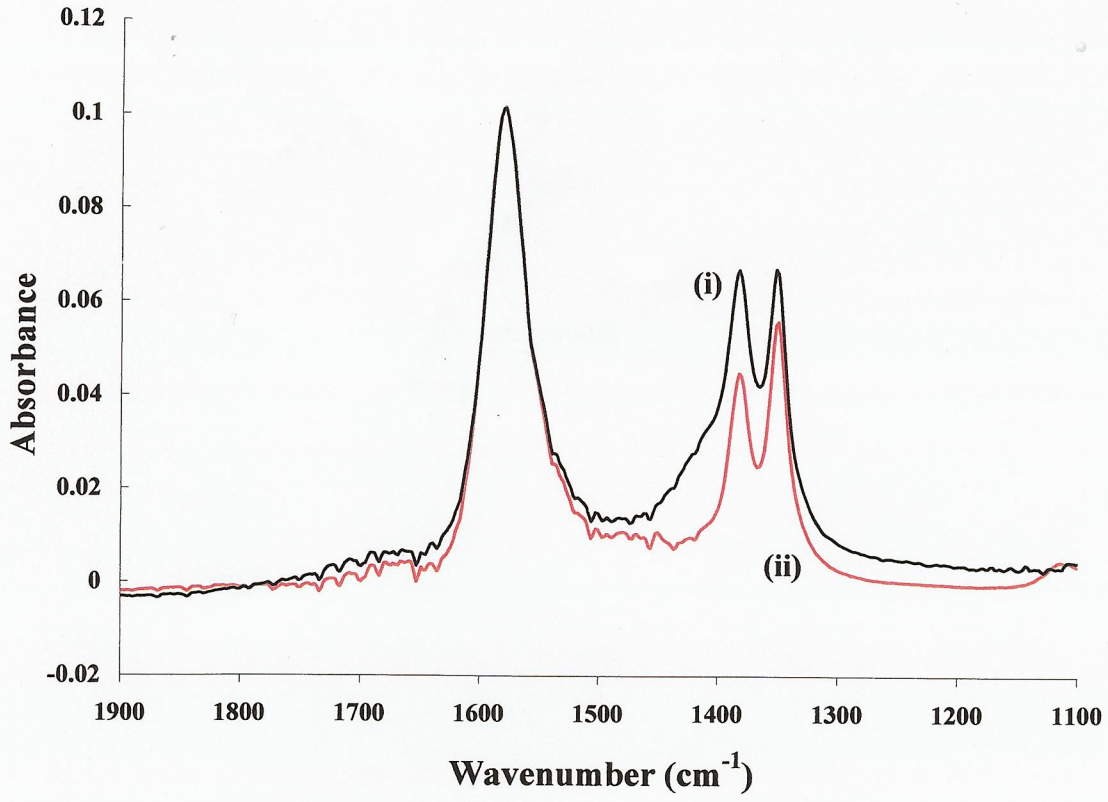

(c)

Figure 3.3. (a) In situ FTIR spectra from the Pt electrode in figure 3.1 immersed in N_2- saturated 0.1 M KOH + 5 M CH_3OH as a function of potential between -0.85 V and -0.5 V vs. MMO normalized to the reference spectrum taken at -0.85 V vs. MMO. (b) Spectra collected at the end of diffusion experiments in which (i) 0.1 M NaOOCH + 0.1 M KOH, (ii) 0.1 M $NaHCO_3$, and (iii) 0.1 M Na_2CO_3 + 0.1 M KOH were flushed into the FTIR cell after collecting a reference spectrum at open circuit with (i, iii) 0.1 M KOH or (ii) water in the thin layer, (c) Spectrum (i) in (b) for comparison to (ii) the spectrum collected at the end of a diffusion experiment in which 0.1 M NaOOCH + 5 M CH_3OH +0.1 M KOH was flushed into the FTIR cell after collecting a reference spectrum at open circuit with 0.1 M KOH in the thin layer (see text for details). All the spectra in figs. 3.3(a) – (b) consisted of 100 co-added and averaged scans at 8 cm^{-1} resolution.

A broad feature near 1660 cm^{-1} was attributed by Chen et al. [9] to the increase of H_2O in the thin layer. Chbihi et al. [6] attribute a band near 1410 cm^{-1} and a well-defined, more intense feature near 1560 cm^{-1} to the symmetric and asymmetric bands of CO_3^{2-}; the latter assignment seems unlikely in view of the spectrum in fig. 3.3(b). It is more likely that the shoulder to the high frequency side of the 1581 cm^{-1} band is associated with the broad O-H band near 3289 cm^{-1}, which grows steadily as the potential is increased. Distortion of the relative IR band intensities of formate

produced via methanol electro-oxidation in alkaline media is routinely observed, but rarely commented upon in detail [4, 5].

A broad loss feature between 3100 cm^{-1} and 1700 cm^{-1} having minima near 2750 cm^{-1} and 1950 cm^{-1} appears at -0.5 V and grows at higher potentials, i.e. tracking the OH_{ads} feature in the voltammogram (see fig. 3.1). This broad IR band was attributed to the loss of solution OH^- [31], and hence was tentatively assigned to the formation of OH_{ads} from solution OH^-. The assignment of this feature is confirmed in Chapter 4.

In addition to the spectral features discussed above, linearly bonded (CO_L) and multiply bonded (CO_B) CO_{ads} species [9] are also observed in fig. 3.3(a) near 1996 cm^{-1} and 1807 cm^{-1}.

Figure 3.4(a) shows the spectra from -0.5 V to -0.1 V, and fig. 3.4(b) shows the spectra from 0 V to 0.4 V. The behaviour of key features in figs. 3.3(a) and 3.4(a) & (b) is summarized in figs. 3.5(a) & (b); the intensities of the bands are normalized to their maximum value. It is interesting to note that there appears to be no carbonate formation (see fig. 3.3(b)) in figs. 3.3(a) and 3.4(a). Figure 3.4(c) shows spectra taken in an experiment analogous to that depicted in fig. 3.3(a) except employing 2 M NaOOCH instead of 5 M CH_3OH.

The pathlengths in the experiments shown in figs. 3.3(a) and 3.4(c) were the same, ca. 1.8 μm. The formation of aqueous CO_3^{2-} from the oxidation of $HCOO^-$ is clearly observed as a strong feature near 1400 cm^{-1} at -0.5 V in fig. 3.4(c), and it is clear from the figure that very little if any carbonate is present in the spectra in figs. 3.3(a) and 3.4(a) and (b).

At potentials greater than -0.5 V in figs. 3.4(a) and (b), the band due to formate near 1352 cm^{-1} is enhanced in intensity relative to the other formate bands. This may be attributed, on the basis of fig. 3.3(b), to the growth of the 1360 cm^{-1} band of HCO_3^- under the formate feature, causing the latter to be enhanced. The 1360 cm^{-1} HCO_3^- feature appears as a small shoulder between the 1352 cm^{-1} and 1383 cm^{-1} bands. Thus, up to the onset of CO_2 formation at -0.3 V, the only products appear to be formate (both solution and adsorbed) and bicarbonate. The gain of the water features near

3289 cm^{-1} and 1650 cm^{-1} and the loss of the broad OH^- band are also observed in fig. 3.4(c).

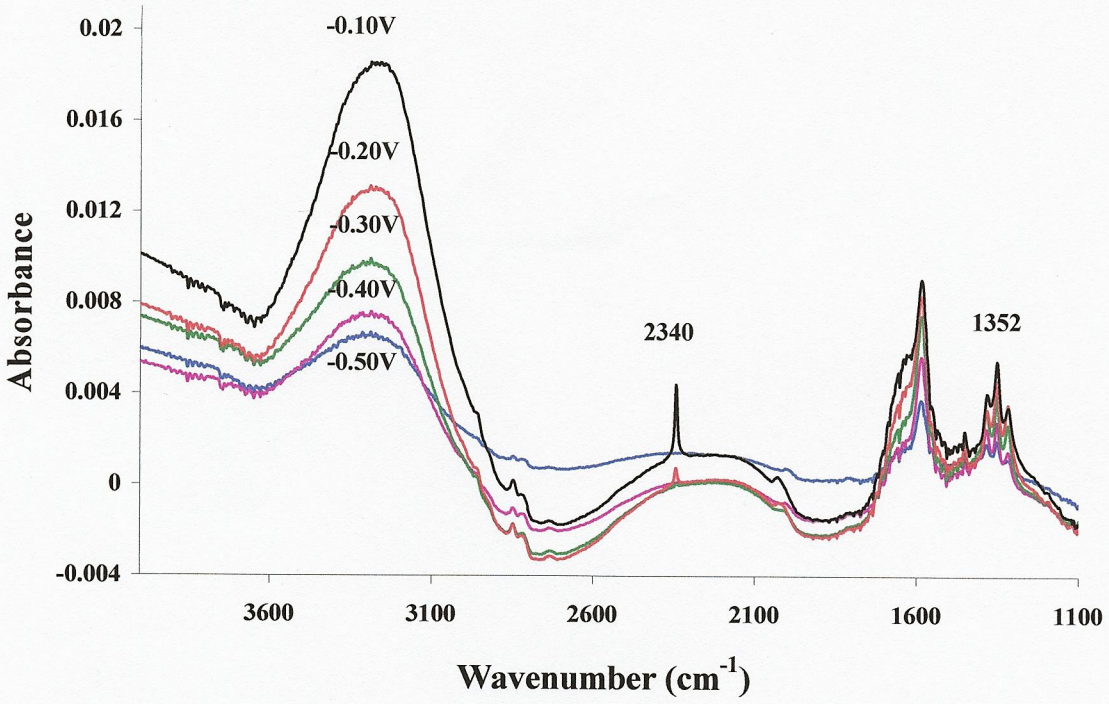

(a)

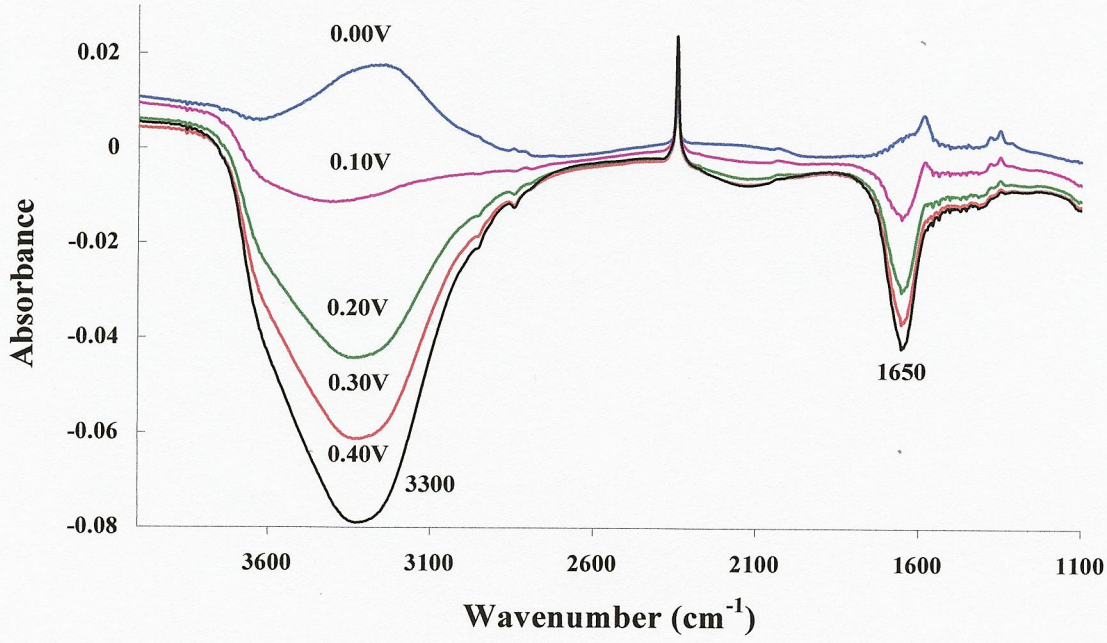

(b)

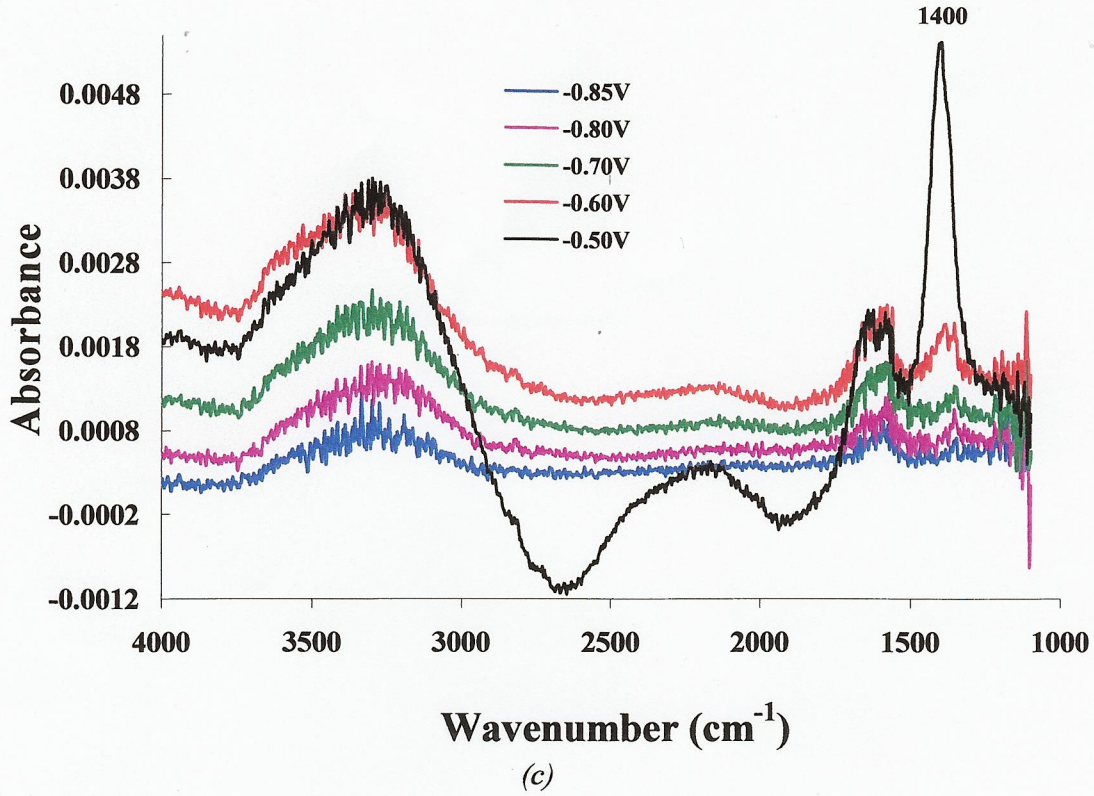

(c)

Figure 3.4. Spectra collected during the same experiment as in Figure 3.3(a) at higher potentials: (a) -0.5 V to -0.1 V and (b) 0 V to 0.4 V. (c) In situ FTIR spectra (100 co-added and averaged scans at 8 cm^{-1} resolution) from the Pt electrode in Figure 3.1 immersed in N_2-saturated 0.1 M KOH + 2 M NaOOCH as a function of potential between -0.85 V and -0.5 V vs. MMO normalized to the reference spectrum taken at -0.85 V vs. MMO.

Interestingly, the onset and subsequent increase in intensity of the CO_2 band near 2340 cm^{-1} is mirrored by the decrease in intensity of the 1317 cm^{-1} $HCOO_{ads}$; moreover, the onset and increase in intensity of the latter feature tracks the charge passed at each potential during the spectral data collection, see fig. 3.5(a). In addition, in experiments employing 0.1 M CH_3OH, this feature was still observed, but at lower intensities.

The band due to linearly bonded CO_L is observed at all potentials greater than -0.8 V, i.e., with an onset in the hydride region between the current maxima for the stripping of strongly and weakly adsorbed hydrogen, and preceding the formation of $HCOO^-$, as can be seen in fig. 3.5(b).

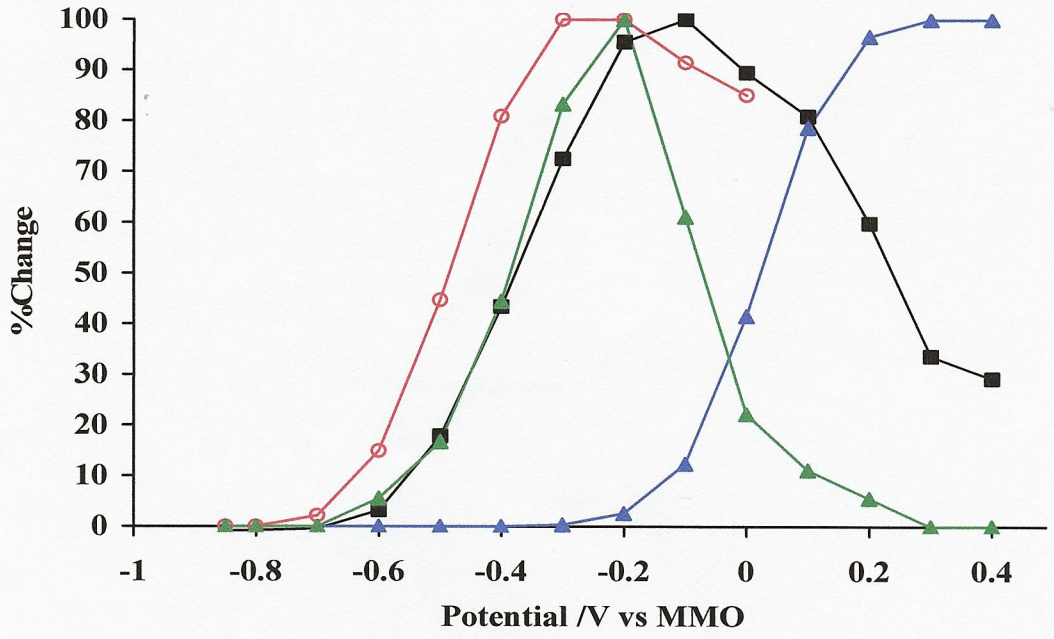

(a)

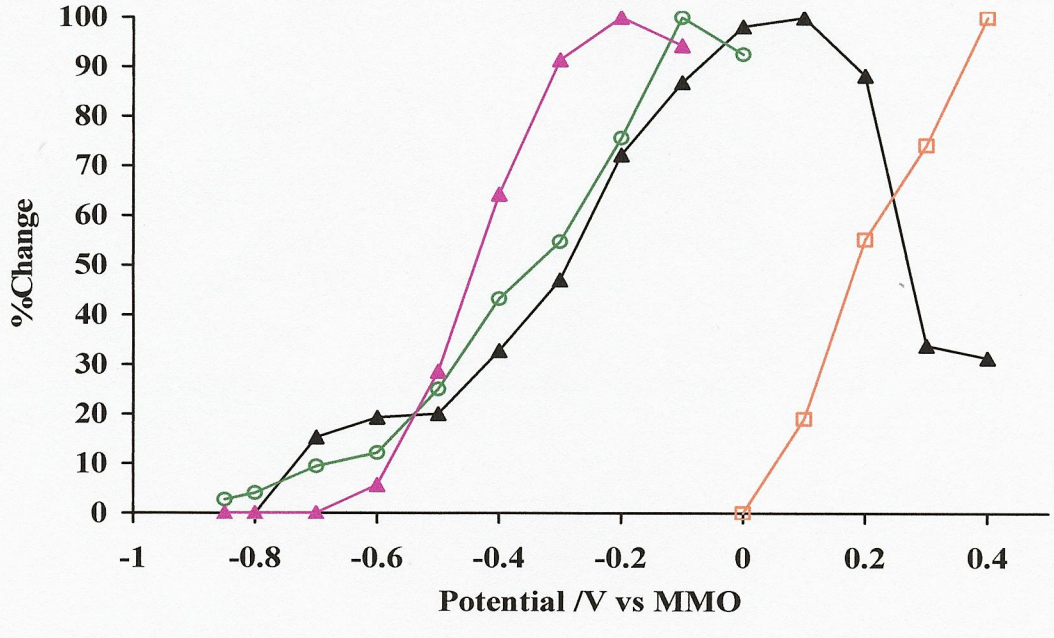

(b)

Figure 3.5. The potential dependences of the key features in Figures 3.3(a) and 3.4(a) and (b), normalized to their maximum values as a function of potential. (a) (■) Charge passed at each step, (▲) the intensity of the CO_2 band at 2340 cm^{-1}, (○) the intensity of the formate band at 1581 cm^{-1}, and (▲) the intensity of the $HCOO_{ads}$ band at 1317 cm^{-1}. (b) (▲) The integrated intensity of the CO_L band, (○) the intensity of the 3289 cm^{-1} gain feature, (▲) the intensity of the loss at 2750 cm^{-1}, and (□) the intensity of the 3300 cm^{-1} loss feature.

In acid solution, Kunimatsu [29] observed that the dehydrogenation of methanol is very low at 0.05 V vs. Reversible Hydrogen Electrode (RHE), with the coverage by CO_L increasing as the potential moves into the double layer region.

The CO_L band remains unipolar, showing clearly that no chemisorption of methanol takes place at the reference potential. Between -0.7 V and -0.5 V, dehydrogenation of methanol takes place after the stripping of weakly adsorbed hydrogen, with the intensity of the CO_L feature almost constant as the potential moves into the double layer region. At potentials between -0.5 V and 0.1 V there is a steady increase in intensity, after which there is a slow decrease to 0.2 V and a more rapid decrease at higher potentials. It may be seen from fig. 3.5(b) that the CO_L intensity appears to track that of the 3289 cm^{-1} water gain feature, but the absence of a CO_L band in fig. 3.4(c) suggests that the two are not linked.

At potentials where the intensity of the CO_2 feature levels out, two intense loss features near 3300 cm^{-1} and 1650 cm^{-1} appear and grow, which would seem to be due to water being excluded from the thin layer due to CO_2 gas bubble formation. A comparison of these features with the single beam reference spectrum collected at -0.85 V confirms they may be attributed to highly hydrogen-bonded [34] bulk (water + HO^-). An experiment in which O_2 bubbles were generated in the thin layer using 0.1 M KOH in the absence of methanol confirmed this assignment.

3.4. In-situ FTIR data in O_2-saturated solution

Figure 3.6(a) and (b) show representative spectra from an experiment analogous to that depicted in figs. 3.3(a) and 3.4(a) and (b), except using O_2-saturated 0.1 M KOH, and figs. 3.7(a)-(e) compare plots of the intensities, or integrated intensity in the case of the CO_L band, as a function of potential from the spectra obtained in both experiments.

In essence, the same features observed in both experiments except, in the O_2-saturated solution:

- There is no gain of the water bands near 3289 cm^{-1} and 1650cm^{-1} at lower potentials.

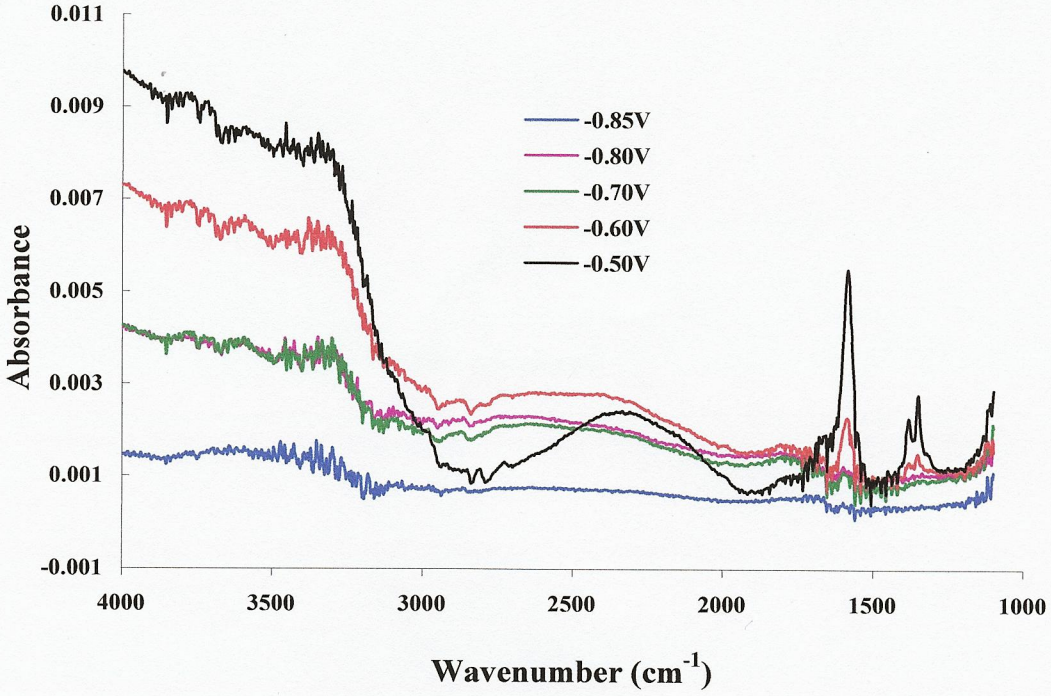

(a)

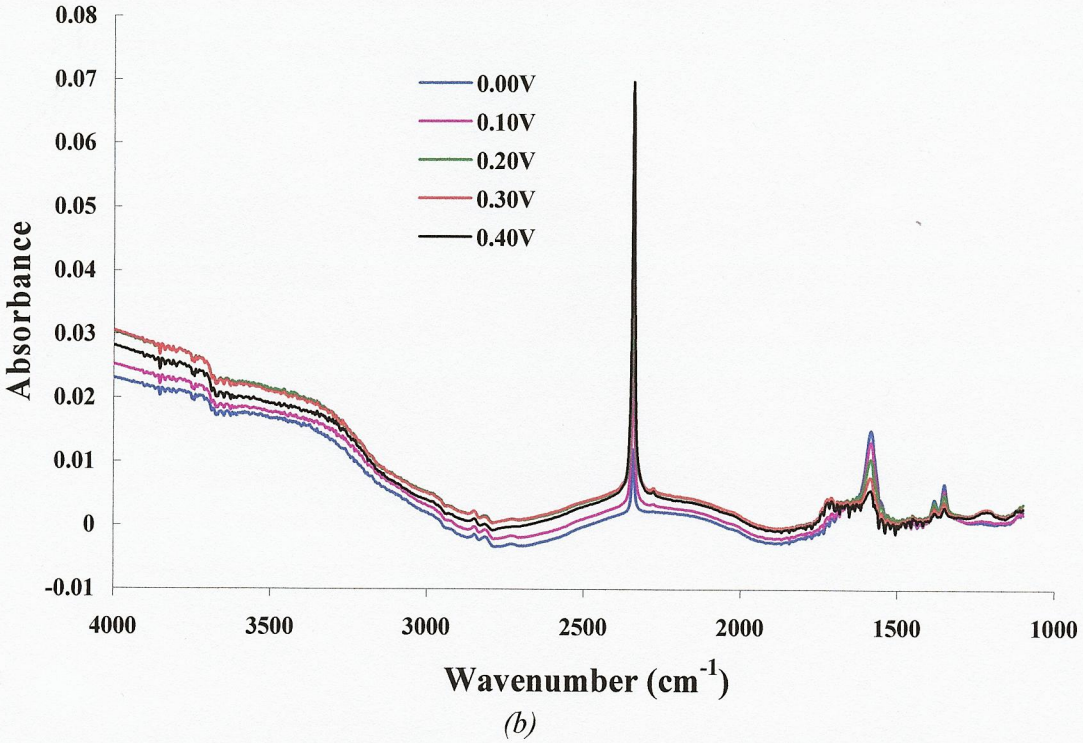

(b)

Figure 3.6. (a) In-situ FTIR spectra (100 co-added and averaged scans at 8 cm^{-1} resolution) analogous to those depicted in Figures 3.3(a) and 3.4(a) and (b), except using O_2-saturated 0.1 M KOH + 5 M CH_3OH: (a) -0.85 V to -0.5 V and (b) 0 V to 0.4 V vs. MMO normalized to the reference spectrum taken at -0.85 V vs. MMO.

- There is no loss of the intense water features near 3300cm^{-1} and 1650cm^{-1} due to CO_2 bubble formation at higher potentials.
- No CO_L is observed.

All of these points suggest a major change in the surface structure of the Pt in O_2-saturated solution.

Figure 3.7(a) shows plots of the CO_2 absorbance in the N_2 and O_2 experiments showing that CO_2 evolution is comparable at lower potentials in both solutions before increasing rapidly above that observed in N_2-saturated solution at potentials greater than 0 V and ending 2.5-fold higher at 0.4 V, without showing any leveling out of intensity. Thus it does not seem unreasonable to postulate that the presence of O_2 (or at least the residual species from O_2 reduction at -0.85 V) has very significantly increased the activity of the surface as well as reduced the nucleation sites for CO_2 bubble formation. In the N_2 experiment, the intensity of the CO_2 feature remains constant at higher potentials as the excess CO_2 is forced into the gas phase.

As may be seen from fig. 3.7(b), the coverage by adsorbed HCOO is reduced by ca. 66% in O_2-saturated KOH compared to N_2 solution; moreover, in agreement with the CVs in fig. 3.2, the onset of the band occurs at a higher potential. The 1581 cm^{-1} solution formate feature is, in contrast, increased 2.5-fold (as was observed with the CO_2 band) in O_2-saturated solution (fig. 3.7(c)), and the 1352 cm^{-1} HCO_3^- band is increased 1.9-fold (fig. 3.7(d)). The 2-fold increase in intensity of the OH^- loss feature, measured at 2750cm^{-1} (see fig. 3.7(e)), is in reasonable agreement with the enhancement in the anodic peak in the voltammetry, and supports the observed enhanced activity of the Pt anode in O_2-saturated solution.

3.5. Discussion.

3.5.1. The intermediate in the direct pathway.

It is generally accepted that the oxidation of methanol at Pt-based anodes takes place via at least two parallel paths, one involving CO_{ads} as the reactive intermediate (the indirect or CO path), and one involving another reactive intermediate (the direct, or

non-CO path), and a variety of species have been postulated as the non-CO_{ads} intermediates [24, 29, 30].

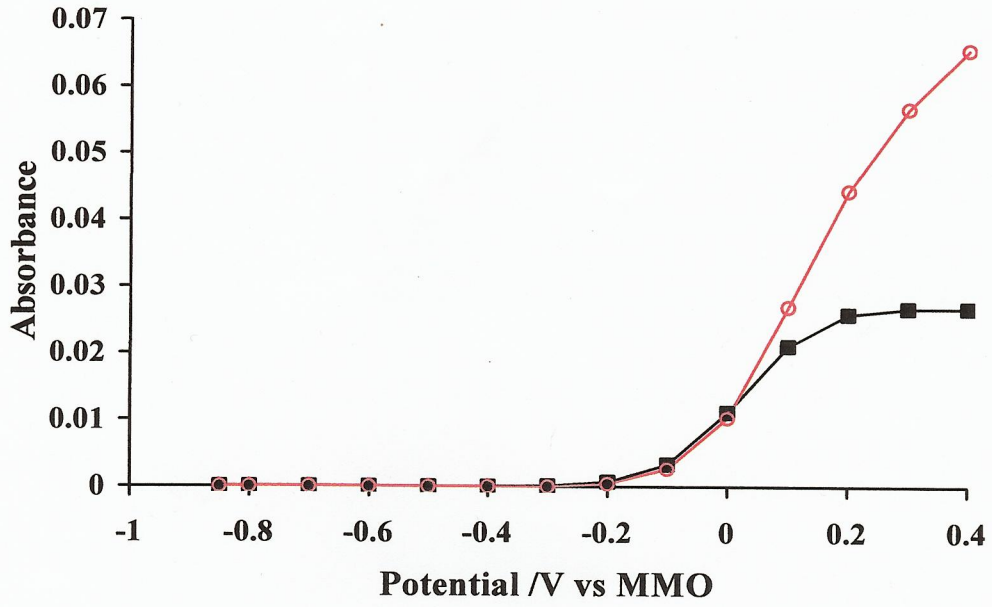

(a)

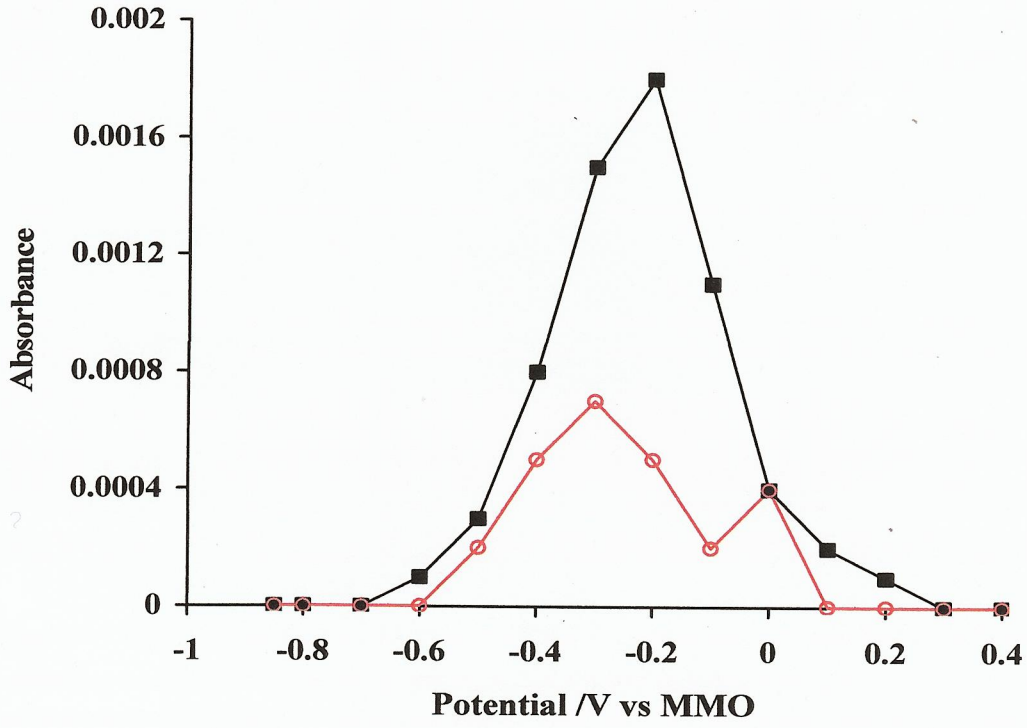

(b)

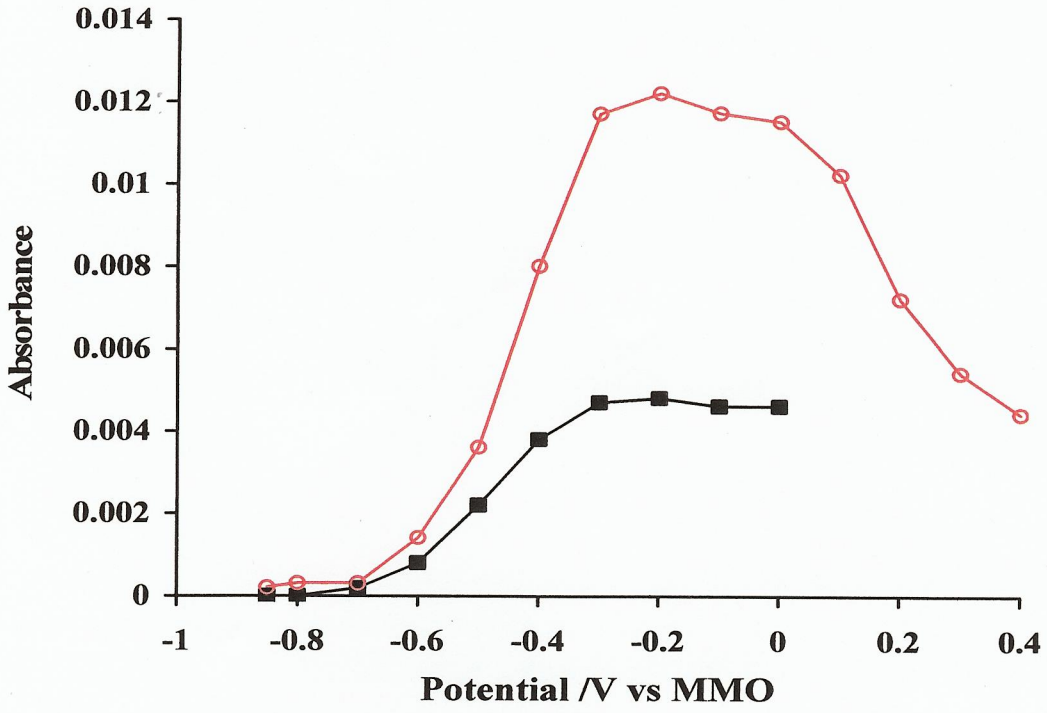
0.014
0.012
0.01
0.008
0.006
0.004
0.002
0
Absorbance
-1
-0.8
-0.6
-0.4
-0.2
0
0.2
0.4
Potential /V vs MMO

(c)

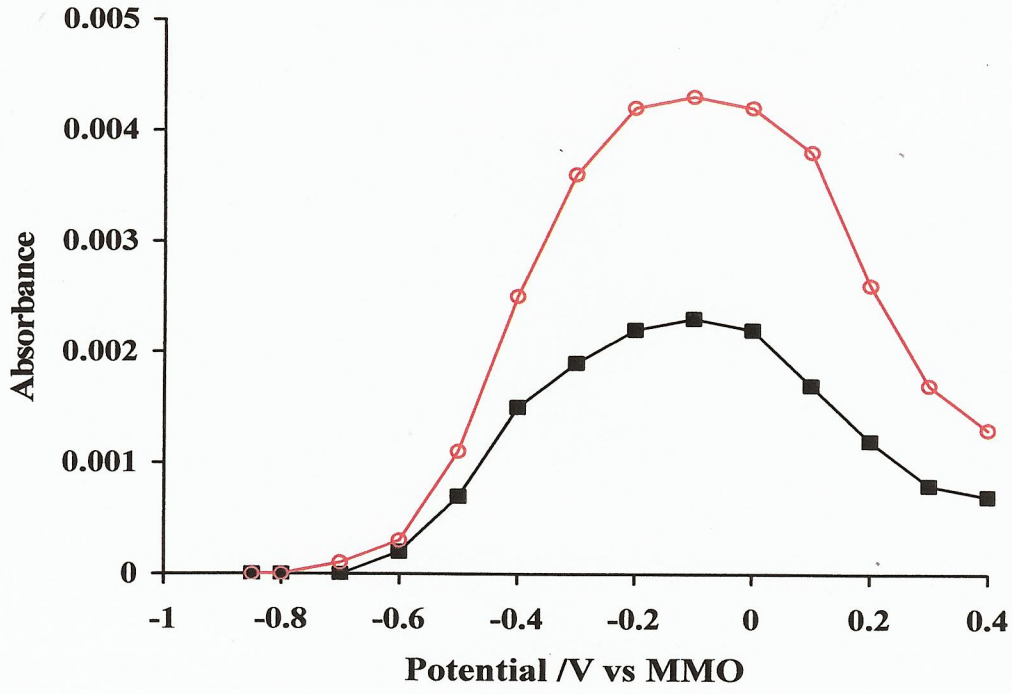
0.005
0.004
0.003
0.002
0.001
0
Absorbance
-1
-0.8
-0.6
-0.4
-0.2
0
0.2
0.4
Potential /V vs MMO

(d)

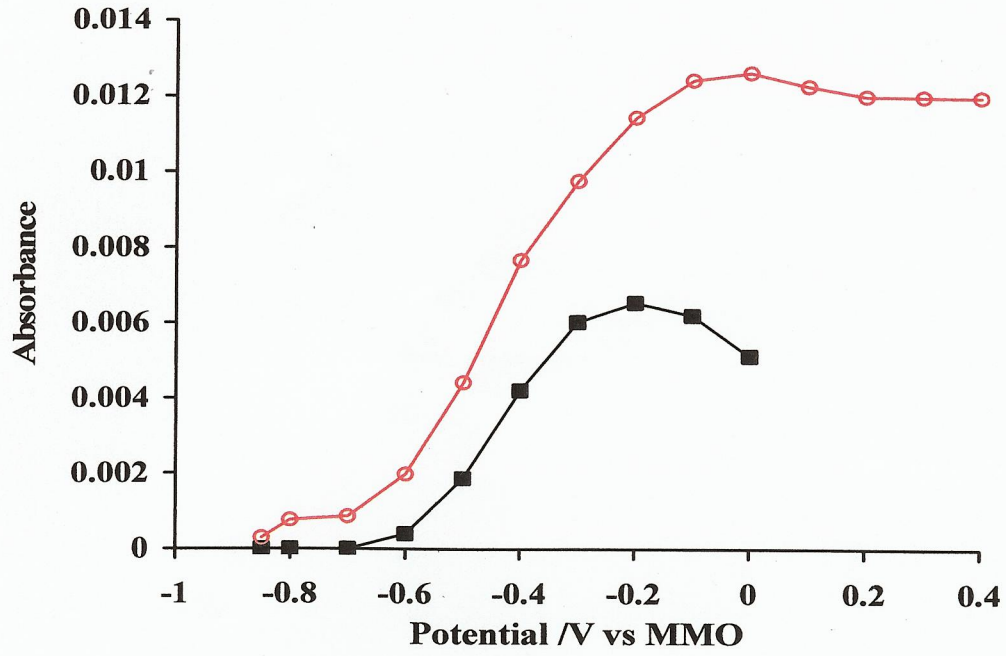

(e)

Figure 3.7. Comparison of the in-situ FTIR data obtained in (■) N_2- and (○) O_2-saturated solutions as function of potential: (a) 2340 cm^{-1} CO_2 band; (b) 1317 cm^{-1} $HCOO_{ads}$ band; (c) 1581 cm^{-1} $HCOO^-$ band; (d) 1352 cm^{-1} HCO_3^- band; (e) 2750 cm^{-1} OH^- band.

As was stated above, a band near 1320 cm^{-1} has been observed by a number of authors [9, 23-30] employing predominantly surface enhanced infrared spectroscopy (SEIRAS) to study methanol oxidation at Pt film electrodes deposited on Si prisms in acid solution [23-29], and this band is attributed to formate adsorbed through both oxygen atoms. This adsorbed formate has been postulated as the intermediate in the "direct" pathway [24, 30], but this is controversial, with other workers postulating that it is a poison [27, 29] and, as it is only observed at high potentials in acid solution, is of little relevance to the electrocatalytic processes taking place at the anode under the operating conditions of a Direct Methanol Fuel Cell (DMFC) [29].

Kunimatsu et al. [29] dismissed adsorbed formate as the direct path intermediate on the basis that the coverage did not change appreciably on increasing the concentration of methanol from 0.04 M to 1 M, and that the formate only appears at relatively high potentials (> 0.6 V vs. RHE), too high to be relevant to the operation of the DMFC. In addition, the authors cited work in the literature [27, 35] in which it was shown that

the band intensity of adsorbed formate increases as Pt(111) > Pt(100) > Pt(110) at 0.7-1.0 V, which is opposite in ranking in terms of methanol activity.

In contrast to Kunimatsu et al., Chen and co-workers [24] and Xue et al. [30] take the observation that the coverage of $HCOO_{ads}$ tracks the anodic current as evidence for the direct role of adsorbed formate in methanol oxidation in acid solution. Chen et al. [24] observed that the dehydrogenation of methanol took place at 100 mV vs. RHE, i.e. in the hydride region and that the intensity of the resulting CO_L species remained essentially constant up to the onset of the methanol oxidation reaction (MOR) at 0.5 V, after which it declined rapidly. This decrease was mirrored by an increase in the intensity of the $HCOO_{ads}$ and of the anodic current, and $HCOO_{ads}$ was postulated by the authors to be the intermediate in the direct pathway.

The discussion of the role of adsorbed formate in methanol electro-oxidation at Pt in acid solution in the SEIRAS/attenuated total reflectance (ATR) literature is hampered by a major disadvantage of the ATR approach, which is the insensitivity of the technique to solution species. This means that key solution intermediates and products such as formate, bicarbonate and CO_3^{2-}/CO_2 cannot be monitored, and the discussion in the SEIRAS literature is based only on correlating the IR bands of adsorbed species with anodic current; thus there is a clear advantage in having the capability to observe both adsorbed and solution species with external reflectance IR spectroscopy.

As was discussed above, both Chen et al. [24] and Kunimatsu et al. [29] postulate that methanol is oxidized by OH_{ads} to generate $HCOO_{ads}$, although the latter group believes that the contribution of this process to methanol oxidation in the DMFC is small. The present results show that the coverage of $HCOO_{ads}$ tracks the anodic current (see fig. 3.5(a), suggesting that adsorbed formate is the (or an important) intermediate in the indirect path mechanism under our experimental conditions. If it is accepted that the loss of solution OH^- at potentials greater than -0.6 V in fig. 3.3(a) is due at least in part to the oxidation of OH^- to OH_{ads} (as well as its consumption by protons produced during the oxidation of methanol), then the observation that the intensity of this feature tracks the coverage of $HCOO_{ads}$, and the anodic current supports the role of adsorbed formate in the direct path mechanism. In addition, the coexistence of adsorbed CO and adsorbed formate is direct evidence for the

mechanism. In contrast to the case in acid solution, the onsets of OH_{ads} formation, the anodic current, and $HCOO_{ads}$ formation are all -0.6 V, i.e. 0.25 V vs. RHE, a value well within the operational range of anode potentials of a hypothetical alkaline DMFC. If $HCOO_{ads}$ is the intermediate in the direct pathway in alkaline solution, then the fact that the coverage of the intermediate tracks the anodic current suggests that attack on the $HCOO_{ads}$ is the rate-limiting step rather than its formation. Interestingly, the rapid decline in coverage of $HCOO_{ads}$ (and the increase in CO_2) commences with the onset of oxide formation at -0.2 V, suggesting, perhaps, that the oxidation of the former is via a Langmuir-Hinshelwood reaction with the oxide.

The absence of significant absorptions due to CO_3^{2-} between -0.85 V and -0.5 V suggest that, over this potential range, the predominant solution product is formate due to desorption of the intermediate. At higher potentials, first bicarbonate is formed, then CO_2 as well as formate, with formate formation ceasing at 0 V, when it is presumably entirely converted to HCO_3^-/CO_3^{2-}.

It is interesting that there appears to be no/very little conversion of formate to carbonate in the CH_3OH experiments, in contrast to experiments in which formate was employed as the reactant, suggesting effective blocking of the relevant active sites.

3.5.2. The effect of oxygen on the voltammetry and in-situ FTIR data.

The presence of oxygen clearly has a significant effect on the voltammetric response in the presence and absence of methanol, as well as on the FTIR data, and this effect is heavily leveraged, i.e. the oxygen cannot be directly involved in the oxidation of methanol since the concentration of methanol is considerably in excess of the O_2 (the concentration of oxygen in O_2-saturated solution at 298 K is ca. 1.3 mM [36]); the oxygen must modify the surface in some way as to generate highly active sites giving rise to the enhanced production of CO_2, formate, and HCO_3^-, evinced by the plots in figs. 3.7(a), (c)-(e). In terms of the voltammetry, as well as suppressing H_{ads} formation, it is interesting that the passivation of the Pt at high potentials with respect to methanol oxidation only becomes apparent when the sweep is reversed. In the presence of oxygen, no passivation is seen. The reversal of the sweep causes oxide formation to cease: this formation is believed to be through a place-exchange

mechanism [37, 38] driven by the potential difference between the Pt and the surrounding electrolyte; such a mechanism continually draws Pt ions to the electrolyte/oxide interface, and these are obviously critical to methanol oxidation. If oxygen is adsorbed at lower potentials, e.g. as OH_{ads}, this may substantially affect the nature of the oxide film; perhaps it is significantly more porous in the presence of oxygen, and maybe, as suggested by Hu and Liu [39] the coexistence of bare Pt, Pt-OH, and Pt(IV) is necessary for the oxidation of methanol (at least in acid), and porous open films with O_2 stabilizing the Pt(IV) are required. Reversing the sweep in the absence of O_2, particularly if the film is less porous, would lead to inhibition.

The presence of adsorbed OH inhibits methanol chemisorption, particularly if such adsorption requires the presence of specific sites such as edge or corner sites. In that way, a relatively small amount of strongly adsorbed oxygen species could prevent methanol adsorption on such sites, with the subsequent formation of CO_{ads}. It is also confirmatory evidence that formation of adsorbed formate is through a different, Eley-Rideal mechanism. Clearly the high concentration of methanol also plays a role here in determining the film morphology. It would also appear that the effect of oxygen is to modify the nucleation characteristics of the oxide film such that CO_2 bubble formation no longer occurs.

The oxidation of methanol requires both free Pt and $Pt\text{-}O(H)_{ads}$, and it is possible in the presence of oxygen, there is considerable adsorbed peroxy species, which inhibit the chemisorption of methanol, this would certainly explain the absence of any adsorbed CO in the oxygen saturated solution spectra. This would not block the formation of adsorbed formate if this takes place via an Eley-Rideal-type mechanism between solution methanol and OH_{ads} as inferred by, for example, Chen et al. [24] and Kunimatsu et al. [29].

3.6. Conclusions

The formation of OH_{ads} can be inferred from the loss of bands due to solution OH^-. In complete contrast to the accepted mechanism of methanol oxidation at Pt in acid solution, adsorbed CO is a spectator species in alkaline solution; the active intermediate is $HCOO_{ads}$ adsorbed through both O atoms, formed *via* the reaction of solution methanol on OH_{ads} *via* an Eley-Rideal mechanism. The rate determining step

is attack on the adsorbed intermediate by OH_{ads} *via* a Langmuir-Hinshelwood mechanism. In contrast to the dual path mechanism, $HCOO_{ads}$ is the common intermediate in the formation of both solution formate and CO_2 (as HCO_3^-). Interestingly, the solution formate is not oxidised to CO_2, as is observed if sodium formate is oxidised at Pt under the same condition, suggesting that the actives sites for the latter reaction have been blocked by adsorbed species, possibly due to the re-adsorption of formate to form adsorbed CO.

The presence of dissolved O_2 has a marked effect upon the observed electrochemistry, due to the enhanced formation of OH_{ads}, which inhibits methanol chemisorption and promotes the formation of adsorbed formate.

3.7. References

1. Christensen P. A., (2010). *In-situ Fourier transform infra red spectroelectrochemistry as a probe of electrocatalysis*, in: Spectroscopic properties of inorganic and organometallic compounds, Royal Society of Chemistry, Cambridge,. p. 125 - 165.
2. Wang Q., Sun G.Q., Jiang L.H., Xin Q., Sun S.G., Jiang Y.X., Chen S.P., Jusys Z., and Behm R.J., (2007). Physical Chemistry Chemical Physics, 9, 21, pp. 2686-2696.
3. Heinen M., Jusys Z., and Behm R.J., (2010). The Journal of Physical Chemistry C, 114, 21, pp. 9850-9864.
4. Morallón E., Rodes A., Vázquez J.L., and Pérez J.M., (1995). Journal of Electroanalytical Chemistry, 391, 1-2, pp. 149-157.
5. Ortiz R., Marquez O.P., Marquez J., and Gutierrez C., (1996). The Journal of Physical Chemistry, 100, 20, pp. 8389-8396.
6. Chbihi M.E.M., Takky D., Hahn F., Huser H., Léger J.M., and Lamy C., (1999). Journal of Electroanalytical Chemistry, 463, 1, pp. 63-71.
7. Couto A., Rincôn A., Pérez M.C., and Gutiérrez C., (2001). Electrochimica Acta, 46, 9, pp. 1285-1296.
8. Demarconnay L., Brimaud S., Coutanceau C., and Léger J.M., (2007). Journal of Electroanalytical Chemistry, 601, 1-2, pp. 169-180.
9. Chen Q.-S., Sun S.-G., Zhou Z.-Y., Chen Y.-X., and Deng S.-B., (2008). Physical Chemistry Chemical Physics, 10, 25, pp. 3645-3654.
10. Beden B., Kadirgan F., Lamy C., and Leger J.M., (1982). Journal of electroanalytical chemistry, 142, 1-2, pp. 171-190.
11. Tripković A.V., Popović K.D., Momčilović J.D., and Dražić D.M., (1996). Journal of Electroanalytical Chemistry, 418, 1-2, pp. 9-20.
12. Tripković A.V., Popović K.D., and Lović J.D., (2001). Electrochimica Acta, 46, 20-21, pp. 3163-3173.
13. Tripković A.V., Popović K.D., Lović J.D., Jovanović V.M., and Kowal A., (2004). Journal of Electroanalytical Chemistry, 572, 1, pp. 119-128.
14. Jin J.M., Lin W.F., and Christensen P.A., (2004). Journal of Electroanalytical Chemistry, 563, 1, pp. 71-80.

15. Christensen P.A., Jin J.-M., Lin W.-F., and Hamnett A., (2004). The Journal of Physical Chemistry B, 108, 11, pp. 3391-3394.
16. Jin J.M., Lin W.F., and Christensen P.A., (2008). Physical Chemistry Chemical Physics, 10, 25, pp. 3774-3783.
17. Gottesfeld S. and Pafford J., (1988). Journal of The Electrochemical Society, 135, 10, pp. 2651-2652.
18. Jusys Z. and Behm R.J., (2004). The Journal of Physical Chemistry B, 108, 23, pp. 7893-7901.
19. Tingelöf T., Hedström L., Holmström N., Alvfors P., and Lindbergh G., (2008). International Journal of Hydrogen Energy, 33, 8, pp. 2064-2072.
20. Hamann C.H., Hamnett A., and Vielstich W., (2007). *Electrochemistry*, 2 ed. Weinheim: Wiley-VCH. 531.
21. Yu E.H., Scott K., and Reeve R.W., (2003). Journal of Electroanalytical Chemistry, 547, 1, pp. 17-24.
22. Abdel Rahim M.A. and Hassan H.B., (2009). Thin Solid Films, 517, 11, pp. 3362-3369.
23. Endo M., Matsumoto T., Kubota J., Domen K., and Hirose C., (2000). The Journal of Physical Chemistry B, 104, 20, pp. 4916-4922.
24. Chen Y.X., Miki A., Ye S., Sakai H., and Osawa M., (2003). Journal of the American Chemical Society, 125, 13, pp. 3680-3681.
25. Yan Y.G., Li Q.-X., Huo S.-J., Ma M., Cai W.-B., and Osawa M., (2005). The Journal of Physical Chemistry B, 109, 16, pp. 7900-7906.
26. Shiroishi H., Ayato Y., Kunimatsu K., and Okada T., (2005). Journal of Electroanalytical Chemistry, 581, 1, pp. 132-138.
27. Nakamura M., Shibutani K., and Hoshi N., (2007). ChemPhysChem, 8, 12, pp. 1846-1849.
28. Yajima T., Uchida H., and Watanabe M., (2004). The Journal of Physical Chemistry B, 108, 8, pp. 2654-2659.
29. Kunimatsu K., Hanawa H., Uchida H., and Watanabe M., (2009). Journal of Electroanalytical Chemistry, 632, 1-2, pp. 109-119.
30. Xue X.-K., Wang J.-Y., Li Q.-X., Yan, Liu J.-H., and Cai W.-B., (2007). Analytical Chemistry, 80, 1, pp. 166-171.
31. Christensen P.A. and Hamnett A., (1989). Journal of Electroanalytical Chemistry and Interfacial Electrochemistry, 260, 2, pp. 347-359.
32. Osawa M., Shi-Gang S., Christensen P. A., and Andrzej W., (2007). *Electrocatalytic Reactions on Platinum Electrodes Studied by Dynamic Surface-Enhanced Infrared Absorption Spectroscopy (SEIRAS)*, in: In-situ Spectroscopic Studies of Adsorption at the Electrode and Electrocatalysis, Elsevier Science B.V., Amsterdam, p. 209-246.
33. Nakamoto K., (1986). *Infrared and Raman spectra of inorganic and coordination compounds*, 4 ed. New York: Wiley Interscience. 484.
34. Wandlowski T., Ataka K., Pronkin S., and Diesing D., (2004). Electrochimica Acta, 49, 8, pp. 1233-1247.
35. Kuzume A., Mochiduki Y., Tsuchida T., and Ito M., (2008). Physical Chemistry Chemical Physics, 10, 16, pp. 2175-2179.
36. (1994). CRC Handbook of Chemistry and Physics 74th Edition, ed. D.R. Lide. Boca Raton, FL.: CRC Press/Taylor and Francis. 2,376.
37. Alsabet M., Grden M., and Jerkiewicz G., (2006). Journal of Electroanalytical Chemistry, 589, 1, pp. 120-127.

38. Jerkiewicz G., Vatankhah G., Lessard J., Soriaga M.P., and Park Y.-S., (2004). Electrochimica Acta, 49, 9-10, pp. 1451-1459.
39. Hu C.-C. and Liu K.-Y., (1999). Electrochimica Acta, 44, 16, pp. 2727-2738.

4. Formate electro-oxidation in aqueous KOH

In the previous chapter, *in-situ* FTIR studies were reported on the electro-oxidation of methanol at polycrystalline Pt (pc-Pt) in aqueous KOH. The work showed that: (1) formate adsorbed through both oxygen atoms is an important intermediate in the oxidation of methanol under such conditions, and (2) adsorbed CO appears to be a spectator species rather than an intermediate, in complete contrast to the situation in acid solutions ([1,2] and references therein), both are important observations.

As was stated in chapter 3, formate adsorbed through both oxygen atoms has also been observed during the oxidation of methanol at Pt in acid solutions, but whether it is an intermediate in methanol oxidation in acid remain controversial [1, 3, 4] not least because the coverage of formate does not correlate with methanol concentration [1] and it is now generally accepted that in acid electrolyte methanol chemisorbs through the carbon atom via sequential stripping of hydrogen atoms, with Pt_3COH or PtCO as important intermediates, depending upon methanol concentration [5].

In alkaline solution this would not appear to be the dominant pathway with alternatives routes involving Pt-O available. Furthermore, the activation energies of these alternatives pathways seem to be sufficiently similar that small changes can cause the methanol oxidation reaction to 'flick' across to a different pathway. This was shown [6] in the experiment in O_2-saturated methanolic KOH where no evidence for linearly adsorbed CO (CO_L) was seen at all, and all the methanol consumption appeared to be via the adsorbed formate intermediate (see section 3.5.1). In addition, when the concentration of solution formate built up sufficiently, re-adsorption of formate to CO_L was observed, reinforcing the postulated non-linear and dynamic nature of methanol oxidation under alkaline conditions.

In order to explore the above concepts further, it was decided to investigate the oxidation of formate at polycrystalline Pt in both nitrogen- and oxygen-saturated aqueous KOH, and the results so obtained are presented below.

4.1. Previous work on formate oxidation in alkaline solution.

There is a significant literature on formate as a reactant and intermediate in electrochemical oxidation in acid solution, (see for example [7], and references therein), including a large number of *in-situ* infrared studies, see for example [2-4, 8, 9]. The literature on formate as a reactant or product during electrolysis under alkaline conditions is not so numerous, and is principally concerned with methanol electro-oxidation. In that respect, the discussion in section 3.1 is also relevant to this chapter.

It is necessary to recall, that the model postulated by Tripković et al. [10-12], included two types of adsorbed oxygen species: Pt-OH or $Pt(OH)_{ads}$ the "reversibly adsorbed" OH which is the active intermediate, and the strongly adsorbed $Pt\text{-}O^-$. The formation of $Pt\text{-}O^-$ at higher potentials was taken as the reason for the inhibition of the methanol oxidation reaction and concomitant drop in current. Tripković et al. [12] also postulated that HCO_3^- and CO_3^{2-} block the surface to Pt-OH formation, causing a decrease in activity [10, 13-15]. The latter also forms a key element of the model reported by Garcia and Koper [16] to explain their I/V data on the electro-oxidation of CO_{ads} at stepped Pt electrodes in 0.1 M NaOH.

The work of Tripković et al. and Garcia and Koper is important as it may provide a possible explanation for our observation that CO_L is a spectator species rather that intermediate; thus, Garcia and Koper found that the mobility of CO at Pt(111) in aqueous alkaline solution was very low and interpreted this in terms of the blocking of the surface by co-adsorbed CO_3^{2-}. They develop a model in which again, OH_{ads} is a reactive intermediate, and CO_{ads} oxidation is initiated at defects, steps and kinks, with the most facile oxidation involving OH adsorbed at step sites and CO adsorbed nearby, see fig. 4.1(a).

Carbonate produced from the oxidation of CO blocks the active sites, so the oxidation of CO_{ads} present on terrace sites remote from the active sites takes place slowly via terrace adsorbed OH, see fig. 4.1(b). Terrace CO also diffuses to unblocked defect sites where it can be oxidized, fig 4.1(c). The slowest reaction is between CO_{ads} species at defect sites blocked by CO_3^{2-} which must react with Pt-OH on the terraces, see fig. 4.1(d).

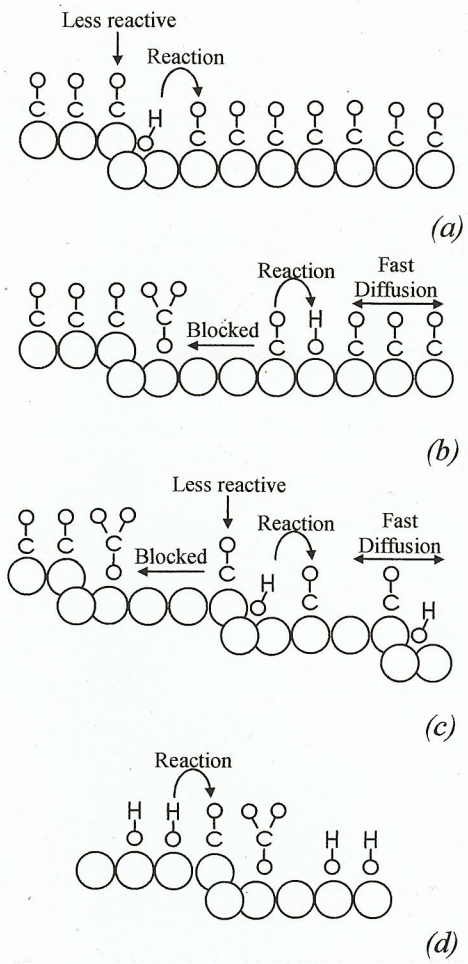

Figure 4.1. Proposed mechanism for CO oxidation on stepped platinum electrodes in alkaline media: (a) initiation at steps and defects at low potential; (b) terrace oxidation on Pt(111) for E > 0.75 V (steps blocked by carbonate); (c) oxidation at partially blocked steps at stepped electrodes for E < 0.75 V; (d) oxidation of step-bound CO by adsorbed OH for E > 0.75 V from [16].

Unfortunately, whilst studies on the adsorption of CO_3^{2-} and HCO_3^- at Pt electrodes have been reported [17-19], these concerned adsorption in acid solution; to date, there are no *in-situ* IR studies on formate as a reactant at Pt or Pt based electrodes in alkaline solution.

In-situ FTIR studies on methanol oxidation at Pt-based electrodes, where formate is reported as a product, are confined to Morallón et al. [20] (on single crystal Pt electrodes), Zhou et al. [21] (on nano-structured Pt) and Chen et al. [22] (CoPt core shell nano-particles). In essence, none of these papers are representative of methanol electro-oxidation at 'normal' Pt surfaces.

In the paper by Morallón et al. [20], the FTIR spectra were obtained using the SNIFTIRS (Subtractively Normalized *In-situ* Fourier Transform Infra-Red Spectroscopy) approach in which the potential of the electrode is switched repeatedly between reference and sample values. The SNIFTIRS potential protocol is not representative of most electrochemical experiments which are commonly constant potential (or current) electrolyses.

The paper by Zhou et al. [21] and Chen et al. [22] both rely upon the use of nano-structured particles to generate Abnormal Infrared Effects AIRE's [23]. One of the phenomena associated with AIRE's is significant enhancement of IR adsorption; however, AIRE's are not currently understood, and the electrodes exhibiting such effects not representative of catalytic electrodes [23], All three groups interpreted their data in terms of the dual path mechanism, with CO_{ads} the strongly adsorbed poison, oxidation of which leads to CO_3^{2-}, and unspecified reactive intermediate leading to solution formate, which is further oxidized to CO_3^{2-}; the groups did not report the observation of adsorbed CO_3^{2-} or adsorbed HCOO.

4.2. Voltammetry

The cyclic voltammetric response of polycrystalline Pt, (pc-Pt) in N_2 and O_2-saturated 0.1 M KOH was discussed in a previous paper [6]; briefly, when compared with the voltammetry in acid solution, there is an additional, small wave having an onset near -0.5 V vs. MMO which may be attributed to the reversible formation of OH_{ads} [22]. This peak is enhanced in O_2-saturated KOH.

4.3. In-situ FTIR experiments

4.3.1. The current response observed during the in-situ FTIR experiments.

The changes in current observed during the FTIR experiments in N_2 and O_2 are shown in fig. 4.2. In both N_2 and O_2 saturated solution there is cathodic current passed until -0.6 V, with large increases in anodic current at -0.5 V to -0.3 V; up to -0.6 V, the cathodic component of the nett current, due to oxygen reduction, is significantly greater in O_2 saturated solution, as may be expected [24], The large increase in anodic current at potentials > -0.5 V may indicate the involvement of OH_{ads} in the electrochemical process [1, 16, 25].

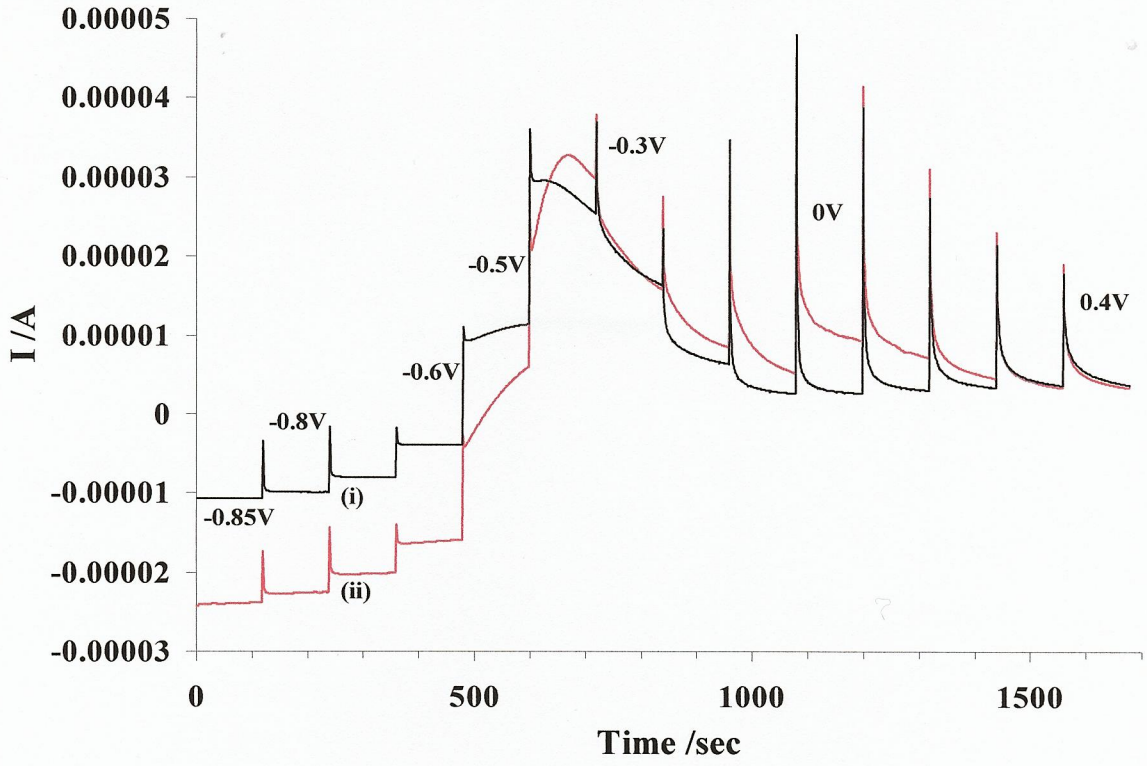

Figure 4.2. The variation in the current observed during the in-situ FTIR experiments on the oxidation of 0.1 M NaOOCH in (i) N_2 and (ii) O_2 -saturated 0.1 M KOH.

4.3.2. The spectra up to -0.6 V

Figure 4.3 shows the spectra collected at -0.8 V to -0.6 V, i.e. potentials where a nett cathodic current flows, in N_2 saturated 0.1 M KOH + 0.1 M NaOOCH. As may be seen from the figure, both linearly adsorbed CO (CO_L, 2005 cm^{-1}) and bridge-bonded CO (CO_B, 1805 cm^{-1}) [6, 20, 21, 26] are formed from the chemisorption of formate; the fact that neither of these features are bipolar indicates that there is no, or very little, adsorbed CO present in the reference spectrum collected at -0.85 V, and hence the CO_L and CO_B species result from chemisorption of formate at potentials > -0.85 V. This observation is in agreement with the fact that, during methanol oxidation under the same conditions [6], high concentrations of formate resulted in re-absorption to form CO_L. Solution carbonate is formed at -0.6 V, band near 1400 cm^{-1} [6, 26, 27], presumably due to the participation of OH_{ads}; however, there is no clear decline in the intensity of the CO_L or CO_B features at -0.6 V which would suggest their oxidation to CO_3^{2-}.

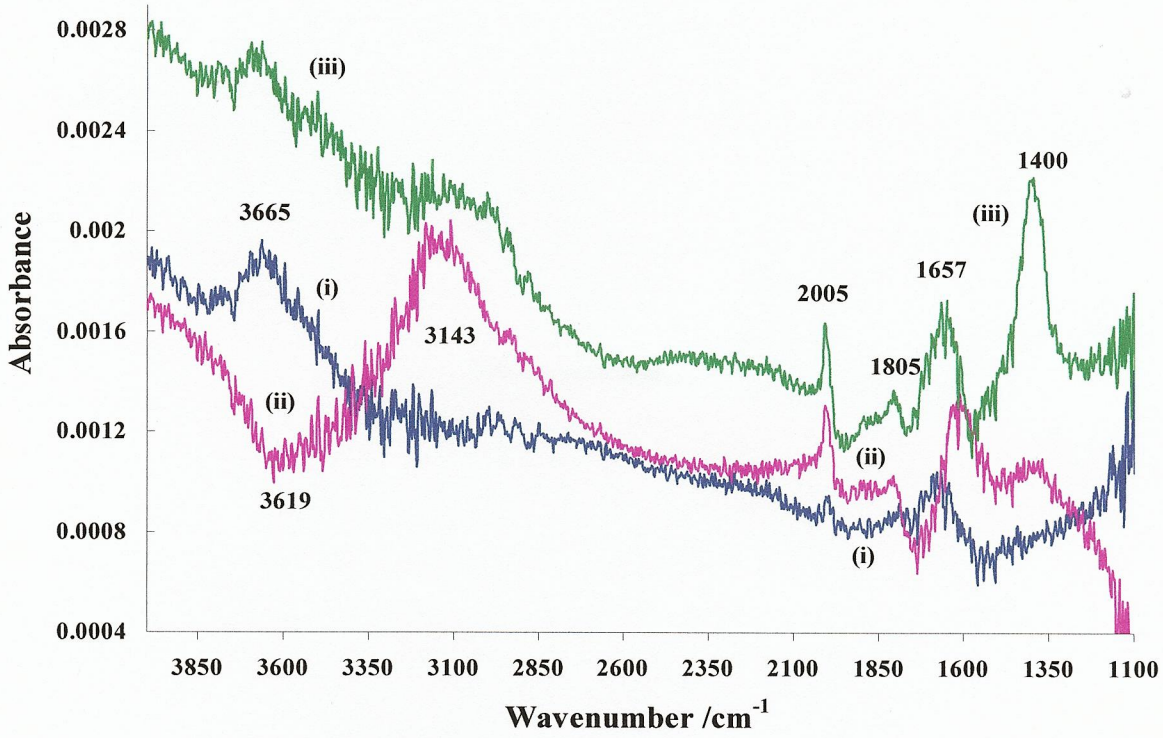

Figure 4.3. In-situ FTIR spectra (100 co-added and averaged scans, 8 cm^{-1} resolution) of a polycrystalline Pt electrode (0.64 cm^2) immersed in N_2-saturated 0.1 M NaOOCH + 0.1 M KOH collected at (i) -0.8 V, (ii) -0.7 V and (iii) -0.6 V. The reference spectrum was taken at -0.85 V vs. MMO and a second, absorbance spectrum collected at the same potential to ensure the system was stable with respect to, for example, electrode movement.

Features near 1657 cm^{-1} and associated with the appearance of HCO_3^- or CO_3^{2-}, are often attributed to uncompensated water in the thin layer or to the instability of the latter [18, 21, 22, 26, 27], It is surprising that carbonate is formed at a potential lower than the onset of OH_{ads} formation. However, in acid solution, formic acid oxidation by the 'direct pathway', i.e. via a weakly adsorbed reactive intermediate, does not require an external oxidation source such as OH_{ads} and hence formic acid oxidation can take place at more negative potentials than required for H_2O dissociation on Pt [4].

In addition to the bands due to adsorbed CO and CO_3^{2-} in fig. 4.3, there is clearly a major change in the nature of the water layer adjacent to the electrode, as may be seen from the behaviour of the water bands, particularly at -0.7 V where the water features are seen as two bipolar bands, centred near 3300 cm^{-1} and 1660 cm^{-1}, showing that both the O-H stretch and H-O-H deformation of the interfacial water are shifting to lower frequency as the potential is increased from -0.85 V to -0.7 V, suggesting a

concomitant increase in hydrogen bonding, perhaps due to association with a charged ion [28-30] such as OH^- or CO_3^{2-}.

Figure 4.4 shows analogous spectra to those in fig. 4.3 from the experiment conducted in O_2-saturated KOH. A consistent observation is that there are very clear differences between the spectra in O_2-saturated electrolyte as compared to N_2-saturated: in O_2, in contrast to the case in N_2-saturated solution, there is a clear, steady gain of bands associated with interfacial water, with the frequencies of both the O-H stretch and H-O-H deformation jumping to lower values at -0.7 V with the appearance of CO_L; i.e. 3584 to 3370 cm^{-1} and 1669 to 1644 cm^{-1}, respectively suggesting an increase in hydrogen bonding. In contrast, in acid solution, the formation of a hydrophobic CO_{ads} layer is often associated with water bands shifting to higher frequency, due to a decrease in hydrogen bonding associated with the water molecules adjacent to, or buried within, the CO_{ads} domains [9].

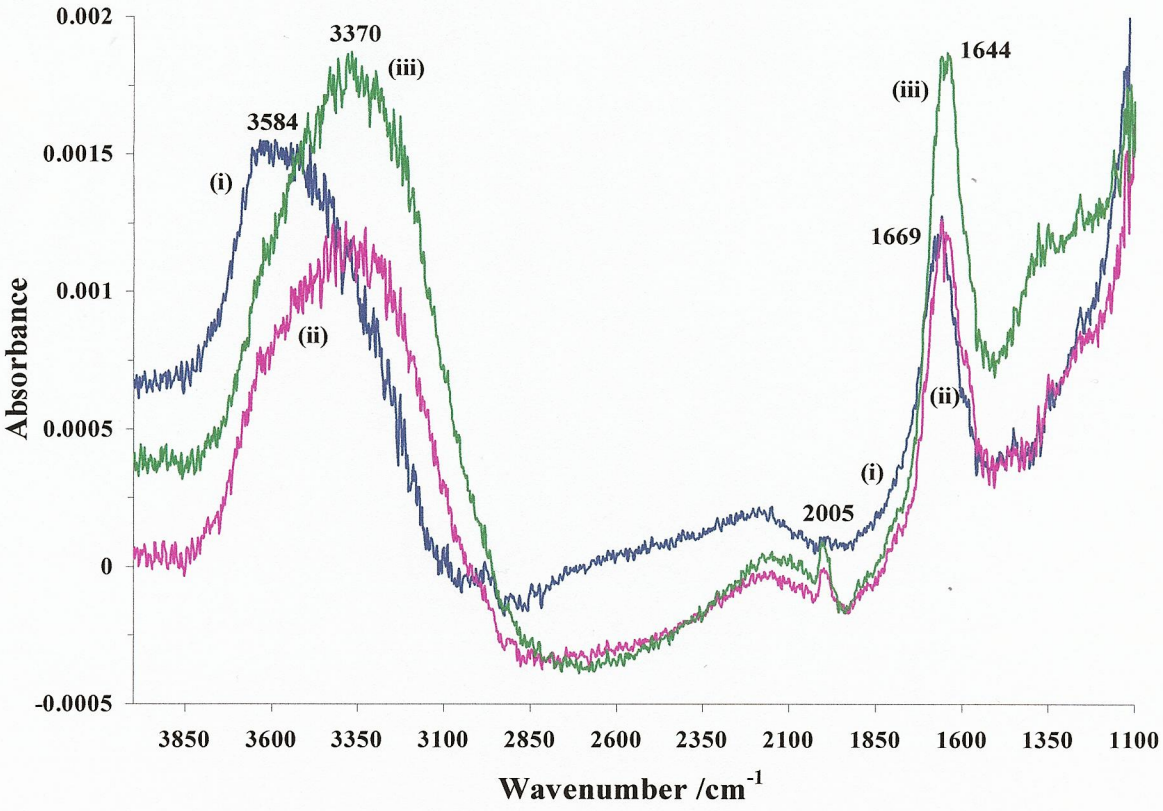

Figure 4.4. In-situ FTIR spectra of the polycrystalline Pt electrode (0.64 cm^2) immersed in O_2-saturated 0.1 M NaOOCH + 0.1 M KOH collected at (i) -0.8 V, (ii) -0.7 V and (iii) -0.6 V. The reference spectrum was taken at -0.85 V vs. MMO.

Figure 4.2 shows that marked O_2 reduction is taking place in the potential region depicted in fig. 4.4; Christensen [31] also reported that O_2 reduction at Au in aqueous KOH was accompanied by the gain of water features near 3300 and 1640 cm^{-1}.

A very significant difference between figs. 4.3 and 4.4 is the absence of CO_3^{2-} in the latter; this is not observed until -0.5 V in O_2-saturated solution (see fig. 4.7 below) and suggests that the reduction of oxygen at the electrode is inhibiting the formation of the reactive intermediate on the path to CO_3^{2-}, but not the chemisorption of formate to CO_L, which is formed in both N_2 and O_2 saturated solutions, albeit the absorbance of the feature in the latter experiment is halved from 3.0×10^{-4} in N_2 to 1.5×10^{-4} at -0.6 V. This suggests that, as was observed during the oxidation of methanol under similar conditions [22], adsorbed CO is a spectator rather than participant in the oxidation of formate to CO_3^{2-}.

Umeda and co-workers [24] have reported that methanol oxidation at electro-catalysts produced by co-sputtering Pt and C is enhanced in the presence of O_2 for certain compositions. The authors interpreted their data in terms of a model in which the reduction of O_2 at Pt generates adsorbed OH which inhibits the oxygen reduction reaction, but enhances methanol oxidation through the removal of adsorbed CO [32].

$$Pt\text{-}CO + Pt\text{-}OH \rightarrow 2Pt + CO_2 + H^+ + e^- \qquad (4.1)$$

4.3.3. The spectra from -0.6 V to -0.4 V.

Figure 4.5 shows spectra collected from -0.6 V to -0.4 V in the N_2 experiment depicted in fig. 4.3. As may be seen from the figure, at -0.5 V and -0.4 V, a broad loss feature between 3100 cm^{-1} and 1700 cm^{-1} appears with minima near 2750 cm^{-1} and 1950 cm^{-1} and grows at higher potentials, i.e. tracking the OH_{ads} feature in the voltammograms. This broad IR band was attributed to the loss of solution OH^- [6] (see section 3.3) and tentatively assigned to the formation of OH_{ads} from solution OH^-. Confirmation of the assignment of the broad loss band comes from the work of Śmiechowski and Stangret [33] who deconvoluted the IR spectrum of 'MOH affected water' (M = Li, Na and K) and assigned bands at 2845 and 2020 cm^{-1} so obtained to the continuum absorbance [34, 35] which is largely absent in bulk, neutral water. The O-H stretches and H-O-H deformations are present in both forms of water, and hence

consumption of OH^- in the thin layer would be expected to result in the loss of these continuum absorptions, compare figs. 4.6(a) and (b) [33].

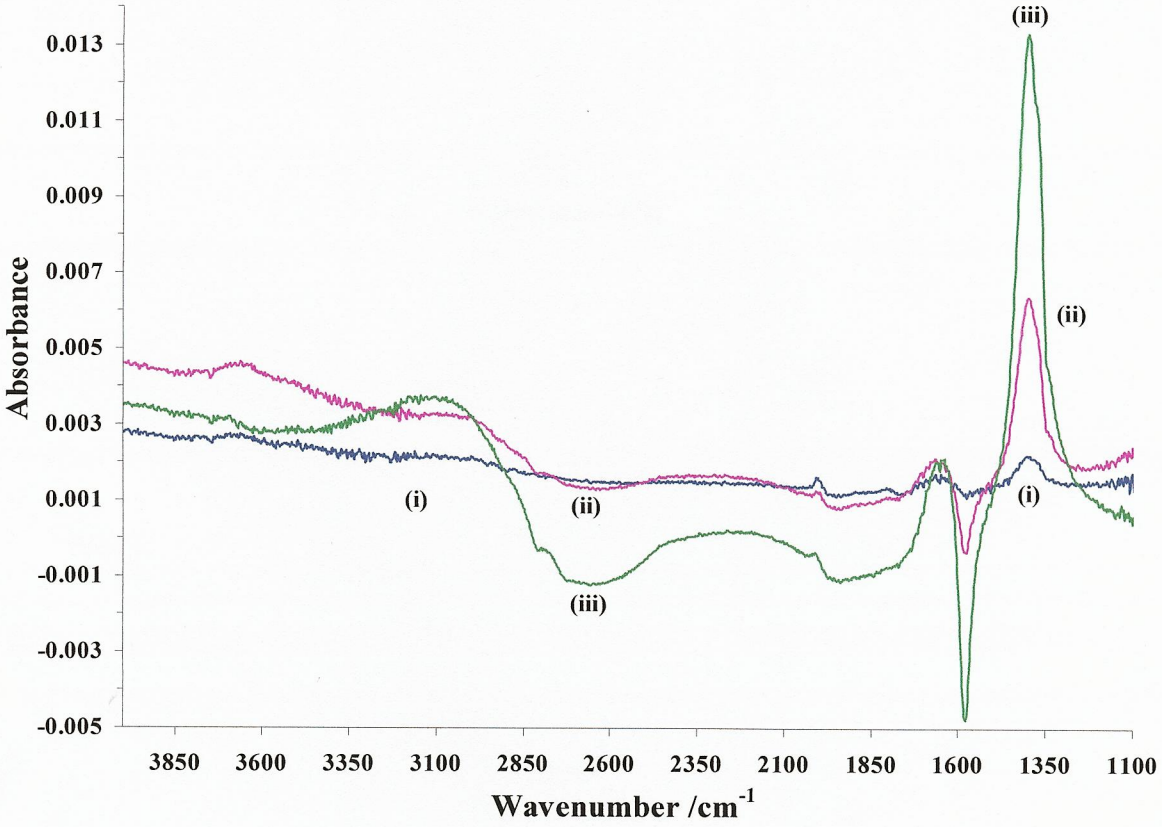

Figure 4.5. In-situ FTIR spectra of the polycrystalline Pt electrode (0.64 cm^2) immersed in N_2-saturated 0.1 M NaOOCH + 0.1 M KOH collected at (i) -0.6 V, (ii) -0.5 V and (iii) -0.4 V. The reference spectrum was taken at -0.85 V vs. MMO.

It is clear from fig. 4.5 that CO_L is present throughout the potential range of the figure, and that the production of CO_3^{2-} increases significantly at -0.5 V and -0.4 V, with the concomitant loss of the solution formate band near 1581 cm^{-1} [6].

The analogous experiment in O_2 saturated KOH to that depicted in fig. 4.5 is shown in fig. 4.7. Again, CO_L is present at all potentials and CO_3^{2-} is produced at potentials $\geq$ -0.5 V; however, in contrast to the experiment in N_2, the formate loss feature is only observed at -0.4 V and, as was mentioned above, the appearance of the carbonate is 100 mV higher than in N_2 saturated KOH. Furthermore, in fig. 4.7, the water gain features are more intense than in fig. 4.5.

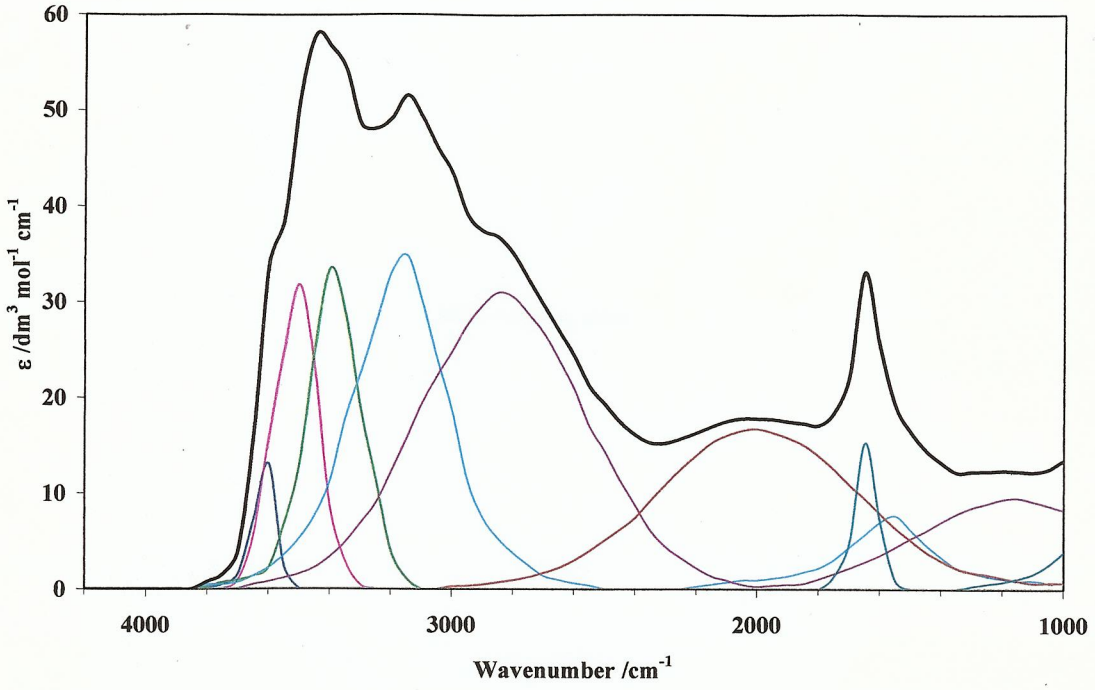
60
50
40
30
20
10
0
ε /dm3 mol-1 cm-1
4000
3000
2000
1000
Wavenumber /cm-1

(a)

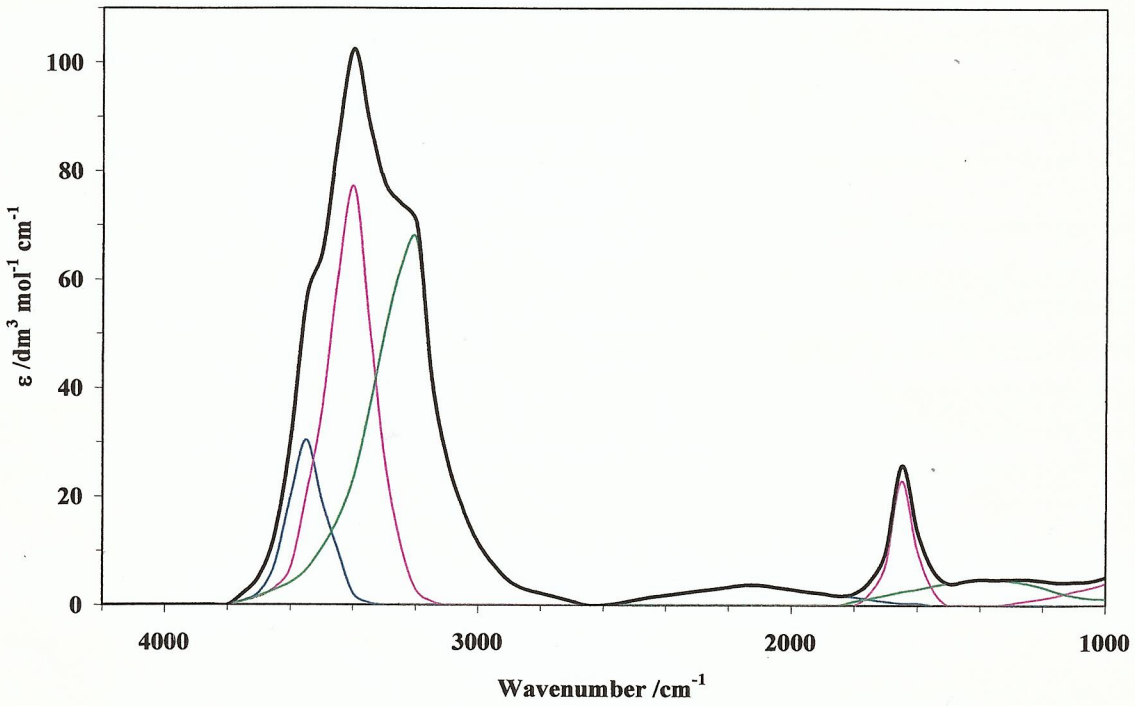
100
80
60
40
20
0
ε /dm3 mol-1 cm-1
4000
3000
2000
1000
Wavenumber /cm-1

(b)

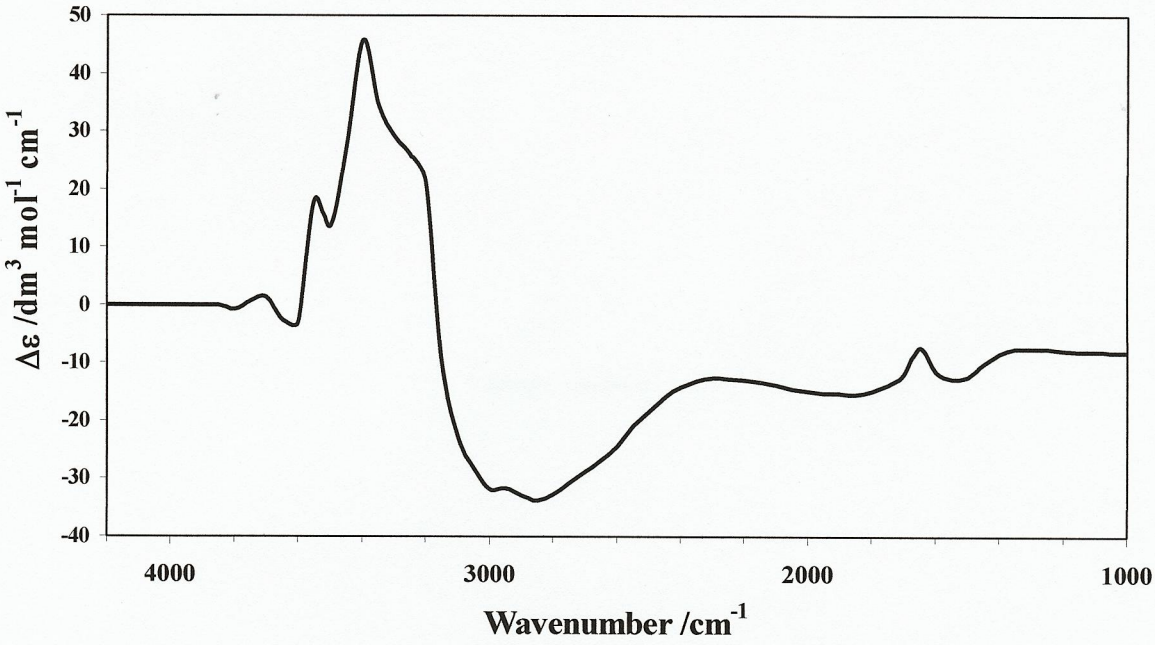

(c)

Figure 4.6. (a) Deconvoluted MOH affected H_2O spectrum for NaOH; (b) deconvoluted bulk H_2O spectrum; (c) difference spectrum resulting from subtracting the spectrum in (a) from that in (b). Figures 4.6(a) and (b) are redrawn from [33].

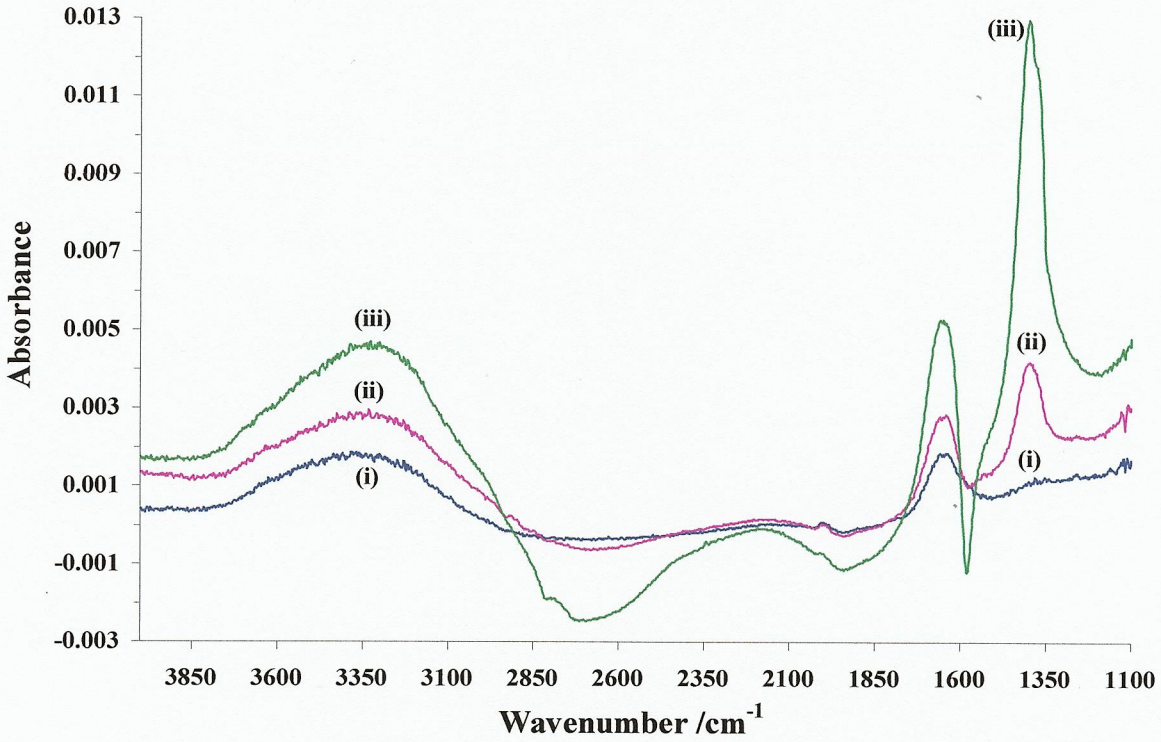

Figure 4.7. In-situ FTIR spectra of the polycrystalline Pt electrode immersed in O_2-saturated 0.1 M NaOOCH +0.1 M KOH collected at (i) -0.6 V, (ii) -0.5 V and (iii) -0.4 V. The reference spectrum was taken at -0.85 V vs. MMO.

4.3.4. The spectra from -0.4 V to +0.4 V.

The differences in the IR response between N_2 and O_2 saturated KOH are even more marked over the potential range -0.4 V to -0.2 V, see figs. 4.8 and 4.9.

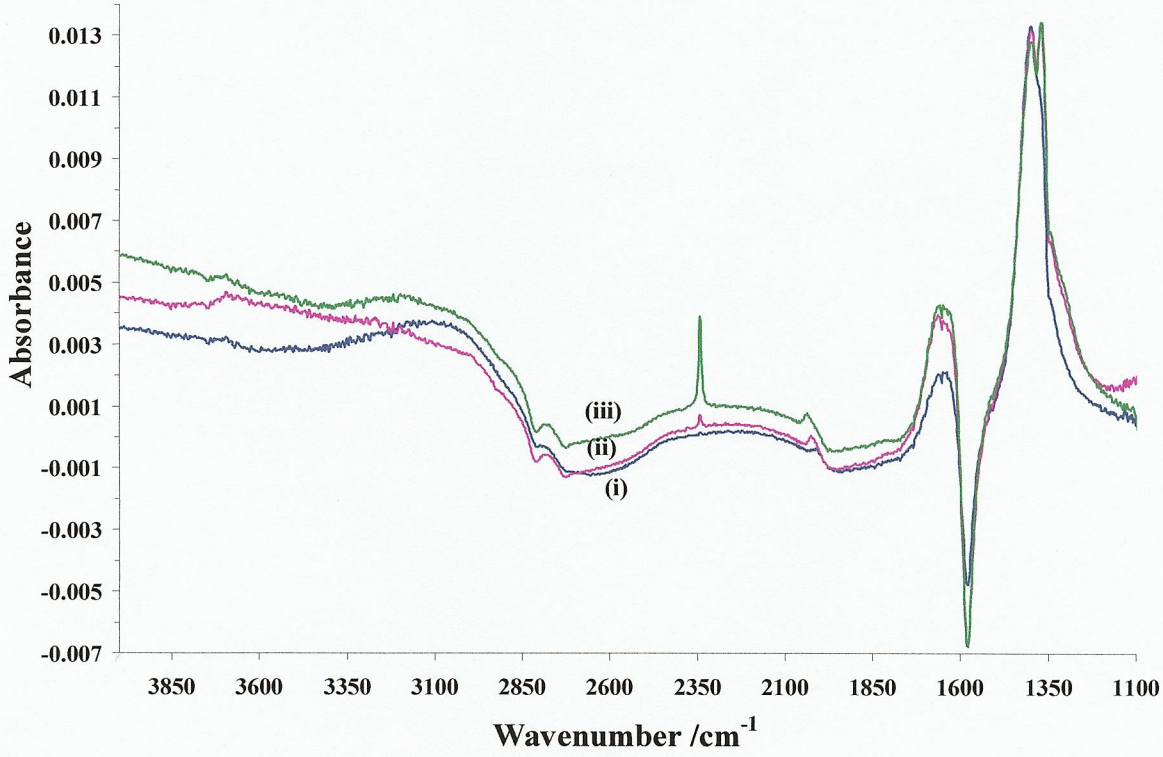

Figure 4.8. In-situ FTIR spectra of the polycrystalline Pt electrode immersed in N_2-saturated 0.1 M NaOOCH + 0.1 M KOH collected at (i) -0.4 V to (iii) -0.2 V. The reference spectrum was taken at -0.85 V vs. MMO.

A comparison of the spectra collected at -0.4 V and -0.1 V in the experiments depicted in figs. 4.8 and 4.9 is presented in figs. 4.10(a) and (b), respectively, and plots of the CO_2 absorbance observed in the N_2 and O_2 experiments between -0.85 V and +0.4 V are shown in fig. 4.10(c).

The differences in behaviour between N_2 and O_2 saturated KOH are clear in the figures. The feature at 2340 cm^{-1} may be attributed to solution CO_2, the onset potential of which is -0.3 V in both O_2 and N_2 saturated electrolyte (see fig. 4.10(c)), and which suggests the pH in the thin layer is comparable to or less than $pK_{\alpha,1}$, of carbonic acid (6.37; $pK_{\alpha,2}$ = 10.25 [34]) at the potentials in the figure. From fig. 4.10(c) it can be seen that the CO_2 produced in the two experiments is significantly different,

with ca. 5 times more generated in the O_2 experiment, supporting our postulate that the mechanism is very finally balanced.

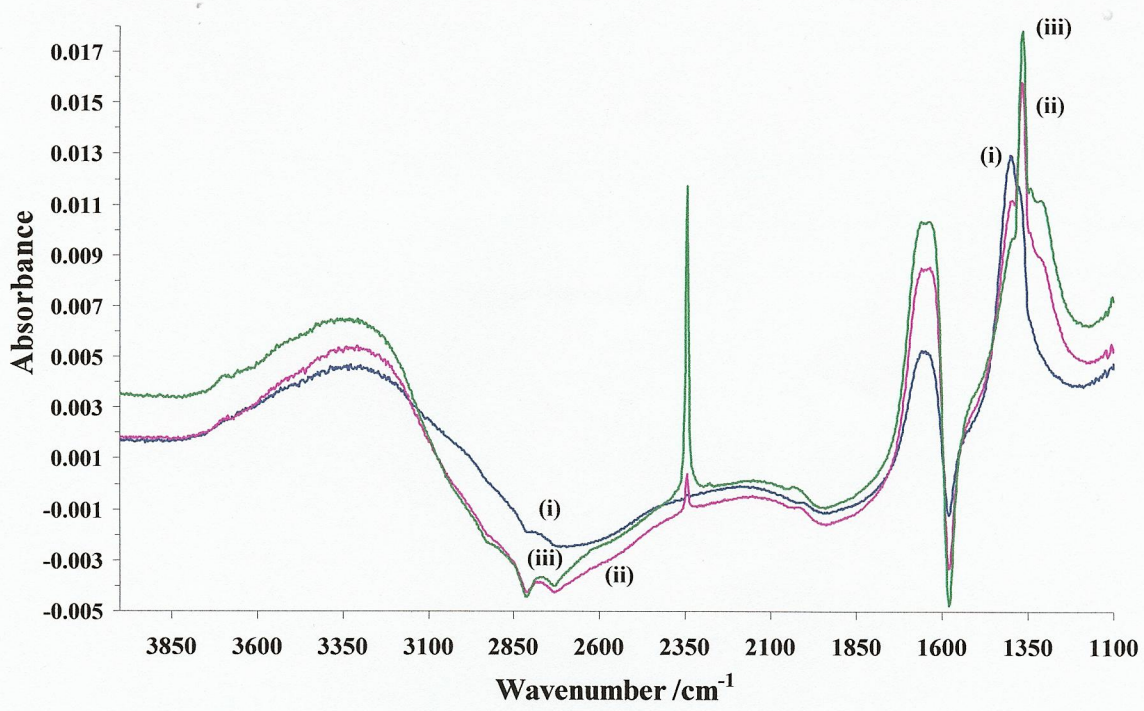

Figure 4.9. In-situ FTIR spectra of the polycrystalline Pt electrode immersed in O_2-saturated 0.1 M NaOOCH + 0.1 M KOH collected at (i) -0.4 V to (iii) -0.2 V. The reference spectrum was taken at -0.85 V vs. MMO.

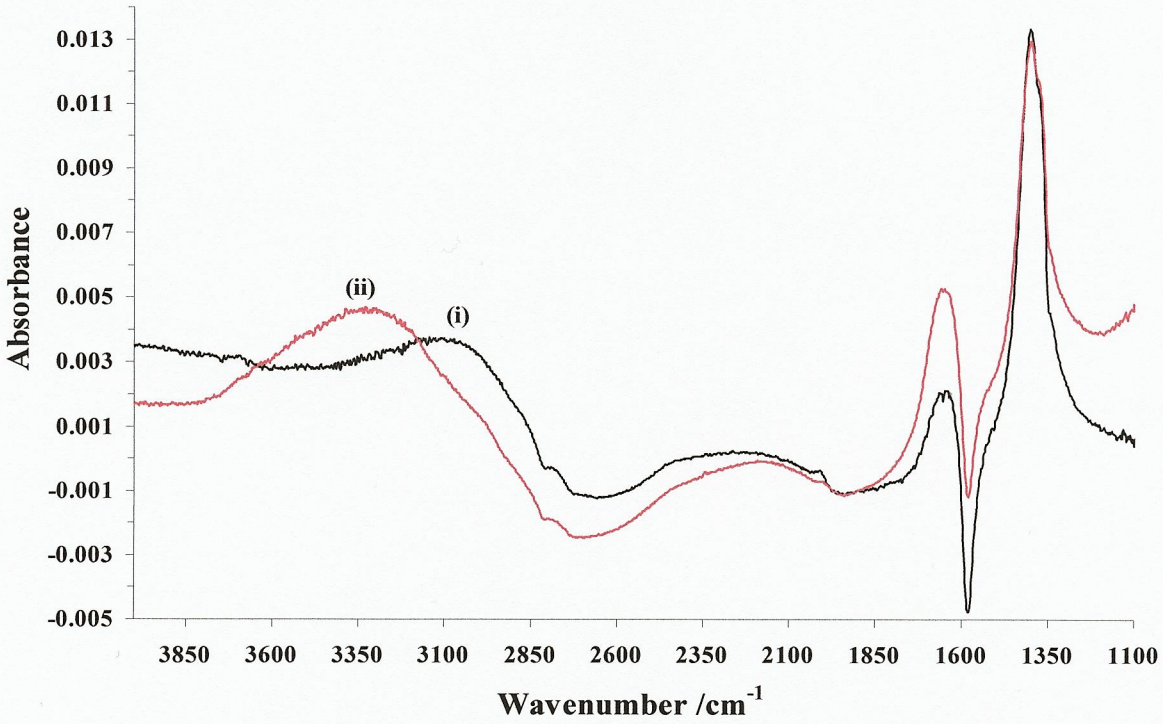

(a)

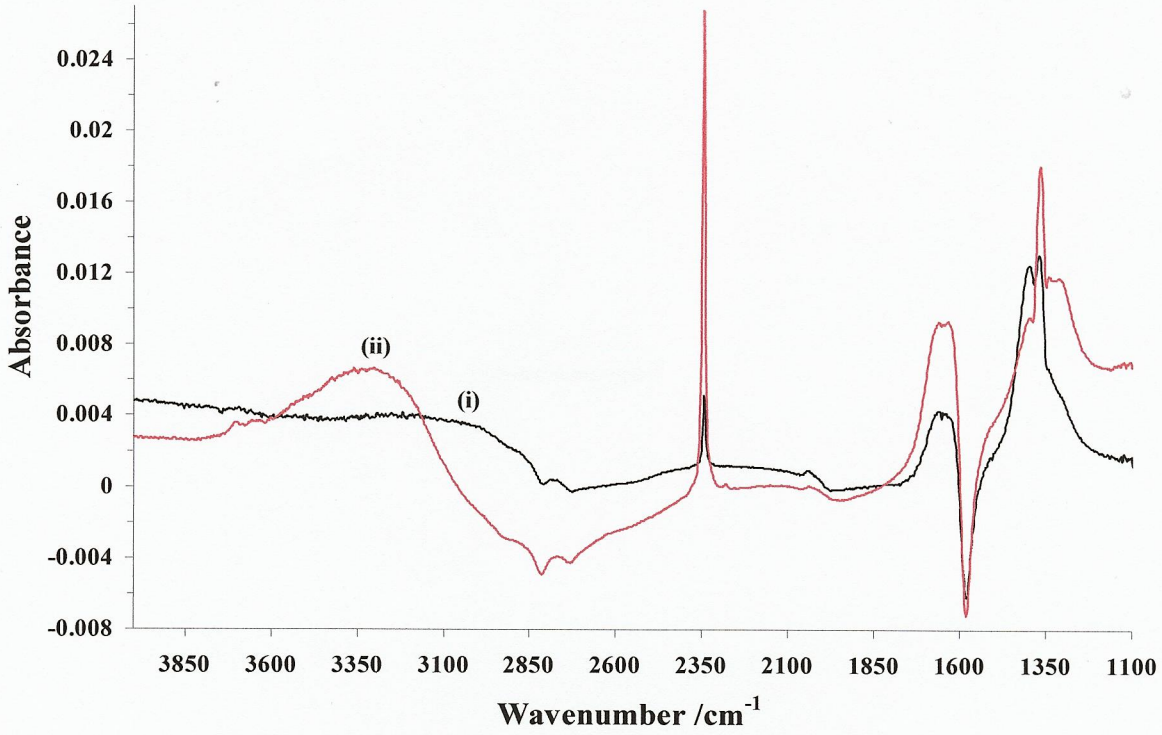

(b)

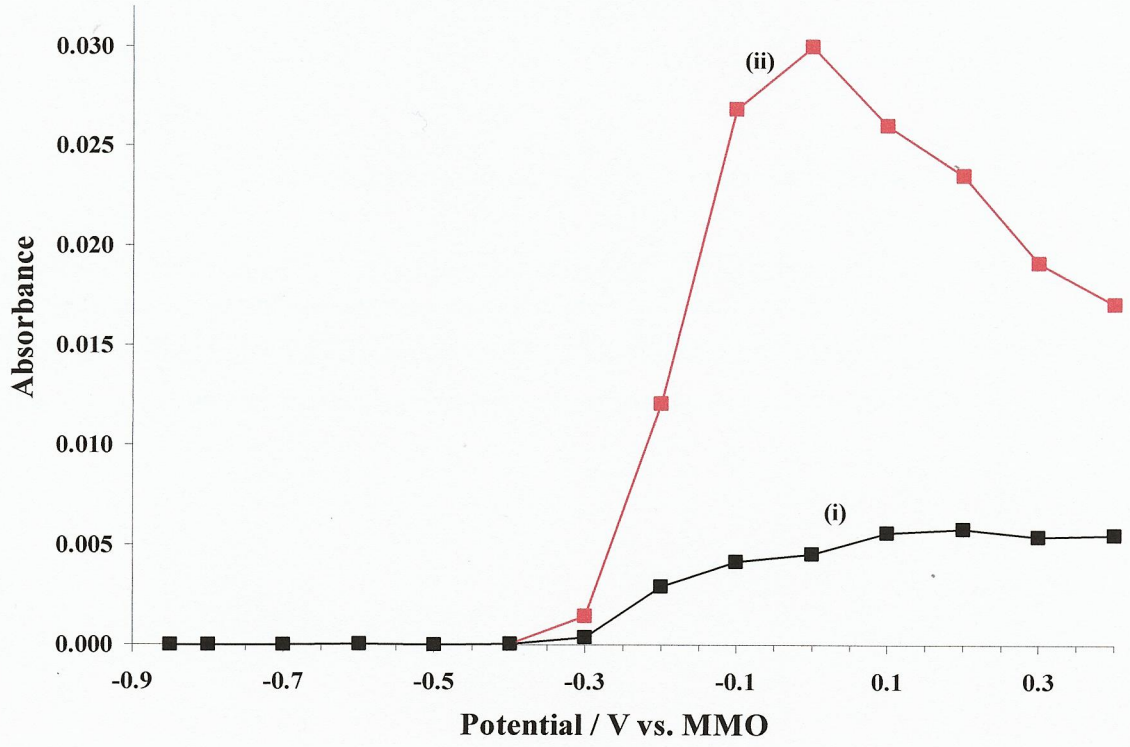

(c)

Figure 4.10. The spectra collected at (a) -0.4 V in (i) figs. 4.8 and (ii) 4.9, and (b) -0.1 V in the same experiments, (c) plots of CO_2 absorbance at 2340 cm^{-1} from the experiments depicted in (i) figs. 4.5 and (ii) 4.7.

The decrease in the CO_2 absorbance at potentials > 0 V is due to the CO_2 forming bubbles and pushing the electrolyte out of the thin layer [6].The prominent broad loss feature between ca. 2250 and 3250 cm^{-1} in figure 4.9 that distorts the OH^- loss feature may be unequivocally attributed to formate; see fig. 4.11. Figure 4.11 shows the spectrum collected 20 minutes after an aqueous solution of 0.1 M NaOOCH was diffused into the IR cell containing initially 0.1 M KOH [6]. From a comparison of figs. 4.9 and 4.11 it can also be seen that the weak loss features near 2250 cm^{-1} in fig. 4.9 may also be attributed to formate.

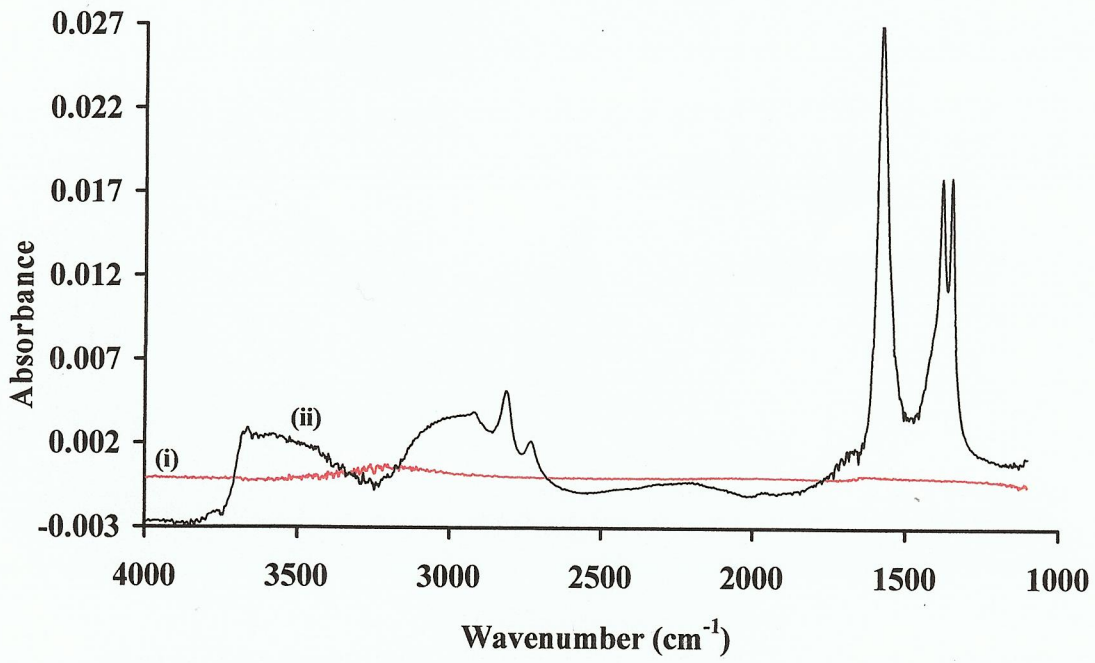

Figure 4.11. The spectra collected (i) 0 min and (ii) 20 min after an aqueous solution of 0.1 M NaOOCH + 0.1 M KOH was flushed into the IR cell containing initially 0.1 M KOH.

Figure 4.10(a) shows also the spectra collected at -0.4 V in the N_2 and O_2-saturated electrolyte; apart from the changes in the interfacial water structure, there is very little difference between the two spectra, and the absorptions of the CO_3^{2-} bands are comparable. Closer inspection of both the CO_3^{2-} features in fig. 4.10(a) suggest a shoulder to the CO_3^{2-} feature on the low wave-number side, and this is seen more clearly in fig. 4.10(b), and figs. 4.8 and 4.9, where a sharper feature grows in at 1366 cm^{-1} in both experiments. However, whilst the feature grows on the side of the carbonate peak in N_2-saturated solution, it dominates the spectra collected in O_2-

saturated KOH, increasing to a maximum intensity at -0.1 V, with a concomitant decrease in the 1400 cm^{-1} CO_3^{2-} band.

The data in figs 4.8, 4.9, 4.10(a) and (b) suggest the 1366 cm^{-1} band grows with the carbonate band up to -0.4 V, before the division in behaviour takes place. The broad band in the H-O-H deformation region near 1650 cm^{-1} seems to grow with the 1366 cm^{-1} feature. The former is clearly not entirely due to water as there is no matching increase in the O-H stretching region, compare figs. 4.10(a) and (b), and the 1366 and 1650 cm^{-1} bands may be attributed to the symmetric and asymmetric stretching bands of HCO_3^- in solution [27], However, this would require CO_3^{2-}, HCO_3^- and CO_2 to be present at the same time in the spectra in figs. 4.8 – 4.10, which clearly is not a viable option if the solution is homogeneous.

In fact the situation with regard to the very thin-layer cell used in electrochemical reflectance IR is such that under a wide variety of conditions a substantial pH gradient can form across the radial dimension of the electrode surface. The reason for this is that lateral diffusion of OH^- is extremely slow compared to diffusion between electrode and window, and this was modelled by Professor Andrew Hamnett using the equations for cylindrical diffusion, as described by Crank [36]. The details of the model are given in Appendix I, and a representative result is given in the Appendix for the oxidation of an organic molecule in which OH^- is consumed at the rate of four ions for every organic molecule oxidised, and we assume for simplicity that the initial concentrations of the organic and hydroxyl ion are the same as are their diffusion coefficients. In practice, qualitatively similar results are obtained for a very wide variety of input conditions; the essential point is that the formation of a pH gradient is almost inevitable in the types of thin-layer cell used in specular reflection FTIR, and must be borne in mind in interpreting the data.

The possibility that the 1366 cm^{-1} band is due to HCO_3^- in ionically isolated regions of electrolyte is supported by its persistence. The band is present as a gain feature in both N_2 and O_2 spectra up to +0.4 V normalised to the reference taken at -0.85 V, see figs. 4.12(a) and (b).

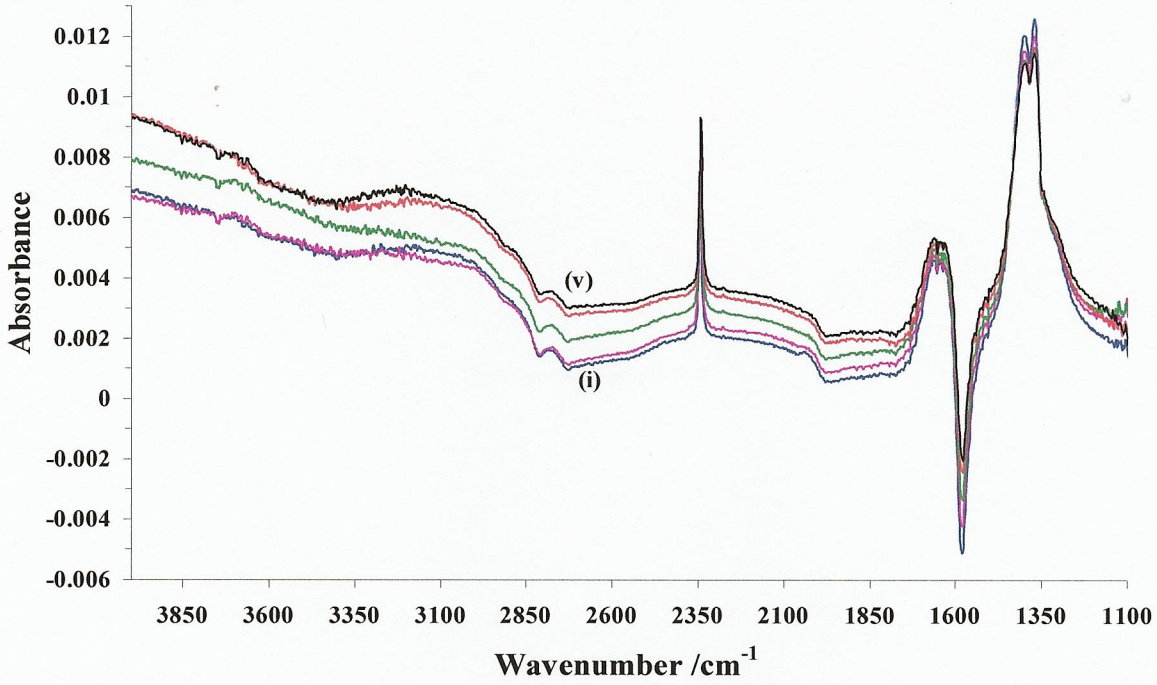

(a)

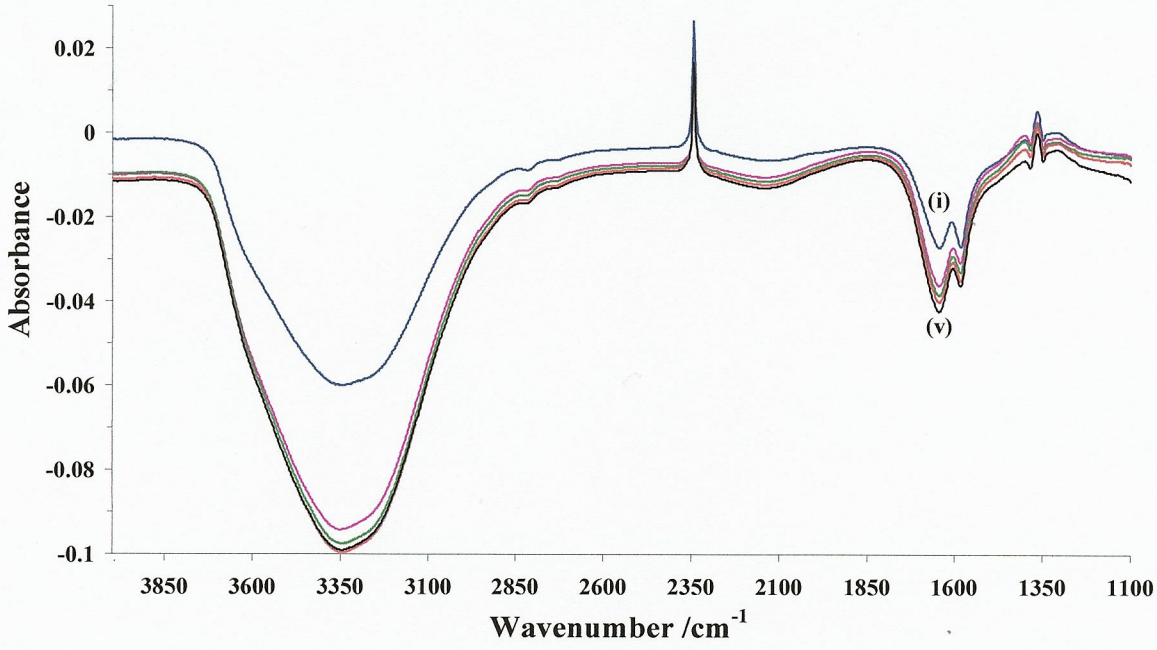

(b)

Figure 4.12. In-situ FTIR spectra of the polycrystalline Pt electrode immersed in (a) N_2 and (b) O_2-saturated 0.1 M NaOOCH + 0.1 M KOH collected at (i) 0 V, (ii) 0.1 V, (iii) 0.2 V (iv) 0.3 V and (v) 0.4 V. The reference spectra were taken at -0.85 V vs. MMO.

For example, in O_2 saturated KOH, see fig. 4.12(b), the CO_2 gas evolution is such that the solution is pushed out of the thin layer, as shown by the large loss features near

3300 cm^{-1} and 1650 cm^{-1} due to 'MOH affected' bulk water [33], and the solution formate bands near 1581, 1382 and 1351 cm^{-1}, yet the 1366 cm^{-1} band is relatively unchanged over the potential range from 0 V to 0.4 V. The CO_2 evolution in fig. 4.12(a) is insufficient for bubbles to form, see fig. 4.10(c). Figure 4.12(a) also clearly shows the persistence of the CO_L feature, which is retained throughout the -0.8 V to -0.2 V potential range, albeit at a lower intensity in O_2 saturated KOH than N_2 saturated.

4.4. Discussion.

The results of the methanol oxidation experiments described in chapter 3 clearly demonstrate that the main active intermediate in methanol oxidation in alkaline solution is not carbon-bonded but rather bonded through oxygen. This is quite different from the situation in acidic electrolytes, where carbon-bonded intermediates appear to constitute the major mechanistic pathways, and it raises the question of why, in alkaline solution, there is such a difference. One important distinction in alkaline solutions is the presence of significantly higher concentrations of OH_{ads} which will tend to polarise the Pt atoms at the surface through the adsorbed σ-acceptor hydroxy-species leading to stabilisation of bonding to surface-adsorbed σ-donors such as formate and related species.

It is unclear whether this is a dominant effect, however; one important aspect of the oxidation of even simple organic species is the apparently very small energy differences between different reaction pathways, and small differences in the nature of the electrode surface may be able to tip reactions into very different routes. This effect is exacerbated by the non-linearity of the kinetic equations; this non-linearity can lead to very complex and unpredictable behaviour that has been recognised for many years [37], giving rise to phenomena such as oscillations in the reaction rate. It is important to recognise that this sensitivity to reaction condition means that experiments in which the morphology of the Pt is substantially altered, or in which the potential protocol departs too far from that normally found in fuel cells, may well lead to different pathways dominating.

It is also clear from the results above that Pt-C bonds do indeed form in alkaline solution, and both CO_L and CO_B can be identified in the spectra. However, the

potential dependence of these bands suggests that they are not participants in the electrochemical processes on the surface, but rather simply play a spectator role. The coverage of CO_{ads} is also rather insensitive to the formate concentration. At -0.6 V, for example, in 1 M formate, the 1R absorbance is 4 x 10^{-4} and in 0.1 M formate, the absorbance is very similar: 3.3 x 10^{-4} and this rather suggests that there is a proportion of the surface, perhaps a facet of a particular face such as Pt(111), that does adsorb CO but on other facets OH_{ads} successfully competes, destabilising the CO_{ads} and stabilising O-bonded adsorbates. Support for this notion comes from the work of Tripković and co-workers [10, 13, 14] and Garcia and Koper [16]. Further support comes from our observation that in the presence of O_2, very much less CO_{ads} is seen; in 1 M formate/O_2 the CO_{ads} is undetectable, and in 0.1 M formate, the absorbance is only 1.5 x 10^{-4}.

This is an interesting observation, since it suggests that the main role of the oxygen is to increase the coverage of OH_{ads}, which has the two consequences of reducing surface-blocking by CO_{ads} and enhancing the stability of active O-bonded intermediates. The total charge passed in the presence of O_2 is significantly larger than that passed in the presence of N_2, i.e. by a factor of about 20%, accounting for the difference in overall product quantities seen in the two experiments. Given the relative quantities of formate oxidised and O_2 present, this must be a catalytic effect rather than involving the direct participation of O_2 itself, and it would appear that the model of the OH_{ads} as an important promoter in this system, and particularly its ability to prevent surface blocking by CO_{ads}, is supported by the experimental evidence above.

Finally, the results shed light on the assignment of the IR features due to OH^-(aq.); the broad loss features normally observed in external reflectance IR spectra in alkaline solution and associated with the consumption of OH^- ions may be attributed to the continuum absorptions of aqueous OH^-.

4.5. Conclusions

Formate is oxidised to CO_2, initially as CO_3^{2-} and then HCO_3^- as the pH in the thin layer falls. For the first time, the existence of isolated regions of electrolyte (due to the

formation of CO_2 as gas bubbles) is reported and the effect of this phenomenon modelled.

The FTIR data for the oxidation of formate in alkaline electrolyte demonstrate that adsorbed hydroxyl species can have a major effect on steering the reaction mechanism as well as participating directly in the oxidation of intermediates in the formate oxidation itself. Part of the surface is covered with OH_{ads} even in the presence of N_2, and it would appear that coverage of part of the surface with adsorbed CO is inhibited by the OH_{ads}. In the presence of O_2, additional OH_{ads} forms as a result of O_2 reduction at lower potentials, so that as the potential is ramped up, even less CO_{ads} forms than in the presence of N_2, giving a more active surface. The presence of OH_{ads} has two effects: it prevents part of the surface being blocked by adsorbed spectator species such as CO_{ads} and it facilitates adsorption of active O-bonded species. At higher potentials, once OH_{ads} has formed, it can be replenished by oxidation of water, and the surface retains a high coverage of OH_{ads} giving it a high activity.

As well as the importance of OH_{ads} in the oxidation of small organic molecules at Pt in alkaline solution, this chapter supports the previous one in that the data show that the oxidation of even simple organic species can proceed by a number of paths, with small differences in activation energy between these paths, such that small changes in, for example surface morphology, can cause the electrochemical process to flip to a different route. Again, in contrast to the case in acid solution, the active intermediates involve Pt-O rather than Pt-C bonded species.

4.6. References

1. Kunimatsu K., Hanawa H., Uchida H., and Watanabe M., (2009). Journal of Electroanalytical Chemistry, 632, 1-2, pp. 109-119.
2. Yajima T., Uchida H., and Watanabe M., (2004). The Journal of Physical Chemistry B, 108, 8, pp. 2654-2659.
3. Chen Y.X., Heinen M., Jusys Z., and Behm R.J., (2006). Langmuir, 22, 25, pp. 10399-10408.
4. Chen Y.X., Ye S., Heinen M., Jusys Z., Osawa M., and Behm R.J.r., (2006). The Journal of Physical Chemistry B, 110, 19, pp. 9534-9544.
5. Hamnett A., (1990). *Section IV. Mechanism of Methanol Electro-Oxidation*, in: Interfacial electrochemistry. theory, experiment, and applications, A. Wieckowski [Editor], Marcel Dekker, Inc., New York, Basel, p. 843.
6. Christensen P.A. and Linares-Moya D., (2009). The Journal of Physical Chemistry C, 114, 2, pp. 1094-1101.

7. Dimos MM. and Blanchard G.J., (2010). The Journal of Physical Chemistry C, 114, 13, pp. 6019-6026.
8. Gómez R. and Weaver M.J., (1997). Journal of Electroanalytical Chemistry, 435, 1-2, pp. 205-215.
9. Miki A., Ye S., and Osawa ML, (2002). Chemical Communications, 14, pp. 1500-1501.
10. Tripković A.V., Popović K.D., Momčilović J.D., and Dražić D.M., (1996). Journal of Electroanalytical Chemistry, 418, 1-2, pp. 9-20.
11. Tripković A.V., Popović K.D., and Lović J.D., (2001). Electrochimica Acta, 46, 20-21, pp. 3163-3173.
12. Tripković A.V., Popović K.D., Lović J.D., Jovanović V.M., and Kowal A., (2004). Journal of Electroanalytical Chemistry, 572, 1, pp. 119-128.
13. Tripković A.V., Popović K.D., Momčilović J.D., and Drazic D.M., (1998). Journal of Electroanalytical Chemistry, 448, 2, pp. 173-181.
14. Tripkovic A.V., Popovic K.D., Momcilovic J.D., and Dražić D.M., (1998). Electrochimica Acta, 44, 6-7, pp. 1135-1145.
15. Yu E.H., Scott K., and Reeve R.W., (2003). Journal of Electroanalytical Chemistry, 547, 1, pp. 17-24.
16. García G. and Koper M.T.M., (2009). Physical Chemistry Chemical Physics, 11, 48, pp. 11437-11446.
17. Iwasita T., Nart F.C., Rodes A., Pastor E., and Weber M., (1995). Electrochimica Acta, 40, 1, pp. 53-59.
18. Iwasita T., Rodes A., and Pastor E., (1995). Journal of Electroanalytical Chemistry, 383, 1-2, pp. 181-189.
19. Berná A., Rodes A., Feliu J.M., Illas F., Gil A., Clotet A., and Ricart J.ML, (2004). The Journal of Physical Chemistry B, 108, 46, pp. 17928-17939.
20. Morallón E., Rodes A., Vazquez J.L., and Pérez J.M., (1995). Journal of Electroanalytical Chemistry, 391, 1-2, pp. 149-157.
21. Zhou Z.-Y., Tian N., Chen Y.-J., Chen S.-P., and Sun S.-G., (2004). Journal of Electroanalytical Chemistry, 573, 1, pp. 111-119.
22. Chen Q.-S., Sun S.-G., Zhou Z.-Y., Chen Y.-X., and Deng S.-B., (2008). Physical Chemistry Chemical Physics, 10, 25, pp. 3645-3654.
23. Christensen P. A., (2010). *In-situ Fourier transform infra red spectroelectrochemistry as a probe of electrocatalysis*, in: Spectroscopic properties of inorganic and organometallic compounds, Royal Society of Chemistry, Cambridge, .p. 125 - 165.
24. Umeda M., Nagai K., Shibamine M., and Inoue M., (2010). Physical Chemistry Chemical Physics, 12, 26, pp. 7041-7049.
25. Chen Y.X., Miki A., Ye S., Sakai H., and Osawa M., (2003). Journal of the American Chemical Society, 125, 13, pp. 3680-3681.
26. García G., Rodríguez P., Rosca V., and Koper M.T.M., (2009). Langmuir, 25, 23, pp. 13661-13666.
27. Arihara K., Kitamura F., Ohsaka T., and Tokuda K., (2001). Journal of Electroanalytical Chemistry, 510, 1-2, pp. 128-135.
28. Kitamura F., Ohsaka T., and Tokuda K., (1997). Electrochimica Acta, 42, 8, pp. 1235-1238.
29. Futamata M., (2003). Journal of Electroanalytical Chemistry, 550-551, pp. 93-103.
30. Wandlowski T., Ataka K., Pronkin S., and Diesing D., (2004). Electrochimica Acta, 49, 8, pp. 1233-1247.

31. Brooker J., Christensen P.A., Hamnett A., He R., and Paliteiro C.A., (1992). Faraday Discussions, 94, pp. 339-360.
32. Watanabe M. and Motoo S., (1975). Journal of electroanalytical chemistry, 60, 3, pp. 267-273.
33. Śmiechowski M. and Stangret J., (2007). Journal of Molecular Structure, 834-836, pp. 239-248.
34. Librovich N.B., Sakun V.P., and Sokolov N.D., (1979). Chemical Physics, 39, 3, pp. 351-366.
35. (1985). *CRC Handbook of Chemistry and Physics 66th Edition*, ed. D.R. Lide. Boca Raton, FL.: CRC Press/Taylor and Francis. 2, 376.
36. Crank J., (1975). *The Mathematics of Diffusion*, 2 ed: Oxford science publications. 415.
37. Vielstich W., (1965). *Brennstoffelemente : moderne Verfahren zur elektrochemischen Energiegewinnung*. Monographien zu "Augewandte Chemie" und "Chemie-Ingenieur-Technik", Nr. 82. Weinheim: Weinheim/Bergstr. : Verlag Chemie. 388.

5. The oxidation of ethanol

5.1. Introduction

The work in this chapter follows on from the previous two chapters, in seeking to assemble a database of relevant spectra and to further develop the energy model of small organic fuel oxidation at Pt in alkaline solution.

5.2. Previous in-situ FTIR studies on ethanol oxidation at Pt in alkaline solutions.

As usual, in contrast to the *in-situ* FTIR literature on the electro-oxidation of ethanol in acid solutions, studies in alkaline solution are sparse; in fact, only one example of ethanol oxidation at Pt electrodes in alkaline solution could be found. Thus, López-Atalaya and co-workers [1] employed the Subtractively Normalized Interfacial Fourier Transform Infra-Red Spectroscopy (SNIFTIRS) [2] approach to study ethanol electro-oxidation at Pt(110) and Pt(100) electrodes in aqueous NaOH and Na_2CO_3.

In the SNIFTIRS approach, the potential is stepped back and forth in a square wave, see fig. 5.1, the co-added and averaged scans collected at 0.35 V were normalized to those taken at 0.05 V according to the data manipulation in equation (5.1). The authors observed linearly bonded CO at Pt(110) and multibonded CO at Pt(100), the authors claimed to have also detected linearly adsorbed CO at both Pt(110) and Pt(100), but the intensities of these bands appear to have been comparable to the noise.

$$\frac{\Delta R}{R} = \frac{R(E_S) - R(E_R)}{R(E_R)} \qquad (5.1)$$

The SNIFTIRS approach is a method of increasing signal-to-noise, but is only suitable for absorptions that: (i) shift in frequency with potential and (ii) do so in a completely reversible manner as the potential is switched repeatedly. Any absorptions arising from species produced in an irreversible manner will be averaged out. In addition there is some concern that such potential modulation can influence the surface chemistry taking place [2, 3].

López-Atalaya et al. also collected *in-situ* FTIR spectra in a more conventional manner, i.e. during a slow potential scan from 0.05 V to 1.00 V at 1 mV s^{-1}. The spectra were collected over small potential ranges, and were identified with the mid point potential of the range, normalized to the reference spectrum collected at 0.05 V according to the data manipulation shown in equation (5.1).

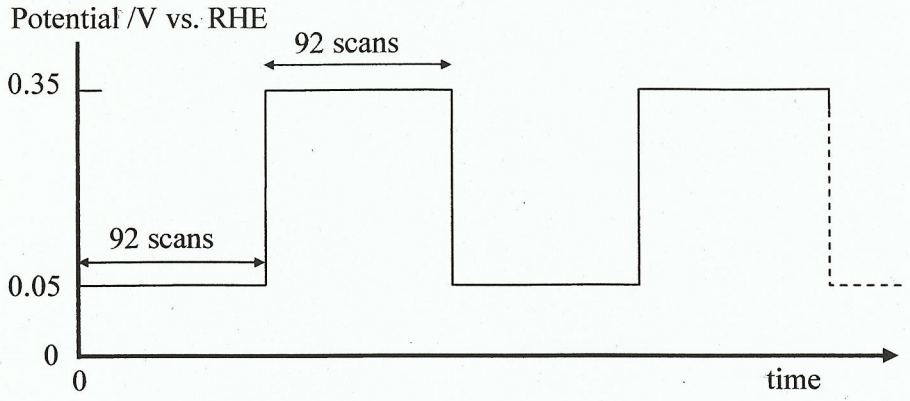

Figure 5.1. The potential profile employed by López-Atalaya et al. in their SNIFTIRS experiments [1], 92 scans (2 scans per second, 8 cm^{-1} resolution) were co-added and average at each potential. Ten steps were employed. The solution contained 0.1 M ethanol and 0.1 M NaOH.

Whilst the authors observed (very weak) bands due to linear CO_{ads} at Pt(110) and multiply bonded CO at Pt(100), the spectra were dominated by features due to the loss of OH^- (which were not assigned by the authors) and to the gain of acetate ions at 1550 cm^{-1} and 1415 cm^{-1}, attributed to the symmetric and asymmetric stretches of COO^- (ν_s and ν_{as} respectively). The authors did not attempt to place their data in the context of a model for ethanol oxidation at Pt.

Two papers have been published recently concerning *in-situ* FTIR studies of ethanol oxidation in alkaline solution, but both report data using polycrystalline Pd electrodes [4, 5] and hence are not relevant to the present study, save in providing band assignments for intermediates and product of ethanol oxidation. In particular, Zhou et al. [4] obtained their assignments for acetate by comparison with the transmission spectrum of $NaOOCCH_3$. They also provide assignments for C_2H_5OH bands. Their assignments are presented in table 5.1.

Band / cm^{-1}	Assignment
1551	ν_s, CH_3COO^-
1415	ν_{as} CH_3COO^-
1348	CH_3COO^-
1018	CH_3COO^-
1390	CO_3^{2-}
1085	C-O stretch C_2H_5OH
1045	C-O stretch C_2H_5OH

Table 5.1. Assignment of the spectral features observed by Zhou et al. [4],

5.3. Cyclic voltammetry of ethanol at polycrystalline Pt in 0.1 M KOH.

Figure 5.2 shows cyclic voltammograms of the Pt electrode in 0.1 M KOH in (i) the absence of ethanol and (ii) in the presence of 1 M ethanol.

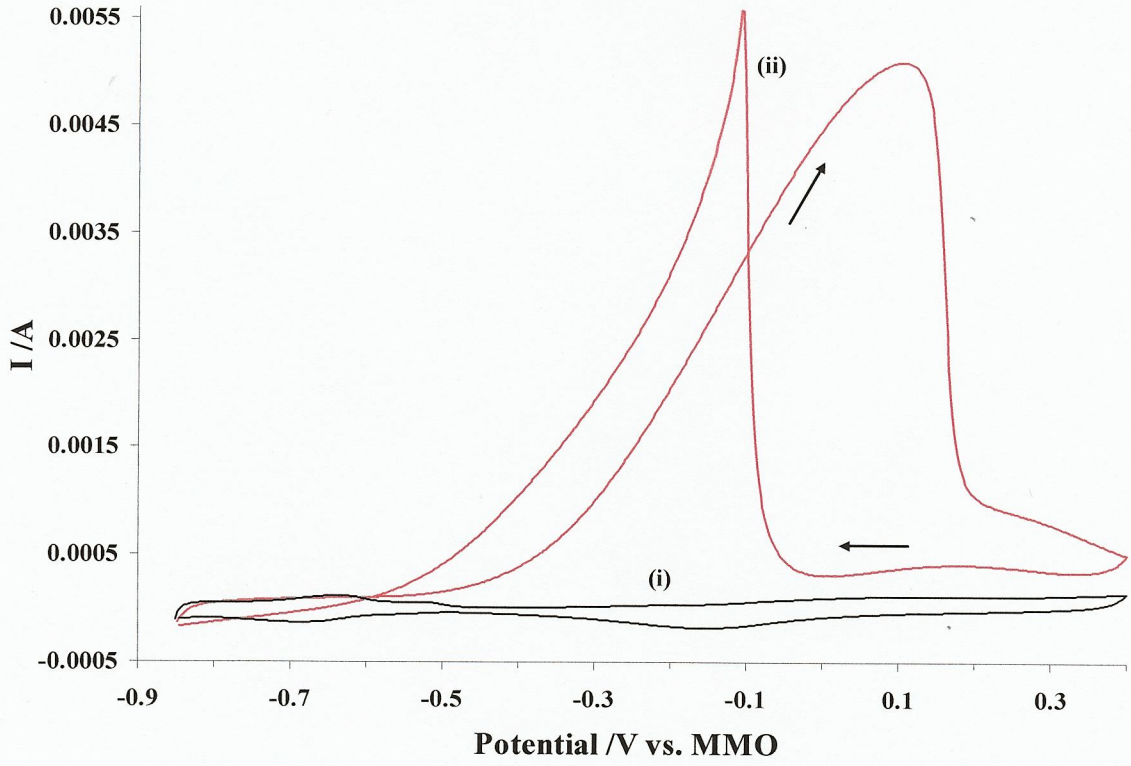

Figure 5.2. CV of the Pt electrode in 0.1 M KOH in (i) the absence and (ii) the presence of 1 M ethanol; scan rate 100 mV s^{-1}.

As may be seen from the figure, the onset of ethanol oxidation is ca. -0.6 V vs. MMO, in agreement with the postulate that OH_{ads} formation occurs at this potential, i.e. prior

to the completion of the stripping of the hydrogen under potential deposition (H_{upd}) layer [6] at stepped surfaces. Figure 5.2 shows considerable hysteresis between the anodic and cathodic scans. Lai and Koper [7] found very little hysteresis between the anodic and cathodic sweeps below 0.65 V vs. RHE (ca. -0.2 V vs. MMO) in the cyclic voltammetry of polycrystalline Pt in 0.5 M EtOH/0.1 M NaOH, see fig. 5.3.

The authors suggested that this absence of hysteresis may indicate that: (1) the oxidation of adsorbed species does not play a mayor role; (2) surface species are formed but are stable up to 0.65 V vs. RHE; or (3) the oxidation of surface species does occur but is very slow compared to the timescale of the CV experiment.

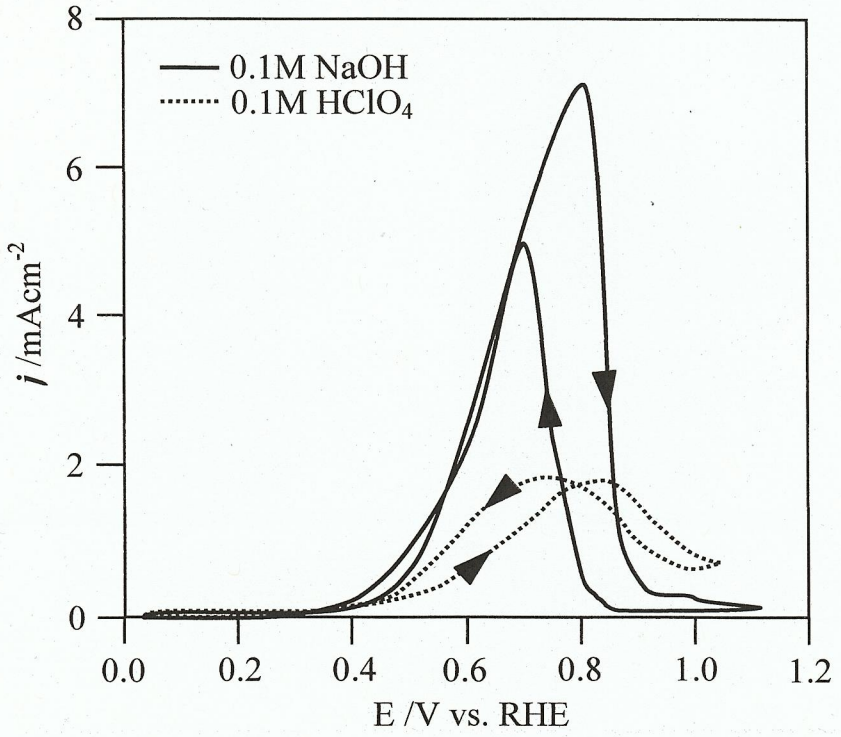

Figure 5.3. Cyclic voltammograms (first cycles) for the electro-oxidation of 0.5 M ethanol in 0.1 M NaOH (solid line) and 0.1 M $HClO_4$ (dashed line) on polycrystalline platinum as reported by Lai and Koper. The voltammograms were recorded at 10 mV s^{-1} and the arrows indicate the scan direction. Redrawn from [7].

Dimos and Blanchard [8] also found little hysteresis in their CV's of planar Pt in 1 M EtOH/ 1 M KOH. Both Lai & Koper and Dimos & Blanchard conducted their voltammetry experiments at 10 mV s^{-1}. In contrast, Chen and Schell [9] performed their CV's at the same scan rate as was employed in fig. 5.2, 100 mV s^{-1}, and

observed voltammograms very similar to that in fig. 5.2, i.e. with considerable hysteresis. In general, as has been stated, it is accepted that, in alkaline solution, the "reversible oxide" (forming at -0.6 V vs. MMO) is essential for the oxidation of small organic fuel molecules such as methanol and ethanol, whilst oxide formation inhibits organics oxidation at potentials ≥ 0.1 V vs. MMO [10]; the latter can be seen plainly in fig. 5.2. The hysteresis in fig. 5.2 suggest that stripping the oxide results in a more active surface than was present during the anodic scan. Removal of the "phase oxide" on Pt is known to result in a roughened surface which could have more active sites, see [11] and references therein.

5.4. In-situ FTIR experiments in N_2 saturated KOH.

5.4.1. The current response during the in-situ FTIR experiments.

Figure 5.4 shows the current observed during the FTIR experiment in N_2 saturated 0.1 M KOH + 1.0 M EtOH, in which the potential was stepped from -0.85 V to +0.4 V vs. MMO; fig. 5.4 is in broad agreement with the CV in fig. 5.2(ii) in that the maximum current occurs at +0.1 V after which there is a rapid decline.

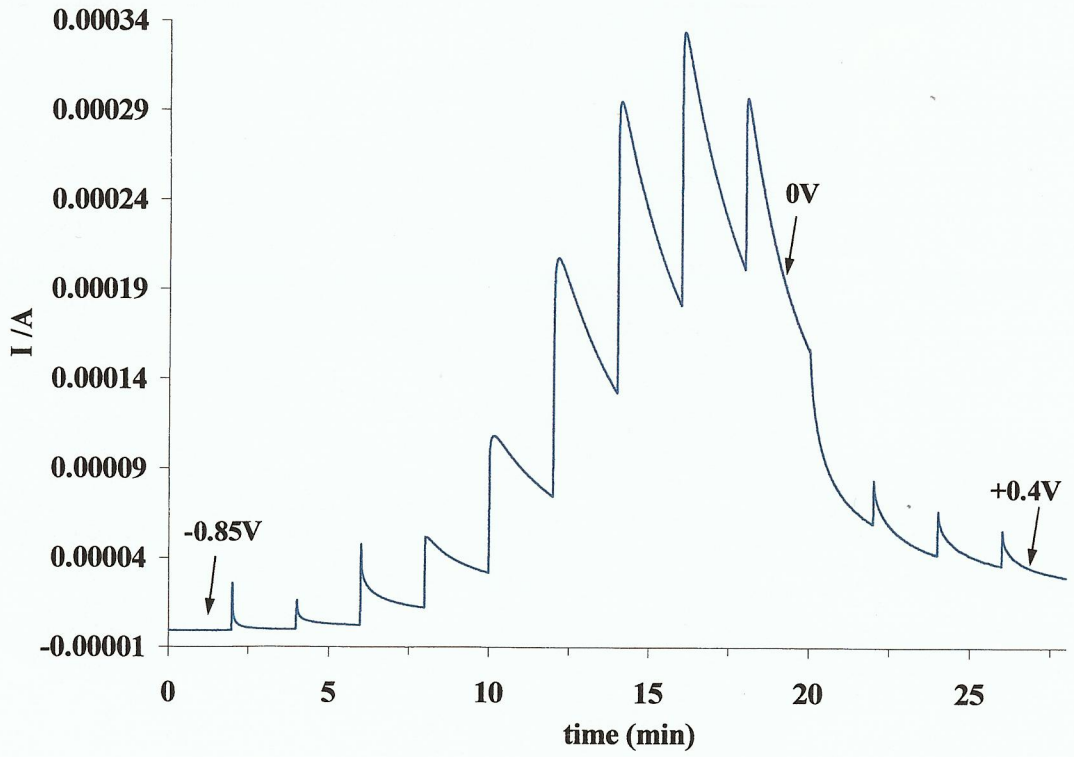

Figure 5.4. Current observed during the FTIR experiment in N_2 saturated 0.1 M KOH + 1 M EtOH. Potential was stepped from -0.85 V to +0.4 V vs. MMO.

In contrast to the methanol and formate experiments described in Chapters 3 & 4, no cathodic currents were observed in the experiment in fig. 5.4.

5.4.2. The spectra up to -0.6 V

Figure 5.5 shows the spectra (8 cm^{-1} resolution, 100 scans, 47 s per scan set) collected at -0.85 V (i), -0.7 V (ii) and -0.6 V (iii) during the experiment in which the potential of the polycrystalline Pt electrode was held at -0.85 V vs. MMO in N_2 saturated 0.1 M KOH, ethanol added to a final concentration of 1 M and the electrode pushed against the CaF_2 prism window of the cell.

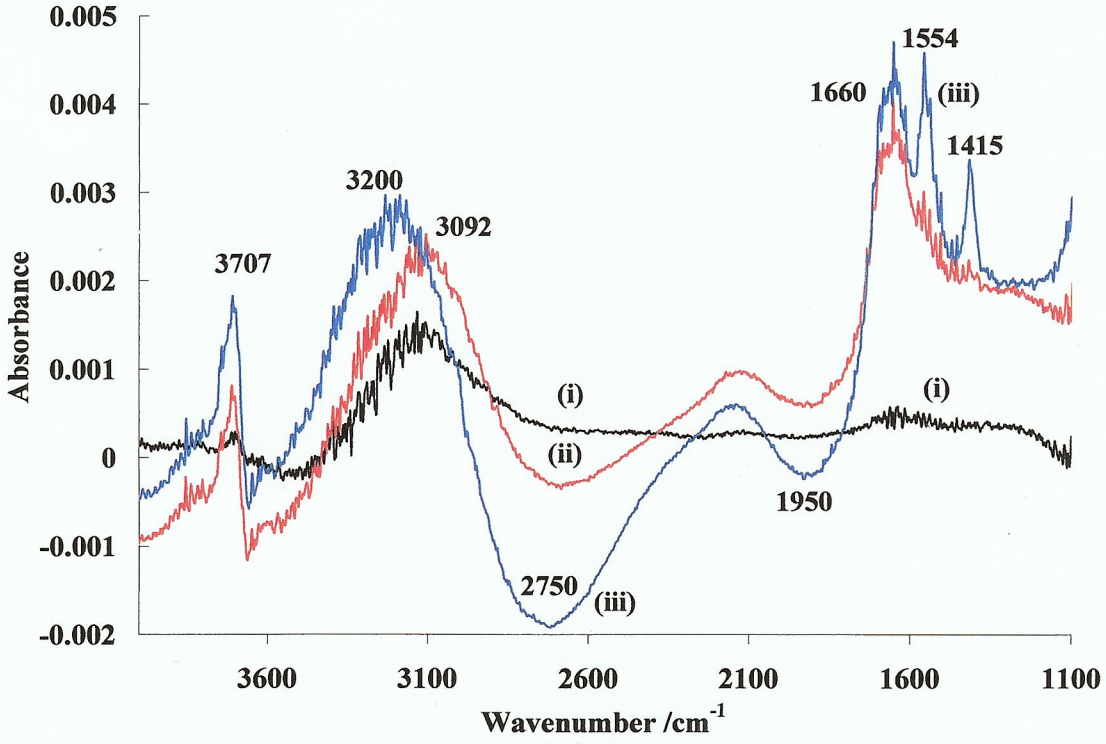

Figure 5.5. Spectra (8 cm^{-1} resolution, 100 scans, 47 s per scan set) collected from -0.85 V (i), -0.7 V (ii) and -0.6 V (iii) during an experiment in which the potential of the polycrystalline Pt electrode was held at -0.85 V vs. MMO in N_2 saturated 0.1 M KOH, ethanol added to a final concentration of 1 M and the electrode pushed against the CaF_2 prism window.

Once the spectrometer had been purged of atmospheric water vapour and CO_2 (ca. 30 minutes), the reference spectrum was collected at -0.85 V vs. MMO, after which a sample spectrum was collected at the same potential to assess if the system was stable. The potential was then stepped to -0.80 V and then in 100 mV stages up to +0.4 V,

with sample spectra collected at each step and normalized to the reference according to the data manipulation given in equation (2.1).

As may be seen from fig. 5.5, the spectra [12, 13] are dominated by the solution OH^- loss feature (see section 3.3) with peaks near 2750 cm^{-1} and 1950 cm^{-1}, and gain features due to water, O-H stretch 3200 – 3092 cm^{-1} and HOH deformation near 1660 cm^{-1} at -0.8 V, the former distorted at higher potentials due to the OH^- loss feature. In addition there is the gain of a narrow (half width ca. 70 cm^{-1}) band at ca. 3707 cm^{-1}, without any attendant band around 1600 – 1660 cm^{-1} and the appearance of features at -0.6 V near 1554 cm^{-1} and 1415 cm^{-1} which may be attributed unambiguously to acetate ions in solution (see table 5.1 and, for example, [1, 5, 14, 15]). Figure 5.6 shows plots of the various features observed during the experiment depicted in fig. 5.4.

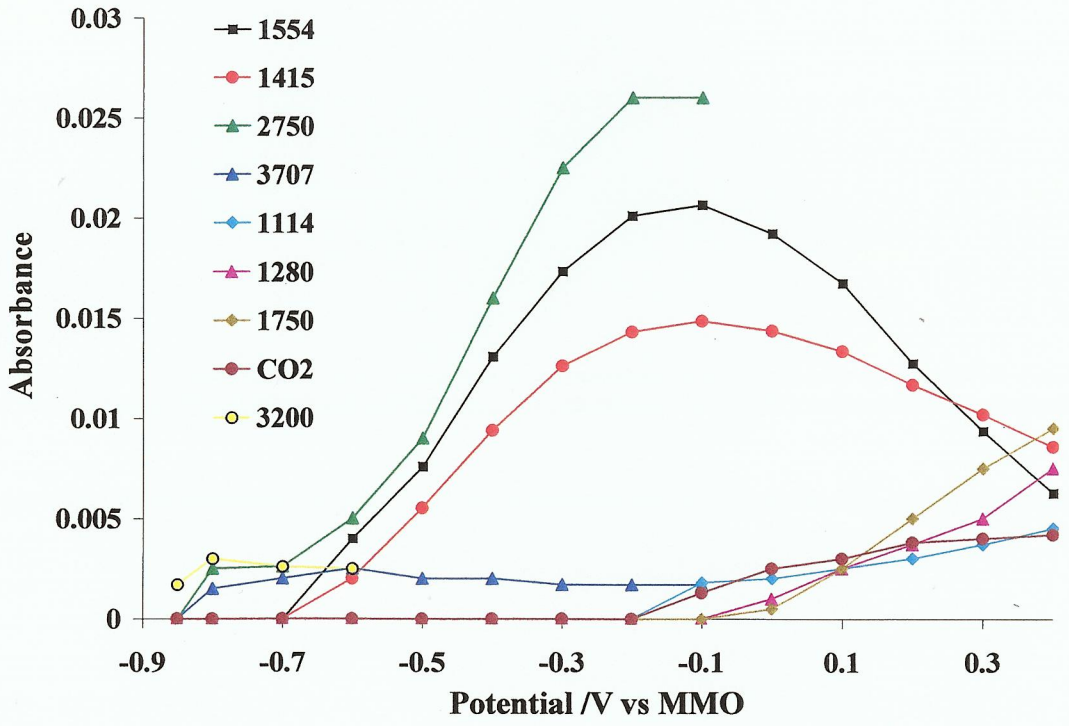

Figure 5.6. The features observed during the experiment depicted in figs. 5.4 and 5.5.

The intense water bands in fig. 5.5 dominate the spectra and hence warrant some explanation. Firstly, it is important to try and assess whether they are artefacts, at least in the region between 2750 cm^{-1} and 3750 cm^{-1}; i.e. the spectral range in which the ν_s and ν_{as} O-H (symmetric and asymmetric respectively) stretches absorb strongly [16].

To this end, fig. 5.7 show the single beam reference spectrum collected at -0.85 V vs. MMO during the experiment in fig. 5.5. As may be seen from the figure, there is significant source energy, particularly in the region of the 3707 cm^{-1} band. In addition, the absorption changes at the edges of the (ν_s + ν_{as}) band are comparable, or less 'steep', than the edges of the 1640 cm^{-1} H-O-H scissor vibration (δ). Finally, there is very significant literature precedent for sharp O-H stretches around 3700 – 3600 cm^{-1} (see for example [17-24] and references therein).

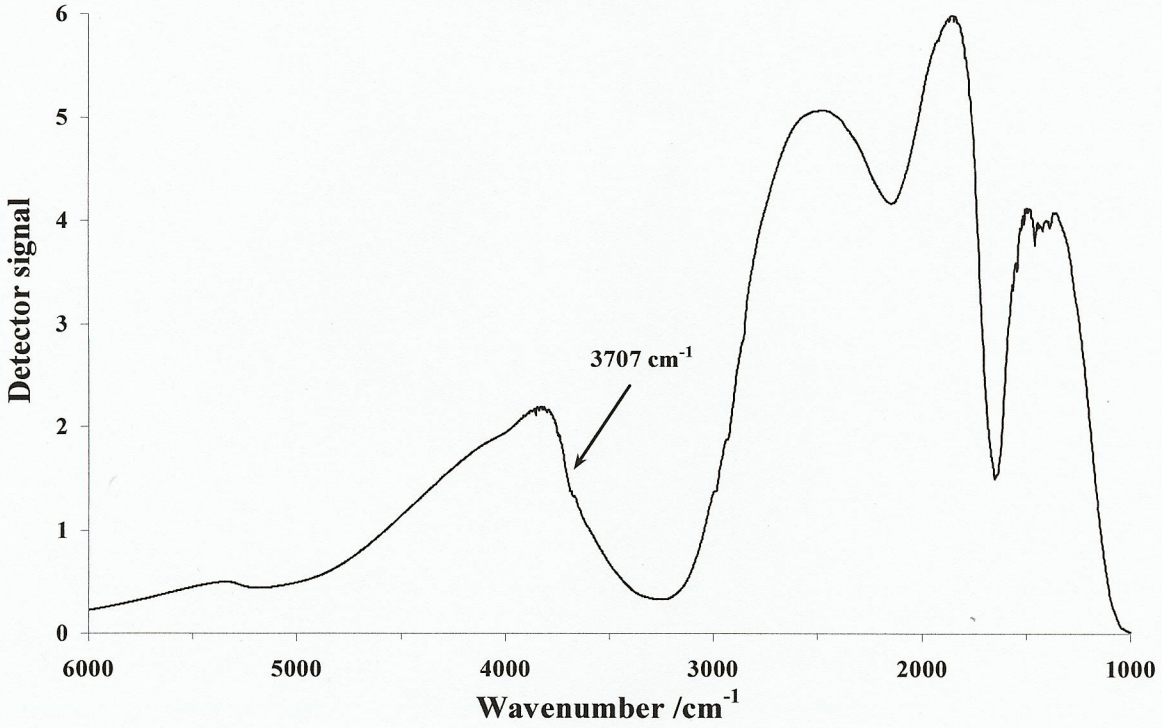

Figure 5.7. The single beam reference spectrum collected at -0.85 V vs. MMO during the experiment in fig. 5.5.

In general, models of the behaviour of interfacial water in the *in-situ* FTIR literature (1) are largely confined to acid electrolytes and (2) stem from a limited number of primary concepts and papers. Thus, liquid water is, in broad terms, accepted as being highly hydrogen bonded with three important absorptions in the IR (see [25] and references therein): 3615 cm^{-1} (O-H symmetric stretch, ν_{s1} or ν_s), 3450 cm^{-1} (O-H asymmetric stretch, ν_{as} or ν_{as3}) and 1640 cm^{-1} (H-O-H deformation, ν_2 or δ). The Raman and sum-frequency generation literature provides a more sophisticated model of liquid water (see [26-28] and references therein) wherein liquid water has both symmetrically and asymmetrically hydrogen-bonded molecules. Asymmetrically hydrogen-bonded water may be represented as in fig. 5.8. Such asymmetrically

bonded water has been reported has having an IR band around 3600-3650 cm^{-1} [29]. However, there is some confusion in the literature as to the assignment of this band. Du and co-workers [27] attribute this band near 3600 cm^{-1} and 3450 cm^{-1} to the symmetric and asymmetric stretches (respectively) of asymmetrically hydrogen-bonded water; Verma et al. [30] also attribute bands near 3616 & 3550 cm^{-1} to these vibrations. In contrast, Dreesen et al. [31] attributes a band near 3670 cm^{-1} to an O-H stretch free from hydrogen-bonding, as does Berna et al. [32].

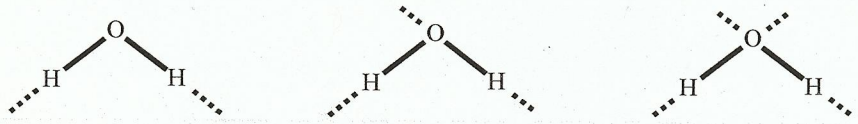

Figure 5.8. Asymmetrically hydrogen-bonded water: (H...) depicts strong and (H....) depicts weak hydrogen bond with neighbouring water molecules; redrawn from [26].

Dreesen et al. [31] and Gragson et al. [33] attribute bands near 3450 cm^{-1} to asymmetrically hydrogen-bonded water or water molecules with "bifurcated hydrogen bonds".

The concept of the O-H moiety free from hydrogen bonding seems to arise from a consideration of the IR absorptions of the water of hydration and O-H stretches in ionic crystals [16]. Certain ionic crystals have OH^- ions essentially free from hydrogen bonding. Free OH species in the gas phase absorb at ca. 3556 cm^{-1} [34] in agreement with theoretical calculations [35] and estimates from the spectra of hydroxides with non-hydrogen bonded OH^- ions [36], However frequencies as high as 3700 cm^{-1} have been observed, e.g. $Mg(OH)_2$ [37]. This has been interpreted in terms of metal-oxygen interactions strengthening O-H bonds, something not predicted by theory [35].

The paper by Lutz [16] develops the model of the IR response of water, using the ν_{as}, ν_s and δ absorptions of liquid water as a benchmark; thus, decreasing hydrogen bonding results in ν_s moving to higher frequencies and δ moving to lower values. In addition, half widths decrease as does band intensity [16, 36, 38] if water acts as a proton donor or as a proton acceptor, the O-H bond is weakened and ν_s falls (co-operative effect [36]). The O-H stretching frequency also falls when water co-ordinates to metal ions due to the weakening of intramolecular O-H bonds, increased

donor strength (acidity, of the H atom) and strengthened hydrogen bonds (synergetic effect [36]).

The frequency of the δ absorption decreases as hydrogen bonding decreases, and are also decreased by metal oxygen interactions [39]. The latter was placed into the context of the electrode electrolyte interface by Iwasita and Xia [25], Water absorbed through the oxygen atom at a Pt electrode experience increasing donation from the lone pairs on the oxygen to the electrode as the coverage increases due to a concomitant increase in the work function of the Pt. One lone pair is non bonding, the other partly non bonding and partly bonding. Hence donation of the latter causes the H-O-H bond angle to increase and the δ absorption to decrease in energy. Low (e.g. 1612 cm^{-1}) deformation frequencies have been postulated as signalling the presence of adsorbed water in a form immediately prior to dissociation to M-OH:

$$Pt(H_2O)_{ads} \rightarrow PtOH + H^+ + e^- \qquad (5.2)$$

The final 'primary' source is a paper by Bertie and Whalley [40] on the infrared spectra of ice. The authors assign various features, but the most often cited is a strong absorption near 3200 cm^{-1} attributed to "ice like" water; i.e. water tetrahedrally co-ordinated by hydrogen bonds [19, 33]. In the paper by Bertie and Whalley, the δ band is very broad and weak, and barely discernible in the spectrum. However, 'ice like', highly hydrogen bonded water has been reported as having an associated deformation band near 1640 cm^{-1} [19].

Returning to the spectra in fig. 5.5, it is clear that solution OH^- is being consumed at E > -0.85 V which would be expected to result in the expulsion of K^+ from the thin layer. Potassium cations are known to disrupt the hydrogen bonding of water [41]; and their expulsion should lead to an increase in strongly hydrogen bonded water and, as a consequence, a decrease in stretching frequencies (ν_s/ν_{as}) and an increase in the frequency of the deformation mode. It is reasonable, therefore, to suggest that the growth of the bands near 3092 cm^{-1} and 1660 cm^{-1} in the figure at potentials ≤ -0.7 V reflects the establishing of highly hydrogen bonded water in the thin layer. At -0.6 V, the (ν_s/ν_{as}) stretch of water appears to have shifted to 3200 cm^{-1}, but the absence of a corresponding shift in the O-H deformation suggest that the 3200 cm^{-1} band has

grown alongside the 3092 cm^{-1} feature, possibly due to the formation of less hydrogen-bonded water associated with the appearance of acetate (and hence some disruption of the hydrogen bonding network), with any deformation band obscured by the stronger 1660 cm^{-1} feature.

Based on the discussion above, the most likely assignment of the 3707 cm^{-1} band is to isolated Pt-OH; the width at half peak height of this feature at 70 cm^{-1} is comparable to that observed by Ataka et al. [19]. It is not impossible that this is due to the "reversibly adsorbed" OH. Unlike the experiments reported in the previous chapters on formate and methanol, positive current was observed from the start of the experiment in fig. 5.4, suggesting chemisorption of the ethanol, furthermore consumption of OH^- was not observed at potentials < -0.6 V in the formate and methanol experiments. There is no evidence in fig. 5.4 for adsorbed CO, suggesting that any chemisorption has not led to C-C bond scission.

In their studies on ethanol electro-oxidation at Pd in alkaline solutions, Bianchini and co-workers [42] have suggested that the initial steps in ethanol electro-oxidation are sequential dehydrogenation and that the presence of adsorbed OH is essential to this process *via* the instantaneous removal of hydrogen atoms which otherwise block the chemisorption. In contrast, it does not seem unreasonable to postulate that the anodic current at low potentials in fig. 5.4 is the adsorption of ethoxide, $CH_3CH_2O^-$ (EtO), which displaces adsorbed hydrogen:

$$CH_3CH_2O^- + Pt\text{-}H \rightarrow CH_3CH_2OPt + H^+ + 2e^- \qquad (5.3)$$

The adsorbed ethoxy so formed will present a relatively hydrophobic interface: any adsorbed Pt-OH co-existing with EtO_{ads} will, therefore, be somewhat isolated from the electrolyte, giving rise to a sharp, isolated absorption. In order for ethoxide to adsorb at these low potentials, it must compete with surface adsorbed hydride, and it would appear that ethoxide can do this, whereas methanol and formate cannot, and for these, therefore, the Pt-OH absorption is hidden under the (ν_s / ν_{as}) OH stretches of interfacial water. It is difficult to see how this could be the case if adsorption of ethoxide is taking place through the C-OH carbon atom, but ethoxide is a powerful nucleophile and attack on the surface by the oxygen is a much more likely scenario,

with the surface adsorbed species being Pt-O-CH_2-CH_3 and this structure would also maximise the hydrophobicity of the interface.

5.4.3. The spectra from -0.5 Vto -0.2 V

Figure 5.9 shows the spectra collected at potentials from -0.5 V to -0.2 V in the experiment depicted in fig. 5.4. As may be seen, the bands due to acetate ion at 1554 cm^{-1} and 1415 cm^{-1} increase steadily in intensity as the potential is increased. In addition, the weak acetate feature near 1348 cm^{-1} is evident.

The acetate bands track the OH^- loss features (e.g. 2750 cm^{-1}), as may be seen from fig. 5.6, and more clearly from fig. 5.10 which shows the plots in fig. 5.6 normalised to their maximum intensity.

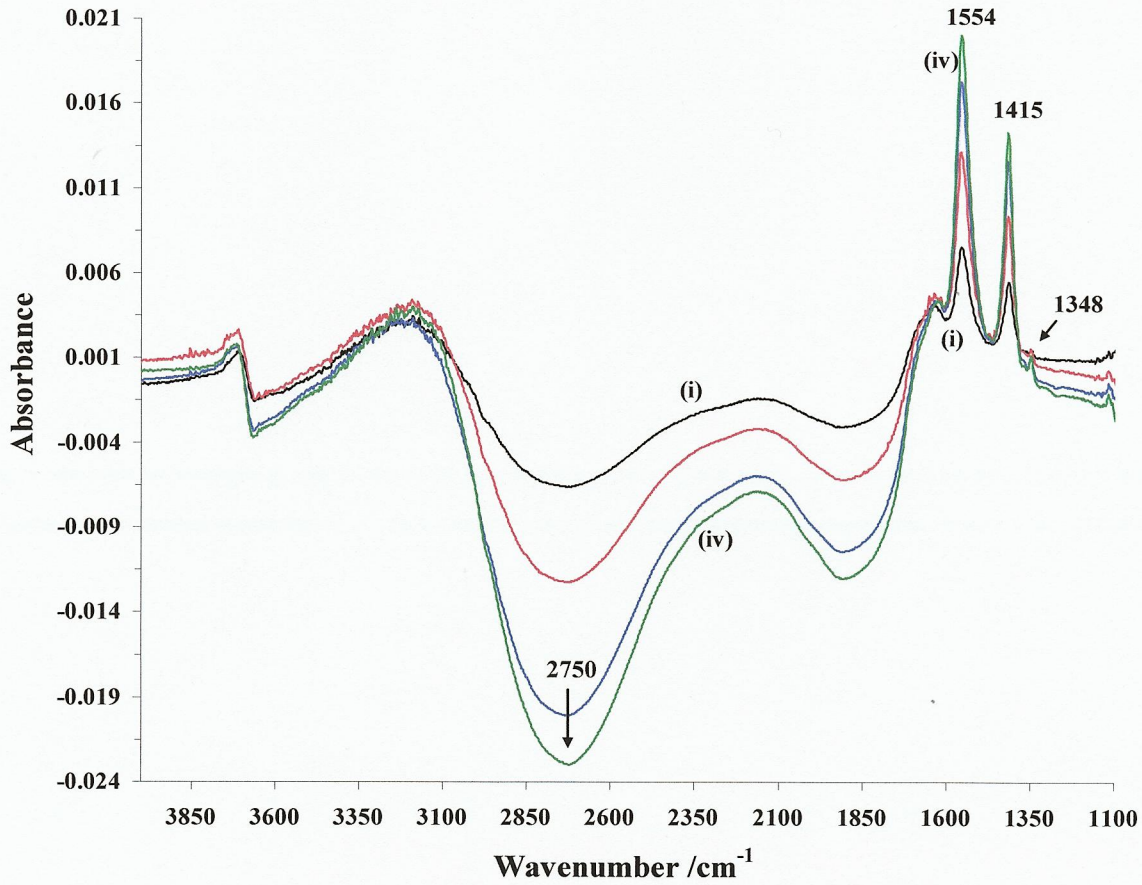

Figure 5.9. The spectra collected at (i) -0.5 V to (iv) -0.2 V in 100 mV steps during the experiment depicted in fig. 5.4 & 5.5.

Given the fact that the pH in the thin layer in the experiments drops at higher potentials due to the consumption of hydroxide ion (see previous chapters), and there is little molecular information in the literature on the electro-oxidation of ethanol at Pt in alkaline solution, it seems sensible to review the key findings from on ethanol electro-oxidation at Pt in acidic solution.

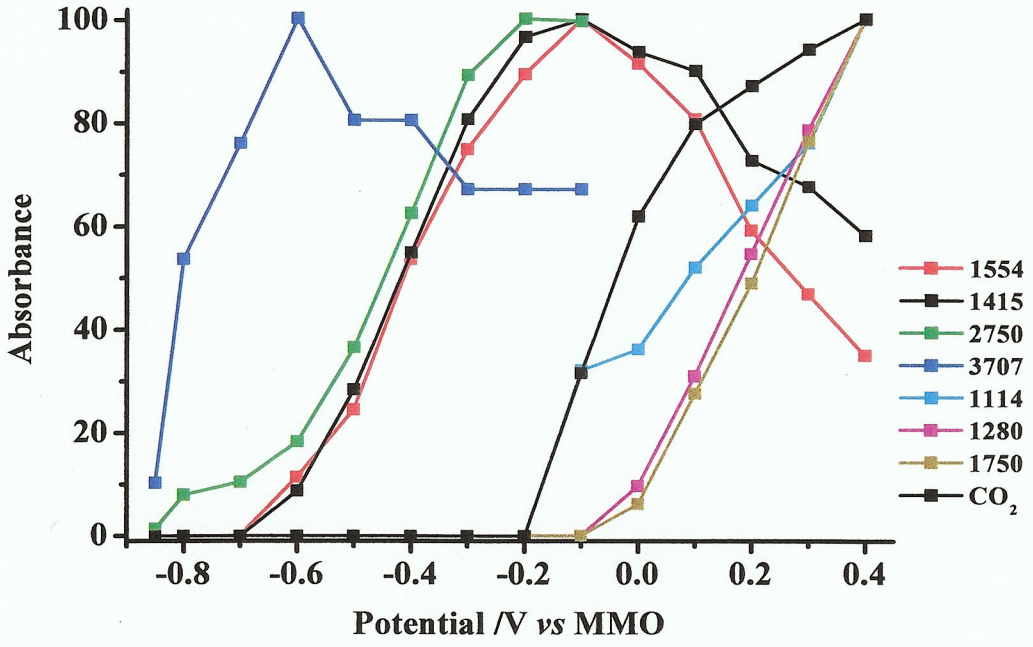

Figure 5.10. Plots of the intensities of the various features observed in the IR spectra collected during the experiment depicted in fig. 5.4 normalized to their maximum intensities.

The mechanism of ethanol electro-oxidation at Pt in acid electrolyte depends critically upon whether ethanol is removed from solution following chemisorption; if it is removed, oxidation of the chemisorptions fragments leads only to CO_2 [43-45]. In contrast, in the presence of ethanol, < 2% of the product is CO_2 (most likely due to the oxidation of initially adsorbed ethanol) with acetaldehyde and acetic acid as the major products, the distribution of the products depending upon ethanol concentration and potential [14, 44-49].

Iwasita and co-workers [44, 45] postulated that the chemisorption of ethanol at Pt results in CO_{ads}, Pt-OCH_2CH_3 (adsorbed ethoxy), Pt_2COHCH_3 and $PtCOCH_3$, all of which are oxidised only to CO_2. This work was supported by Ianniello et al. [43] who

studied the chemisorption of ethanol at porous Pt electrodes. Iwasita postulated that, apart from CO_{ads}, > 60% of the chemisorbed fragments were due to C_2 species, and hence that C-C bond cleavage occurs predominantly only at higher potentials (i.e. 0.7 V vs. RHE), and hence after chemisorption. In contrast, other workers [50-52] postulate that chemisorption is primarily dissociative, resulting in CO_{ads} and other C_1 fragments.

The dual path mechanism is usually invoked to explain the oxidation of ethanol in solution, see fig. 5.11. The presence of CO_{ads} is taken as evidence for the "indirect path" (steps 1,3,5 and/or 1,4,5 in fig. 5.11) resulting in bond cleavage and CO_2 formation. The "direct path" (steps 1 and 2) produces acetic acid and acetaldehyde, both of which are stable with respect to further oxidation due, it is generally believed, to the blocking of the Pt surface by some of the chemisorbed fragments [46, 53]; Shao and Adzic [46] suggest that the blocking of active sites is due to adsorbed acetate. In addition, the intermediates in the formation of acetaldehyde and acetic acid remain unclear [47, 49, 54]. Hence, whilst there is general agreement around the broad principles encapusulated by fig. 5.11, the exact details of the mechanism whereby solution ethanol is oxidised to acetic acid, acetaldehyde and small amounts of CO_2 remains controversial. [54]

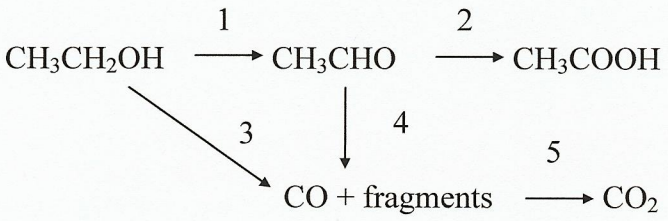

Figure 5.11. The dual path mechanism.

In alkaline solution there is very limited information: apart from very weak absorptions due to multiply-bonded, adsorbed CO; López-Atalaya et al. [1], observed only acetate in the FTIR spectra obtained during the electro-oxidation of ethanol at Pt(100), Pt(111), and Pt(110) in 0.1 M NaOH; they claim also to observe a feature near 1350 cm^{-1} they 'tentatively attributed' to HCO_3^-, but this was not evident in the spectra presented in the paper, and the potential at which the species was observed not specified.

Bianchini et al. [5] and Sun and co-workers [4] infer the production of HCO_3^- and CO_3^{2-}, respectively, from the asymmetry of the 1415 cm^{-1} acetate band, Bianchini refers to this band being present in the spectra in figs. 2(e) & (f) in the paper; unfortunately, these figures are omitted. Sun postulates that CO_3^{2-} is produced at higher potentials, i.e. ≥ +0.2 V vs. SCE (approximately +0.14 V vs. MMO).

Figure 5.12 shows a spectrum of $NaOOCCH_3$ in 0.1 M KOH obtained by diffusing 0.1 M $NaOOCCH_3$ + 0.1 KOH into the spectroelectrochemical cell containing 0.1 M KOH (see Chapter 3 for details). The bands in fig. 5.12 clearly match those in figs. 5.5 and 5.9 that we attribute to acetate ions in solution.

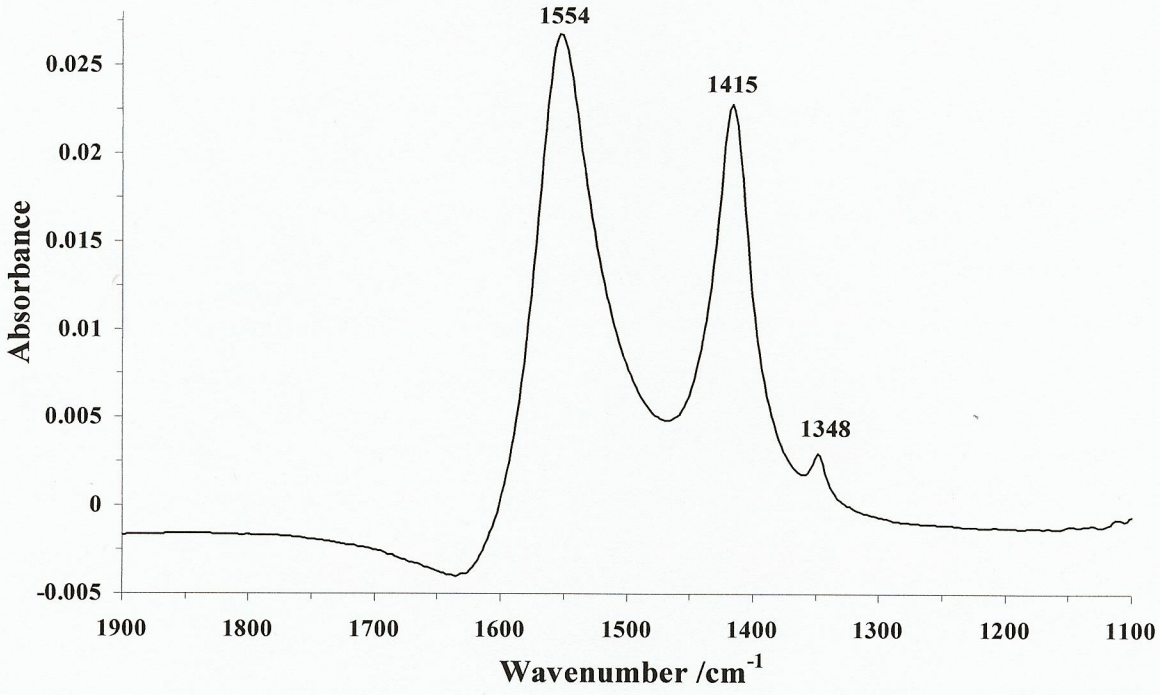

Figure 5.12. Spectrum collected 30 minutes after diffusing an aqueous solution of 0.1 M $NaOOCCH_3$ + 0.1 M KOH into the spectroelectrochemical cell initially containing 0.1 M KOH. See text for details.

Figure 5.13 compares fig. 5.12 with the spectrum in fig. 5.9 collected at -0.2 V. The baselines have been moved to ca. zero at 1480 cm^{-1} and the spectrum collected at -0.2 V increased slightly so the 1415 cm^{-1} features overlie. As can be seen, the 1415 cm^{-1} bands overlie exactly, showing clearly that there are no underlying absorptions due to HCO_3^- or CO_3^{2-}, and hence that the polycrystalline Pt electrode is selective for acetate, with no evidence for cleavage of the C-C bond below -0.2 V despite clear loss

features suggesting significant depletion of OH^- in the thin layer, and hence a decrease in pH, presumably due to the production of acetate. It is possible that acetaldehyde is produced as well as acetate; however, under alkaline conditions, acetaldehyde polymerizes to form a mixture of compounds *via* an Aldol-type mechanism [55]. Thus, if acetaldehyde is added to 0.1 M KOH to 1 M, a bright orange solution results with weak, ill-defined IR bands near 1650 cm^{-1}, 1400 cm^{-1} and 1100 – 1160 cm^{-1} which would be difficult to discriminate in the spectra in figs. 5.5 & 5.9.

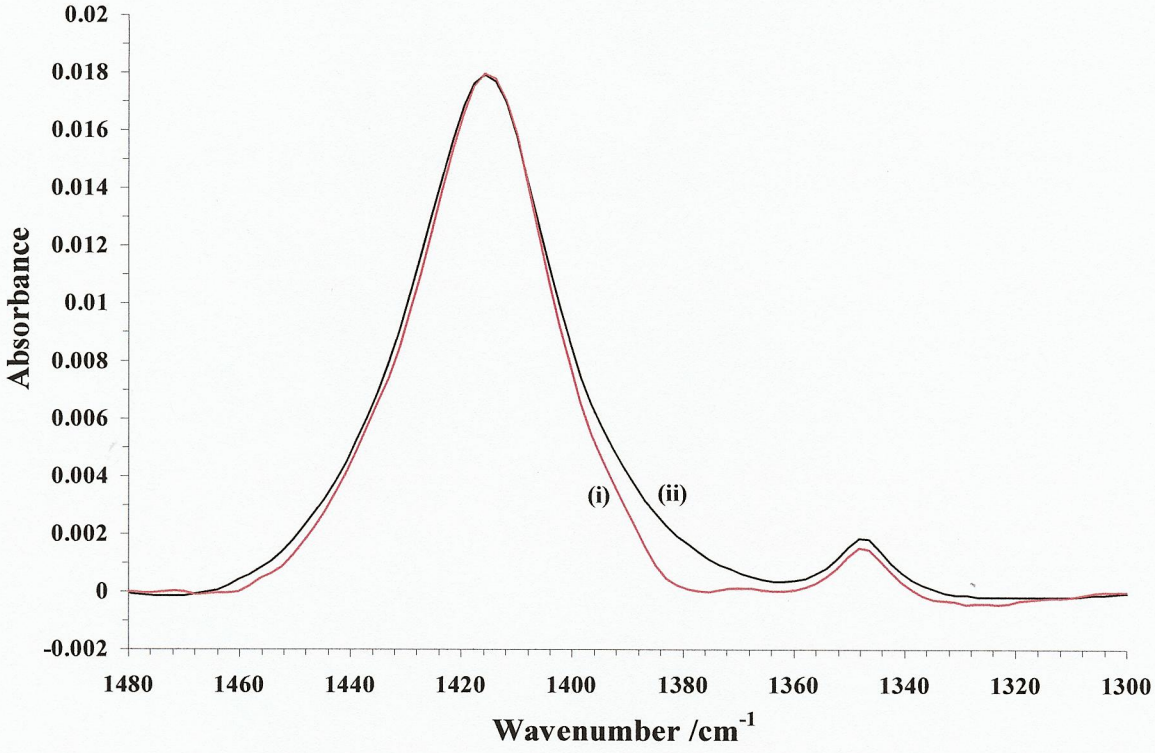

Figure 5.13. The spectrum collected at -0.2 V in fig. 5.9 (i), compared to the spectrum in fig. 5.12 (ii). Both spectra have been shifted down such that the baseline is zero at 1480 cm^{-1}, and the intensity of the 1415 cm^{-1} band in (i) has been increased by a factor of 1.38.

5.4.4. The spectra from -0.1 V to +0.4 V

Figure 5.14(a) shows the spectra collected at potentials from -0.1 V to +0.4 V in the experiment depicted in fig. 5.4. It appears that the acetate features decrease in intensity as the potential is increased, whilst new features grow-in at 1715 cm^{-1} ca. 1368 cm^{-1}, 1280 cm^{-1} and 1114 cm^{-1}. In addition, there appears to be a decrease in absorption near 3200 cm^{-1}, a decrease in the intensity of the broad OH^- loss feature and the appearance of the band attributed to CO_2 at 2340 cm^{-1} [12, 56]. These

observations are confirmed by fig. 5.14(b) which shows the spectra in fig. 5.14(a) normalized to the spectrum collected at -0.2 V in fig. 5.9.

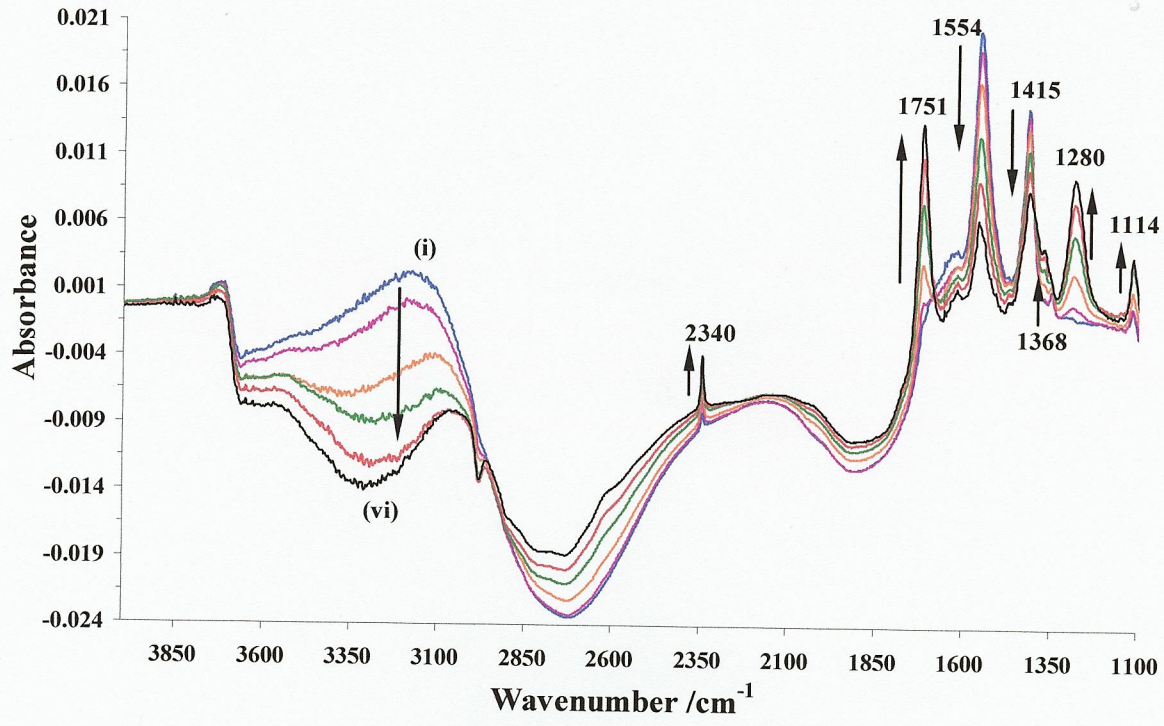

(a)

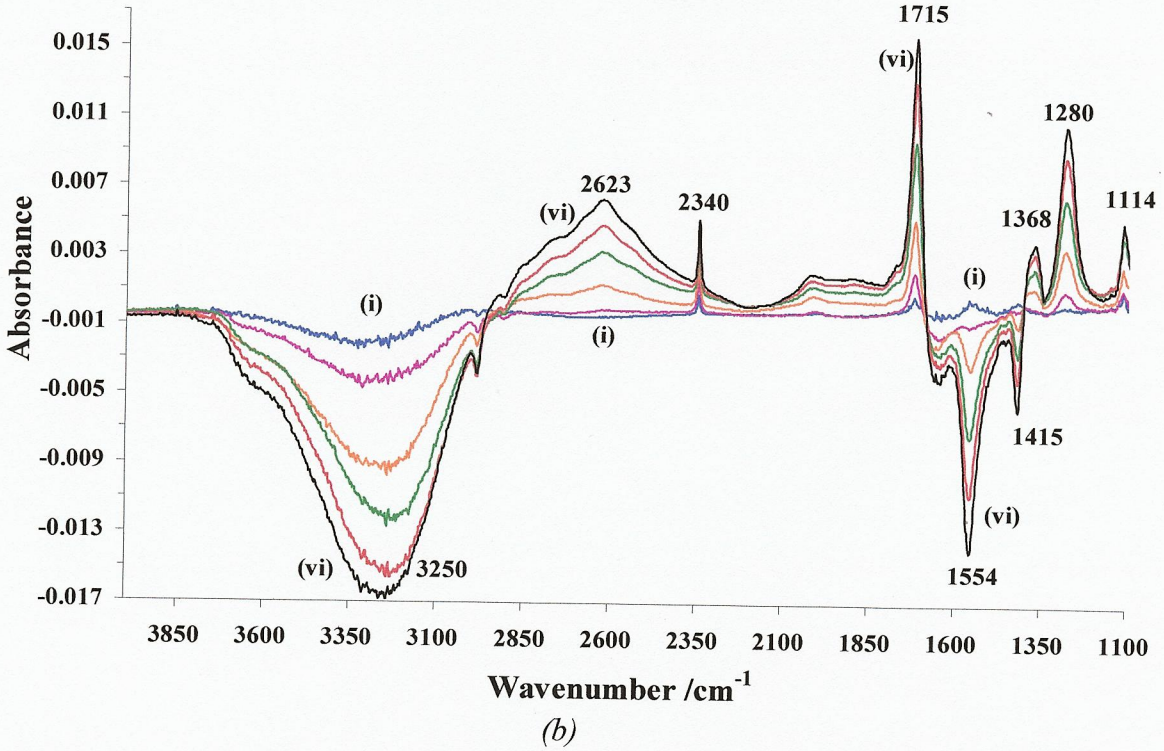

(b)

Figure 5.14. (a) The spectra collected at (i) -0.1 V to (vi) 0.4 V in 100 mV steps during the experiment depicted in fig. 5.4 normalised to the reference spectrum collected at -0.85 V vs. MMO. (b) The spectra in (a) normalised to the spectrum taken at -0.2 V in fig. 5.9.

From figs. 5.14(b), 5.4 and 5.10 it can be seen that the broad feature near 2623 cm^{-1}, and the 1715 cm^{-1}, 1368 cm^{-1} and 1280 cm^{-1} bands track each other and are due to the same species, but this is not the species responsible for the 1114 cm^{-1} feature.

The appearance of CO_2 suggest that C-C bond cleavage does take place (in the radially more central part of the thin layer) where the pH has dropped (see chapter 4), to a value comparable to or less than 4.75, $pK_{\alpha,1}$ for acetic acid [57]. The drop in pH is also seen in the position of the equilibrium:

$$CH_3COOH + H_2O \leftrightarrow CH_3COO^- + H_3O^+ \qquad (5.4)$$

Which shifts to the left due to the production of protons in the thin layer.

From fig, 5.4 it can be seen that very little charge flows at potentials > 0 V and this is reflected in the lack of additional Faradaic products apart from the small amount of CO_2 and the species responsible for the 1114 cm^{-1} band, which is not acetic acid. To investigate this, a diffusion experiment was carried out in which 0.1 M acetic acid in water was diffused into the spectroelectrochemical cell containing water, and the entry of the acid into the thin layer monitored, and a typical spectrum so obtained is shown in fig. 5.15 and the principal features listed in table 5.2, along with their assignments.

Band /cm^{-1}	**Assignment**	**Reference**
1283	O-H deformation in COOH group.	[14, 47, 58- 60]
1369 – 1375	Acetaldehyde, possible contribution of formate or CO_3^{2-} in alkaline solution.	[5, 22, 60, 61]
1390 – 1392	C-O stretching in COOH group.	[4, 14]
1715	Acetic acid	[14, 47, 58- 61]
2616 – 2625	O-H stretch broad band	[58, 59, 61]

Table 5.2. The assignments of the bands attributable to CH_3COOH in figs. 5.14(b) & 5.15.

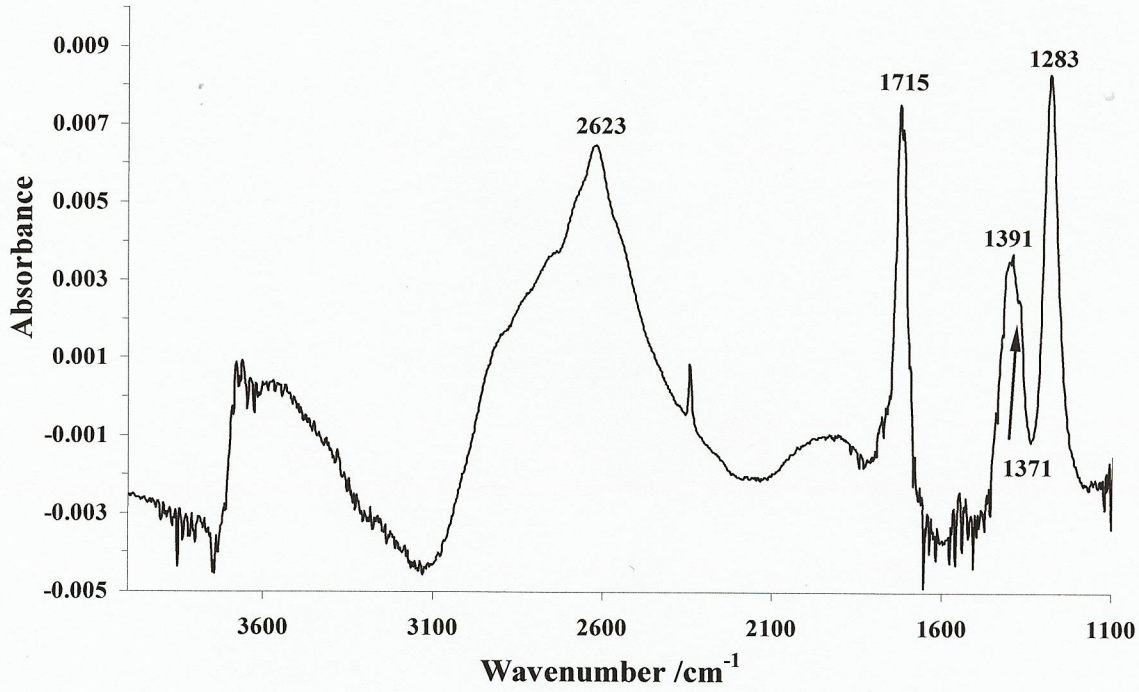

Figure 5.15. Spectrum (8 cm^{-1} 100 scans co-added and averaged) collected 25 minutes after diffusing an aqueous solution of 0.1 M CH_3COOH into the spectroelectrochemical cell initially containing water. See text for details.

It is clear from fig. 5.15 that the 1114 cm^{-1} feature is not due to acetic acid. Yu and Chuang [22] employed FTIR spectroscopy to study the adsorption of ethanol from the gas phase at TiO_2 powder (Degussa P25). They observed a band near 1113 cm^{-1} which they attribute to adsorbed ethoxy ($CH_3CH_2O_{ads}$); this feature was accompanied by bands near 2971, 2931, 2872 and 2869 cm^{-1}.

Iwasita and Pastor [44, 45] also attributed bands at 2960 cm^{-1}, 2920 cm^{-1} and 2850 cm^{-1} to adsorbed ethoxy following ethanol chemisorptions at Pt in aqueous $HClO_4$ & H_2SO_4; they were unable to observe the C-O stretching region (1000 - 1200 cm^{-1}) due to anion absorptions. There are no bands attributable to the C-H stretches of adsorbed ethoxy in figs. 5.14(a) and (b). However, the O-H stretches of the hydrated form of acetaldehyde absorb near 1108 cm^{-1}, with the $\delta_{C\text{-}H}$ band near 1368 cm^{-1} ([14] and references therein); the latter may be present in fig. 5.14(b) but distorted by the 1415 cm^{-1} acetate loss feature and 1390 cm^{-1} acetic acid gain. It is clear from figs. 5.6 & 5.10 that the 1114 cm^{-1} feature is due to a stable species and acetaldehyde is stable at Pt even to high potentials in acid [45, 53, 62].

Up to -0.2 V, the potential range over which the thin layer remains largely alkaline, there is, therefore, clearly no cleavage of the C-C bond when ethanol was present in the electrolyte. In order to determine if C-C cleavage could occur, it was decided to replicate the experiments carried out by Iwasita and co-workers, Ianniello et al., etc. in acidic solution [43-45] in which ethanol is chemisorbed after which the electrolyte is replaced by ethanol-free solution. Thus, fig. 5.16 shows the spectrum collected at -0.3 V vs. MMO during an experiment in which 1 M ethanol + 0.1 M KOH was admitted into the IR cell containing 0.1 M KOH at -0.65 V vs. MMO and the potential held for 30 minutes, after which the electrolyte was replaced by 0.1 M KOH (still holding the potential at -0.65 V), reducing the ethanol concentration in solution to $< 10^{-7}$ M.

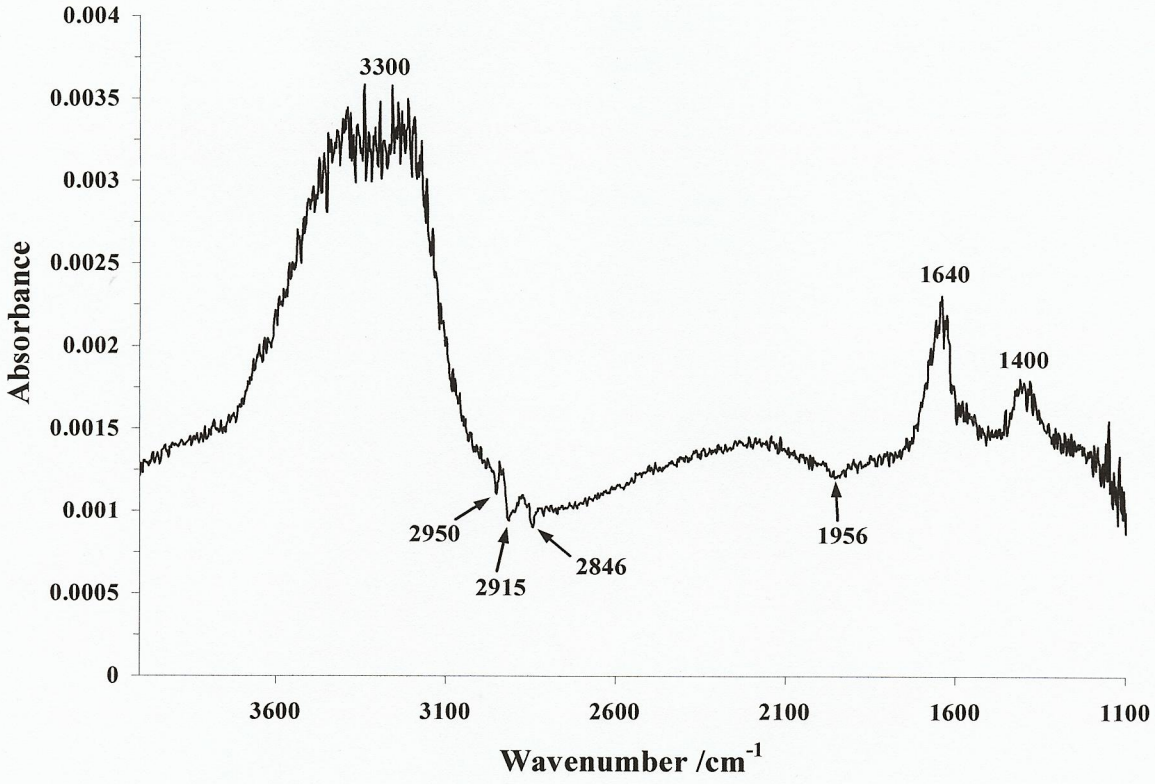

Figure 5.16. Spectrum collected at -0.3 V vs. MMO following adsorption of ethanol at -0.65 V vs. MMO and removal of solution ethanol. Electrolyte 0.1 M KOH. See text for details.

The electrode was then pushed against the prismatic cell window and the FTIR flushed with nitrogen for 60 minutes; a reference spectrum was collected after which the potential of the Pt electrode was stepped up, further spectra taken and normalised to the reference spectrum according to the manipulation in equation (2.1). As can be seen from the spectrum in fig. 5.16 there are clear loss features near 2950 cm^{-1}, 2915

cm^{-1} and 2846 cm^{-1} which we attribute to adsorbed ethoxy [22, 44, 45], a loss feature near 1956 cm^{-1} due to linearly adsorbed CO and a gain feature near 1400 cm^{-1} due to CO_3^{2-}, as well as gain features near 3300 cm^{-1} and 1640 cm^{-1} due to interfacial water.

This is a most interesting result, evidence that ethanol (probably as ethoxide) strongly adsorbs on Pt; it is evident that in the absence of competing solution ethanol, the initial oxidation product(s) at higher potential, which are presumably adsorbed acetal and acetate type moieties, do not desorb to give solution acetaldehyde and acetate species, but remain on the surface and are subject to further oxidation. A possible mechanism for this would involve initial removal of one of the hydrogens attached to the CH_3 group by OH^- followed by oxidation of the carbanion formed at the relatively elevated potentials, to form adsorbed CH_2OH-COO-Pt which could then cyclise and undergo C-C bond scission. It is evident that the reason this does not happen under normal circumstances is that ethanol adsorbs more strongly that acetate or acetal and these species are displaced from the surface more rapidly than they can be further oxidised. It is not, therefore, the case that the Pt surface is inactive for the complete oxidation of ethanol, but rather that the partial oxidation products are lost before complete oxidation can take place.

5.5. Conclusions

The oxidation of ethanol at Pt in aqueous KOH is selective for the formation of acetate; there is no evidence for C-C bond cleavage. As was stated by Iwasita [44], cleavage of C-C bonds occurs only if the molecule is in intimate contact with the Pt. We would modify this slightly and state that it is clear from the literature (see discussion above) that both the carbon atoms of ethanol must be in contact with the Pt, either directly or indirectly through the oxygen atom, for C- C bond cleavage to occur. In the presence of ethanol, it is postulated that adsorption of ethoxide takes place according to equation (5.3) to form a hydrophobic layer. As the potential of the Pt is increased, oxidation of the adsorbed ethoxide to adsorbed acetate takes place; however, this is displaced by the adsorption of ethanol: in other words, ethanol adsorbs more strongly than acetate. In the absence of ethanol, however, the adsorbed acetate is not displaced and the combination of the positive electrode and the presence of the carbonyl group activates the C-H bond of the methyl group towards (slow) proton abstraction by OH^-. At this point there is no choice but to speculate on the

details of the mechanism; given the relative simplicity of the chemical composition of the thin layer, it does not seem unreasonable to postulate that loss of one electron to the anode results in a five membered ring (Pt-O-CO-CH_2-Pt), removal of two electrons results in a six membered ring (Pt-O-CO-CH_2-O-Pt). Further oxidation of either of these species leads to C-C bond scission, and CO_{ads} & CO_3^{2-} formation. If this model is correct, the development of a direct alcohol fuel cell could be facilitated by identifying a catalyst or co-catalyst able to retain adsorbed acetate to allow further attack by hydroxide ions.

Overall, the work in this chapter again reinforces the concept that a key differential between the mechanisms of alcohol oxidation at polycrystalline Pt electrodes in alkaline, as opposed to acidic, solution is that, in the former, adsorption primarily takes place through the oxygen atom rather than through carbon-metal bond formation.

5.6. References

1. López-Atalaya M., Morallón E., Cases F., Vázquez J.L., and Pérez J.M., (1994). Journal of Power Sources, 52, 1, pp. 109-117.
2. Russell A.E., Blackwood D., Anderson M.R., and Pons S., (1991). Journal of Electroanalytical Chemistry, 304, 1-2, pp. 219-231.
3. Christensen P. A. and Hamnett A., (1989). *In-situ Infrared Studies of the Electrode-Electrolyte Interface*, in: Comprehensive Chemical Kinetics Vol 29. New Techniques for the Study of Electrodes and their Reactions, R.G. Compton and A. Hamnett Editors, Elsevier, Amsterdam, p. 1 -77.
4. Zhou Z.-Y., Wang Q., Lin J.-L., Tian N,, and Sun S.-G., (2010). Electrochimica Acta, 55, 27, pp. 7995-7999.
5. Fang X., Wang L., Shen P.K., Cui G., and Bianchini C., (2010). Journal of Power Sources, 195, 5, pp. 1375-1378.
6. Schmidt T.J., Ross P.N., and Markovic N.M., (2001). The Journal of Physical Chemistry B, 105, 48, pp. 12082-12086.
7. Lai S.C.S. and Koper M.T.M., (2009). Physical Chemistry Chemical Physics, 11, 44, pp. 10446-10456.
8. Dimos M.M. and Blanchard G.J., (2010). The Journal of Physical Chemistry C, 114, 13, pp. 6019-6026.
9. Chen S. and Schell M., (1999). Journal of Electroanalytical Chemistry, 478, 1- 2, pp. 108-117.
10. Tripković A.V., Popović K.D., and Lović J.D., (2001). Electrochimica Acta, 46, 20-21, pp. 3163-3173.
11. Christensen P.A. and Hamnett A., (1994). *Techniques and Mechanisms in Electrochemistry*, 1 ed. Oxford: Blackie Academic & Professional, an imprint of Chapman & Hall. 396.
12. Christensen P.A. and Linares-Moya D., (2009). The Journal of Physical Chemistry C, 114, 2, pp. 1094-1101.

13. Christensen P.A. and Hamnett A., (1989). Journal of Electroanalytical Chemistry and Interfacial Electrochemistry, 260, 2, pp. 347-359.
14. Wang Q., Sun G.Q., Jiang L.H., Xin Q., Sun S.G., Jiang Y.X., Chen S.P., Jusys Z., and Behm R.J., (2007). Physical Chemistry Chemical Physics, 9, 21, pp. 2686-2696.
15. DeLima R.B. and Varela H., (2008). Gold Bulletin, 41, 1, pp. 15-22.
16. Lutz H., (1988). *Bonding and structure of water molecules in solid hydrates. Correlation of spectroscopic and structural data*, in: Solid Materials, Springer Berlin / Heidelberg, p. 97-125.
17. Kunimatsu K., Sato T., Uchida H., and Watanabe M., (2008). Langmuir, 24, 7, pp. 3590-3601.
18. Hirota K., Song M.-B., and Ito M., (1996). Chemical Physics Letters, 250, 3-4, pp. 335-341.
19. Ataka K.-i., Yotsuyanagi T., and Osawa M., (1996). The Journal of Physical Chemistry, 100, 25, pp. 10664-10672.
20. Kitamura F., Ohsaka T., and Tokuda K., (1996). Journal of Electroanalytical Chemistry, 412, 1-2, pp. 183-188.
21. Futamata M. and Luo L., (2007). Journal of Power Sources, 164, 2, pp. 532-537.
22. Yu Z. and Chuang S.S.C., (2007). Journal of Catalysis, 246, 1, pp. 118-126.
23. Watanabe M., Sato T., Kunimatsu K., and Uchida H., (2008). Electrochimica Acta, 53, 23, pp. 6928-6937.
24. Kunimatsu K., Hanawa H., Uchida H., and Watanabe M., (2009). Journal of Electroanalytical Chemistry, 632, 1-2, pp. 109-119.
25. Iwasita T. and Xia X., (1996). Journal of Electroanalytical Chemistry, 411, 1-2, pp. 95-102.
26. Sastry M.I.S. and Singh S., (1987). Journal of Molecular Structure, 158, pp. 195-204.
27. Du Q., Freysz E., and Shen Y.R., (1994). Physical Review Letters, 72, 2, pp. 238-241.
28. Scherer J.R., Go M.K., and Kint S., (1974). The Journal of Physical Chemistry, 78, 13, pp. 1304-1313.
29. Walrafen G.E., (1974). *Spontaneous and stimulated Raman spectra from Water and Aqueous Solutions*, in: Structure of Water and Aqueous Soultions, W.A.P. Luck [Editor], Verlag Chemie-Physik Verlag, Marburg, p. 302-321.
30. Verma D., Katti K., and Katti D., (2007). Spectrochimica Acta Part A: Molecular and Biomolecular Spectroscopy, 67, 3-4, pp. 784-788.
31. Dreesen L., Humbert C., Hollander P., Mani A.A., Ataka K., Thiry P.A., and Peremans A., (2001). Chemical Physics Letters, 333, 5, pp. 327-331.
32. Berná A., Delgado J.M., Orts J.M., Rodes A., and Feliu J.M., (2008). Electrochimica Acta, 53, 5, pp. 2309-2321.
33. Gragson D.E., McCarty B.M., and Richmond G.L., (1997). Journal of the American Chemical Society, 119, 26, pp. 6144-6152.
34. Owrutsky J.C., Rosenbaum N.H., Tack L.M., and Saykally R.J., (1985). Journal of Chemical Physics, 83, 10, pp. 5338-5339.
35. Werner H.J., Rosmus P., and Reinsch E.A., (1983). Journal of Chemical Physics, 79, 2, pp. 905-916.
36. Lutz H.D., Eckers W., and Haeuseler H., (1982). Journal of Molecular Structure, 80, pp. 221-224.
37. Stanek T. and Pytasz G., (1977). Acta Physica Polonica, A52, pp. 119.

38. VanThiel M., Becker E.D., and Pimentel G.C., (1957). Journal of Chemical Physics, 27, 2, pp. 486-490.
39. Fifer R.A. and Schiffer J., (1971). Journal of Chemical Physics, 54, 12, pp. 5097-5102.
40. Bertie J.E. and Whalley E., (1964). Journal of Chemical Physics, 40, 6, pp. 1637-1645.
41. Kitamura F., Ohsaka T., and Tokuda K., (1997). Electrochimica Acta, 42, 8, pp. 1235-1238.
42. Cui G., Song S., Shen P.K., Kowal A., and Bianchini C., (2009). The Journal of Physical Chemistry C, 113, 35, pp. 15639-15642.
43. Ianniello R., Schmidt V.M., Rodríguez J.L., and Pastor E., (1999). Journal of Electroanalytical Chemistry, 471, 2, pp. 167-179.
44. Iwasita T., Dalbeck R., Pastor E., and Xia X., (1994). Electrochimica Acta, 39, 11-12, pp. 1817-1823.
45. Iwasita T. and Pastor E., (1994). Electrochimica Acta, 39, 4, pp. 531-537.
46. Shao M.H. and Adzic R.R., (2005). Electrochimica Acta, 50, 12, pp. 2415- 2422.
47. Camara G.A. and Iwasita T., (2005). Journal of Electroanalytical Chemistry, 578, 2, pp. 315-321.
48. Camara G.A., de Lima R.B., and Iwasita T., (2005). Journal of Electroanalytical Chemistry, 585, 1, pp. 128-131.
49. Colmati F., Tremiliosi-Filho G., Gonzalez E.R., Berná A., Herrero E., and Feliu J.M., (2009). Faraday Discussions, 140, pp. 379-397.
50. Gootzen J.F.E., Visscher W., and van Veen J.A.R., (1996). Langmuir, 12, 21, pp. 5076-5082.
51. Beden B., Morin M.C., Hahn F., and Lamy C., (1987). Journal of Electroanalytical Chemistry and Interfacial Electrochemistry, 229, 1-2, pp. 353-366.
52. Schmiemann U., Müllier U., and Baltruschat H., (1995). Electrochimica Acta, 40, 1, pp. 99-107.
53. Leung L.-W.H., Chang S.-C., and Weaver M.J., (1989). Journal of Electroanalytical Chemistry and Interfacial Electrochemistry, 266, 2, pp. 317-336.
54. Heinen M., Jusys Z., and Behm R.J., (2010). The Journal ofPhysical Chemistry C, 114, 21, pp. 9850-9864.
55. Wurtz C.A., (1872). Bulletin de la Société Chimique de France, 17, pp. 436-442.
56. Christensen P.A., Hamnett A., and Linares-Moya D., (2011). Physical Chemistry Chemical Physics, in press.
57. (1994). *CRC Handbook of Chemistry and Physics 74th Edition*, ed. D.R. Lide. Boca Raton, FL.: CRC Press/Taylor and Francis. 2,376.
58. Socrates G., (1980). *Infrared Characteristic Group Frequencies*, 1 ed, ed. J.W.a. Sons. Bath: Wiley Interscience. 153.
59. Xia X.H., Liess H.D., and Iwasita T., (1997). Journal of Electroanalytical Chemistry, 437, 1-2, pp. 233-240.
60. Vigier F., Coutanceau C., Hahn F., Belgsir E.M., and Lamy C., (2004). Journal of Electroanalytical Chemistry, 563, 1, pp. 81-89.
61. Iwasita T., Rasch B,, Cattaneo E., and Vielstich W., (1989). Electrochimica Acta, 34, 8, pp. 1073-1079.
62. Leung L.W.H. and Weaver M.J., (1988). The Journal of Physical Chemistry, 92, 14, pp. 4019-4022.

6. Direct alcohol alkaline fuel cell test.

6.1. Introduction

In recent years there has been a major focus on the synthesis of monodisperse electrocatalyst nanoparticles for applications in two main fields: as magnetic storage devices [1] and fuel cells [2]; several routes have been reported for such synthesis, which can be classified in two main groups: impregnation, and colloid methods [3]. In the impregnation methods, metal salt precursors are deposited followed by chemical reduction in aqueous solution using reducing agents [4], Although it has been shown that impregnation methods can be used for the synthesis of multifunctional systems (e.g. bi- and tri-metallic catalysts), they require the use of high surface area carbon support and do not allow high dispersion in the presence of high metal loadings [3]. $Pd_{40}Ni_{60}$ on porous carbon was manufactured by this method using $NaBH_4$ as reducing agent, based in the work by Zhao et al. [5] (see section 2.3).

In the colloid method, the reduction of the metallic precursor salts is carried out in an organic solvent, normally in the presence of stabilisers to prevent aggregation, with the advantage of producing small and homogeneously distributed, carbon-supported metal nanoclusters [3]. However, this methodology is very complex due to the number of steps, is expensive [6-8], and the solvents may adsorb onto the catalyst and poison the active sites, requiring high temperatures for removal [9]. The simplest approach to colloid method is called 'hot soap' or 'polyol' method where only simple polyhydric alcohols (e.g. ethylene glycol) are used, performing different functions [9]; the inorganic precursor salt/s is/are dissolved in alkaline solution containing the polyol (which is chosen depending upon the precursors), the porous carbon substrate is introduced and the solution heated to reduce the ethylene glycol to glycolate which co-ordinates to, and stabilises, the nanoparticles so formed. The organic residue (glycolate) is then removed by heating in air at temperatures low enough to avoid sintering of the metal particles. The synthesis of $Ru_{72}Ni_{28}$ and $Co_{50}Ni_{50}$ catalysts on porous carbon was achieved using this method (see section 2.3); and although a paper by Luna et al. [10] hints at the synthesis of CoNi nanoparticles, there are no reports in the literature to my knowledge of the synthesis of RuNi nanoparticles using the polyol approach.

6.2. Characterization of catalyst.

The micrographs and EDX spectra presented below are typical of the catalysts investigated; hence > 5 areas were examined in each case and typical data are presented.

6.2.1. SEM/TEM

The SEM was a XL30 ESEM-FEG (environmental scanning electron microscopy / field emission gun) [11], A 1 cm^2 aluminium disk (cover with an adhesive for SEM) was employed as the support for the catalyst samples. A small amount (< 1 mg) of the catalyst under study was pasted onto the surface and allowed to dry for 24 hours. The magnification of the Newcastle SEM is 10^5x, and this was routinely employed.

A typical SEM image obtained using the Newcastle SEM is shown in fig. 6.1, the sample was $Ru_{72}Ni_{28}/C$.

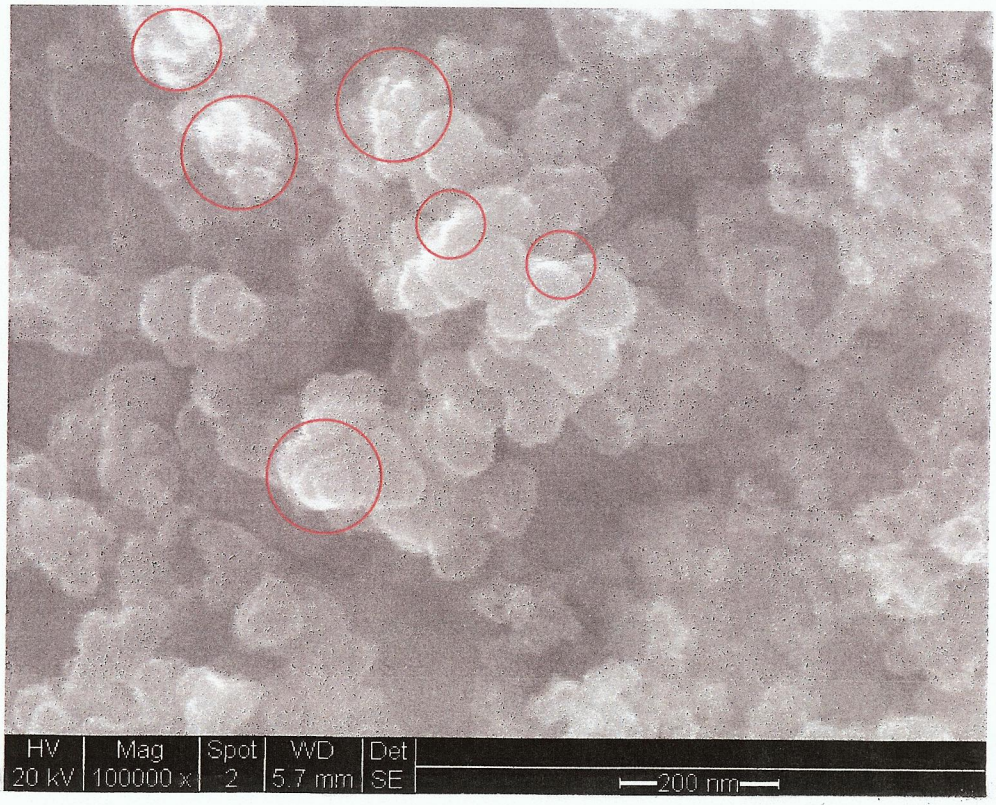

Figure 6.1. Scanning electron micrograph of the $Ru_{72}Ni_{28}/C$ catalyst.

Unfortunately, as may be seen from the figure, whilst the carbon support is clearly visible as white "globules", the resolution of the SEM was insufficient to resolve the metal nanoparticles. However, the agglomeration of the metal nanoparticles can be seen as bright 'disks' on the edges of the carbon particles (ringed in red). Hence, TEM was employed to try and see the metal catalyst particles.

The TEM instrument was a Philips CM 100 TEM with high resolution digital image capture [12]. 1 mg of the carbon supported catalyst was suspended in deionised water, and sonicated for 5 minutes; the suspension was then dropped on to a grit mesh sample holder immediately prior to each run. TEM images were routinely obtained at a magnification of 245,000x and images of the $Co_{50}Ni_{50}/C$, $Ru_{72}Ni_{28}/C$, and $Pd_{40}Ni_{60}/C$ catalyst are shown in figs. 6.2 – 6.4 respectively.

In figs. 6.2 and 6.3, the $Co_{50}Ni_{50}$ and $Ru_{72}Ni_{28}$ particles can be seen as dark 'freckles' on the circular carbon particles; with respect to the former, TEM images show the metal particles forming clusters as in fig. 6.5(b) which is consistent with the SEM analysis (not shown).

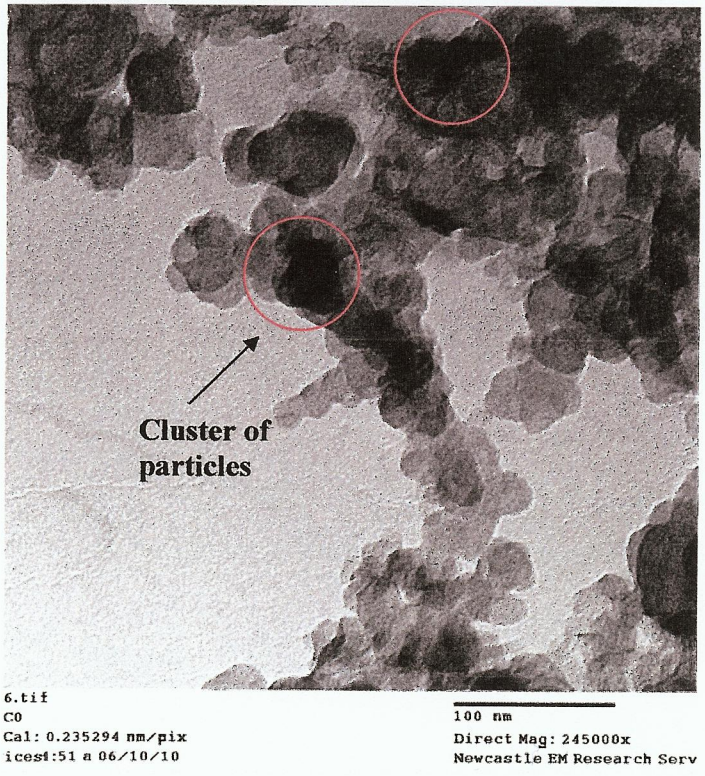

Figure 6.2. Transmission electron micrograph image of the $Co_{50}Ni_{50}/C$ catalyst (x245000).

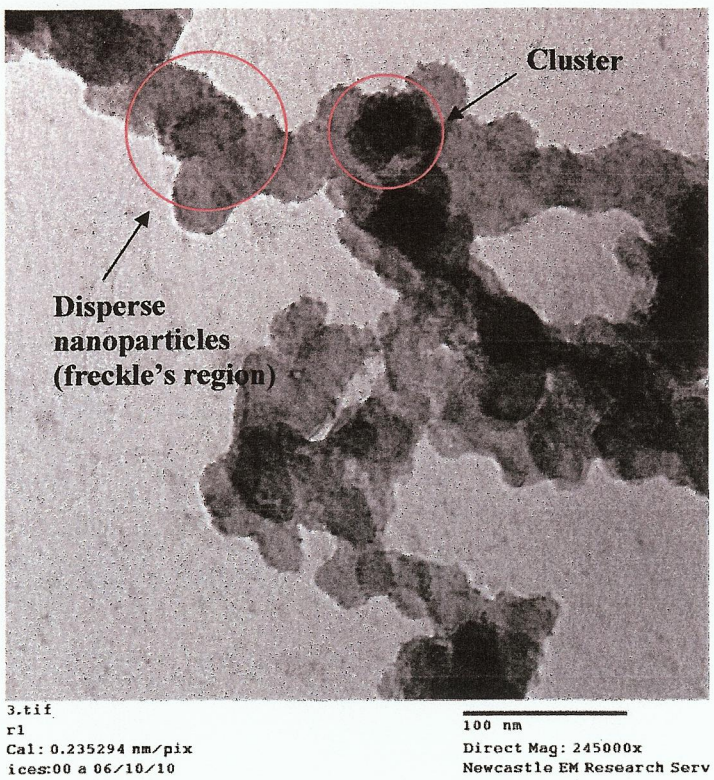

Figure 6.3. Transmission electron micrograph image of the $Ru_{72}Ni_{28}/C$ catalyst (x245000).

From fig. 6.3 it can be seen that there are a number of black 'lumps' due to agglomerated catalyst (ringed in red); however, it can also be seen clearly that there is a considerable amount of the catalyst that is well disperse as in figure 6.5(a); this is in agreement with previous work by Deng et al. [13] who employ the flash spray-pyrolysis process to deposit 5 μm RuNi nanoparticles on to carbon.

In contrast to the CoNi and RuNi catalyst, the particles of PdNi catalyst have quite clearly agglomerated significantly (see fig. 6.4, ringed in red) to form 'flocks' on the carbon substrate, as shown in fig. 6.5(c).

This 'flocking' is typical of palladium, see for example Sun et al. [14], when a protective agent such as polyvinyl alcohol is not employed to aid dispersion and/or when nucleation takes place at oxygenated defects [15, 16].

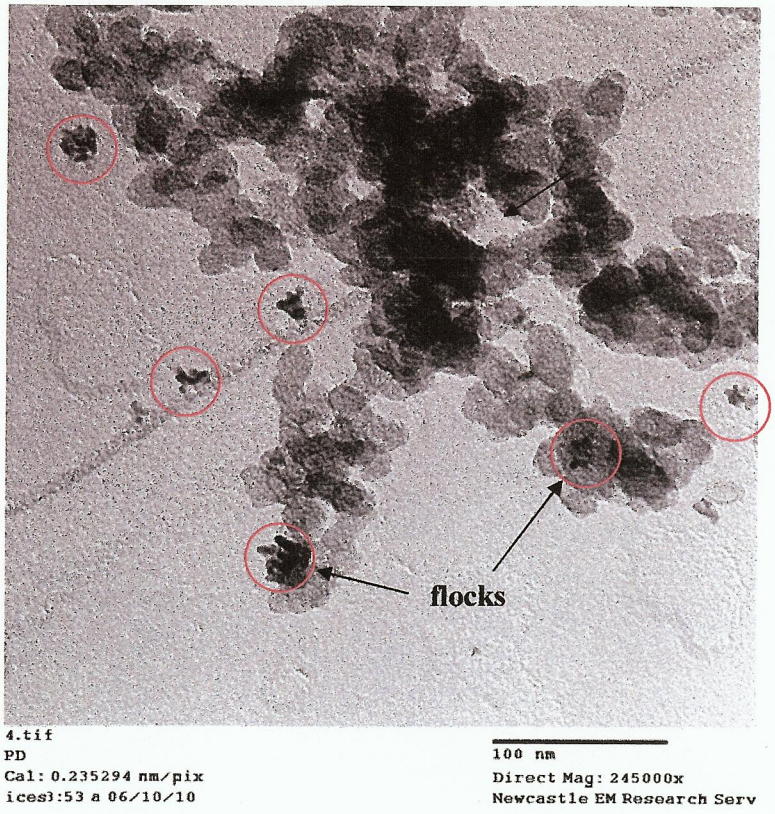

Figure 6.4. Transmission electron micrograph image of the $Pd_{40}Ni_{60}$/C catalyst (x245000).

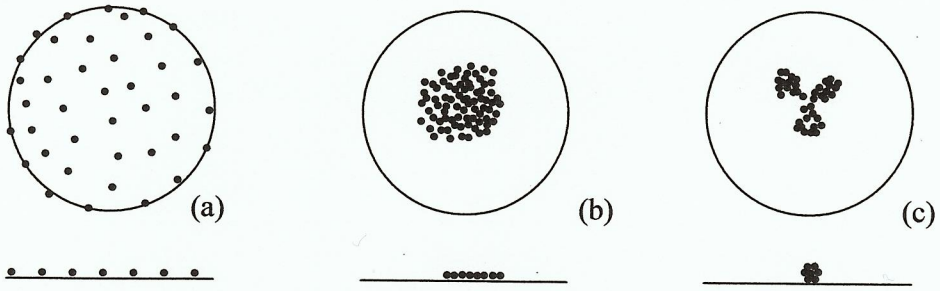

Figure 6.5. Schematic representation of the distributions of the metal particles in figs 6.2 – 6.4, (a) homogenously distributed or 'freckles', (b) clusters or 'lumps', (c) multiple nuclei or 'flocks'.

6.2.2. EDX

Figure 6.6 shows a typical EDX spectrum of the $Co_{50}Ni_{50}$/C catalyst. In all the spectra, the peaks due to carbon were extremely intense and hence the y-axes were expanded to show the metal peaks. From the areas of the relevant peaks the Co and Ni appear to be in the predicted 50:50 ratio; however, the large background and low intensities of the features rendered it difficult to obtain accurate data. As may be seen from the

figure, Na and Cl were present as expected residues from the synthesis; however, Si and S were also presents as impurities, possibly from the mortar and pestle employed to grind up the catalyst.

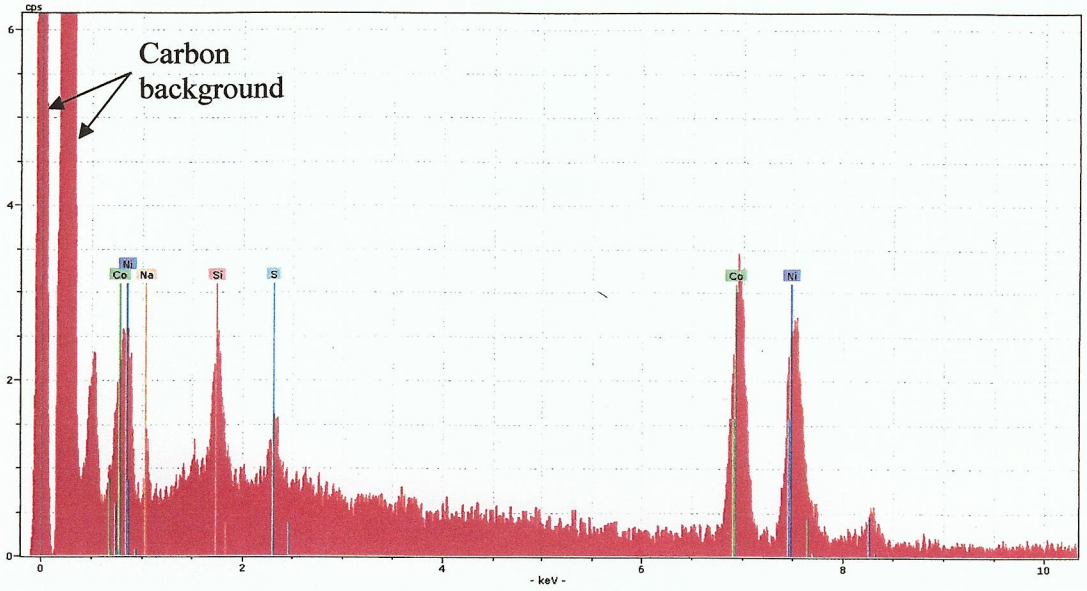

Figure 6.6. EDX spectrum of the $Co_{50}Ni_{50}$/C catalyst.

Figure 6.7 shows the EDX spectrum of the $Ru_{72}Ni_{28}$ catalyst. It is clear from the figure that the amount of Ru apparently present in the catalyst is too low.

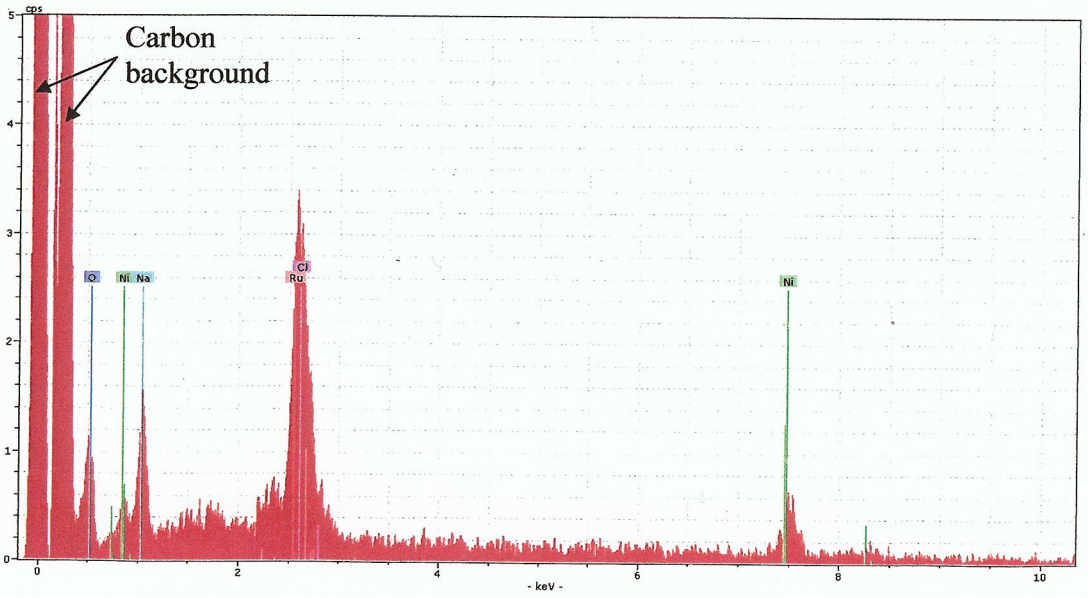

Figure 6.7. EDX spectrum of the $Ru_{72}Ni_{28}$/C catalyst.

This observation has also been reported by Deng and co-workers [13], who attribute this to the formation of Ru core and Ni shell structures, with the EDX technique hence being blind to the Ru cores. Again, Na and Cl were present as (expected) impurities.

Figure 6.8 shows a typical EDX spectrum of the $Pd_{40}Ni_{60}/C$ catalyst, as may be seen, the Ni peak is absent. Ferrando et al. [17] also observe this phenomenon, and concluded that the most stable configuration of this material at low temperature was Ni core/Pd shell. Zhao and co-workers [5] agreed with this postulate. More recently Scott et al. [15] found that EDX could detect Ni in PdNi nanoparticles supported on carbon nano-tubes (CNT), due to the lower carbon signal of CNT.

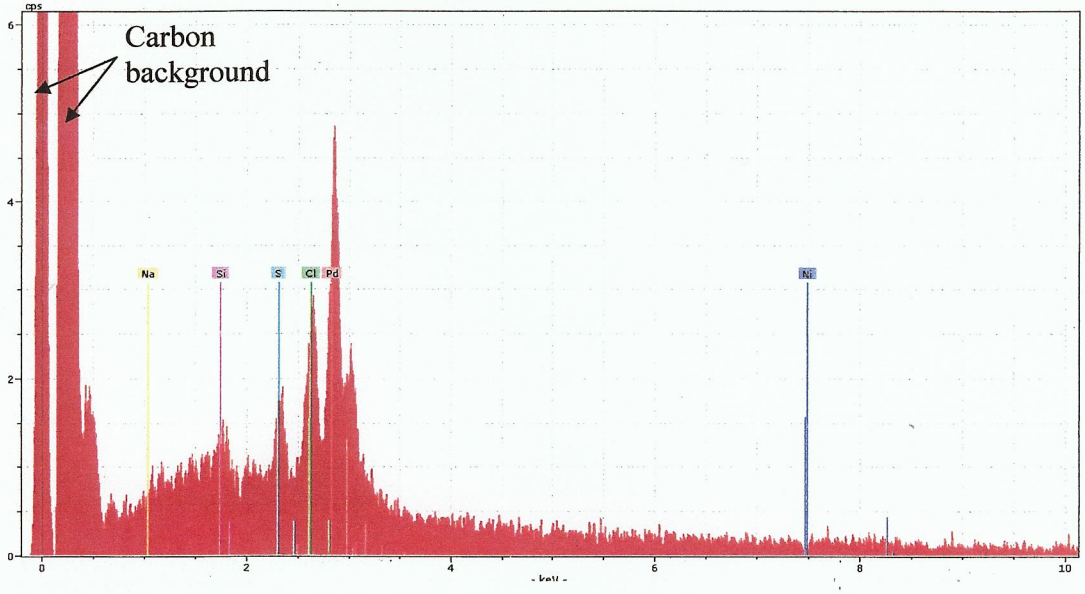

Figure 6.8. EDX spectrum of the $Pd_{40}Ni_{60}/C$ catalyst.

6.2.3. Particle size determination from TEM images.

A number of commercial software packages may be employed to determine particle sizes from TEM images; the one employed was Adobe Photoshop™. Thus, three separate TEM images (of different areas of the catalyst), of each catalyst were chosen at random. Each image was divided into a grid pattern of cells, each 'cell' being 50 nm x 50 nm. Each cell was pixelated: dark spots were assigned to metal particles and light spots to the carbon substrate. The size of each group of pixels was then determined using the 'rule' software tool. Seven cells were analysed from each image, amounting to ca. 300 particles per catalyst sample, and the data so obtained are presented in figs. 6.9 – 6.11.

Figure 6.9 shows the frequency plot for the $Co_{50}Ni_{50}$/C catalyst. As may be seen, the particle size was distributed about 1.3 nm, with no particles ≥ 2.1 nm.

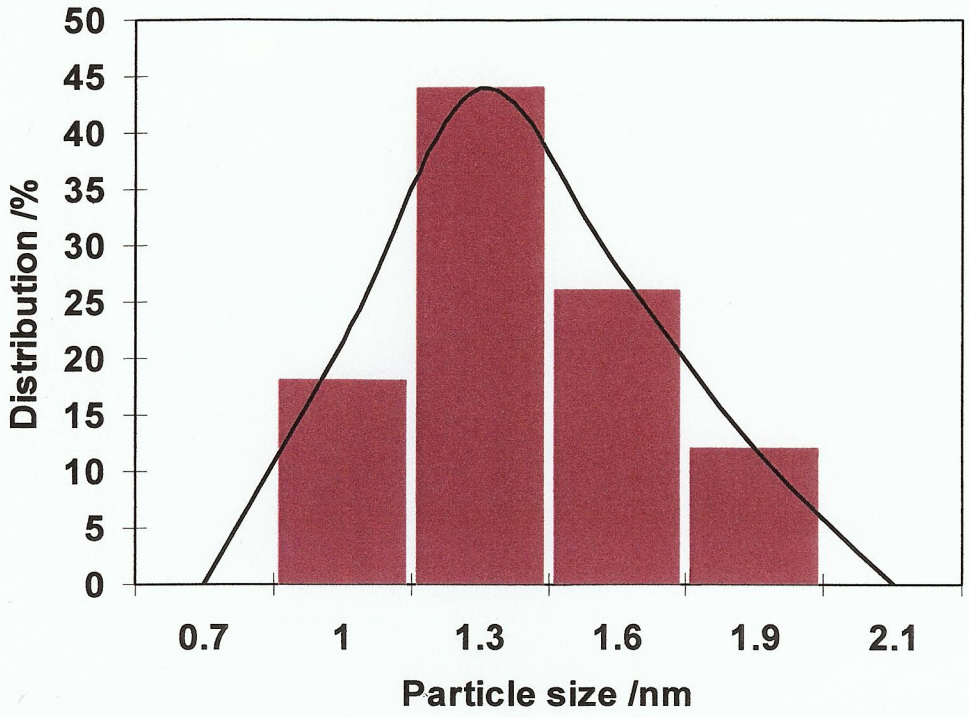

Figure 6.9. Visual count frequency plot for the $Co_{50}Ni_{50}$/C catalyst.

Such a distribution was predicted by Ferrando and co-workers [17], and Toneguzzo et al. [18] who conclude that particle size will be determined by the trade-off between the rapid Co nucleation rate and the rapid growth of Ni on the Co 'seed'. According to the literature [19, 20], particle growth is impeded by a number of factors, including the chemical composition of the precursors (e.g. Cl^- vs. NO_3^-) and the polyol, due to the formation of the metal-polyol complex being a key step in determining the physical characteristic of the final product. Ung and co-workers [21], also conclude this.

Figure 6.10 shows the particle size distribution of the $Ri_{72}Ni_{28}$/C catalyst; this has a mean of 2.4 nm (in agreement with Deng et al. [13]), and a wide spread from 1.5 nm to 3.6 nm. The synthesis employed during the work reported in this thesis has not been reported previously, but is similar to that of Chen and co-workers [22] who employed it to synthesize Ru nanoparticles using Poly (N-vinyl-2-Pyrrolidone) (PVP) as a stabilizer. However Chen obtained larger particle sizes, i.e. 3.8 - 7.3 nm.

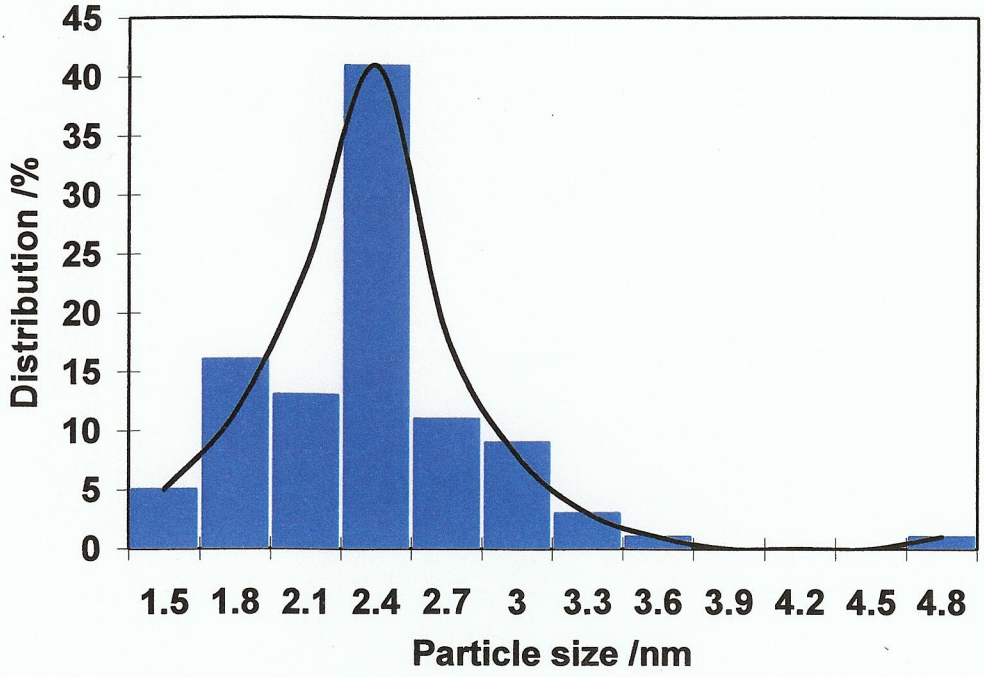

Figure 6.10. Visual count frequency plot for the $Ru_{72}Ni_{28}$/C catalyst.

Figure 6.11 shows the particle size distribution of the $Pd_{40}Ni_{60}$ catalyst with a mean of 6 nm, in agreement with Sun and co-workers [14], but larger than the size reported by Zhao et al. [5] (3.7 nm) and Scott et al. [15] (4.0 nm).

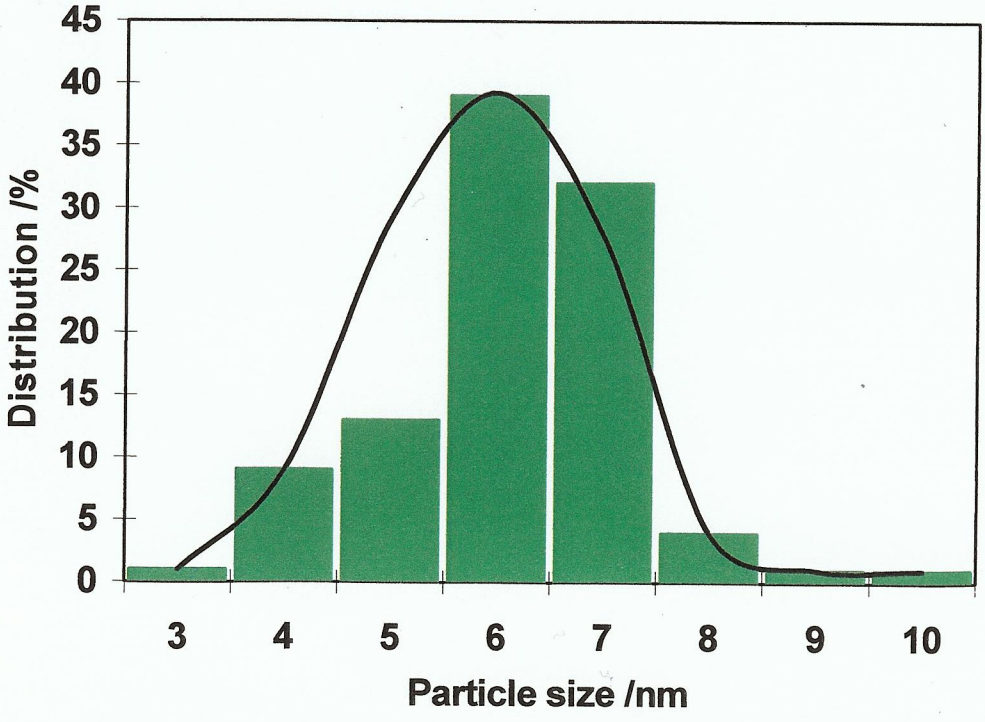

Figure 6.11. Visual count frequency plot for the $Pd_{40}Ni_{60}$/C catalyst.

This discrepancy is unsurprising given the fact that it has been reported that the shape and size of PdNi nanoparticles are affected by palladium content [5], and even by the way the precursors are mixed [23].

6.2.4. Particle size determination from XRD.

Figure 6.12 shows XRD data for the $Co_{50}Ni_{50}$/C catalyst. Unfortunately, the peaks at $2\theta = 44.5°$, 51.3° and 76.4° (characteristic of the face centred cubic (fcc) structure of CoNi nanoparticles [20]) are too broad to be resolved unequivocally. Luna et al. [10], attribute an increase in the asymmetry (broadening) of the fcc (111) reflection to a decrease in particle size to values < 10 nm. The formation of metal oxides, due to the presence of some adventitious water, will also affect the resolution [10].

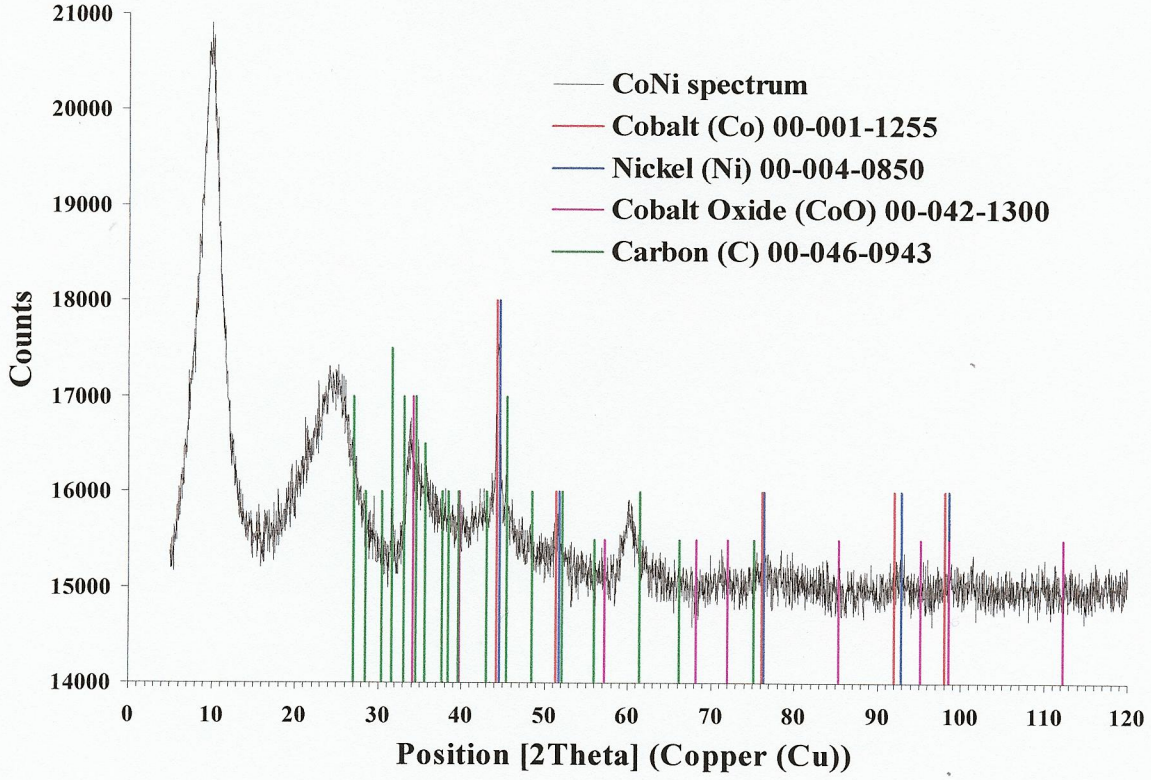

Figure 6.12. XRD data analysis of the $Co_{50}Ni_{50}$/C catalyst

Using Scherrer's equation [24]:

$$d = \frac{0.9\lambda}{B_\theta \cos\theta} \tag{6.1}$$

Where λ = X-ray wavelength (1.54 Å), θ is the angle of the reflection maximum (2θ = 44.50° in this case) and B_θ is the full width of the peak at the half height (or integral breadth), the particle size was calculated as show in table 6.1

Peak identification	2θ angle	B_θ (integral breadth) /rad	d /Å
Cobalt (Nickel overlapped)	44.50	6.981×10^{-3}	214.4

Table 6.1. Average particle size calculated using Scherrer's equation from the 2θ = 44.50° diffraction in fig. 6.12.

The particle size of 21.4 nm (214 Å) is consistent with the work of Panday et al. [20] who found a particle size of 17 – 25 nm. However, this value is significantly larger than the 1.3 nm determined from the TEM images, suggesting that the XRD technique gives an average value of the diameter of polycrystalline clusters of $Co_{50}Ni_{50}$ particles (see fig. 6.5(b) and (c)), rather that the diameter of individual particles, as described by Luna and co-workers [10].

Figure 6.13 shows XRD data for $Ru_{72}Ni_{28}/C$.

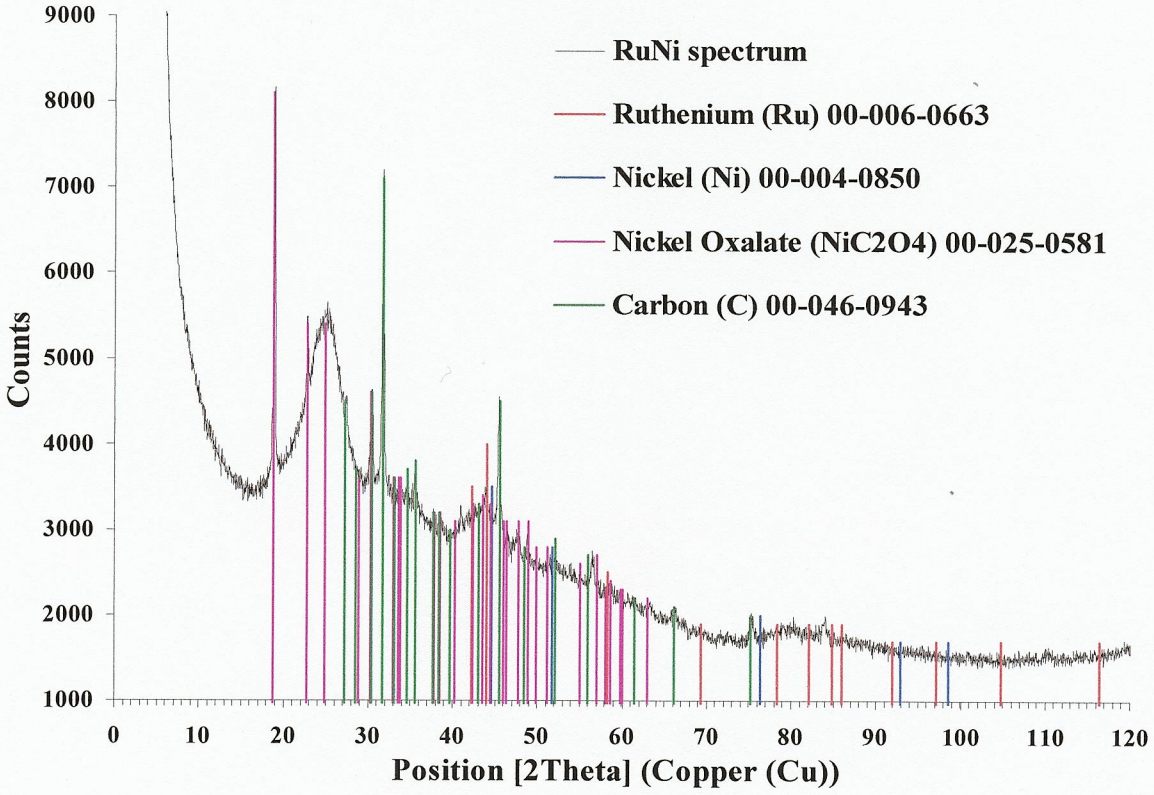

Figure 6.13. XRD data analysis of the $Ru_{72}Ni_{28}/C$ catalyst.

Such data have not been reported previously in the literature; hence, comparison was made to data on Ru supported on carbon [25, 26]. An obvious omission from fig. 6.13 are any reflections due to Ru, which are expected at [25, 26]: 38.39°, 42.28°, 43.84°, 58.04° and 69.07°. However, the presence of Ru was confirmed by EDX (see fig. 6.7), and hence the Ru must be covered by Ni (or carbon + nickel), as was observed by Deng and co-workers [13]. Surprisingly, fig. 6.13 show the presence of reflections due to nickel oxalate (at 2θ = 18.85°, 22.5°, 30.2° [27-29]), suggesting that ethylene glycol employed in the synthesis of these nanoparticles, is being reduced. Luna et al. [10] also describe this as organic impurities adsorbed from the reaction media, in the manufacture of CoNi nanoparticles.

Using Scherrer's equation (6.1), and the nickel oxalate peak at 18.85°, gives a particle size of 44.5 nm (see table 6.2), again significantly larger than the 2.4 nm determined from the TEM data, but not different of those found by Jung et al. [28] (20 - 50 nm for Ni oxalate).

Peak identification	2θ angle	B_θ (integral breadth) /rad	d /Å
Nickel (oxalate)	18.85	3.159×10^{-3}	444.7

Table 6.2. Average particle size calculated using Scherrer's equation from the 2θ = 18.85° diffraction in figure 6.13.

Figure 6.14 shows XRD data for the $Pd_{40}Ni_{60}$/C catalyst, this time there are no reflections attributable to Ni, in agreement with the EDX (fig. 6.8) and suggesting Ni core/Pd shell particles [17, 30].

Table 6.3 shows the crystallite size calculated from the main reflections for Pd at [29] 40.5°, 46.8°, 68.4°, giving values between 9.2 nm and 12.1 nm; these are comparable to the 16 nm observed by Yu and co-workers [31], but somewhat larger than the 4-6 nm observed by Sun et al. [14], Zhao et al. [5] and Scott and Maiyalagan. [15].

Peak identification	2θ angle	B_θ (integral breadth) /rad	d /Å
Palladium	40.5	12.217×10^{-3}	120.7
Palladium	46.8	16.406×10^{-3}	91.96
Palladium	68.4	16.930×10^{-3}	98.81

Table 6.3. Average particle size calculated using Scherrer's equation for the Pd diffraction lines in figure 6.14.

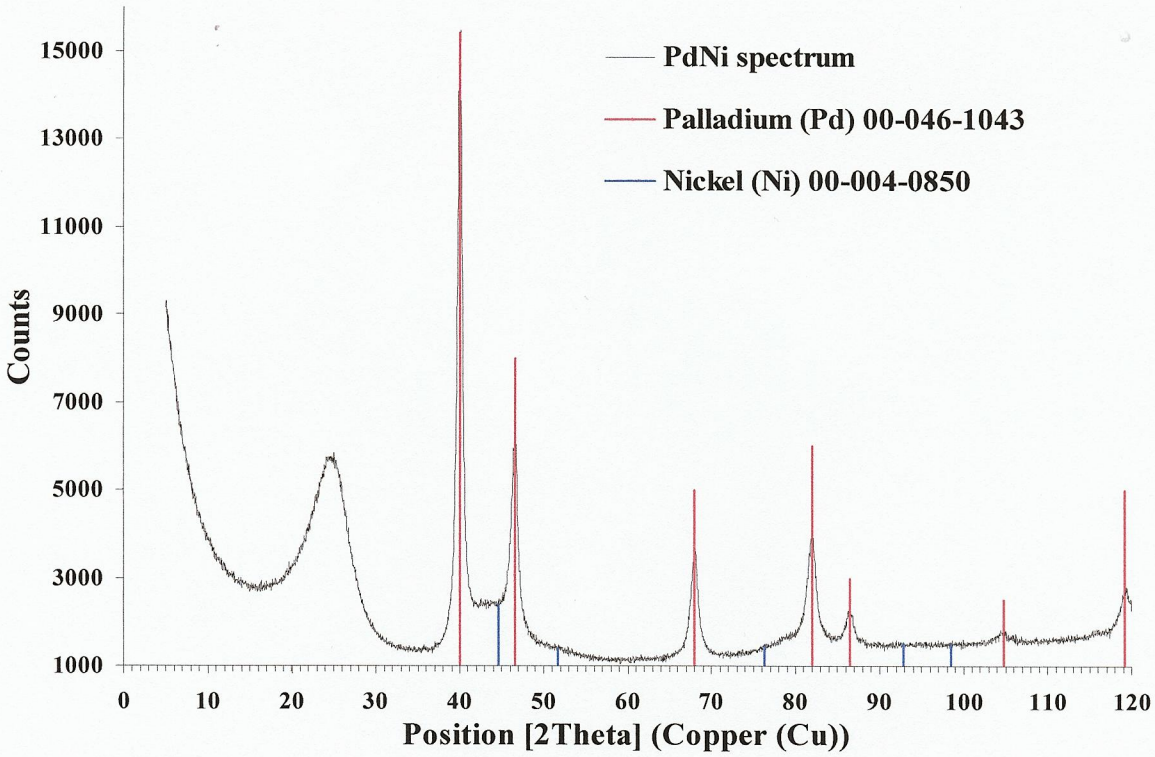

Figure 6.14. XRD data analysis for $Pd_{40}Ni_{60}$ catalyst.

6.3. Electrochemical evaluation of the nanoparticle catalysts

6.3.1. $Co_{50}Ni_{50}$ catalyst:

Figure 6.15(a) shows a cyclic voltammogram collected using carbon paper strips (Toray TGPH-060 not Teflon treated) coated with (1 cm^2 area) $Co_{50}Ni_{50}$ /C catalyst, using Nafion Ionomer-to-Carbon ratio (I/C) of 0.3 (or 24 wt. % dry mass), with a load of 0.8 mg metal cm^{-2}; and figure 6.15(b) shows the same voltammogram with an expanded y-axis to highlight the smaller peaks. More details about catalyst synthesis, ink preparation and the experimental set-up are given in sections 2.3, 2.4 and 2.5, respectively.

As this catalyst has not been studied before, the assignments of the various anodic and cathodic waves were based on literature work on the two individual metals. Dealing with the anodic peaks first (see fig 6.15(b)), the feature Co^{I}_{a} at -0.369 V vs. MMO was assigned by Behl and Toni [32] (and references therein) to the couple CoO/Co_3O_4:

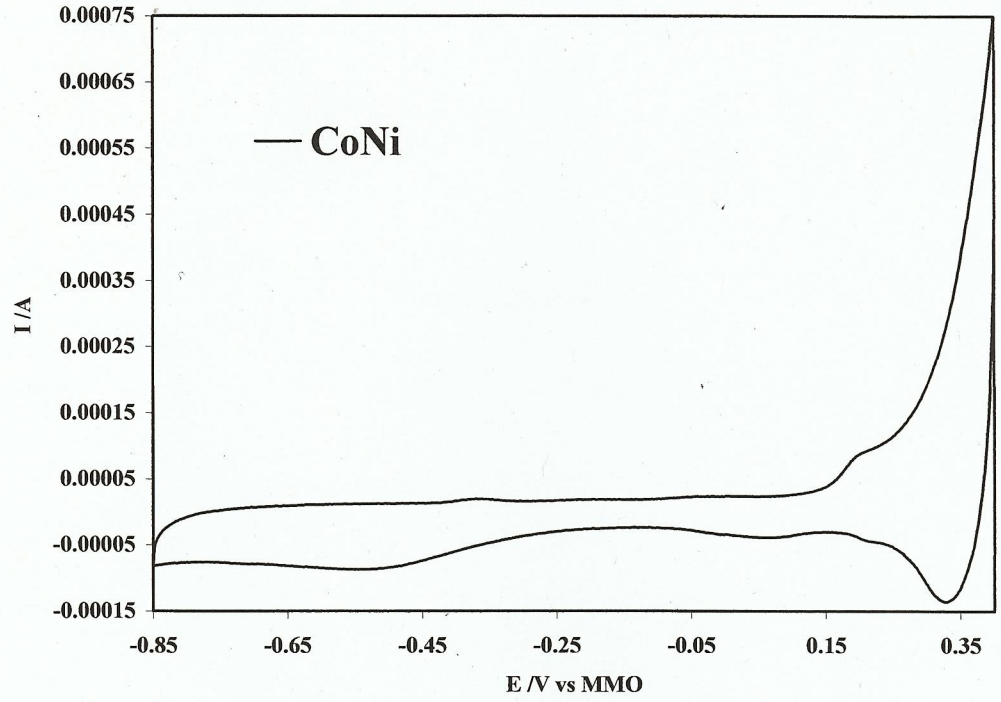

(a)

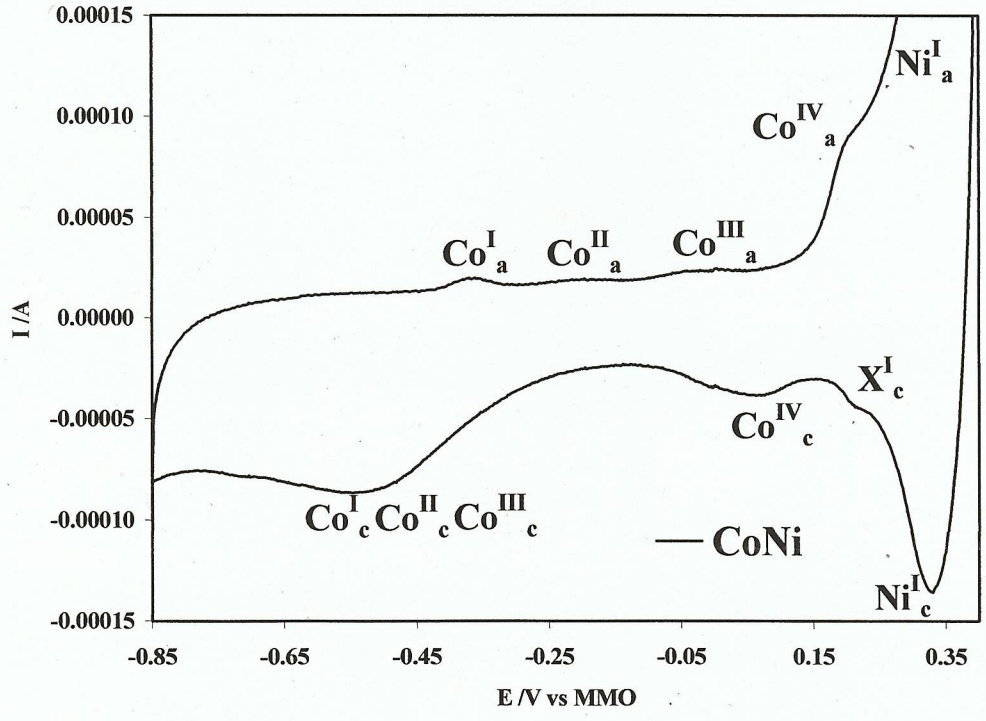

(b)

Figure 6.15. (a) Cyclic voltammogram obtained using a 1 cm^2 carbon paper electrode coated with 0.8 mg $Co_{50}Ni_{50}$ cm^{-2} dispersed on XC72 carbon + Nafion ionomer (24 wt.% dry mass) immersed in N_2-saturated 1 M KOH, scan rate 1 mV s^{-1}. (b) The scan in (a) with expanded y-axis.

$$3CoO+2OH^- \rightarrow Co_3O_4 + H_2O + 2e^- \quad (6.3)$$

The wave Co^{II}_a at -0.200 V has been assigned [32, 33] to the oxidation of hydrated cobalt oxide:

$$3Co(OH)_2 + 2OH^- \rightarrow Co_3O_4 + 4H_2O + 2e^- \quad (6.4)$$

Behl and Toni [32], Gomez Meier et al. [34, 35] and Vitanov et al. [36], attribute a "small hump" near -0.05 V (Co^{III}_a) to an additional process involving the oxidation of hydrated CoO:

$$Co(OH)_2 + OH^- \rightarrow CoOOH + H_2O + e^- \quad 6.5)$$

At the anodic limit of the voltammogram there is a very complex system of redox couples overlapping each other, and there could be a large number of possible explanations for this behaviour. However, this is beyond the scope of this work.

Several authors [32-36] attribute a peak near +0.220 V (Co^{IV}_a) to the oxidation of Co_3O_4 produced via reaction (6.6):

$$Co_3O_4 + OH^- + H_2O \rightarrow 3CoOOH + e^- \quad (6.6)$$

However, this potential region is dominated by the broad feature Ni^{I}_a, having a maximum potential near ca. +0.35 V, which has been assigned tentatively [37, 38] to the transition α-$Ni(OH)_2$ to γ-NiOOH (reaction 6.7). The formation of β-NiOOH has been discarded by Barnard et al. [39, 40] as this only occurs significantly at potentials > +0.5 V vs. MMO.

$$\alpha\text{-}Ni(OH)_2 + OH^- \rightarrow \gamma\text{-}NiOOH + e^- + H_2O \quad (6.7)$$

According to the model proposed by Behl and Toni [32], there is an additional process that is thermodynamically possible at +0.246 V:

$$Co(OH)_2 + 2OH^- \rightarrow CoO_2 + 2H_2O + 2e^- \quad (6.8)$$

However, if it is present, it is hidden by Ni^I_a.

The interpretation of the cathodic features in figs. 6.15(a) and (b) is complicated by the complex mix of oxides generated during the positive going scan of the cyclic voltammogram, and the processes taking place are not yet well understood [10, 20]. Oliva et al. [41] attribute a wave at +0.324 V vs. MMO (Ni^I_c) to the reduction of the couple α-$Ni(OH)_2$/γ-NiOOH (reaction 6.7); however, they found this potential changes in time with every CV cycle, due to the formation of the more thermodynamically stable (β-phase (ca. +0.5 V vs. MMO).

Another reduction wave ($X^I c$) may be seen at +0.21 V, and there is no consensus in literature on what it might be; however, Behl and Toni [32] suggest the following reduction reaction at +0.195 V vs. MMO.

$$CoO_2 + H_2O + 2e^- \rightarrow CoO + 2OH^- \quad (6.9)$$

This theory is based in the fact of the presence of Co(IV) oxide, and as previously said, if such oxides are present, they are hidden by Ni^I_a.

Peaks Co^{IV}_c and Co^I_c, Co^{II}_c, Co^{III}_c, have been assigned by Casella and Gatta [33]: Co^{IV}_c was attributed to the reduction of CoOOH produced *via* reaction (6.6), and the broad wave with a peak near -0.52 V to the reduction of Co_3O_4 and CoOOH produced by reactions (6.3) to (6.5). Previous XPS studies by the same group show the presence of various Co(III) oxides simultaneously, however, the cathodic peaks of these processes are too close to be able to discriminate them [42].

Figures 6.16 (a) and (b) show cyclic voltammograms using the $Co_{50}Ni_{50}$ catalyst in the presence of methanol and ethanol. Methanol did not affect the cobalt anodic waves significantly, showing that the organic had essentially no impact on formation of these oxides. The current at the anodic limit was 1.14 mA, compared to 0.70 mA in the absence of methanol. It is clear that oxidation of methanol is taking place in the potential region where γ-NiOOH is being formed.

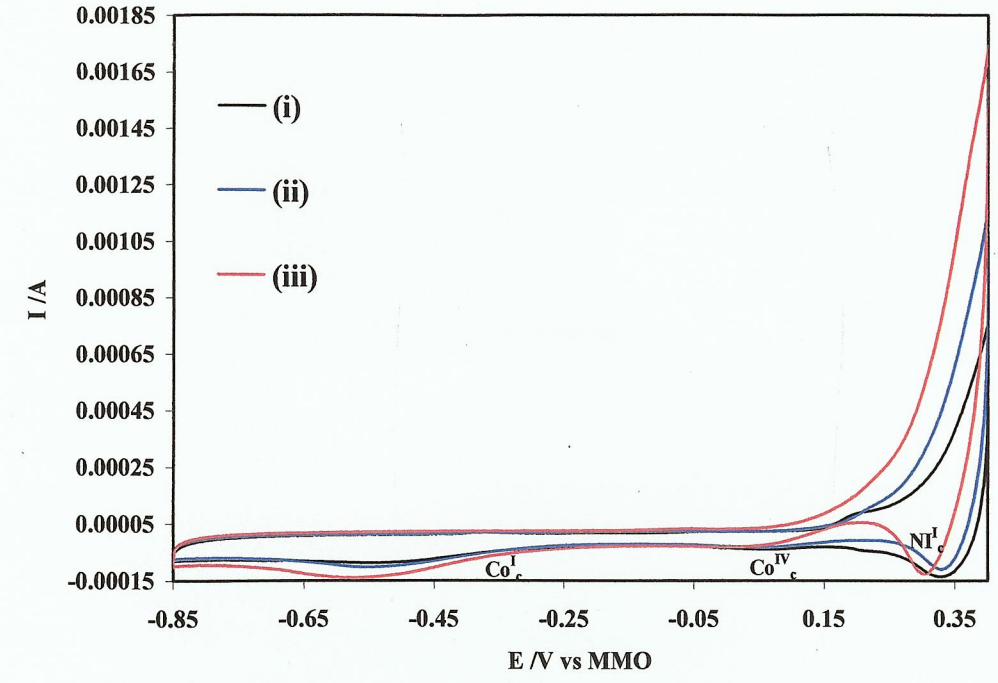

(a)

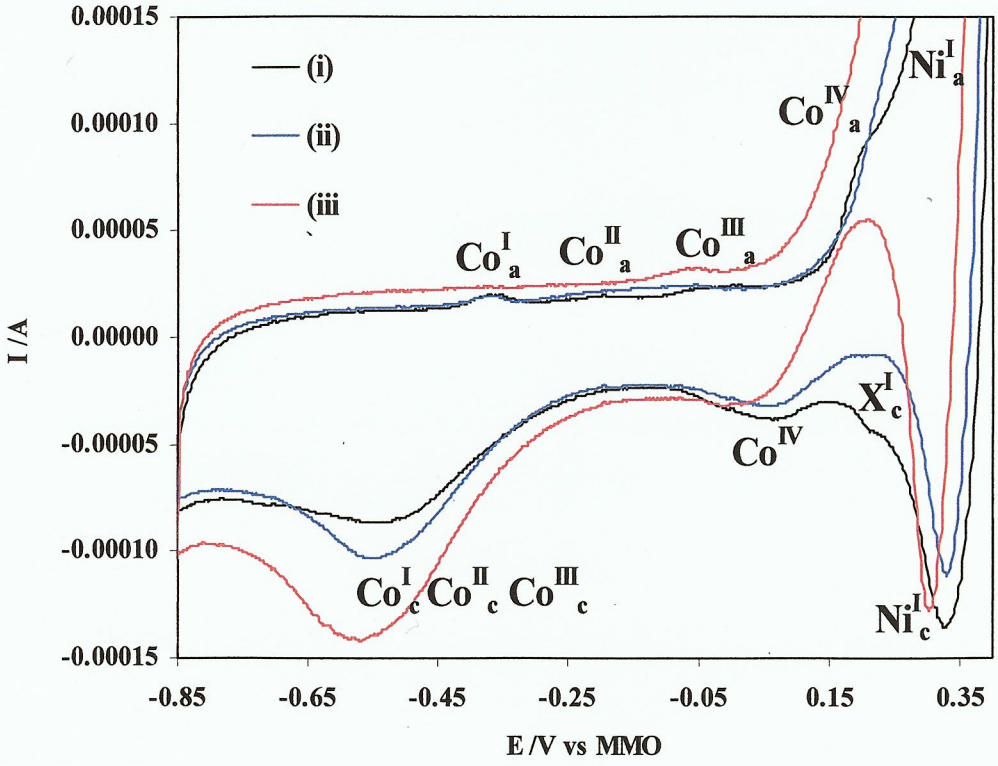

(b)

Figure 6.16. (a) Cyclic voltammogram obtained using $Co_{50}Ni_{50}$ as per fig. 6.15 in N_2-saturated: (i) 1 M KOH, (ii) 1 M KOH + 1 M methanol and (iii) 1 M KOH + 1 M ethanol. (b) The scan in (a) with expanded y-axis.

Golikand et al. [43] also reported this current enhancement, when organic residues adsorb on Ni anodes, and Jafarian et al. [44] have found methanol oxidation on Co at potential where the formation of CoOOH would be expected.

Methanol oxidation at Ni in alkaline solution has been extensively studied [38, 43, 45, 46]; however, the role of Co in methanol oxidation under the same conditions remains still largely unknown [44].

Jafarian et al. [44] have proposed the following simple steps for methanol oxidation:

$$Co(IV) + CH_3OH \rightarrow \text{intermediates} + Co(III) \quad (6.10)$$

$$Co(IV) + \text{intermediates} \rightarrow \text{products} + Co(III) \quad (6.11)$$

The main product of the reaction was identified by Jafarian et al. as formate. This simplified mechanism requires the presence of highly oxidised states of cobalt (reaction (6.8)), only possible at potentials over +0.246 V; this may explain why X^I_c at +0.21 V is suppressed in the CV in the presence of alcohol, because once formed, the active oxide (CoO_2) becomes the site for adsorption of both methanol and ethanol.

In the case of ethanol, as may be seen from fig. 6.16(b), there is a clear oxidation process taking place with an onset near 0 V vs. MMO. The Ni^I_c wave is also distorted by a small auto-oxidation peak due to ethanol oxidation at the Ni surface formed when NiOOH is stripped.

Fleischmann and co-workers [45, 47] and Kim and Park [48, 49] proposed the following simple ethanol oxidation mechanism at nickel:

$$Ni(OH)_2 + OH^- \rightarrow NiOOH + H_2O + e^- \quad (6.12)$$

$$NiOOH + CH_3CH_2OH \rightarrow \text{Intermediate 1} + Ni(OH)_2 \quad (6.13)$$

$$NiOOH + \text{Intermediate 1} \rightarrow CH_3CHO + Ni(OH)_2 \quad (6.14)$$

$$NiOOH + CH_3CHO \rightarrow \text{Intermediate 2} + Ni(OH)_2 \quad (6.15)$$

$$NiOOH + \text{Intermediate 2} \rightarrow CH_3COOH + Ni(OH)_2 \quad (6.16)$$

These steps were believed to occur at the anodic limit (ca. +0.400 V vs. MMO) which is in agreement with figs. 6.16(a) and (b).

There is no reported data on ethanol oxidation at Co; however, the lower onset potential for ethanol oxidation, in the region where Co(III) oxides are formed, is in agreement with the work of Jafarian and colleagues [44].

Cathodic waves are extremely difficult to explain due to the combination of not only many different oxides, but adsorbed products and intermediates formed during oxidation. What can be clearly observed is the suppression of X^I_c, which is probably due to the formation of adsorbed species [32].

In any operating alkaline fuel cell, the anodic potential is likely to be in the range between -0.65 V and 0 V vs. MMO [50-52]; clearly, this is not possible using the $Co_{50}Ni_{50}$ catalyst. Hence, work using this material was discontinued.

6.3.2. $Ru_{72}Ni_{28}$ catalyst:

Figure 6.17(a) and (b) show a typical cyclic voltammogram obtained using the $Ru_{72}Ni_{28}$ catalyst in 1 M KOH. Broad waves are characteristic of catalysts containing Ru [53]; the shapes of which depend mainly on pH and anodic potential limit of the voltammogram [53-55].

It should be noted that the activity of the catalyst will depend mostly on the nickel shell (rather than the Ru core), but because Ru precursor was used in large excess, it is almost certain that nickel-less Ru nanoparticles have been formed.

The first wave Ru^I_a at -0.340 V has been assigned by Burke and Whelan [53] to the oxidation of Ru(III) to Ru(IV).

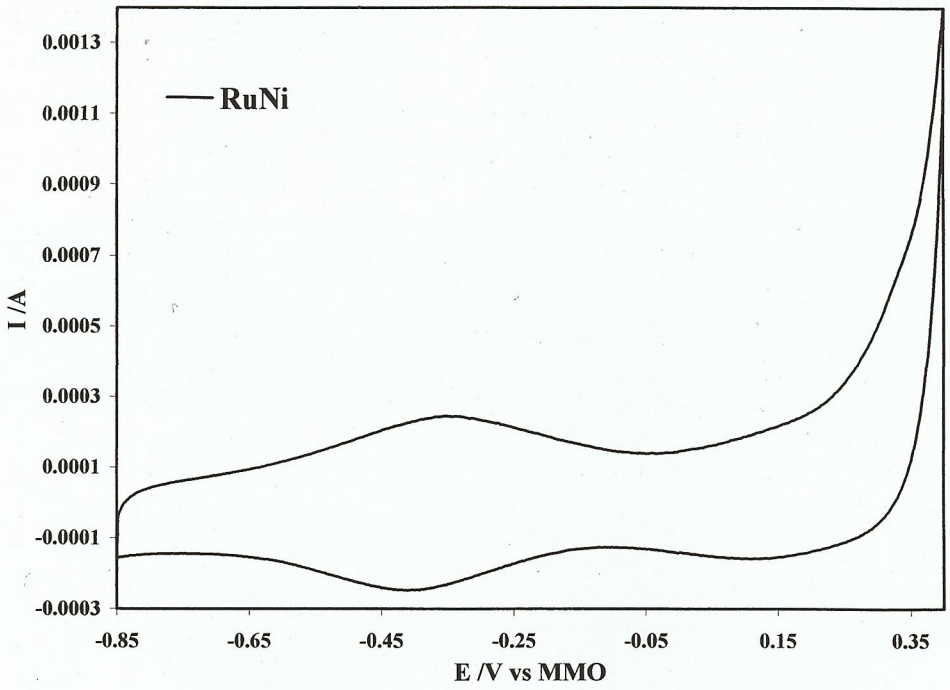

(a)

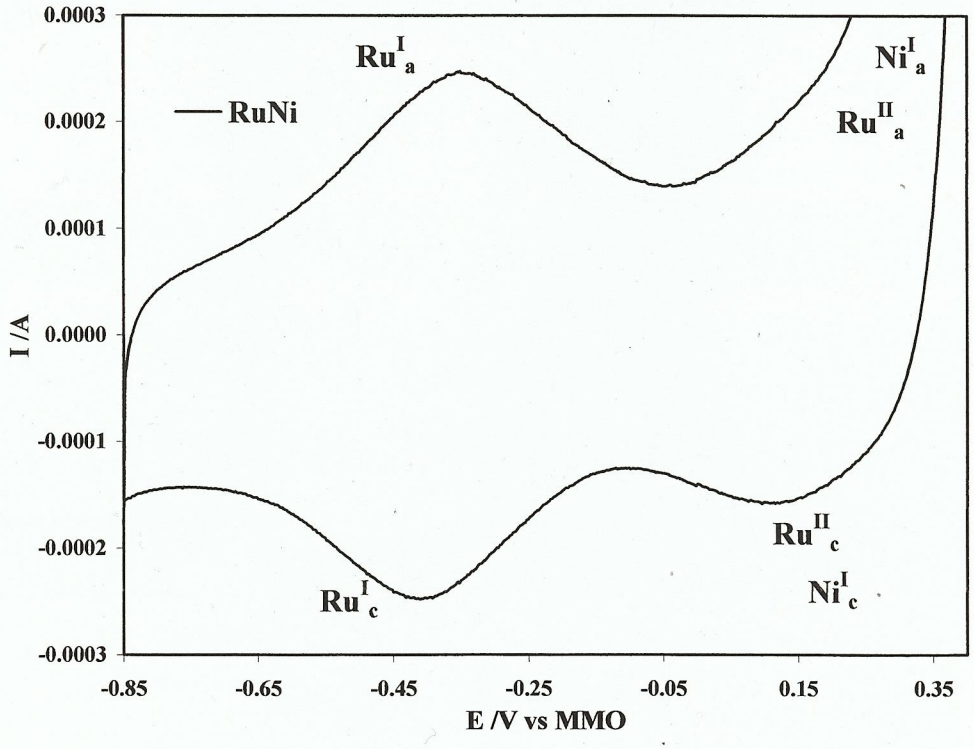

(b)

Figure 6.17. (a) Cyclic voltammogram obtained using a 1 cm^2 carbon paper electrode coated with 0.8 mg $Ru_{72}Ni_{28}$ cm^{-2} dispersed on XC72 carbon + Nafion ionomer (24 wt.% dry mass) immersed in N_2-saturated 1 M KOH, scan rate 1 mV s^{-1}. (b) The scan in (a) with expanded y-axis.

$$Ru_2O_3 + 2OH^- \rightarrow 2RuO_2 + H_2O + 2e^- \quad (6.17)$$

But because of their instability in alkaline media, hydration of the RuO_2 occurs spontaneously:

$$RuO_2 + 2OH^- + 2H_2O \rightarrow Ru(OH)_6^{2-} \quad (6.18)$$

Further oxidation occurs at higher potentials (ca. +0.150 V vs. MMO), i.e. Ru^{II}_a [53]:

$$Ru(OH)_6^{2-} + 2OH^- \rightarrow RuO_4^{2-} + 4H_2O + 2e^- \quad (6.19)$$

Again, however, this process can only be postulated due to the presence of N^I_a.

A third oxidation wave from Ru(IV) to Ru(VII), is predicted to occur near ca. +0.400 V vs. MMO [53]:

$$RuO_4^{2-} \rightarrow RuO_4^- + e^- \quad (6.20)$$

And this potential region is also obscured by Ni^I_a.

When using Ni electrodes it is generally accepted that the cathodic peak N^I_c corresponding to N^I_a is expected around +0.320 V to +0.35 V vs. MMO [37, 41, 46, 49, 56]; however, this does not appear to be the case with the $Ru_{72}Ni_{28}$ catalyst. One possible explanation for this absence is that the formation of nickel oxalate during synthesis (see section 6.2.4) can stabilise the β-phase of NiOOH, which normally is the result of aging of the electrodes, shifting the reduction wave for nickel toward more cathodic potentials, i.e. +0.12 V to +0.15 V. It does not seem unreasonable also to postulate that, if R^{II}_a is present under Ni^I_a, the corresponding cathodic peak Ru^{II}_c is that near +0.15 V.

Methanol and ethanol have definite effects on the electrochemical behaviour of $Ru_{72}Ni_{28}$ catalyst, as can be seen from figs. 6.18(a) and (b); the decreasing current on the Ru waves (anodic and cathodic) for both alcohols is accompanied by significant increases in the irreversible oxidation currents at potentials > 0 V vs. MMO.

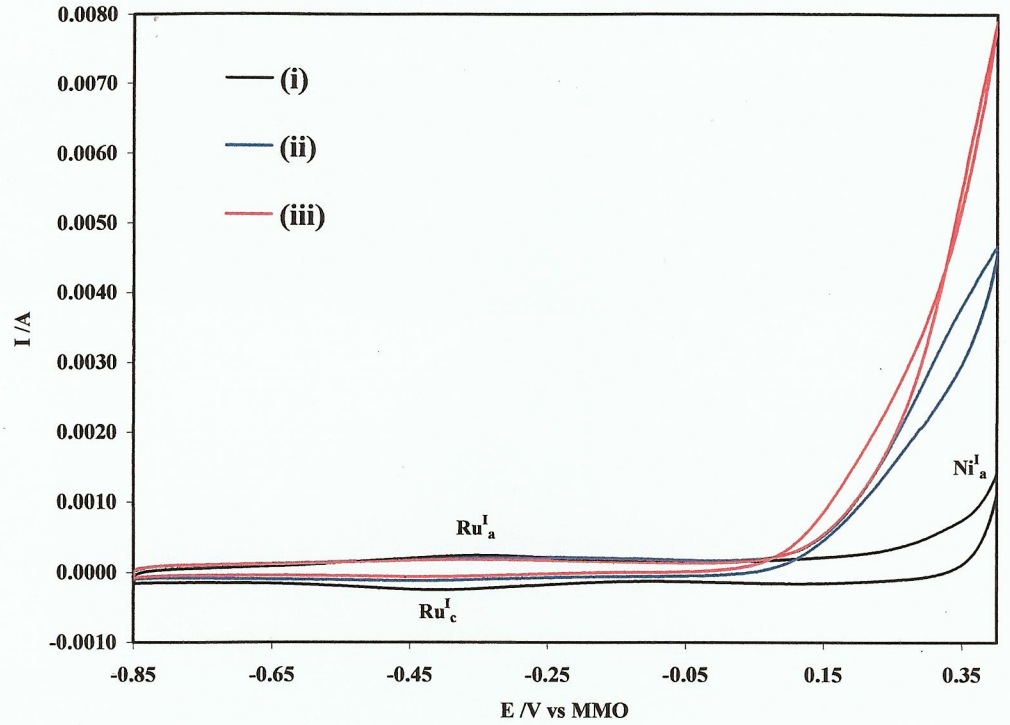

(a)

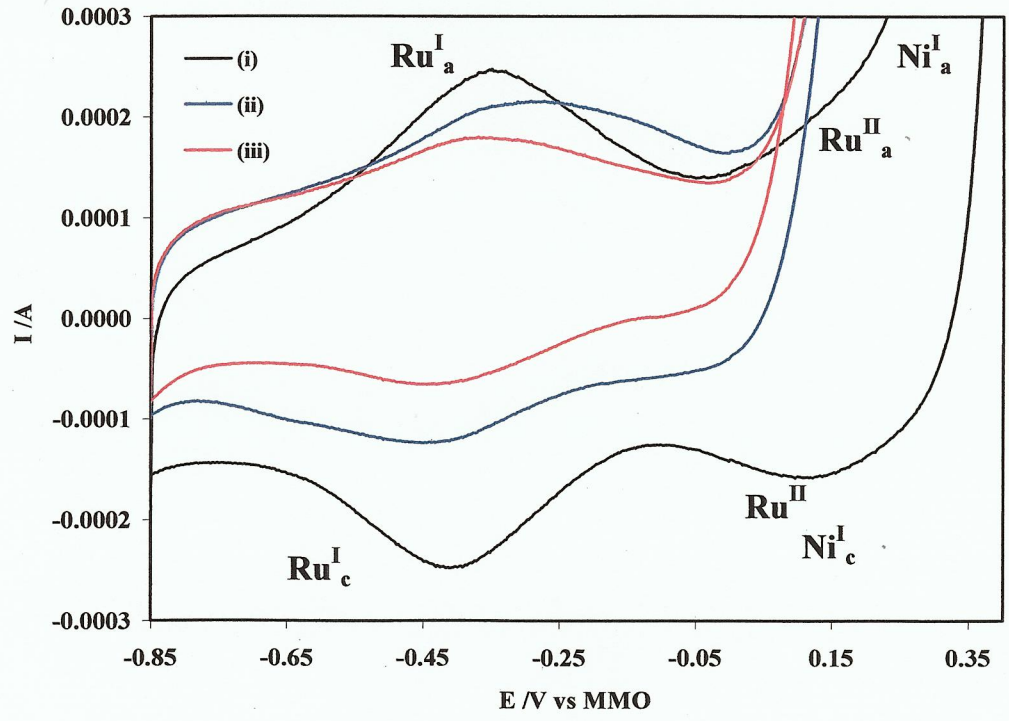

(b)

Figure 6.18. (a) Cyclic voltammogram obtained using $Ru_{72}Ni_{28}$ as per fig. 6.17 in N_2-saturated: (i) 1 M KOH, (ii) 1 M KOH + 1 M methanol and (iii) 1 M KOH + 1 M ethanol. (b) The scan in (a) with expanded y-axis.

In the presence of both alcohols, the Ru waves were suppressed, and the onset of the oxidation of both alcohols was ca. 0 V vs. MMO. In addition, in the presence of ethanol, the irreversible current showed crossover points at +0.06 V and +0.32 V vs. MMO suggesting, perhaps, enhancement in the oxidation due to the presence of RuO_4^{2-} and/or NiOOH.

Shieh and Hwang [57] propose a mechanism for ethanol oxidation on ruthenium oxides in alkaline media as follows:

$$RuO_4^{2-} \rightarrow RuO_4^{-} + e^{-} \quad (6.21)$$

$$RuO_4^{-} + CH_3CH_2OH + OH^{-} \rightarrow RuO_4^{2-}CH3C^{\bullet}HOH + H_2O \quad (6.22)$$

$$RuO_4^{2-}CH_3C^{\bullet}HOH + RuO_4^{-} + OH^{-} \rightarrow CH_3CHO + 2RuO_4^{-} + H_2O \quad (6.23)$$

This mechanism can be considered as comparable to the mechanism proposed by Fleischmann and co-workers [45, 47] and Kim and Park [48, 49] for ethanol oxidation on nickel as in reactions (6.12) to (6.16)

Whilst Shieh and Hwang predict the main product of ethanol oxidation on ruthenium is acetaldehyde, Fleischmann et al., and Kim & Park postulated a further oxidation step leading to acetic acid (acetate in alkaline media).

The mechanism of Shieh and Hwang [57] is predicated on the formation of RuO_4^{-}; however, the onset potential for ethanol oxidation in figs. 6.18(a) & (b) is much lower than the potential for RuO_4^{-} formation. It appears that the oxidation of ethanol is associated with the formation of RuO_4^{2-} i.e. Ru^{II}_a. Shieh and Hwang have reported that acetaldehyde is the main product of ethanol oxidation at Ru in alkaline solution, and that acetaldehyde undergoes the aldol condensation reaction according to:

$$CH_3CHO + CH_3CHO \rightarrow CH_3CHOHCH_2CHO \quad (6.24)$$

Again, the activity of this catalyst is outside the operating potential range of a viable direct alcohol alkaline fuel cell, and hence work on it was discontinued.

6.3.3. $Pd_{40}Ni_{60}$ catalyst:

Figure 6.19 shows a cyclic voltammogram collected using the $Pd_{40}Ni_{60}$ catalyst in 1 M KOH; there appears to be no features due to Ni as expected from section 6.2.4. Palladium electrodes have been studied extensively, and Pd^{I}_{a} has been attributed to the oxidation of absorbed (and adsorbed) hydrogen [58-63]:

$$Pd\text{-}H_{abs/ads} + OH^{-} \rightarrow Pd + H_2O + e^{-} \quad (6.25)$$

followed by the adsorption of OH^{-} (Pd^{II}_{a}) [61, 62, 64, 65]:

$$Pd + OH\text{-} \rightarrow Pd\text{-}OH_{ads} + e^{-} \quad (6.26)$$

which partially overlaps the hydrogen desorption peak.

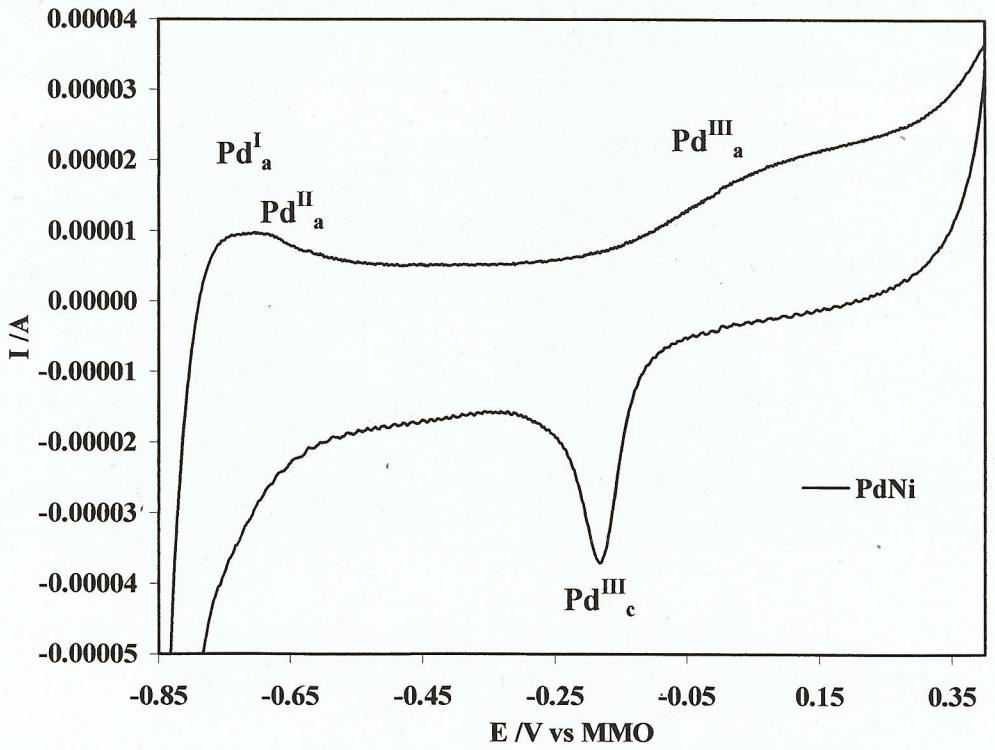

Figure 6.19. Cyclic voltammogram obtained using a 1 cm^2 carbon paper electrode coated with 0.8 mg $Pd_{40}Ni_{60}$ cm^{-2} dispersed on XC72 carbon+ Nafion ionomer (24 wt.% dry mass) immersed in N_2-saturated 1 M KOH, scan rate 1 mV s^{-1}.

Pd^{III}_a, with an onset at -0.20 V vs. MMO, was attributed to the formation of Pd(II) oxides [59-62, 64-66], and although the mechanism for this oxidation process remains unclear [63], it is generally accepted to be:

$$Pd\text{-}OH_{ads} + OH^- \rightarrow PdO + H_2O + e^- \quad (6.27)$$

$$Pd\text{-}OH_{ads} + Pd\text{-}OH_{ads} \rightarrow Pd + PdO + H_2O \quad (6.28)$$

In the cathodic sweep, peak Pd^{III}_c at -0.190 V vs. MMO has been attributed to the reduction of Pd(II) oxides [61, 62, 65].

$$PdO + H_2O + 2e^- \rightarrow Pd + 2OH^- \quad (6.29)$$

It is worthy starting, that an alternative to reaction (6.27 - 6.28) was proposed by Burke and Casey [63], involving the formation of Pd(IV):

$$Pd + 6OH^- \rightarrow [Pd(OH)_6]^{2-} + 4e^- \quad (6.30)$$

Figures 6.20(a) and (b) show cyclic voltammograms of the $Pd_{40}Ni_{60}$ anode immersed in 1 M KOH with 1 M methanol and 1 M ethanol. Again, we must turn to the literature on the components metals, in this case Pd, to gain an understanding of the electrochemistry taking place. Thus, the oxidation of methanol at Pd under alkaline conditions has been studied by Takamura and Minamiyama [58], Enyo and colleagues [67-70], and Prabhuram et al. [59]:

$$2Pd + CH_3OH \rightarrow Pd(CH_3O)_{ads} + PdH \quad (6.31)$$

$$Pd(CH_3O)_{ads} + PdOH \rightarrow Pd_2(CH_2O)_{ads} + H_2O \quad (6.32)$$

$$Pd_2(CH_2O)_{ads} + PdOH \rightarrow Pd_3(CHO)_{ads} + H_2O \quad (6.33)$$

$$Pd_3(CHO)_{ads} + PdOH \rightarrow Pd_2(CO)_{ads} + 2Pd + H_2O \quad (6.34)$$

$$Pd_2(CO)_{ads} + PdOH \rightarrow PdCOOH + 2Pd \quad (6.35)$$

$$PdCOOH + OH^- \rightarrow Pd + CO_2 + H_2O + e^- \quad (6.36)$$

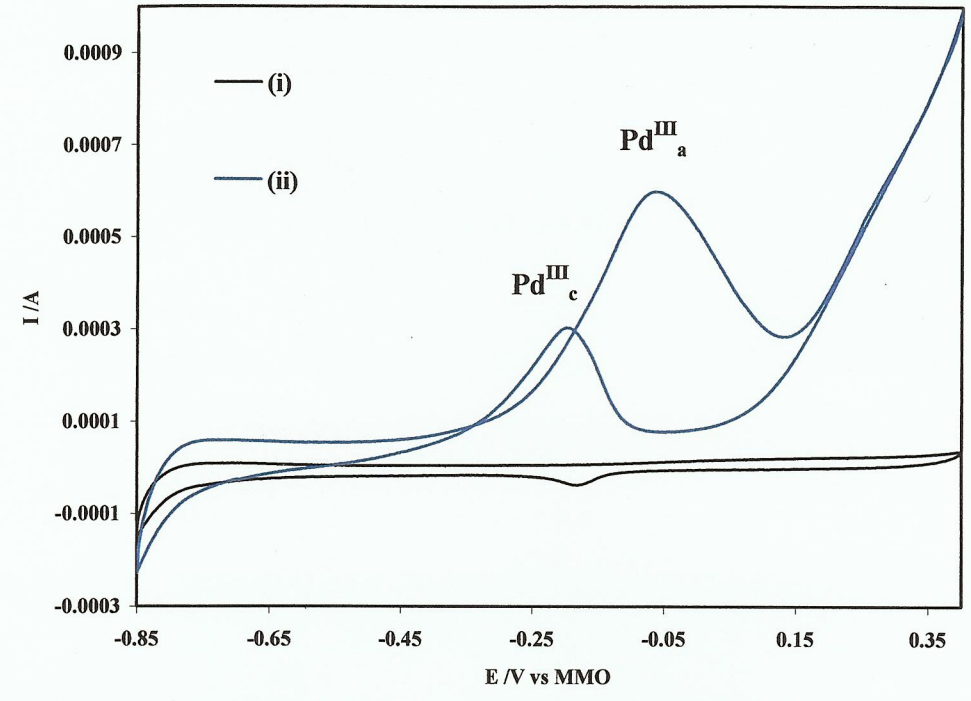

(a)

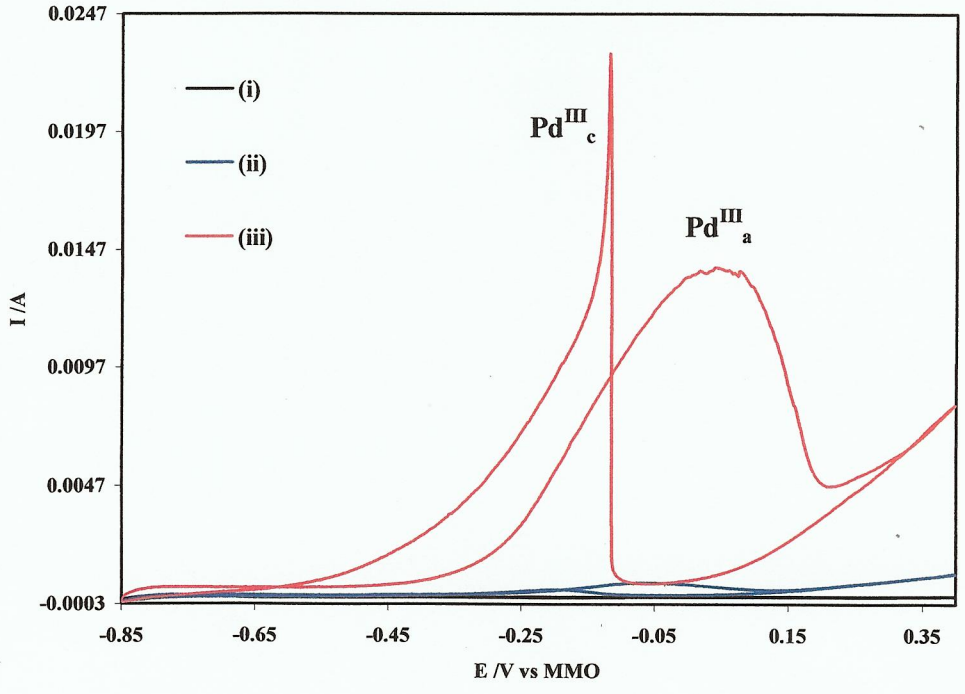

(b)

Figure 6.20. (a) Cyclic voltammogram obtained using $Pd_{40}Ni_{60}$ catalyst as per fig. 6.19 in N_2-saturated: (i) 1 M KOH, (ii) 1 M KOH + 1 M methanol and (b) the scan in (a) with expanded y-axis including (iii) 1 M KOH + 1 Methanol.

The proposed mechanism indicates the main oxidation reaction requires a number of palladium neighbouring sites (i.e. two for formaldehyde, and three to give CO_{ads}) in the case of CO_{ads}, IR spectroscopic studies by Enyo et al. [69] showed the CO present as bridge bonded (i.e. not linearly bonded) this species acting like a powerful poison.

In fig. 6.20(a), the wave Pd^{III}_{a} at -0.06 V vs. MMO coincides with the formation of active palladium oxides, leading to a relatively fast succession of reactions (i.e. equations (6.31) to (6.34)). Reactions (6.35) and (6.36) are significantly slower, due to the inhibition by strongly adsorbed CO, i.e. $Pd_2(CO)_{ads}$ [59, 69]. $Pd_2(CO)_{ads}$ is not oxidised until potentials > 0.14 V vs. MMO. On the reverse scan, oxidation of the CO_{ads} stops until the oxide layer is stripped at potentials < -0.11 V vs. MMO, at which point the adsorbate is oxidised, giving rise to the auto-oxidation peak [59, 69].

Because of the poisoning effect of methanol [59, 69], palladium based catalyst are more usually studied with respect to ethanol electro-oxidation. Zhao et al. [62] proposed the following mechanism:

$$Pd + CH_3CH_2OH \rightarrow Pd\text{-}(CH_3CH_2OH)_{ads} \qquad (6.37)$$

$$Pd\text{-}(CH_3CH_2OH)_{ads} + 3OH^- \rightarrow Pd\text{-}(CH_3CO)_{ads} + 3H_2O + 3e^- \qquad (6.38)$$

Reactions (6.37) and (6.38) occurs at low potentials (e.g. -0.90 V to -0.60 V vs. MMO), and result in the surface being covered with strongly adsorbed ethoxide (CH_3CO_{ads}), which prevent adsorption of hydrogen and hence suppresses the hydrogen adsorption/desorption features. The OH^- species in the equation (6.38) may be actually adsorbed on the Pd (i.e. $Pd\text{-}OH_{ads}$) [62].

As in the previous case for methanol, the formation of Pd(II) oxides (i.e. Pd^{III}_{a} in fig 6.20(b)) with an onset potential near -0.40 V and maxima near 0.05 V vs. MMO trigger the ethanol oxidation reaction, with an anodic peak current ca. 20 times that observed in the presence of methanol.

Mechanistic studies by Zhou et al. [71] on palladium have shown that the main reaction product is acetate rather than acetaldehyde, and the postulated mechanism, along with reactions (6.37) and (6.38), is [62]:

$$Pd\text{-}(CH_3CO)_{ads} + Pd\text{-}OH_{ads} \rightarrow Pd\text{-}CH_3COOH + Pd \quad (6.39)$$

$$Pd\text{-}CH_3COOH + OH^- \rightarrow Pd + CH_3COO^- + H_2O \quad (6.40)$$

Which completes the reaction mechanism for palladium as it is known to date.

During the cathodic sweep, the same effect already explained in the case of methanol is valid, but because the poison $Pd(CH_3CO)_{ads}$ is much more easy to oxidize than $Pd(CO)_{ads}$, the resultant anodic peak (Pd^{III}_c) shows a higher current.

It may be concluded from this work is that the $Pd_{40}Ni_{60}$ system has proved to be an interesting and worthy to research catalyst for alcohol oxidation fuel cells, specifically DEFC. Thus it was decided to focus only on the use of $Pd_{40}Ni_{60}$ catalyst in the direct ethanol fuel cell.

6.4. Polymer electrolyte membrane alkaline fuel cell test.

The challenges facing the development of direct alcohol alkaline fuel cell were discussed in chapter 1 [72-75]. These challenges are yet to be overcome; the most pressing is the development of an alkaline anion exchange membrane (AAEM) [76, 77]. To this end, it was decided to try a potentially new AAEM under development by Dr. S Doherty and Prof. Christensen, arising from the former's work in another research field and based on the polymerization of a pyrrolidinium functionalised norbornene monomer [78-80] (see section 2.8), designated as SD1 in the discussion below.

For comparison, Nafion 117 (K^+ form [81]) was employed, as reported by Scott et al. [81-83] and Iwai and Yamanishi [84]. Ionomeric Nafion in alcohol was employed to bind the anode in order to provide anodic contact between catalyst particles and the Nafion 117 membrane [80]. Ionomers of the SD1 membrane in n-propanol were

employed as appropriate to the membrane [84, 85]. Ethanol and methanol were employed as fuels and 20 wt. % Pt/C (0.4 mg Pt cm^{-2}) as the cathode.

6.4.1. Evaluation of membranes for alkaline fuel cell applications.

Figures 6.21(a) and (b) show the results of conductivity tests as a function of temperature [86] carried out on the Nation 117 and SD1 membranes based on the DC methodology employed by the US Department of Energy (DOE) [87] (see section 2.9).

The Nafion was converted to its K^+ form following the procedure of Scott et al. [81]. As may be seen from fig. 6.21(a), the maximum in plane conductivity was ca. 0.037 S cm^{-1} at 55 °C and ca. 0.012 S cm^{-1} at 35 °C. These results do not agree with the 0.100 S cm^{-1} at 30 °C reported by Walsh and co-workers [88], but are compatible with Scott et al. [81, 89] who found the resistance of the cell much higher using Nafion K^+ form (0.47 Ω), compare to H^+ form (0.05 Ω). It can be seen in fig. 6.21(a) that at 55 °C the Nafion conductivity appears somewhat unstable; this has not been reported previously. In addition, following being tested several times at different temperatures, the Nafion membranes were found to lose mechanical properties.

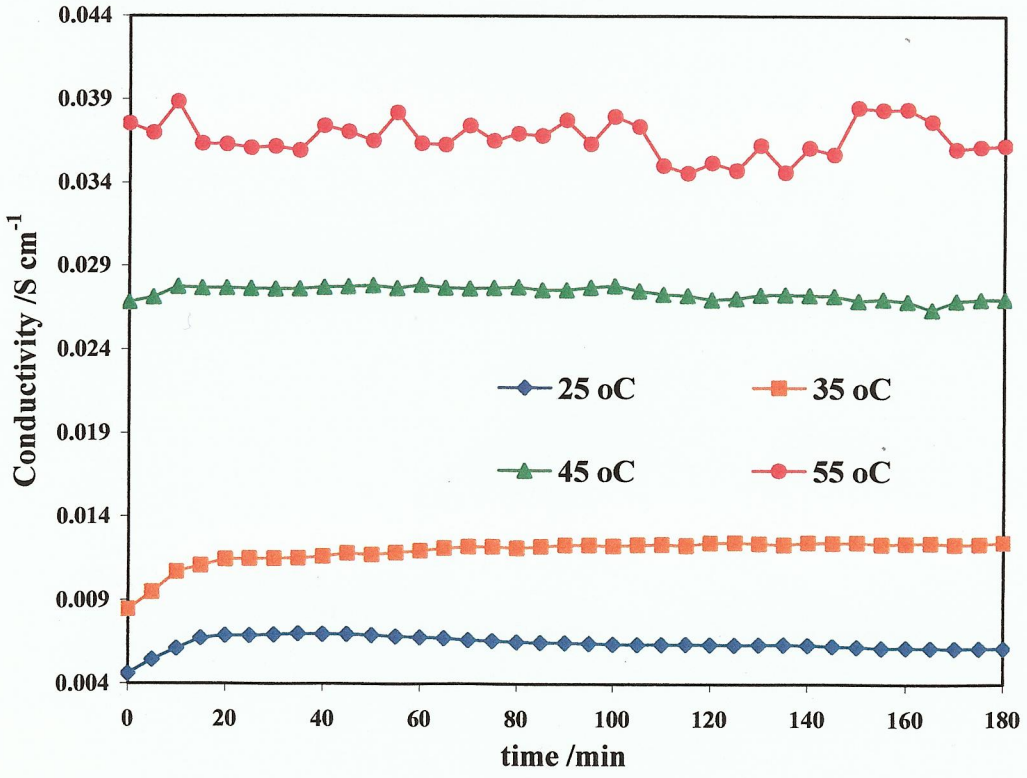

(a)

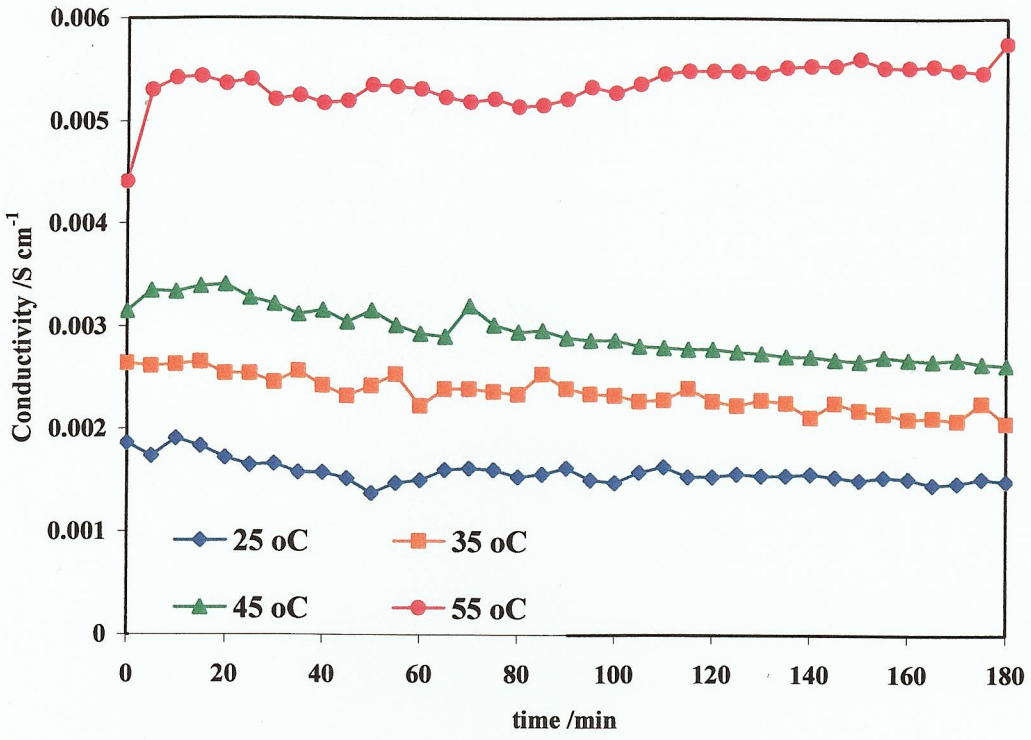

(b)

Figure 6.21. In-plane conductivity measurements as a function of time and temperature for (a) Nafion 117 (K^+ form) (b) SD1 membrane.

Figure 6.21(b) shows the analogous data for the SD1 membrane [78], conductivity at 55 °C is very low (ca. 0.0055 S cm^{-1}), compared to Nafion K^+ form (0.037 S cm^{-1}), and this will make a big difference in the cell performance.

6.4.2. Fuel cell test results.

Figures 6.22(a) and (b) show the result for single fuel cell tests using membrane electrode assemblies (MEA) employing Nafion 117 K^+ form and (a) methanol and (b) ethanol; the oxidant was oxygen from a compressed cylinder flowing at 150 cm^3 min^{-1} at 1.5 bar and 100% RH (at the exit of humidifier). In fig 6.22(a) 1 M methanol solution was flowing into the anode at 10 cm^3 min^{-1}, and in fig (b) 1 M ethanol at the same flow rate.

As can be seen in figure 6.22(a), using methanol as fuel the open circuit voltage was nearly 0.60 V, lower than the 0.80 V reported by Scott et al. [81], and indicative of poorer kinetics. The maximum power density attained was 3.75 mW cm^{-2} (cell voltage 0.365 V), at 45 °C and not 55 °C as would be predicted from the conductivity

measurements above, which may be due to the degradation of the membrane at higher temperature.

Figure 6.22(a) includes the cell voltage vs. current density plot obtained by Scott and co-workers [81]) at 60 °C. As may be seen, the performance obtained using our system is comparable to that of Scott et al. at least at current densities > 15 mA cm^{-2}. It should be noted that the cathode and anode loadings employed by Scott and co-workers were 2 mg Pt cm^{-2} in each electrode, i.e. 4 times those employed by us, the fuel was 2 M methanol and 1 M NaOH was added to the methanol feed to enhance the conductivity; however, Scott et al. used air (rather than oxygen) as the oxidant.

Figure 6.22(b) shows the result for a fuel cell under identical conditions to those in fig. 6.22(a) except using ethanol as fuel. As may be seen from the figure, whilst the maximum open circuit voltage obtained was 0.60 V, as was the case with the overall performance is significantly poorer, with a maximum power density (at 45 °C) of 0.9 mW cm^{-2}.

There is a far more rapid drop in the activation overpotential region of the plots, due to the poorer kinetics of ethanol oxidation [90-92]; however, the very rapid nature of the decrease in cell voltages at low current densities suggest that these are significant problems with the system [74, 93, 94]. Some workers have reported comparable performance when using ethanol as fuel to that observed when using methanol, but these data are obtained at high temperatures, and with NaOH and KOH added to the fuel [94, 95].

Wang and co-workers [92] have postulated that whilst direct alcohol oxidation is kinetically favoured in alkaline conditions, it is thermodynamically disfavoured due to the possible pH gradient between anode and cathode; however, Sun and colleagues [94] have postulated that operating at elevated temperatures should ameliorate this problem. In contrast to AAEM's employing, for example, $-NR_3^+$ head groups, the application of K^+ exchanged Nafion as the membrane introduces specific problems associated with the precipitation of K_2CO_3 [81, 83, 88], However, additional problems arise when using ethanol, rather than methanol, as fuel.

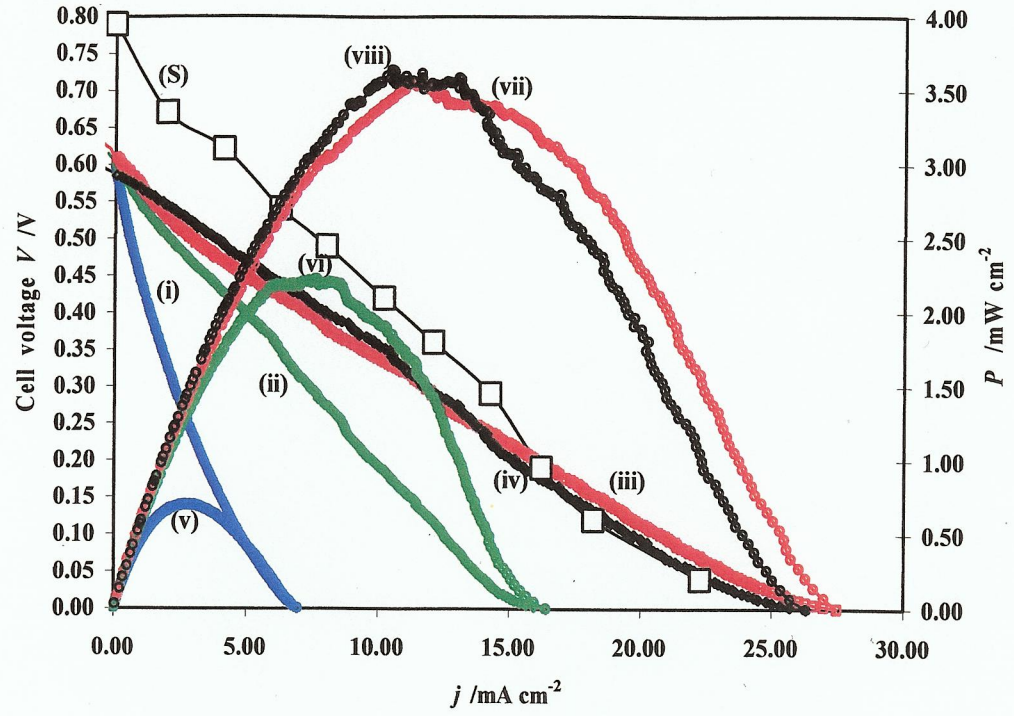

(a)

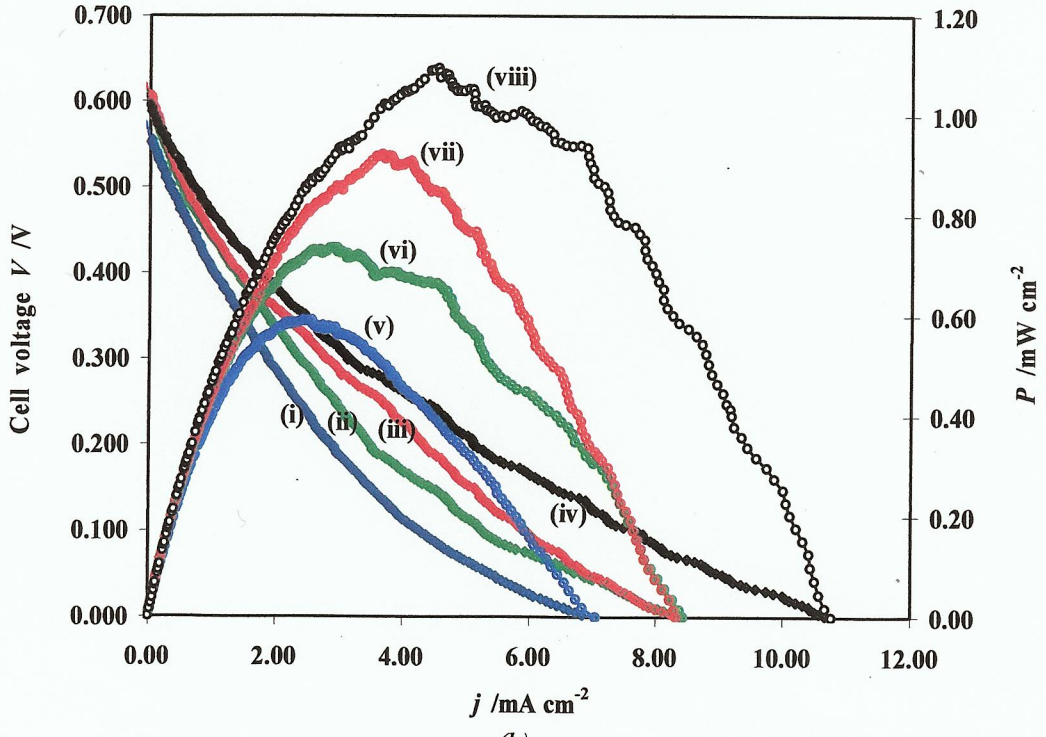

(b)

Figure 6.22. PEM AFC test for (a) anode (3 x 3 cm^2) Pt(40%)Ru(20%) on carbon, 0.50 mg metal cm^{-2}, 1 M methanol, membrane: Nafion 117 (K^+ form), cathode (3 x 3 cm^2) Pt(20%) on carbon 0.4 mg metal cm^{-2}, and O_2 gas at 1.5 bar at: (i) & (v) 25 °C, (ii) & (vi) 35 °C, (iii) & (vii) 45 °C, (iv) & (viii) 55 °C, (S) Scott et al. [81] . (b) Same as (a) but 1 M ethanol flowing in the anode.

In the case of an ethanol fuelled AEM fuel cell, there are specific additional problems [83, 91]: the main reaction product is potassium acetate, which will not precipitate and hence block the micropores of the membrane, but it will create a concentration gradient and therefore a mass transport of acetate ions across the membrane; this causes structural damage to the membrane, loss of ion exchange capacity [85] (fast depolarization), and when it reaches the cathode will form acetic acid (the characteristic odour of this compound was detected in the cathode at the end of the tests) adding more losses to the system.

Figure 6.23 shows the fuel cell performance under the operating conditions as in fig. 6.22(b), except with $Pd_{40}Ni_{60}$ as the anode catalyst.

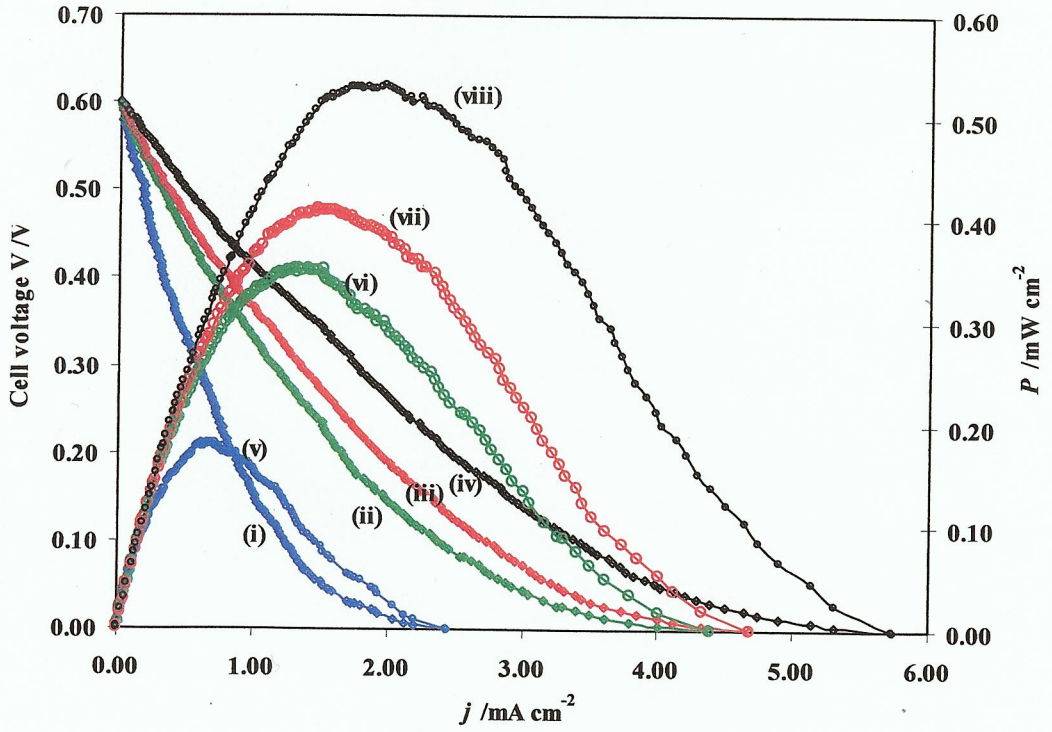

Figure 6.23. PEM AFC test for anode (3 x 3 cm^2 electrodes) $Pd_{40}Ni_{60}$ on carbon 1.0 mg metal cm^{-2}, 1 M ethanol, membrane: Nafion 117 (K^+ form), cathode (3 x 3 cm^2) Pt(20%) on carbon 0.4 mg metal cm^{-2}, and O_2 gas at 1.5 bar at: (i) & (v) 25 °C, (ii) & (vi) 35 °C, (iii) & (vii) 45 °C, (iv) & (viii) 55 °C.

Methanol was not tested as a fuel as a result of the work in section 6.3.3. As may be seen in the figure, the open circuit voltage attained was 0.60 V, as was the case with

the PtRu catalyst, which is encouraging; also encouraging was the fact that this was attained even at 25 °C (in fig. 6.22(b), the OCV at 25 °C is ca. 0.56 V). However, the maximum power density obtained with $Pd_{40}Ni_{60}$ was ca. half that observed using RuPt.

Figure 6.24 shows fuel cell test as a function of temperature using the SD1 membrane, PtRu as anode catalyst and methanol as fuel. As may be expected from the conductivity data, in general, the performance is poorer than those observed using Nafion as membrane. In addition, the performance collapses completely at 55 °C, probably due to the thermal decomposition of the SD1 membrane. Nevertheless the data obtained using the SD1 membrane are the first ever obtained and, despite showing that there are (significant) challenges to overcome, do show promise. The challenges include: the optimization of MEA fabrication, as the SD1 polymer can not be hot-pressed; the efficacy of the ionomer, alcohol crossover, etc.

Time did not allow the assessment of the SD1 membrane with ethanol as fuel and $Pd_{40}Ni_{60}$ as the anode catalyst.

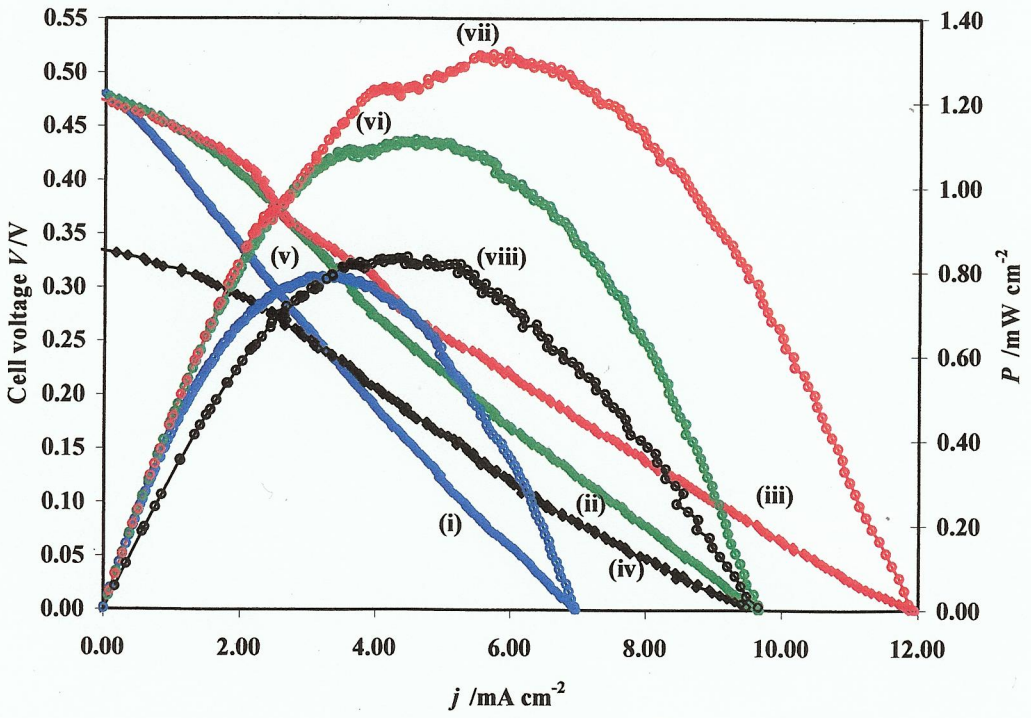

Figure 6.24. PEM AFC test for anode (3 x 3 cm^2 electrodes) Pt(40%)Ru(20%) on carbon, 0.50 mg metal cm^{-2}, 1 M methanol, membrane SD1, cathode (3 x 3 cm^{-2}) Pt(20%) on carbon 0.4 mg metal cm^{-2}, and O_2 gas at 1.5 bar at: (i) & (v) 25 °C, (ii) & (vi) 35 °C, (Hi) & (vii) 45 °C, (iv) & (viii) 55 °C.

6.5. Conclusions.

$Co_{50}Ni_{50}$, $Ru_{72}Ni_{28}$ and $Pd_{40}Ni_{60}$ were synthesised successfully as nano-particles on porous carbon; the synthesis of CoNi and RuNi nano-particles having not been reported previously. The $Co_{50}Ni_{50}$ particles were distributed about 1.3 nm over the range 1 – 2.1 nm; $Ru_{72}Ni_{28}$ distributed about 2.4 nm with range 1.5 – 3.6 nm and $Pd_{40}Ni_{60}$ 6nm over 3 – 10 nm range. The $Ru_{72}Ni_{28}$ and $Co_{50}Ni_{50}$ were evenly distributed over the carbon substrate, but the $Pd_{40}Ni_{60}$ particles showed significant agglomeration. However, of the three catalyst, $Pd_{40}Ni_{60}$ was the only one that showed promising activity with respect to methanol and ethanol oxidation.

Time did not allow for anything other than a preliminary assessment of the SD1 membrane and $Pd_{40}Ni_{60}$ catalyst in the DAAFC system.

The conductivity of the SD1 membrane was very low, 0.005 S cm^{-1} at 55 °C; but that of the K^+ exchanged Nafion was also low compared to some literature values (0.037 S cm^{-1}). Using PtRu as the anode catalyst and methanol as fuel, the maximum current density obtained using SD1, 1.3 mW cm^{-2} at 45 °C, compared favourably with 3.8 mW cm^{-2} obtained using Nafion at the same temperature. Similarly, using Nafion as the AAEM, the 0.5 mW cm^{-2} observed with $Pd_{40}Ni_{60}$ as catalyst was a reasonable result for a first attempt when compared to the 0.9 mW cm^{-2} obtained using PtRu, both at 45 °C.

It may be that the poor membrane characteristic of the SD1 (including thermal degradation) obscured the true activity of the $Pd_{40}Ni_{60}$ catalyst; but the data on both are very encouraging and worthy of further study.

6.6. References

1. Sobal N.S., Ebels U., Möhwald H., and Giersig M., (2003). The Journal of Physical Chemistry B, 107, 30, pp. 7351-7354.
2. Qi Z., (2007). *Surface functionalization of carbon catalyst-support for PEM fuel cells: a review*, in: Fuel cell research trends, L.O. Vasquez [Editor], Nova Science Publisher, Inc., New York. p. 381-410.
3. Kim S. and Park S.-J., (2007). *A study on the role of carbon support materials for fuel cell catalyst*, in: Fuel cell research trends, L.O. Vasquez [Editor], Nova Science Publisher, Inc., New York. p. 411-443.

4. Pozio A., De Francesco M., Cemmi A., Cardellini F., and Giorgi L., (2002). Journal of Power Sources, 105, 1, pp. 13-19.
5. Shen S.Y., Zhao T.S., Xu J.B., and Li Y.S., (2010). Journal of Power Sources, 195, 4, pp. 1001-1006.
6. Bönnemann H., Brijoux W., and Joussen T., (1990). Angewandte Chemie International Edition in English, 29, 3, pp. 273-275.
7. Bönnemann H., Brijoux W., Brinkmann R., Joußen T., Korall B., and Dinjus E., (1991). Angewandte Chemie International Edition in English, 30, 10, pp. 1312-1314.
8. Bönnemann H., Brijoux W., Brinkmann R., Fretzen R., Joussen T., Köppler R., Korall B., Neiteler P., and Richter J., (1994). Journal of Molecular Catalysis, 86, 1-3, pp. 129-177.
9. Oh H.-S., Oh J.-G., Hong Y.-G., and Kim H., (2007). Electrochimica Acta, 52, 25, pp. 7278-7285.
10. Luna C., Morales M.d.P., Serna C.J., and Vázquez M., (2004). Nanotechnology, 15, 4, pp. S293-S297.
11. ACMA, (Accessed 20/07/2011). http://www.ncl.ac.uk/acma/.
12. NU, (Accessed 20/07/2011). http://www.ncl.ac.uk/facilities/microscopy/transmission.htm.
13. Pingali K.C., Deng S., and Rockstraw D.A., (2008). Powder Technology, 187, 1, pp. 19-26.
14. Li H., Sun G., Jiang Q., Zhu M., Sun S., and Xin Q., (2007). Journal of Power Sources, 172, 2, pp. 641-649.
15. Maiyalagan T. and Scott K., (2010). Journal of Power Sources, 195, 16, pp. 5246-5251.
16. Cai Y.Q., Bradshaw A.M., Guo Q., and Goodman D.W., (1998). Surface Science, 399, 2-3, pp. L357-L363.
17. Ferrando R., Jellinek J., and Johnston R.L., (2008). Chemical Reviews, 108, 3, pp. 845-910.
18. Viau G., Toneguzzo P., Pierrard A., Acher O., Fiévet-Vincent F., and Fiévet F., (2001). Scripta Materialia, 44, 8-9, pp. 2263-2267.
19. Joseyphus R.J., Matsumoto T., Takahashi H., Kodama D., Tohji K., and Jeyadevan B., (2007). Journal of Solid State Chemistry, 180, 11, pp. 3008-3018.
20. Panday S., Daniel B.S.S., and Jeevanandam P., (2011). Journal of Magnetism and Magnetic Materials, 323, 17, pp. 2271-2280.
21. Ung D., Viau G., Fiévet-Vincent F., Herbst F., Richard V., and Fiévet F., (2005). Progress in Solid State Chemistry, 33, 2-4, pp. 137-145.
22. Chen Y., Liew K.Y., and Li J., (2008). Materials Letters, 62, 6-7, pp. 1018-1021.
23. Coq B. and Figueras F., (2001). Journal of Molecular Catalysis A: Chemical, 173, 1-2, pp. 117-134.
24. Cullity B.D. and Stock S.R., (2001). *Elements of X-Ray Diffraction*, 3 ed: Prentice Hall. 167-171.
25. Yu G.-Y., Chen W.-X., Zheng Y.-F., Zhao J., Li X., and Xu Z.-D., (2006). Materials Letters, 60, 20, pp. 2453-2456.
26. Harpeness R., Peng Z., Liu X., Pol V.G., Koltypin Y., and Gedanken A., (2005). Journal of Colloid and Interface Science, 287, 2, pp. 678-684.
27. Gao X., Chen D., Dollimore D., Skrzypczak-Jankun E., and Burckel P., (1993). Thermochimica Acta, 220, pp. 75-89.
28. Jung I., Lee Y., Tak Y., and Choi J., (2011). Journal of The Electrochemical Society, 158, 3, pp. D123-D126.

29. JCPDS-ICDD, (2010). PDF2 database, pp. Card 14-0742.
30. Duran Pachon L., Thathagar M.B., Hartl F., and Rothenberg G., (2006). Physical Chemistry Chemical Physics, 8, 1, pp. 151-157.
31. Yu Y., Zhao Y., Huang T., and Liu H., (2009). Pure and Applied Chemistry, 81, 12, pp. 2377-2385.
32. Behl W.K. and Toni J.E., (1971). Journal of Electroanalytical Chemistry and Interfacial Electrochemistry, 31, 1, pp. 63-75.
33. Casella I.G. and Gatta M., (2002). Journal of Electroanalytical Chemistry, 534, I, pp. 31-38.
34. Gomez Meier H., Vilche J.R., and Arvía A.J., (1982). Journal of Electroanalytical Chemistry and Interfacial Electrochemistry, 134, 2, pp. 251-272.
35. Gomez Meier H., Vilche J.R., and Arvía A.J., (1982). Journal of Electroanalytical Chemistry and Interfacial Electrochemistry, 138, 2, pp. 367-379.
36. Nikolova V., Iliev P., Petrov K., Vitanov T., Zhecheva E., Stoyanova R., Valov I., and Stoychev D., (2008). Journal of Power Sources, 185, 2, pp. 727-733.
37. Zhang C. and Park S.-M., (1989). Journal of The Electrochemical Society, 136, 11, pp. 3333-3342.
38. Cappadonia M., Divisek J., von der Heyden T., and Stimming U., (1994). Electrochimica Acta, 39, 11-12, pp. 1559-1564.
39. Barnard R., Crickmore G.T., Lee J.A., and Tye F.L., (1980). Journal of Applied Electrochemistry, 10, 1, pp. 61-70.
40. Barnard R., Randell C.F., and Tye F.L., (1980). Journal of Applied Electrochemistry, 10, l, pp. 109-125.
41. Oliva P., Leonardi J., Laurent J.F., Delmas C., Braconnier J.J., Figlarz M., Fievet F., and Guibert A.d., (1982). Journal of Power Sources, 8, 2, pp. 229-255.
42. Casella I.G. and Guascito M.R., (1999). Journal of Electroanalytical Chemistry, 476, 1, pp. 54-63.
43. Golikand A.N., Asgari M., Maragheh M.G., and Shahrokhian S., (2006). Journal of Electroanalytical Chemistry, 588, 1, pp. 155-160.
44. Jafarian M., Mahjani M.G., Heli H., Gobal F., Khajehsharifi H., and Hamedi M.H., (2003). Electrochimica Acta, 48, 23, pp. 3423-3429.
45. Fleischmann M., Korinek K., and Pletcher D., (1971). Journal of Electroanalytical Chemistry and Interfacial Electrochemistry, 31, 1, pp. 39-49.
46. Zhang C. and Park S.-M., (1987). Journal of The Electrochemical Society, 134, 12, pp. 2966-2970.
47. Fleischmann M., Korinek K., and Pletcher D., (1972). Journal of the Chemical Society, Perkin Transactions 2, 10, pp. 1396-1403.
48. Kim J.-W. and Park S.-M., (2005). Journal of the Korean Electrochemical Society, 8, 3, pp. 117 - 124.
49. Kim J.-W. and Park S.-M., (1999). Journal of The Electrochemical Society, 146, 3, pp. 1075-1080.
50. Hamnett A., (2003). *Introduction to fuel-cell types*, in: Handbook of Fuel Cells Fundamental Technology and Applications, W. Vielstich, A. Lamm, and H.A. Gasteiger Editors, John Wiley & sons Ltd. p. 36-43.
51. Matsuoka K., Iriyama Y., Abe T., Matsuoka M., and Ogumi Z., (2005). Journal of Power Sources, 150, pp. 27-31.
52. Bunazawa H. and Yamazaki Y., (2008). Journal of Power Sources, 182, 1, pp. 48-51.

53. Burke L.D. and Whelan D.P., (1979). Journal of Electroanalytical Chemistry, 103, 2, pp. 179-187.
54. Burke L.D. and Healy J.F., (1981). Journal of Electroanalytical Chemistry, 124, 1-2, pp. 327-332.
55. Burke L.D. and McCarthy M., (1984). Electrochimica Acta, 29, 2, pp. 211-216.
56. Ardizzone S., Fregonara G., and Trasatti S., (1990). Electrochimica Acta, 35, 1, pp. 263-267.
57. Shieh D.T. and Hwang B.J., (1995). Journal of The Electrochemical Society, 142, 3, pp. 816-823.
58. Takamura T. and Minamiyama K.i., (1965). Journal of The Electrochemical Society, 112, 3, pp. 333-335.
59. Prabhuram J., Manoharan R., and Vasan H.N., (1998). Journal of Applied Electrochemistry, 28, 9, pp. 935-941.
60. Grdeń M., Kotowski J., and Czerwiński A., (2000). Journal of Solid State Electrochemistry, 4, 5, pp. 273-278.
61. Grdeń M. and Czerwiński A., (2008). Journal of Solid State Electrochemistry, 12, 4, pp. 375-385.
62. Liang Z.X., Zhao T.S., Xu J.B., and Zhu L.D., (2009). Electrochimica Acta, 54, 8, pp. 2203-2208.
63. Burke L.D. and Casey J.K., (1993). Journal of The Electrochemical Society, 140, 5, pp. 1292-1298.
64. Vracar L., Burojevic S., and Krstajic N., (1998). International Journal of Hydrogen Energy, 23, 12, pp. 1157-1164.
65. Jeong M.-C., Pyun C.H., and Yeo I.-H., (1993). Journal of The Electrochemical Society, 140, 7, pp. 1986-1989.
66. Balaramachandran V., Srinivasan K.N., and Kapali V., (1991). Corrosion Science, 32, 2, pp. 185-191.
67. Nishimura K., Machida K., and Enyo M., (1988). Journal of Electroanalytical Chemistry and Interfacial Electrochemistry, 257, 1-2, pp. 217-230.
68. Nishimura K., Machida K.-i., and Enyo M., (1988). Journal of Electroanalytical Chemistry and Interfacial Electrochemistry, 251, 1, pp. 103-116.
69. Nishimura K., Kunimatsu K., and Enyo M., (1989). Journal of Electroanalytical Chemistry and Interfacial Electrochemistry, 260, 1, pp. 167-179.
70. Nishimura K., Kunimatsu K, Machida K.-i., and Enyo M., (1989). Journal of Electroanalytical Chemistry and Interfacial Electrochemistry, 260, 1, pp. 181-192.
71. Zhou Z.-Y., Wang Q., Lin J.-L, Tian N., and Sun S.-G., (2010). Electrochimica Acta, 55, 27, pp. 7995-7999.
72. Larmine J. and Dicks A., (2003). *Fuel cell systems explained*, 2 ed: John Wiley & Sons Ltd. 406.
73. Qi Z., (2007). *Qualification of fuel cell membrane electrode assemblies*, in: Fuel cell research trends, L.O. Vasquez [Editor], Nova Science Publisher, Inc., New York. p. 3-6.
74. Antolini E. and Gonzalez E.R., (2010). Journal of Power Sources, 195, 11, pp. 3431-3450.
75. Nacef M. and Affoune A.M., (2011). International Journal of Hydrogen Energy, 36, 6, pp. 4208-4219.
76. Poynton S.D., Kizewski J.P., Slade R.C.T., and Varcoe J.R., (2010). Solid State Ionics, 181, 3-4, pp. 219-222.

77. Varcoe J.R., Slade R.C.T., Yee E.L.H., Poynton S.D., and Driscoll D.J., (2007). Journal of Power Sources, 173, 1, pp. 194-199.
78. Doherty S., (2011). *Multifunctional Imidazolium Based Polymers: Synthesis Characterization and Applications (private communication)*. Christensen, [Recip].
79. Robertson N.J., Kostalik H.A., Clark T.J., Mutolo P.F., Abruña H.D., and Coates G.W., (2010). Journal of the American Chemical Society, 132, 10, pp. 3400-3404.
80. Kostalik H.A., Clark T.J., Robertson N.J., Mutolo P.F., Longo J.M., Abruña H.D., and Coates G.W., (2010). Macromolecules, 43, 17, pp. 7147-7150.
81. Yu E., Scott K., and Reeve R., (2006). Journal of Applied Electrochemistry, 36, 1, pp. 25-32.
82. Yu E.H. and Scott K., (2005). Journal of Applied Electrochemistry, 35, 1, pp. 91-96.
83. Yu E.H., Krewer U., and Scott K., (2010). Energies, 3, 8, pp. 1499-1528.
84. Iwai Y. and Yamanishi T., (2009). Polymer Degradation and Stability, 94, 4, pp. 679-687.
85. Li Y.S., Zhao T.S., and Liang Z.X., (2009). Journal of Power Sources, 190, 2, pp. 223-229.
86. Doyle M. and Rajendran G., (2003). *Perfluorinated membranes*, in: Handbook of Fuel Cells Fundamental Technology and Applications, W. Vielstich, A. Lamm, and H.A. Gasteiger Editors, John Wiley & sons Ltd. p. 351-395.
87. FSEC, (2008). *Procedure for performing in-plane membrane conductivity testing*. USDOE, DE-FC36-06G016028, 19.
88. Slade S., Campbell S.A., Ralph T.R., and Walsh F.C., (2002). Journal of The Electrochemical Society, 149, 12, pp. A1556-A1564.
89. Mamlouk M., Scott K., Horsfall J.A., and Williams C., (2011). International Journal of Hydrogen Energy, 36, 12, pp. 7191-7198.
90. Ravishankara A.R. and Davis D.D., (1978). The Journal of Physical Chemistry, 82, 26, pp. 2852-2853.
91. Song S., Wang Y., and Shen P., (2007). Chinese journal of catalysis, 28, 9, pp. 752-754.
92. Wang Y., Li L., Hu L., Zhuang L., Lu J., and Xu B., (2003). Electrochemistry Communications, 5, 8, pp. 662-666.
93. Zhou W.J., Zhou B., Li W.Z., Zhou Z.H., Song S.Q., Sun G.Q., Xin Q., Douvartzides S., Goula M., and Tsiakaras P., (2004). Journal of Power Sources, 126, 1-2, pp. 16-22.
94. Hou H., Wang S., Jin W., Jiang Q., Sun L., Jiang L., and Sun G., (2011). International Journal of Hydrogen Energy, 36, 8, pp. 5104-5109.
95. Wang Y., Chen K.S., Mishler J., Cho S.C., and Adroher X.C., (2011). Applied Energy, 88, 4, pp. 981-1007.

7. Composite Anodes

7.1. Introduction

The initial work in the PAC group on composite anodes arose out of a search for more active TiO_2 photo-anodes for water treatment; hence this chapter starts with a brief description of TiO_2 photoelectrochemistry.

7.1.1. The photochemistry of TiO_2

TiO_2 is a n-type semiconductor with a band gap of a ca. 3.2 eV. If TiO_2 is irradiated with supra-band gap light ($\lambda < 385$ nm anatase or $\lambda < 405$ nm rutile) an electron is promoted into the conduction band of the semiconductor (see fig. 7.1) and a hole left in the valence band.

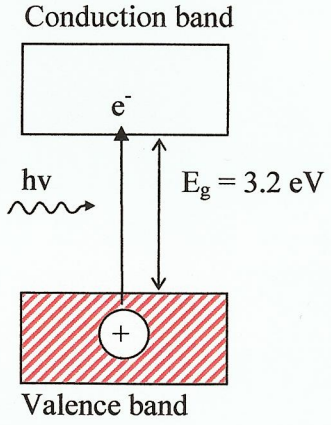

Figure 7.1. The irradiation of TiO_2 with supra-band gap light to form an electron/hole pair.

Whilst most electron/hole pairs recombine under normal circumstances and hence convert photon energy to heat (the quantum yield for $OH^\bullet$ formation by TiO_2 slurries is ca. 5% [1]) where holes reach the surface of the TiO_2, they can oxidize either adsorbed hydroxyl ions or water to form the OH radical [2-4].

$$TiO_2 + hv \rightarrow e^-_{CB} + h^+_{VB} \quad (7.1)$$

$$h^+_{VB} + H_2O_{(ads)} \rightarrow HO^\bullet_{(ads)} + H^+ \quad (7.2)$$

$$h^+_{VB} + OH^-_{(ads)} \rightarrow HO^\bullet_{(ads)} \quad (7.3)$$

7.1.2. TiO_2 slurries and the remediation of contaminated water

Hydroxyl radicals are powerful oxidants, having a standard reduction potential [5] of 2.7 V, second only to F_2 (2.87 V for F_2/F^-). Thus, the use of TiO_2 powder as a slurry has been extensively studied since the early 1980's as a mean of treating water contaminated with chemicals and bacteria ([2, 3, 6, 7] and references therein).

There are two primary disadvantages of using TiO_2 slurries to effect the remediation of contaminated water:

- The minority carrier (hole) length in TiO_2, L_p, i.e. the distance the holes can move in an electric field-free region before recombination with an electron, is ca. 0.1 μm [8, 9], This sets an upper limit to the diameter of the slurry particles, rendering post treatment separation of the slurry from treated water difficult and expensive.

- The low quantum yield for OH radicals [1].

These challenges have proven impossible to overcome and hence there are no commercial, slurry-based photo-reactors for water treatment.

The separation problem can be overcome by immobilising TiO_2 powder on the inside of, for example, the glass tube of a flow-through reactor. However, this causes mass transport problems (absent when using a well stirred slurry) and poor light absorption as TiO_2 has a low light absorption coefficient at energies near that of the band gap [10], If the TiO_2 film thickness is increased to offset the latter, holes will be generated too deep in the film and recombine before reaching the surface.

7.1.3. The photo-electrochemistry ofTiO_2 anodes

Professor Christensen adopted a strategy using TiO_2 electrodes based on Electric Field Enhancement (EFE) to try and ameliorate the light absorption problem, and to couple this with effective photo-reactor design to offset the mass transport problem [7, 10-12]. Thus a positive potential bias is applied to a TiO_2 photo-anode (i.e. a TiO_2 film thermally formed on a Ti plate) with respect to a metal counter electrode such as stainless steel, see fig. 7.2.

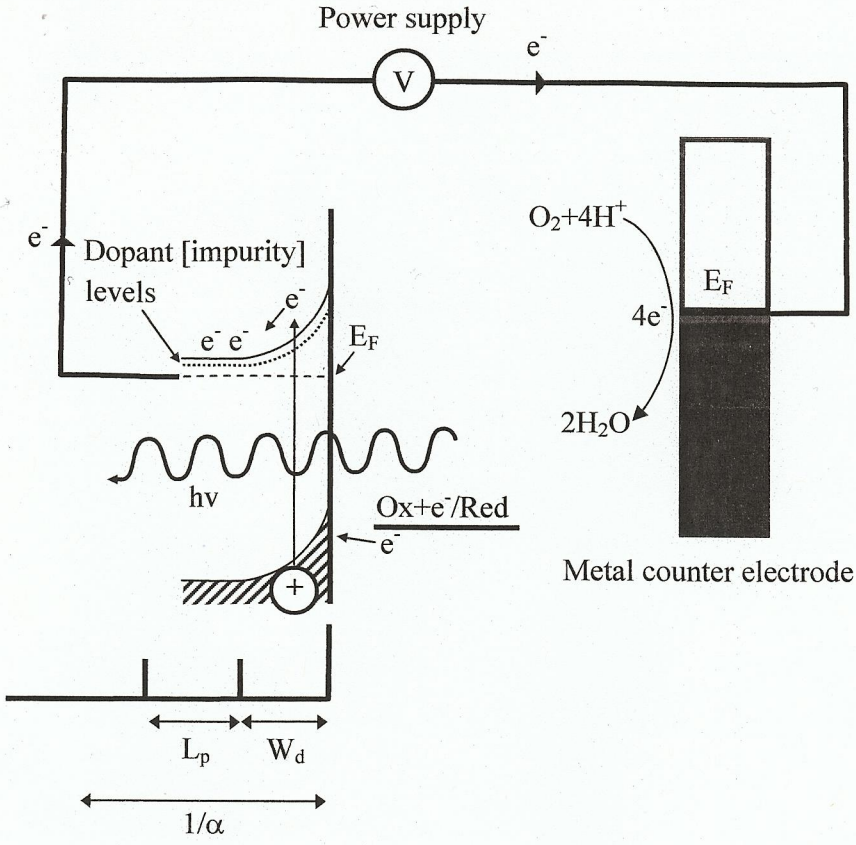

Figure 7.2. Schematic representation of the events taking place during the irradiation of a n-doped semiconductor immersed in aqueous solution and under a positive potential bias, with suprabandgap light. The penetration depth of the light is 1/α., where α is the absorption coefficient (m^{-1}) of the semiconductor at the wavelength of the light; W_d *is the depletion layer width, and* L_p *is the minority carrier length: the distance the minority carriers (i.e. holes in n-TiO_2) move in a field-free region before recombination.* E_F *are the Fermi levels of the counter electrode and TiO_2. [10]*

Providing the electrolyte concentration is larger than the film dopant density (in a n-type semiconductor, doping results in filled states just below the conduction band edge which can thermally populate the conduction band with electrons, giving low electronic conductivity in the absence of light) which in a typical n-TiO_2 film will be $\geq 10^{17}$ cm^{-3} [10] the application of a positive potential to the TiO_2 'pulls' the Fermi level of the semiconductor down (ΔG = -zFE, hence increasing potential = decreasing energy), causing the valence and conduction bands to 'bend', see fig. 7.2. The depth of this electric field into the semiconductor is termed the depletion layer, of width W_d the maximum penetration distance of incident UV light is 1/α where α is the

absorption coefficient of TiO_2 (in m^{-1}) [13]. Any electron/hole pairs generated within a distance W_d of the TiO_2 surface will undergo efficient charge separation as the electrons fall downhill energetically, and the holes 'fall' uphill to the surface. Any electron/hole pairs generated within a distance $W_d + L_p$ of the surface will also undergo efficient charge separation. This, the Electric Field Enhancement (EFE) effect, is highly dependent upon the degree of doping [13], and can arise from the presence of negative charge (or a metal overlayer – see section 7.1.7) as well as from the application of a positive bias.

The EFE effect was shown by several authors [14-16], as well as by Prof. Christensen in a number of papers [7, 10-12]; Christensen's group has reported both detoxification (organic removal) and disinfection in a variety of photo-electrochemical reactors, including vortex & falling film [10] and bubble column [17, 18]. However, despite the Newcastle anodes showing superior photocurrent densities with lower power lamps than employed in the literature, ca. 400 μA cm^{-2} using 36 W 'sun bed' Philips PL-L lamps, λmax = 360 nm, compared to 300 μA cm^{-2} using a 2 kW lamp [19], these photocurrents were still insufficient to make the technology viable, and hence the search was initiated for more active TiO_2 photo-anodes; a key finding is that thin TiO_2 films deposited on 'standard' Si(001) wafers (Si/TiO_2) gave photocurrent densities up to 1.4 mA cm^{-2} [20] using 2 x 36 W PL - L lamps.

7.1.4. The $Si/TiO_2/Au$ composite anode

In order to explore the properties of the Si/TiO_2 films in more detail, a gold grid was deposited on the surface of the TiO_2 to allow transmittance FTIR spectra to be collected as a function of the electric field across the device. The results so obtained [20] suggested that holes were thermally generated in the Si and could move at least as far as the Si/TiO_2 interface. To test this postulate, the system was modelled using semiconductor industry standard 2D simulation software (Atlas from Silvaco Corp.) This software can give a detailed analysis of the current flow mechanism and electric field in such a structure. The simulation results showed quite clearly that under the correct bias condition, a hole inversion layer can be formed under the TiO_2 and that more significantly hole conduction to the TiO_2 electrode surface will be observed – in fact up to 25% of the holes generated in the Si are expected to reach the surface of the TiO_2 and thus be available for the generation of OH radicals. As a further test, a

disinfection experiment was carried out in a simple glass reactor [21, 22] containing a 100 cm^3 suspension of 10^7 colony forming units cm^{-3} of the K-12 strain of *E. coli* (NCIMB 8277) and 0.0014 M Na_2SO_4. The composite anode employed is shown in fig. 2.20(a); the gold grid (5 in fig. 2.20(a)) was biased at various (negative) voltages (V_b) with respect to the Si, and the results are shown in fig. 7.3.

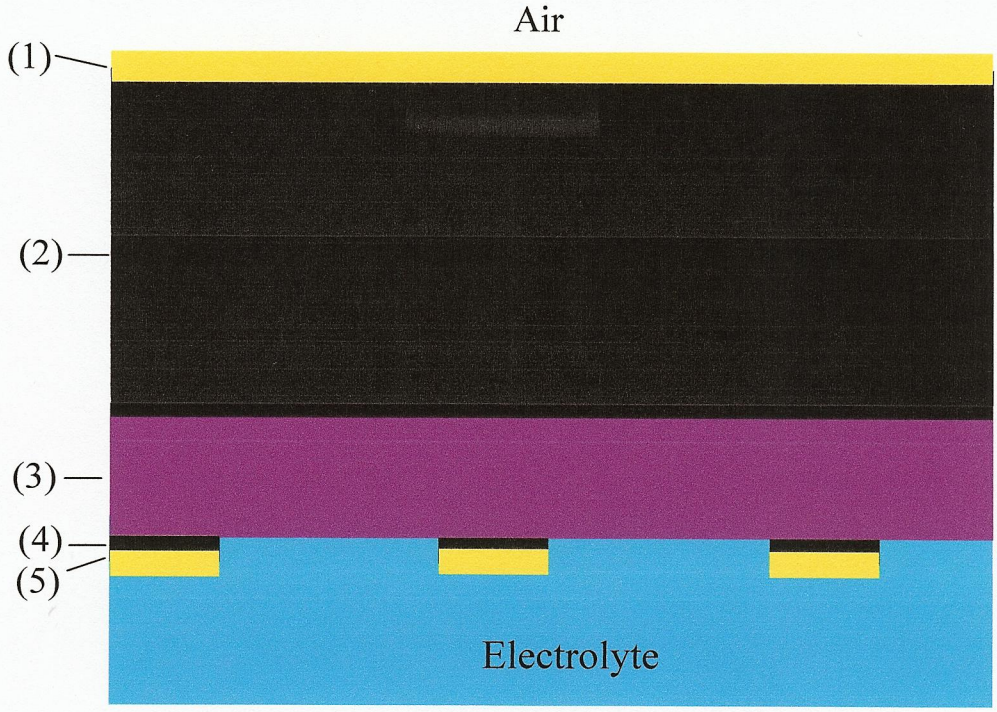

Figure 2.20. (a) Schematic of the composite anode: (1) 100 nm Au Ohmic contact; (2) 300 μm Si wafer; (3) 120 nm TiO_2 layer; (4) 10 nm Ti wetting layer and (5) 120 nm Au grid (see section 2.11).

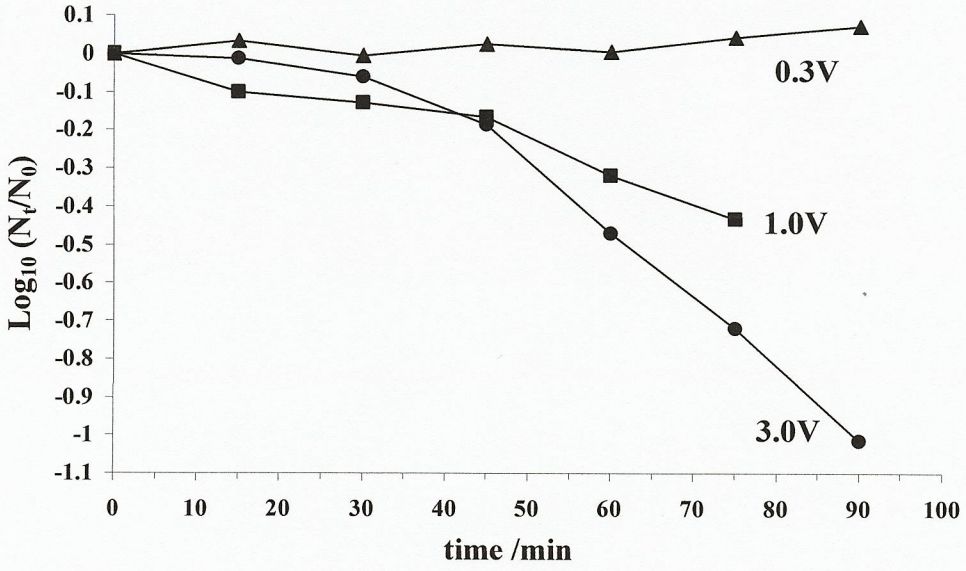

Figure 7.3. Disinfection of ca. 10^7 cfu ml^{-1} E. coli in 100 ml 1.4 mM Na_2SO_4 by an 18 cm^2 n-Si (100)/TiO_2/Au grid [21]).

As may be seen from the figure, as the grid was made more negative, a clear 'kill' of the *E.coli* was observed. On the basis of the results, it was concluded that the activity (i.e. rate of generation of OH radicals per unit area) of the $Si/TiO_2/Au$ anode was comparable to that of 'conventional' TiO_2 photo-anodes, a remarkable result given the composite anode represented an un-optimized technology. Moreover, it should be noted that the $Si/TiO_2/Au$ electrode was generating OH radicals *in the dark* and without any external counter electrode.

7.1.5. Composite anodes and fuel cells

Interest in the potential application of composite anodes in fuel cell technology, particularly 'fuel cells on a chip' stemmed from Prof. Christensen who reasoned that the OH radicals generated at the TiO_2 surface of the composite anodes could be considered to be a form of 'active oxygen', postulated by Watanabe and Motoo [23] in their 'bifuntional mechanism' for CO oxidation at PtRu electrocatalyst. In essence, in the bifuntional mechanism, Ru promotes the oxidation of CO adsorbed on Pt by supplying 'active oxygen' at lower potentials than is possible at Pt itself, via a Langmuir-Hinshelwood mechanism:

$$Pt - CO + Ru - OH \rightarrow Pt + Ru + CO_2 + H^+ + e^- \qquad (7.4)$$

This process stops the Pt being poisoned by the CO and converts the latter from a poison to an intermediate [24]. Prof. Christensen thus decide to explore if the above could be applied to the composite anodes: i.e. could the electro-oxidation of small organic molecules be enhanced at the platinum grid (actually Pt electrodeposited on the Au grid [25] of a $Si/TiO_2/Au$ composite anode).

It was found that the oxidation of methanol was enhanced at the Pt through the application of a bias voltage (V_b, Pt negative with respect to Si [25]). It was also found that the onset potential for methanol oxidation at the composite anode decreased as V_b increased. In addition, in the absence of a bias voltage, both the onset potential and the peak current increased as the perimeter between the Pt and TiO_2 increased.

7.1.6. Summary of previous work on composite anodes

The previous work on the composite anodes showed that the application of a bias potential between the metal grid and Si of the composite anodes: (1) facilitates the transport of holes thermally generated in the Si to the TiO_2 surface; (2) results in the generation of active species at the TiO_2 surface; and that (3) these active species can spillover from the TiO_2 to the metal grid; (4) the rate of spillover can be controlled via the bias voltage. Thus, our composite electrodes offer independent control of spillover at the metal/TiO_2/electrolyte interface, an effect hitherto not available and offering a wholly novel electrocatalytic effect with potential applications in e.g. electro-organic synthesis, water & air detoxification (including via the visible light irradiation of our composite anodes) and fuel cell technology.

The previous work was not a comprehensive research investigation; of necessity (due to lack of funds) it was, at best, a preliminary assessment. Based on, in particular studies of preferential CO oxidation at fine gold particles [26-29] on reducible oxide support, Prof. Christensen formulated a model "Current Induced Generation of Adsorbed Reactive Species, or CIGARS" to explain the chemistry observed at the composite anode, and particularly the very clear effect of the perimeter between the grid and TiO_2. However, the mechanism by which OH radicals were generated at the TiO_2 surface, and their subsequent fate was, in fact, unclear, as was the rôle of the grid. A theoretical framework is essential, if the technology is to realize its potential application in fuel cells. Such a model has been formulated; however the charge transport within the composite anode and across the gold grid/electrolyte interface is highly complex. Hence to aid understanding, the model (formulated on the basis of the data presented below) has been placed first.

7.1.7. The model

The complex electrode structure makes it difficult to predict the detailed potential distribution within the electrode with any degree of certainty. For the isolated components, n-Si and n-TiO_2, the flat-band potentials are both close to 0.1 V [30, 31] and the work-function of gold is ca. 0.6 eV (taking the potential of the SHE as 4.44 eV vs. vacuum [32]). Placing the three components in contact and arranging zero bias between gold and silicon will lead to the situation shown schematically in fig. 7.4(a)

where a small internal potential develops at the TiO_2/Au interface owing to the transfer of some electrons from the TiO_2 to the gold.

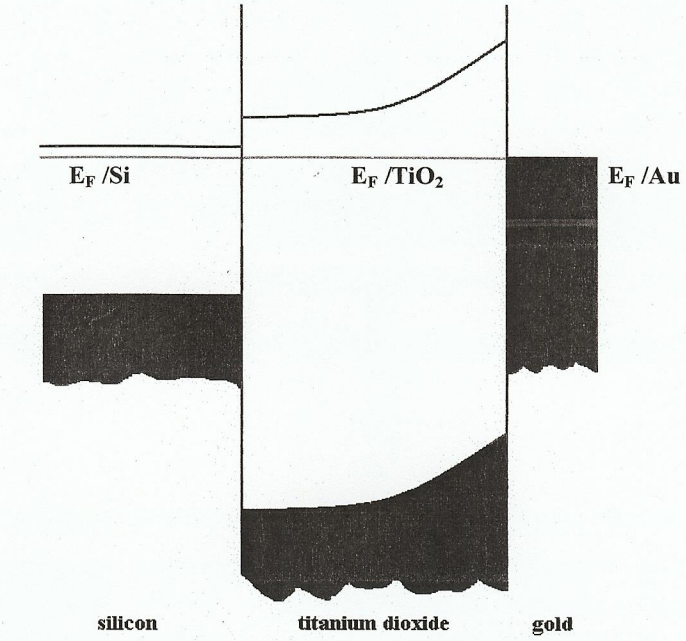

(a)

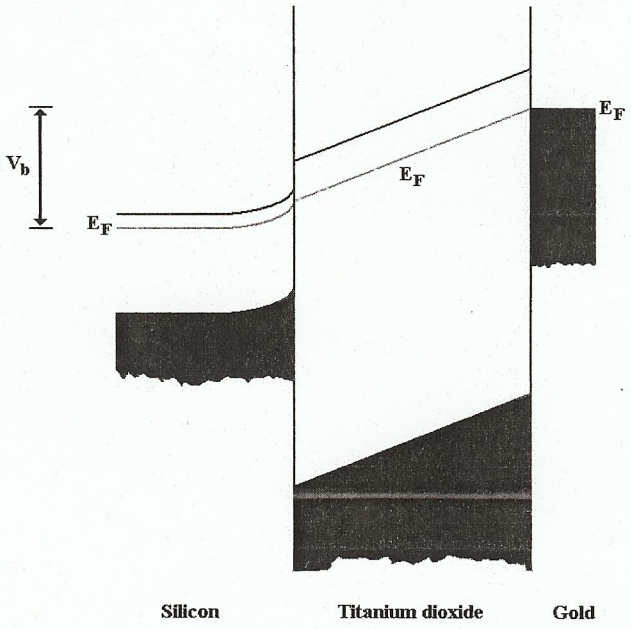

(b)

Figure 7.4. The proposed band structure of the Si/TiO_2/Au composite anode: (a) at zero bias and (b) high positive bias on the Si with respect to the Au. The Fermi levels (E_F) of the Si and TiO_2 are shown in grey.

At the Si/TiO_2 interface, there is probably little charge since the flat-band potentials are similar for these two materials. If the silicon is now biased negative with respect to the gold (corresponding to 'forward bias') then electrons will flow from the n-Si through the Si/TiO_2 interface into the conduction band of the TiO_2 and thence to the gold grid. The rise in electron flow with increased negative V_b will be very pronounced, since electrons have a high mobility in the conduction band of the TiO_2 and at more negative potentials the depletion layer will be neutralised completely; the electron flow will be determined in effect by the build-up of electron density at the Si/TiO_2 interface and by the kinetics of electron flow from the gold either back to the silicon or, in the complete electrode, the flow of electrons into the solution. The high carrier mobility of electrons in the TiO_2 conduction band will mean that there is little potential drop within the TiO_2 itself, and the increasing potential change within the electrode will be accommodated at the Si/TiO_2 interface and the TiO_2/Au interface.

If the polarity of the potential is reversed, so that the n-Si is made more positive than the gold, then a more complex situation develops. The situation shown in fig. 7.4(a) no longer holds; now V_b will be accommodated both at the Si/TiO_2 interface and within the TiO_2 itself. The fact that at least some of the bias potential is dropped within the Si is clearly demonstrated by the fact that, on illumination with visible light of energy above the band gap of silicon but below that of TiO_2, a substantial photocurrent flows (see fig 7.8 and discussion below), and this photocurrent can only be generated by absorption of light in a depletion region formed within the Si at the Si/TiO_2 interface. Some of the potential must also be accommodated within the TiO_2, this is clear because there is no doubt that holes are migrating through the TiO_2, and this must be by some form of field-assisted hopping. It is necessary also to recognise that the TiO_2 is likely to be amorphous, so that the edges of the conduction band and valence band will be much less well defined than in a perfectly crystalline solid [33].

The direction of conventional current flow is now from Si to Au grid and there are two possibilities: electrons pass from the gold grid to the TiO_2 conduction band, either by tunnelling or thermal excitation, and thence to the conduction band of the silicon, or holes form at the Si/TiO_2 interface and pass through the TiO_2 to the gold grid. The former process is almost certainly the dominant one at low positive bias ($V_b > 0$) and in this case, as V_b increases, the potential change will be accommodated primarily at

the Si/TiO_2 interface. As V_b increases, however, (see fig. 7.4(b)) a second possible channel opens in which holes generated at the Si/TiO_2 interface at high positive bias, where an inversion layer forms within the silicon, then pass through the TiO_2 layer.

At first sight, the postulate of a significant contribution to conduction in TiO_2 from hole hopping would appear very counter-intuitive. We would expect the conduction to be dominated by electron flow, particularly as it has been reported that the deposition of metals onto TiO_2 results in the creation of surface states ca. 1 eV below the conduction band edge which would facilitate electron transfer into the conduction band [34, 35]. However, the presence of a hole current from Si to the TiO_2 surface under a suitable bias was predicted by simulation using industry standard, 2D simulation software as was stated in section 7.1.4. In addition, direct observation of hole transport across high dielectric constant materials such as HfO_2 and TiO_2 has been reported by Mizubayashi and co-workers [36], and Deskins and Dupuis [37] have modelled electron and hole transport in TiO_2 and compared their data to experimental results. In addition, the disinfection studies summarised above [21, 22] support the production of OH radicals at the surface of the TiO_2 and it is not unreasonable to postulate that this process takes place via hole transport from the Si.

Given the relatively large thickness of TiO_2 layer, direct elastic tunnelling of holes or electrons through the TiO_2 is highly unlikely, whilst the latter's amorphous nature would suggest Anderson localization [38] within the semiconductor, with conduction *via* Miller-Abrahams hopping [33, 39]. This process will be substantially facilitated by the presence of any potential field that may build up in the TiO_2 itself. Unlike the situation with regard to carriers in the conduction band, the holes will probably be transported by some form of field-assisted hopping, and accommodation of potential change within the TiO_2 will substantially assist this process; it will also facilitate electron tunnelling into the conduction band from the gold grid.

This model does rationalise much of the behaviour of the composite electrode as an isolated artefact, and we now need to consider the effects associated with its immersion in an electrolyte with a counter electrode connected effectively through the potentiostat back to the gold grid. We now have two circuits: the silicon-TiO_2-Au grid-silicon circuit and the TiO_2-gold grid-electrolyte-(counter-electrode)-TiO_2-gold

grid circuit; the common elements being the TiO_2 surface and the gold grid. For $V_b > 0$, positive charges forming at the surface either by electron-transfer to the interior of the TiO_2 (equation (7.5))

$$e^-(Au) \rightarrow e^-(Si) \tag{7.5}$$

or by holes arriving at the TiO_2/Au interface, may then be transferred back to the silicon or may react with oxidisable species present in the electrolyte itself. If we concentrate for a moment on conduction by holes, then once such holes have reached the TiO_2 surface, see equation (7.6) below, several different reactions may take place, see fig. 7.5. Holes arriving beneath the Au grid will be effectively annihilated, equation (7.7), generating heat and contributing to Ib.

$$h^+(Si) \rightarrow h^+(TiO_2) \tag{7.6}$$

$$h^+(TiO_2) + e^-(Au) \rightarrow \text{heat} \tag{7.7}$$

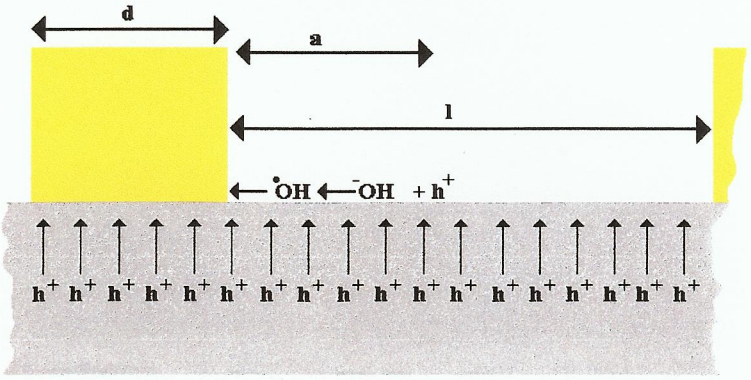

Figure 7.5. The model to describe hole annihilation and capture at the TiO_2 surface. The grid thickness is d, *grid separation is* l *and the diffusion length at the OH radicals is a.*

Holes arriving at the TiO_2 surface physically close to the gold gridlines can hop to the gold where they can be captured, at the metal surface, contributing both to the electrochemical response of the grid (i.e. electrons crossing the grid/electrolyte interface) and I_b. If the holes are not captured by the gold grid, then they may react with water or OH^- ions [40] generating OH radicals at the TiO_2 surface (equation 7.8);

for convenience we may take OH radicals as the hole carriers at the surface, as typical diffusion lengths (*a* in fig. 7.5) are known for these species, of 20 to 75 μm [41-43].

There are several fates for the OH radicals generated at the TiO_2 surface: they may be captured by the gold surface, generating initially AuOH (equation (7.9)), they may re-inject a hole into a suitable surface state of the TiO_2 (see below), they may react with other radical species to generate peroxy compounds, or they may react with adventitious oxidisable impurities. When a grid separation of 1000 μm and a grid width of 375 μm is used and the diffusion lengths quoted above, between 4 and 17% of the bias current goes on to produce OH radicals in a region where subsequent capture by the gold surface is possible. Once the gold is covered with AuOH species, then further interaction with OH radicals may generate oxygen, especially at higher values of V_b:

$$h^+ + TiO_2 + H_2O \rightarrow HO^\bullet + H^+ \qquad (7.8)$$

$$HO^\bullet + Au \rightarrow AuOH \qquad (7.9)$$

$$2AuOH + 2h^+ + TiO_2 \rightarrow 2Au + O_2 + 2H^+ \qquad (7.10)$$

At sufficiently high V_b there is the possibility of still more interesting electrochemistry, as surface states (see fig. 7.6) have been postulated at energies that span almost the entire band-gap of TiO_2: these include states at 1 eV below the conduction band edge [44, 45], 0.5 eV above the valence band edge [46], 1.8 eV above valence band edge [47], and 1.3 – 3.2 eV below conduction band edge [48]. Such surface states could provide acceptor sites at the surface for highly energetic holes. These surface states may then drive quite new electrochemical reactions.

Finally, at sufficiently positive V_b, holes may be sufficiently energetic to be captured by the valence band at the TiO_2 surface, effectively opening up new channels for holes at the surface of the TiO_2. It is clear, then, that the model predicts the possibility of some highly novel chemistry being generated by this composite system, the novelty arising from the presence of highly oxidising species arriving at the surface from the interior of the electrode. In some respects, this is similar to the photoelectrochemical

phenomena observed on TiO_2, but the use of an auxiliary gold electrode permits us to tune the surface in a way that is not really possible with simple photoelectrochemical devices.

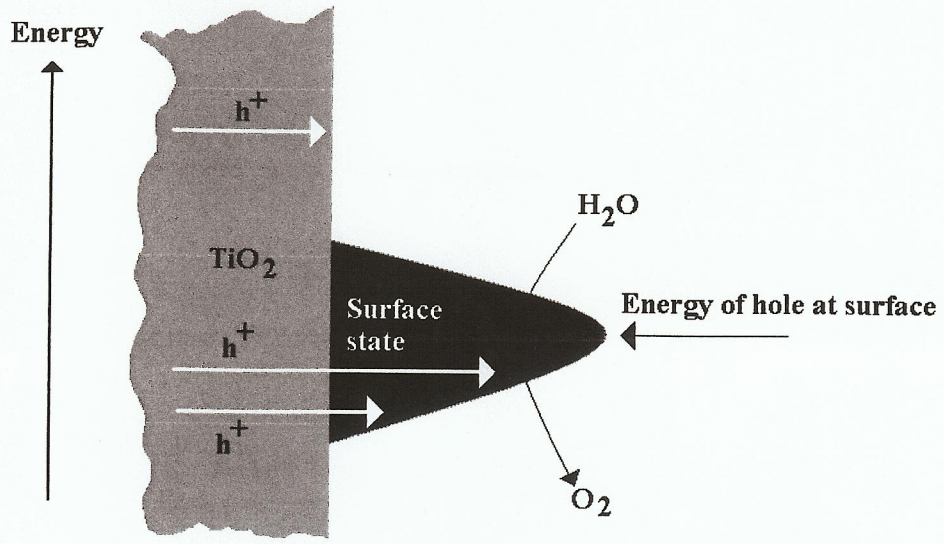

Figure 7.6. Representation of a surface state at TiO_2.

7.1.8. The aims and objectives of this chapter

The aims of the work reported in this chapter were to:

(1) Determine the mechanism by which holes are transported from the Si to the TiO_2 in the composite anodes possible.

(2) Investigate the possible rôles of metal grid and TiO_2 in oxidative processes at the anode electrolyte interface.

(3) To determine the applications of the composite anode technology in, for example, fuel cells and other areas.

7.2. The experimental system

Pictures of a typical Si/TiO_2/Au composite anode, the circuit used to control the bias voltage and the connections to the working electrode (i.e. the gold grid), counter electrode and reference electrode are shown in figures 2.20 to 2.22 in Chapter 2.

There are two components, each comprising two circuits. The first component is the composite anode + external electronic circuit. Electrons flow from gold grid to Si and around the external circuit back to the gold grid and/or holes flow in the opposite direction. In the second component, electrons flow (under anodic potential) from the gold grid and around the external electronic circuit to the cathode, ions transport the charge in the electrolyte, and the two circuits should be thought of as separate.

The results discussed in this chapter were obtained using three $Si/TiO_2/Au$ electrodes, which were three quarter-segments from the same Si wafer.

7.3. Electrochemical studies at $V_b \leq 1$ V

It was decided to start the investigation of the electrochemistry of the $Si/TiO_2/Au$ composite anodes in acid solutions, in order to provide a direct link to the preliminary studies summarized in section 7.1.5 above.

Figure 7.7 shows a more detailed schematic of the wiring of the composite anode, battery circuit (represented by the battery symbol) and potentiostat. For a detailed description of the equipment, including the battery circuit, see section 2.11

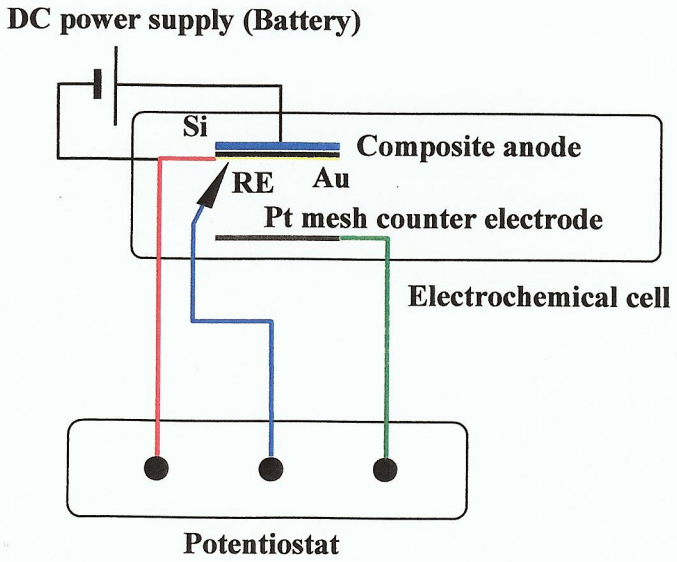

Figure 7.7. Detailed schematic representation of the wiring of the $Si/TiO_2/Au$ composite anodes and the experimental arrangement employed in the cyclic voltammetry experiments.

7.3.1. The current/voltage characteristic of the Si/TiO_2/Au composite electrode in air.

Figure 7.8(i) shows a typical I_b (bias current)/V_b plot for a Si/TiO_2/Au composite anode in air (i.e. not immersed in electrolyte); as may be seen from the plot, at $V_b < 0$ ("forward bias"), the negative current increases steadily with increasing, negative bias voltage. I_b is zero at $V_b = 0$, after which it increases as V_b increases to more positive values until, at $V_b \approx 0.25$ V, there appears to be a significant change in behaviour, as the bias current shows very little dependence upon the electric field across the electrode. The weak field dependent region at $V_b > 0.25$V suggest that: (1) a fraction of V_b is dropped in the TiO_2 and (2) that the thermal generation of holes in the Si is rate limiting. The latter postulate is supported by the data in fig. 7.8(ii) & (iii), which shows plots of bias current vs. bias voltage obtained during the irradiation of a Si/TiO_2/Au anode by a (ii) 635 nm and (iii) 1550 nm LED, compared to the response obtained in the dark (i).

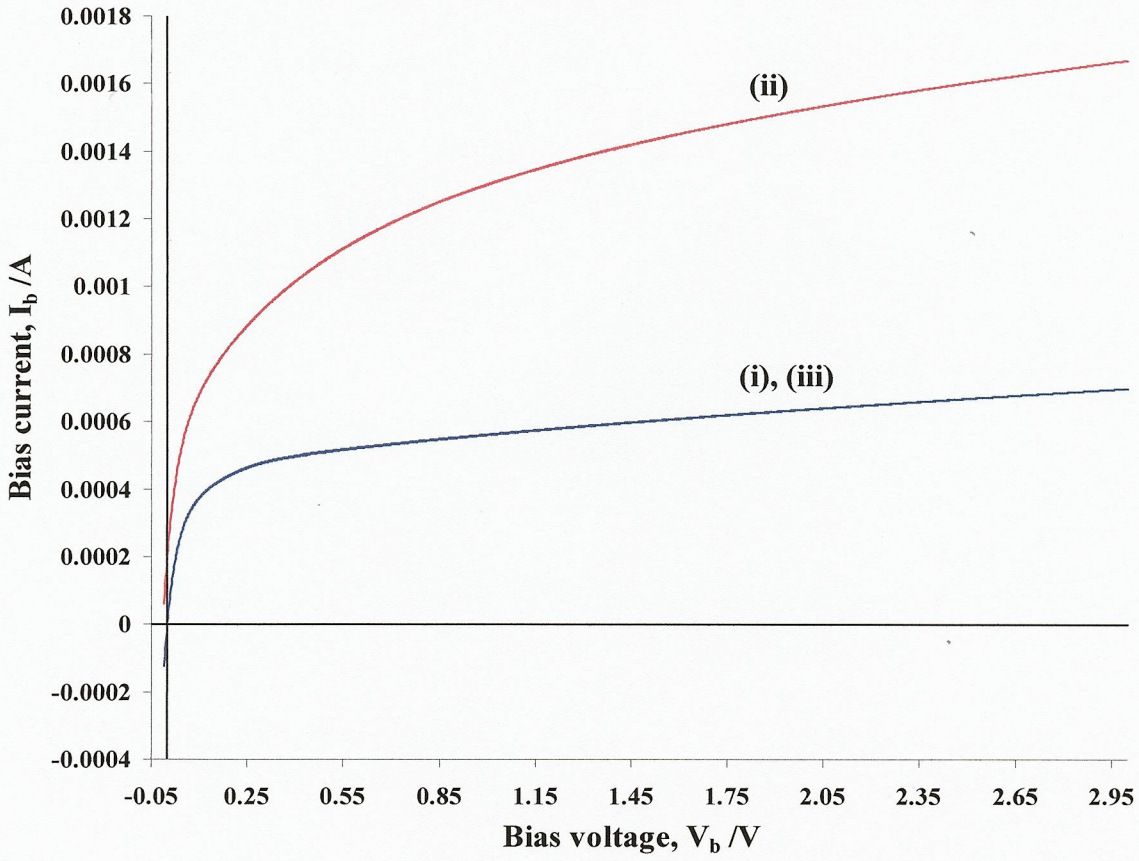

Figure 7.8. Bias current vs. voltage plots for a Si/TiO_2/Au composite anode (i) in the dark, (ii) irradiated by a 635 nm, 4.0 mW LED and (iii) irradiated by a 1550 nm, 2.0 mW LED. The LED's were positioned 1 mm from the TiO_2/Au face of the anode.

The intensities of these two sources (in terms of photon flux) were chosen to be comparable. As may be seen from the figure, whilst the visible LED is incapable of exciting electrons in the TiO_2, it gives a clear photocurrent through excitation of the Si. In contrast, the near-IR is incapable of exciting electrons in either material. In addition, an experiment was conducted in which a Cole Palmer 150 W metal halide lamp/fibre optic system was employed to irradiate the TiO_2 face of the composite anode and the bias current was found to vary as √(intensity), supporting the postulate that the current is dominated by electron/hole recombination in the Si [48].

7.3.2. The initial Cyclic Voltammetry studies.

It was found that the electrochemical response of the composite anodes showed two distinct regions of behaviour, $V_b < 1$ V and $V_b > 1$ V.

Figure 7.9 shows cyclic voltammograms of the composite anode in 0.5 M H_2SO_4 as a function of V_b. With the battery disconnected ($V_b = 0$), the cyclic voltammograms so obtained were very similar to those reported using deposited polycrystalline Au electrodes under similar experimental conditions by other workers [49, 50].

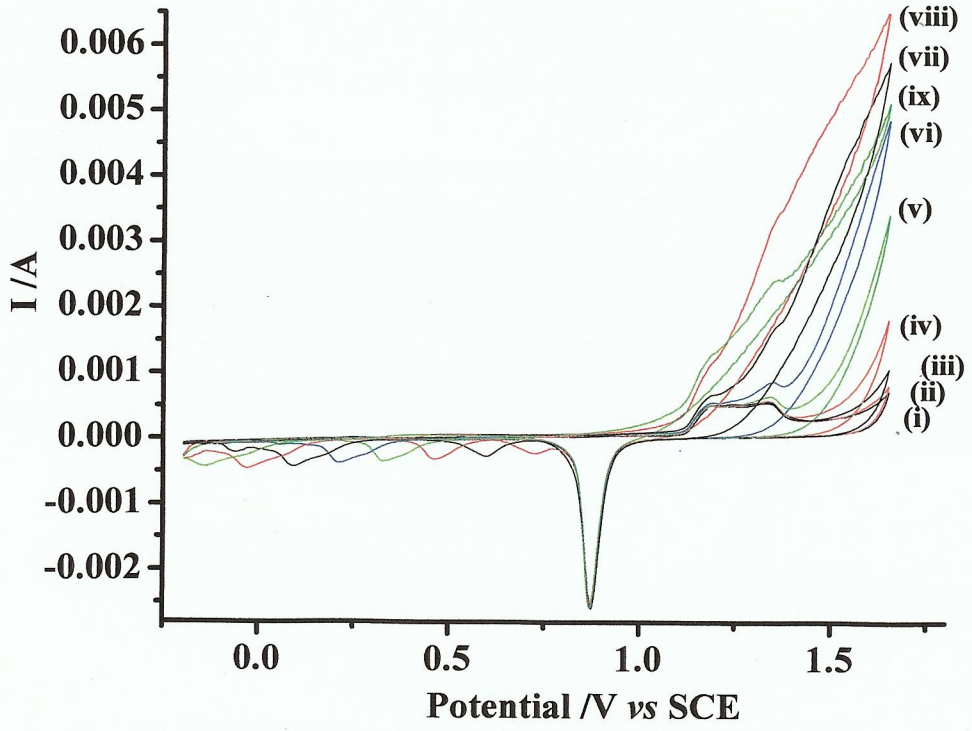

Figure 7.9. Cyclic voltammograms of the composite anode in 0.5 M H_2SO_4 as a function of V_b from (i) 0 V to (ix) V_b = 0.8 V in 0.1 V increments. Scan rate 100 mVs^{-1}.

Using 390 μC cm^{-2} for the charge under the oxide stripping peak [51] near 0.87 V gives an area of 4.4 cm^2, suggesting a roughness factor of ca. 2.

The application of a bias voltage across the composite anode clearly has a major effect upon the electrochemical behaviour of the Au grid. At V_b = 0.1 V, a small anodic current appears to underlie the anodic sweep of the Au voltammogram at potentials > 1.5 V. With increasing V_b, the magnitude of this underlying anodic (and irreversible) current increases, and the onset moves towards more cathodic potentials. The oxide stripping peak near 0.87 V on the cathodic sweep appears to be unaffected by V_b, as do the oxide formation peaks in the anodic sweep; the latter just appear to be superimposed upon the exponentially rising, underlying current. No deterioration of the Au grid electrode was observed in terms of its physical appearance or the charge under the oxide stripping peak near 0.87 V. Similarly, there was no variation in the oxide formation and stripping peaks at V_b = 0 over a number of experiments.

Given the completely unexpected electrochemical response in fig. 7.9, it was decided to carry out a "blank experiment" in which one terminal of a 100 Ω resistor was connected to the counter and reference electrode outputs of the potentiostat. The other terminal of the resistor was connected to one contact of the Au grid and the other contact on the grid connected to the working electrode output of the potentiostat. The Au grid was connected to the Au Ohmic contact on the Si *via* the battery, see fig. 7.10.

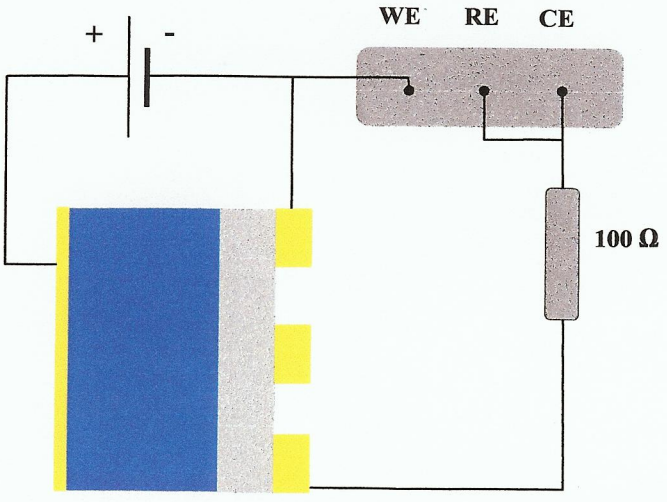

Figure 7.10. The wiring employed in the blank experiment employing the 100 Ω resistor. (See text for details).

The potential of the Au grid with respect to the (counter + reference) electrodes was cycled between -1 V and +1 V (see fig. 7.11) as a function of the bias voltage V_b.

The red plot in fig. 7.11 was the response observed when the 100 Ω resistor was omitted and the RE and CE outputs on the potentiostat were connected directly to the Au grid. The slopes of the two lines correspond to 102 Ω and 2 Ω; i.e. the resistance of the resistor + Au grid and the resistance across the Au grid alone, respectively. The expected ohmic response of the resistor was unaffected by V_b, hence ruling out any electronic artefactual effects being responsible for the results in fig. 7.9

Given the relatively simple composition of the electrolyte in the experiment in fig. 7.9, and the absence of any evidence for the dissolution of the Au grid, the only likely process to account for the V_b-dependent anodic currents observed in the figure is the oxidation of water.

In contrast to the increasing anodic current observed at high potentials as V_b is increased, there is little change in the cathodic sweep of the voltammograms in fig. 7.9 apart from the appearance of a small cathodic peak at V_b = 0.1 V which moves cathodic as V_b is increased, see fig. 7.12.

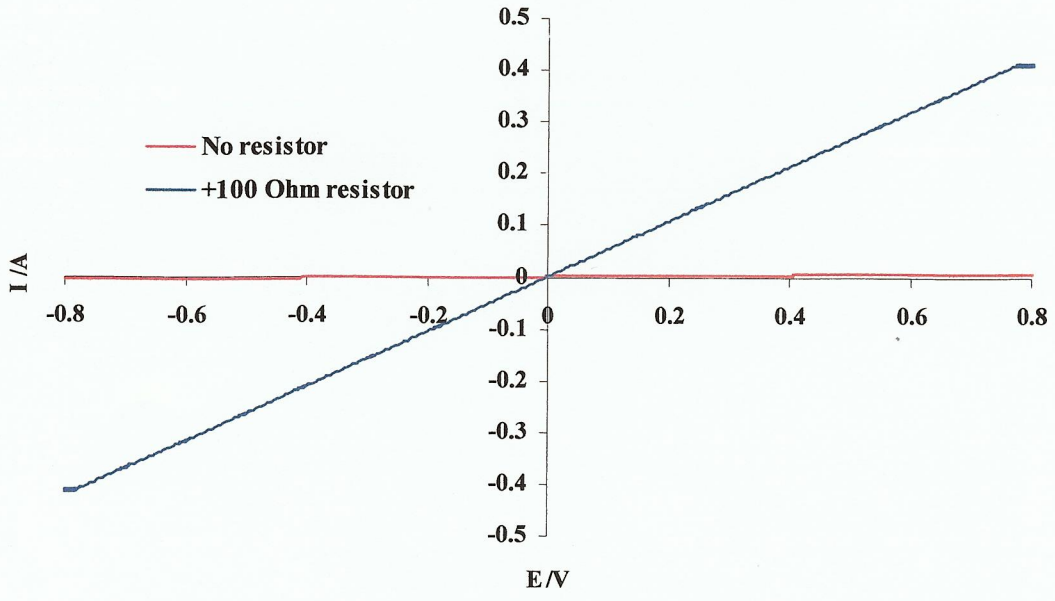

Figure 7.11. Cyclic voltammograms obtained using the circuit in fig. 7.10. The red line is the CV obtained without the 100 Ω resistor, i.e. RE and CE outputs on potentiostat connected directly to Au grid.

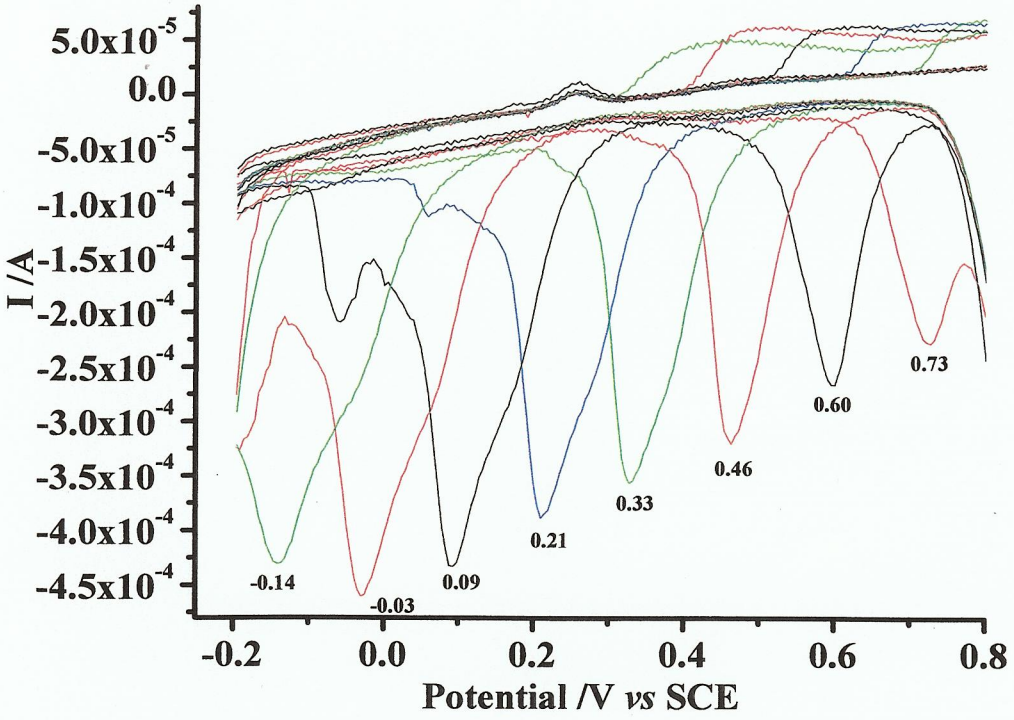

Figure 7.12. The potential region from -0.2 V to 0.8 V vs. SCE of the CV's in fig 7.9.

A plot of peak current of the small cathodic peak vs. V_b is shown in fig. 7.13(a), and of its peak potential vs. V_b in fig. 7.13(b).

The peak current increases essentially linearly with V_b between V_b = 0.1 V and 0.7 V, before decreasing at 0.8 V. The slope of the plot between 0.1 V and 0.7 V in fig. 7.13(a) is 3.9 ± 0.2 x 10^{-4} Ω^{-1}. At V_b > 0.5 V a peak grows in to the cathodic side of the small cathodic peak.

The plot of the small peak potential vs. V_b is a straight line with a slope of -1.2 ± 0.01, see fig. 7.13(b). The intercept at V_b = 0 is 0.84 ± 0.01 V, under the oxide stripping wave, but not at the same potential as the peak current (0.87 ± 0.01 V). Again, given the simplicity of the chemical composition of the system under investigation, the small cathodic peak is probably due to the re-reduction of small regions of the Au grid, most likely the perimeter with the TiO_2, oxidised during the anodic sweep. The area under the small cathodic peak observed at V_b = 0.2 V is ca. 12% of that calculated from the charge under the stripping peak near 0.87 V, equivalent to a surface area of

0.5 cm^2, suggesting an active 'depth' of the gold grid of ca. 27 μm contributing to the small cathodic peak.

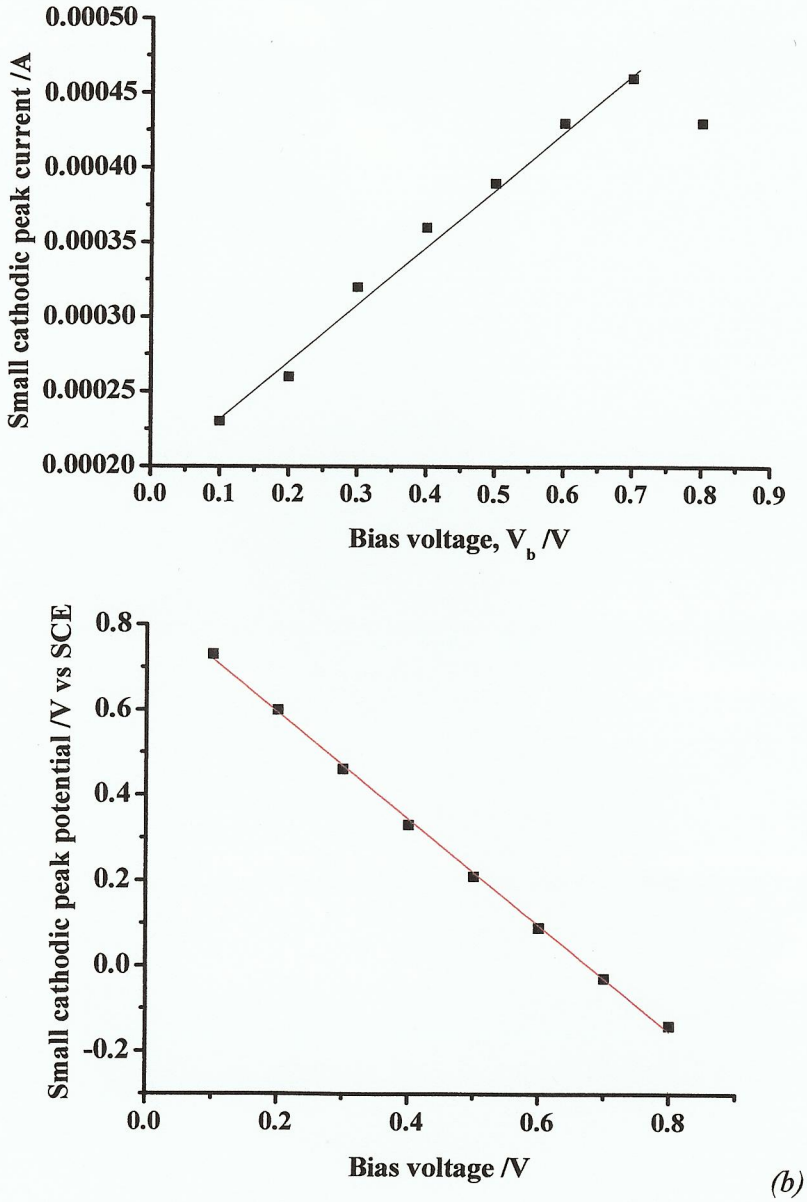

Figure 7.13. Plots of (a) the peak current of the small cathodic peak in figs 7.9 & 7.12 vs. V_b and (b) the peak potential of the small cathodic peak vs. bias voltage (V_b).

7.3.3. The effect of the anodic limit and scan rate on the voltammetric response

It was decided to determine if the appearance of the small cathodic peak depended upon the electrochemical potential cycling through the oxide formation and stripping potentials. To this end, the anodic limit was set at 1.1 V i.e. below the onset of oxide formation on the Au grid (see fig 7.9), and the voltammetric response recorded as a

function of bias voltage, see fig. 7.14(a). Figures 7.14(b) and (c) show the CV's in fig. 7.14(a) collected at no bias and V_b = 0.5 V & 0.9 V; fig. 7.14(c) shows a restricted current range to highlight the effect of the bias voltage.

As expected, the CV recorded without an applied bias voltage is featureless; however, at $V_b \geq 0.2$ V an anodic wave (I) and a cathodic wave (II), similar to those associated with Au oxide formation and stripping appear, see fig. 7.14(b) & (c); the onset potential of the former and the peak potential of the latter move cathodic as V_b is increased, and the charges under both features increase. Table 7.1 shows various characteristic of the voltammograms in fig. 7.14(a) & (b); specifically the onset potential of peak (I) and O_2 evolution (assuming the irreversible exponential increase in current observed at high anodic potentials in figs. 7.14(a) & (b) is O_2 evolution; a not unreasonable assumption given the simple composition of the electrolyte) and the peak potential of peak (II).

The shift in cathodic peak potential resembles the behaviour of the oxide stripping peaks on Pt and gold electrodes when the anodic potential limits increases.

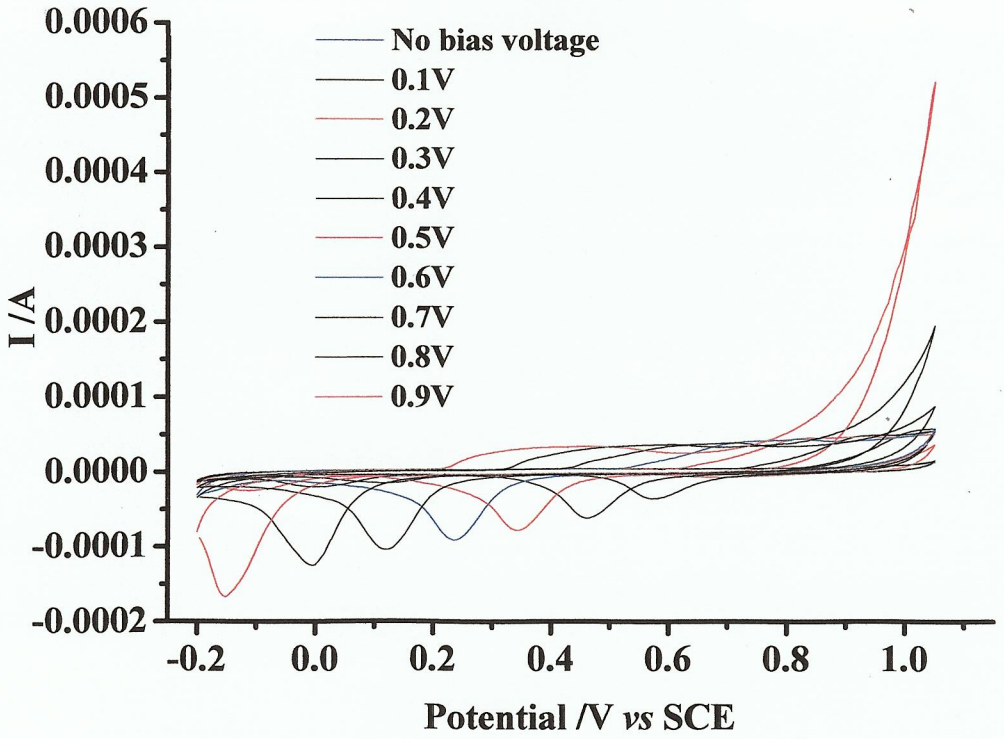

(a)

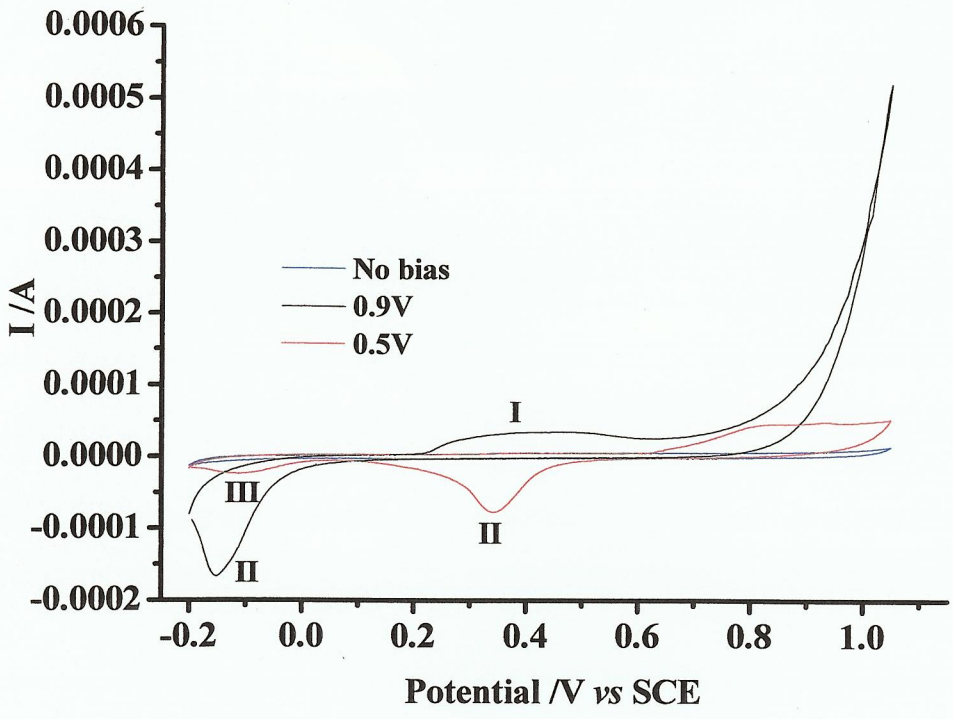

(b)

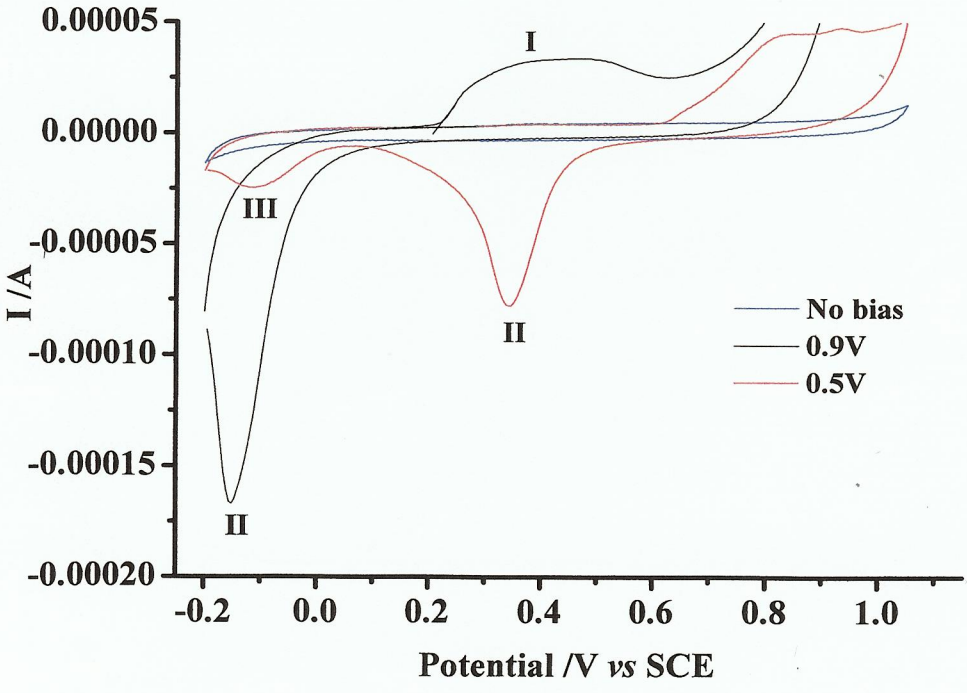

(c)

Figure 7.14. Cyclic voltammograms of the Si/TiO_2/Au composite anode as a function of bias voltage (V_b). (a) Full range of V_b (b) & (c) the CV's taken at V_b = 0, 0.5 V and 0.9 V in (a).

V_b/V	Peak (I) onset potential /V vs. SCE	Peak potential peak (II) /V vs. SCE	Onset of O_2 evolution /V vs. SCE
No bias	-	-	-
0.5	0.62	0.34	1.09
0.9	0.18	-0.15	0.64

Table 7.1. Characteristics of the voltammograms in fig. 7.14(a) & (b)

Thus fig. 7.15 shows cyclic voltammograms of a 16 cm long, 0.2 mm diameter Au wire coiled to expose 1 cm^2 to the 0.5 M H_2SO_4 electrolyte as a function of the anodic limit of the CV. As may be seen from the figure, the oxide stripping peak increases in charge and moves steadily more cathodic as the anodic potential limit is increased. Thus, a first approximation to the data in fig. 7.14(a) is that the actual anodic limit of the CV's in the figure ($E_{a\,act}$) may be written as:

$$E_{a,act} = E_{a,m} + V_b \tag{7.11}$$

Where $E_{a,m}$ is the anodic limit imposed by the potentiostat.

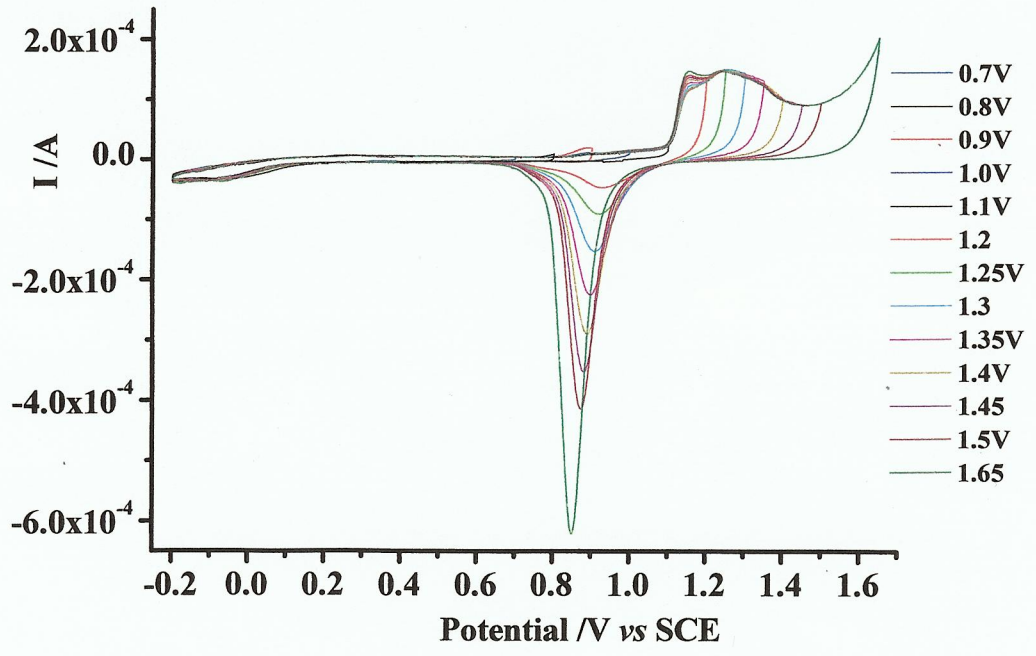

Figure 7.15. Cyclic voltammogramms of a 0.2 mm diameter. 16 cm long Au wire immersed in 0.5 M H_2SO_4 at a scan rate of 100 mV s^{-1}.

This postulate is supported further by the data in fig. 7.16(a) which shows a plot of the peak potential of peak (II) as a function of V_b, the plot has a slope of -1.2, almost the same as the slope of the analogous plot in fig. 7.13(b). However, fig. 7.16(b) shows the corresponding plots for the data in fig. 7.15. Whilst the plot in fig. 7.15 is again linear, the slope is ca. -0.2, suggesting a significantly weaker dependence of the gold wire oxide stripping peak position on the anodic limit compared to the dependence of peak (II) on V_b.

It is also clear from fig. 7.14(b) and figs. 7.17(a) & (b) (the latter show the CV's collected at V_b = 0.5 V and 0.9 V in fig. 7.14(a), respectively) that increasing the bias voltage not only decrease the peak potentials of (I) and (II), but also cause marked changes in the shapes of the features. This argues against the simple 'additive' relationship represented by equation (7.11); furthermore, a second reduction wave is observed (III in figs. 7.14(b) & (c) and 7.17(a)) which behaves in concert with peak II, moving more cathodic as V_b increased and showing a linear dependence of peak potential with V_b, see fig. 7.18, having a slope of ca. -0.97. The peak potential of III moves < -0.2 V vs. SCE when V_b > 0.5 V.

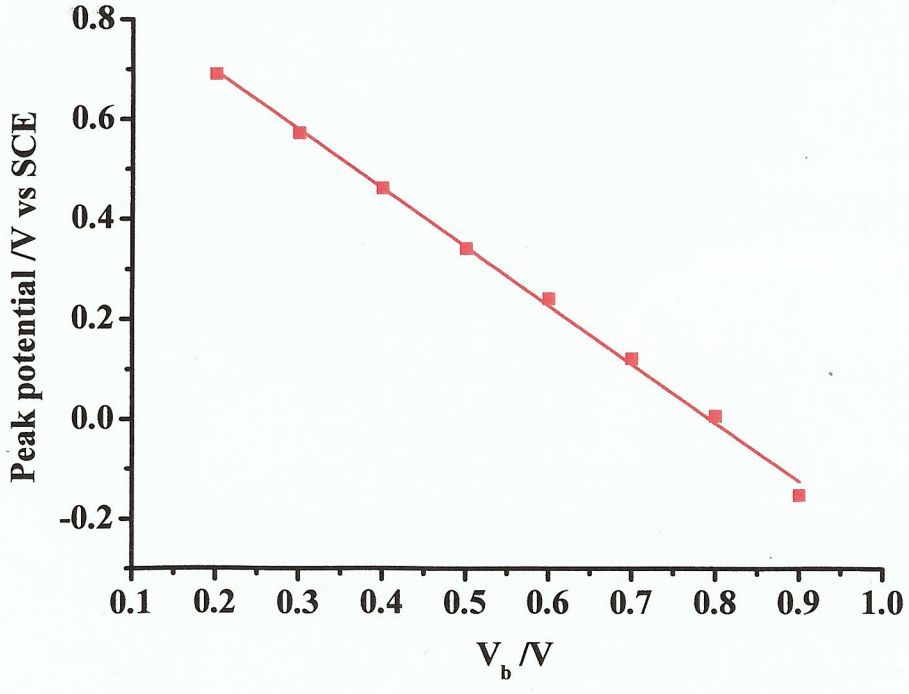

(a)

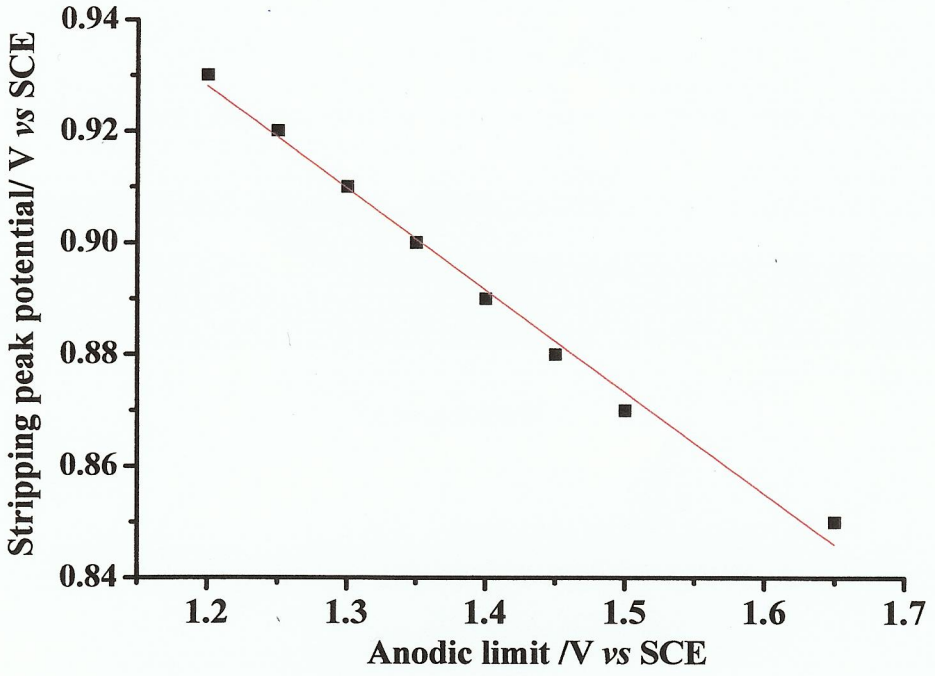

(b)

Figure 7.16. (a) Peak potential of peak (II) in fig. 7.14(b) & (c) as a function of V_b, (b) peak potential of peak (II) in fig. 7.15 as a function of anodic potential limit.

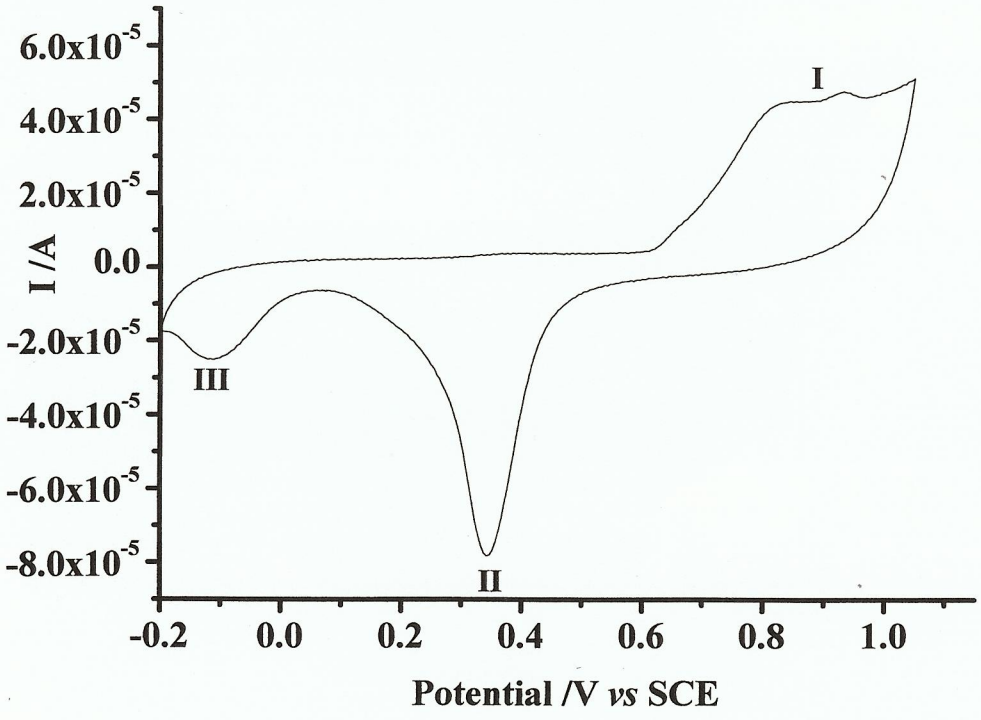

(a)

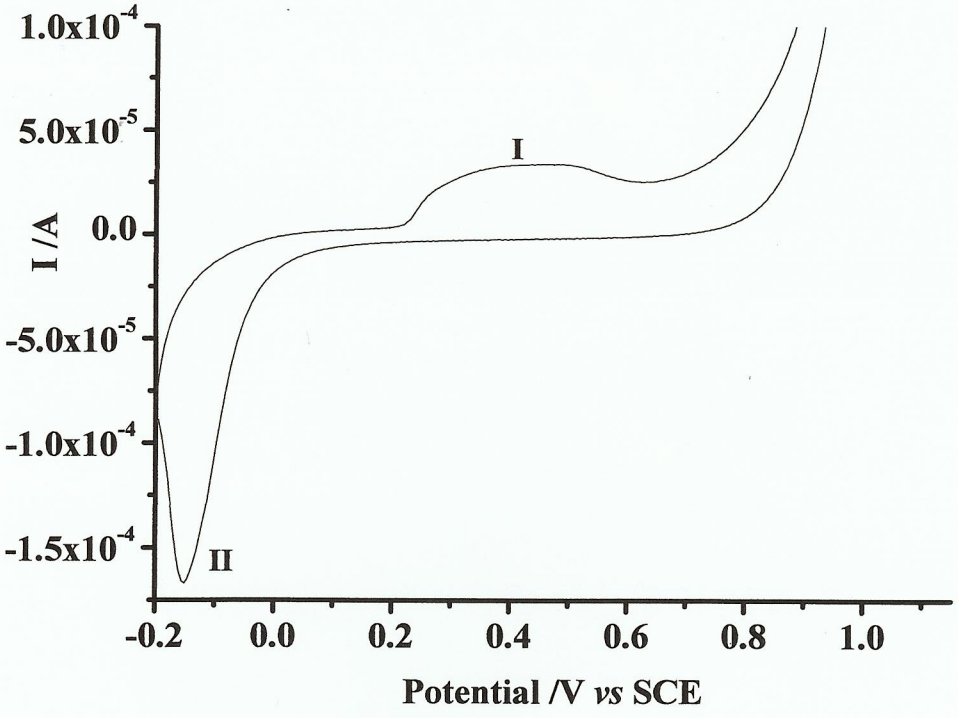

(b)

Figure 7.17. Cyclic voltammograms collected at (a) 0.5 V bias, and (b) 0.9 V bias in fig. 7.14(a)

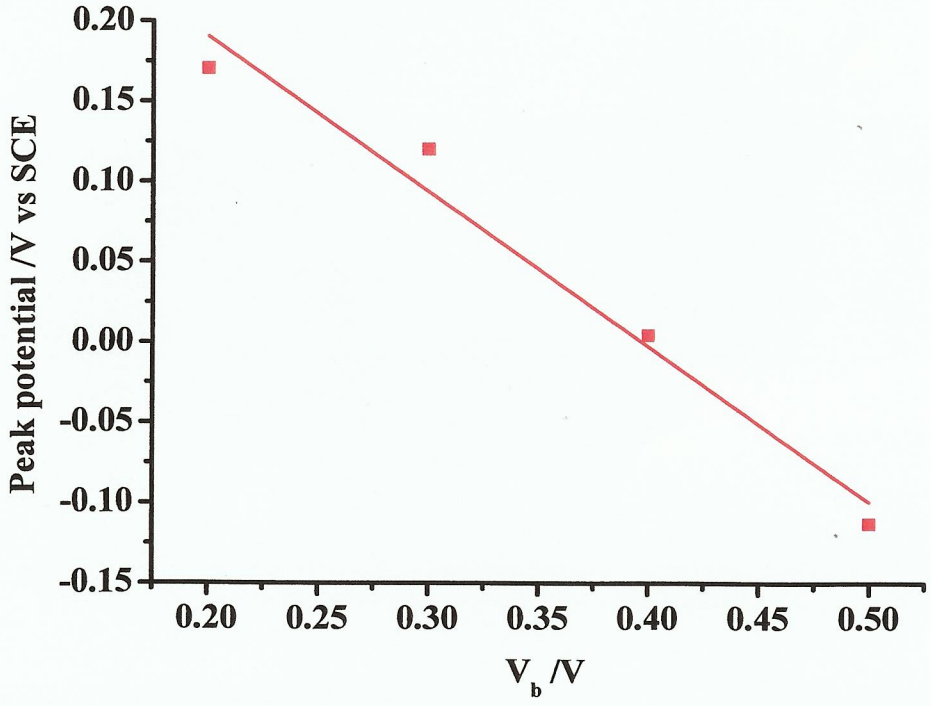

Figure 7.18. Peak potential of peak III in figs. 7.14(b) & (c) and 7.17(a) as a function of V_b.

The charge under peak I in the anodic sweep of the CV collected at the V_b = 0.5 V in figs. 7.14(a)-(c) was ca. 1.6 x 10^{-4} C; this is identical (within experimental error) to the sum of the cathodic charges under peaks II and III.

From the discussion above it appears that applying a bias voltage between the Si and the Au grid of the composite anodes increases the electrochemical potential experienced by the latter, but not in a straightforward manner, in that the electrochemistry observed is not the same as when the electrochemical potential does not have a component supplied by V_b.

In order to investigate the possible origin of the various features in fig. 7.14(a)-(c), scan rate dependence experiments were carried out.

Figures 7.19(a) & (b) show voltammograms collected as a function of scan rate at two bias voltages, 0.3 V and 0.5 V, and figs. 7.19(c) & (d) show the voltammograms collected at 500 mV s^{-1} and 10 mV s^{-1} in figs. 7.19(a) & (b) to allow direct comparison.

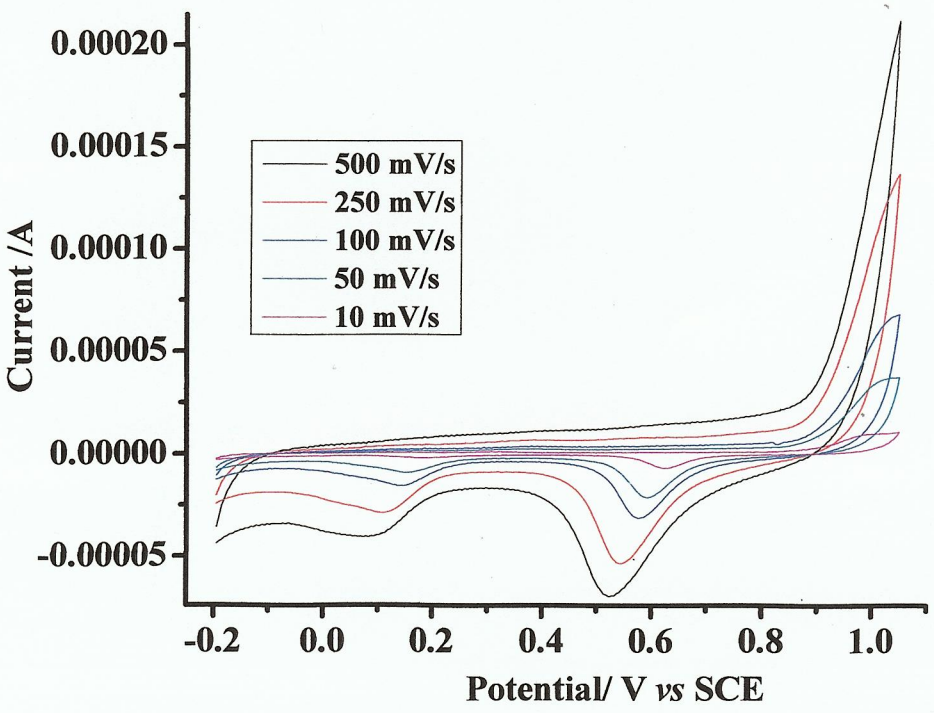

(a)

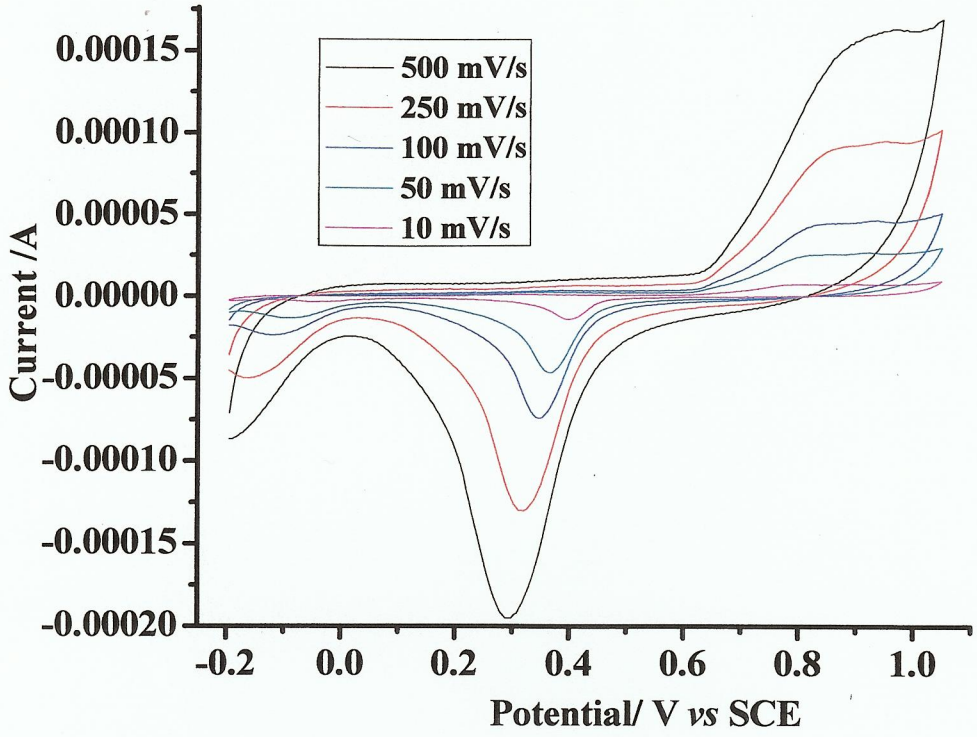
0.00015
0.00010
0.00005
0.00000
-0.00005
-0.00010
-0.00015
-0.00020
Current /A
500 mV/s
250 mV/s
100 mV/s
50 mV/s
10 mV/s
-0.2
0.0
0.2
0.4
0.6
0.8
1.0
Potential/ V vs SCE

(b)

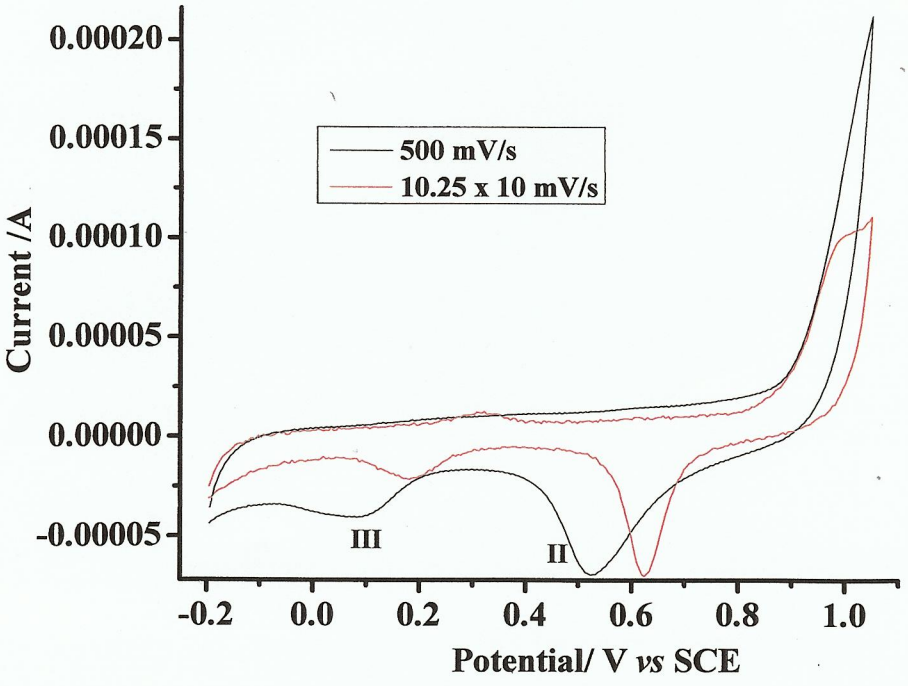
0.00020
0.00015
0.00010
0.00005
0.00000
-0.00005
Current /A
500 mV/s
10.25 x 10 mV/s
III
II
-0.2
0.0
0.2
0.4
0.6
0.8
1.0
Potential/ V vs SCE

(c)

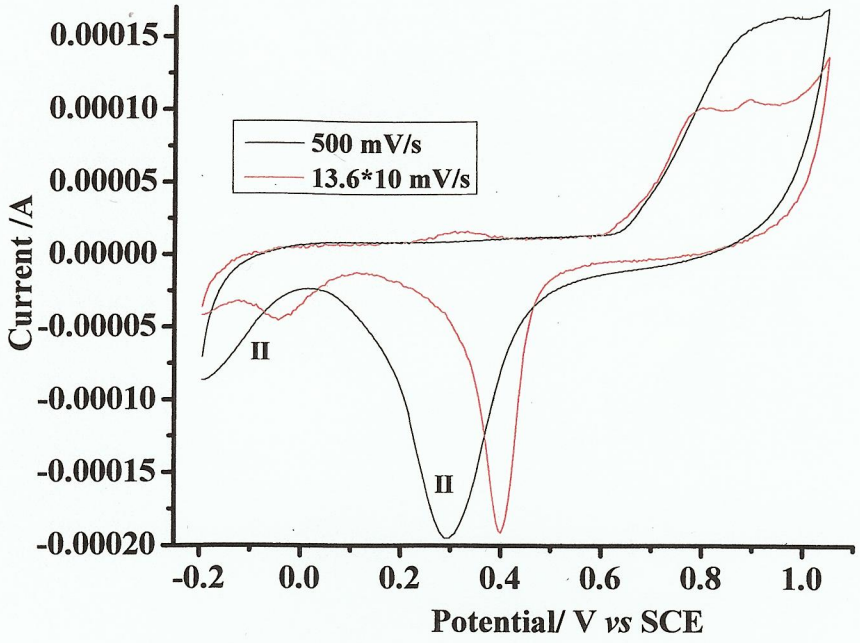

(d)

Figure 7.19. CV of Si/TiO_2/Au electrode at (a) 0.3 V bias , (b) 0.5 V bias as function of scan rate, (c) comparison between 500 mV s^{-1} and 10 mV s^{-1} (x 10.25) in (a), and (d) comparison between 500 mV s^{-1} and 10 mV s^{-1} (xl3.6) in (b).

As may be seen from the figures, increasing the scan rate increases the current of all three features: I, II and III, see fig. 7.19(c) & (d), whilst peaks II and III are broadened and shift to more cathodic potentials. The effect of increasing the bias potential is to move the small cathodic peaks II and III to lower potentials.

Figure 7.20 show plots of peak current vs. square root of scan rate for peaks II and III in figs. 7.19(a) and (b); all are linear with non-zero intercepts. Table 7.2 summarize the slopes of the plots in fig. 7.20.

It is clear that both peaks vary with √(scan rate), show different slopes to each other and that these slopes vary with V_b. This suggest either the reduction of solution species rather than a surface process, unlikely given the voltammetry observed above, or the participation of a surface state on the TiO_2: perhaps holes arriving and emptying the surface states of electrons which are replenished by oxidizing a species in solution (most likely $H_2O \rightarrow O_2$).

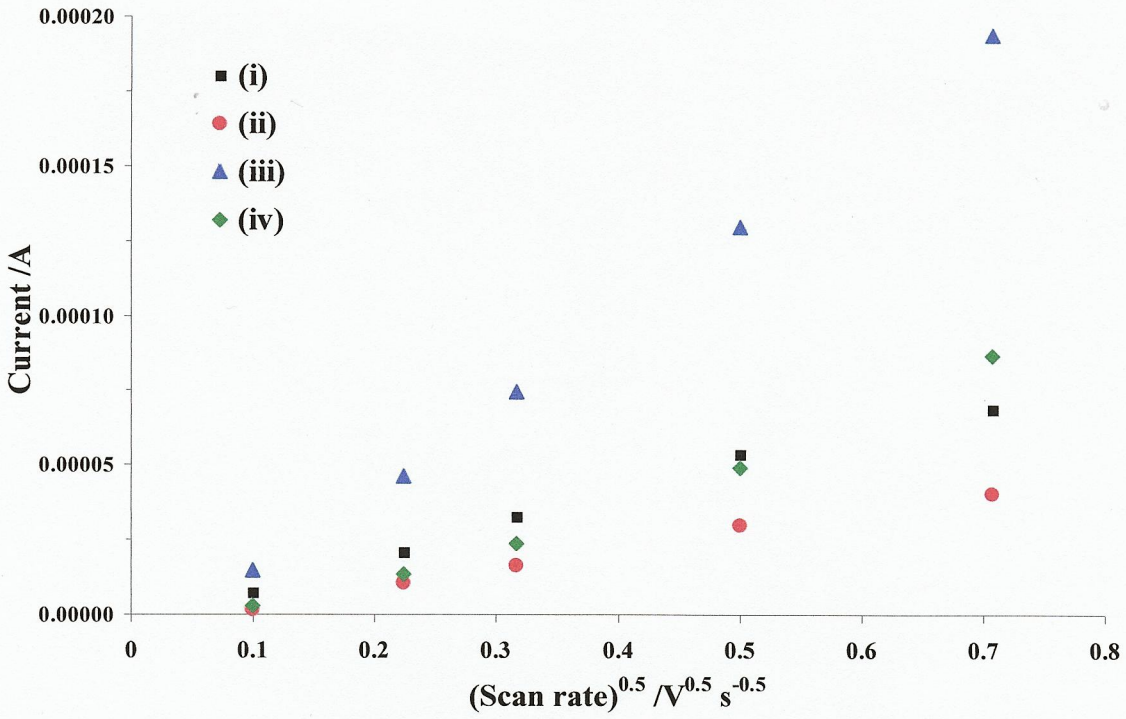

Figure 7.20. Plots of peak current vs. √Scan rate for the cathodic peaks in figs. 7.19(a) & (b). (i) Peak II V_b = 0.3 V, (ii) peak III V_b = 0.3 V, (iii) peak II V_b = 0.5 V and (iv) peak III V_b = 0.5 V.

Peak	Slope /10^{-4} A $V^{-0.5}$ $s^{0.5}$	
	V_b = 0.3 V	V_b = 0.5 V
II	1.0	3.0
III	0.6	1.4

Table 7.2. Slopes of the plots in fig. 7.20.

7.3.4. The effect of KI on the small cathodic peaks in the Si/TiO_2/Au cyclic voltammetry.

It appears from the data above that the small cathodic peaks II & III are due to some electrochemical process-possibly involving surface states on the TiO_2. It was decided to see if the electrodes could be exchanged between the species responsible for the peaks and a solution redox couple. To this end the I_2/I^- couple was chosen, as its E° lies in the region of the higher of the two cathodic peaks [5].

The response of the composite anode in the absence of KI solution was first checked between -0.25 V and 1.05 V, and the data are shown in fig. 7.21(a) whilst fig. 7.21(b)

shows the CV's collected at V_b = 0.2 V to 0.5 V in fig. 7.21(a), being the V_b range relevant to the potential of the I_2/I^- couple.

There are marked differences in behaviour at $V_b > 0.4$ V, i.e. when higher of the small cathodic peak moves through the $I_2 \rightarrow \frac{1}{2}I^- + e^-$ reduction wave (see fig. 7.21(c)); this enhancement remains when the cathodic peak is negative of the iodine reduction wave. The anodic features of the electrode are enhanced at all the bias voltages, and this may be related to the fact that these features are all positive of the I^- re-oxidation wave. This can be more clearly seen in figs. 7.21(d) which compare the CV's in figs. 7.21(b) and (c) at 0.4 V bias.

Figure 7.21(d) clearly show that, at V_b = 0.4 V i.e. where the higher cathodic peak overlies the I_2 reduction wave, there is a large enhancement of all the features in $Si/TiO_2/Au$ voltammogram, both cathodic and anodic. This would seem to mitigate against the features being due to simple surface oxidation and reduction processes at the gold. Figure 7.21(e) shows the enhancement effect even more strikingly.

The data in sections 7.3.3 and 7.3.4 suggest that the small cathodic peaks (II and III) are due to the reduction of Au-OH at the perimeter line between Au and TiO_2. At V_b = 0 V, peak II lies under the bulk Au oxide stripping peak. The peak areas are very small, hence the total areas under peaks II and III are much smaller than area under bulk stripping peak. As V_b increases, the energy of holes increase which can then penetrate through deeper barriers: i.e. more of Au is oxidised near to TiO_2; thus potential required to reduce Au-OH moves negative (higher overpotential), hence the ca. 1:1 relationship between the peak potentials of II and III and V_b.

The KI data suggests that the Au-OH at the perimeter (peak II) is catalytic:

$$Au\text{-}OH + I^- \rightarrow Au + 0.5I_2 + OH^- \qquad 7.12)$$

$$Au + h^+ + H_2O \rightarrow Au\text{-}OH + H^+ \qquad (7.13)$$

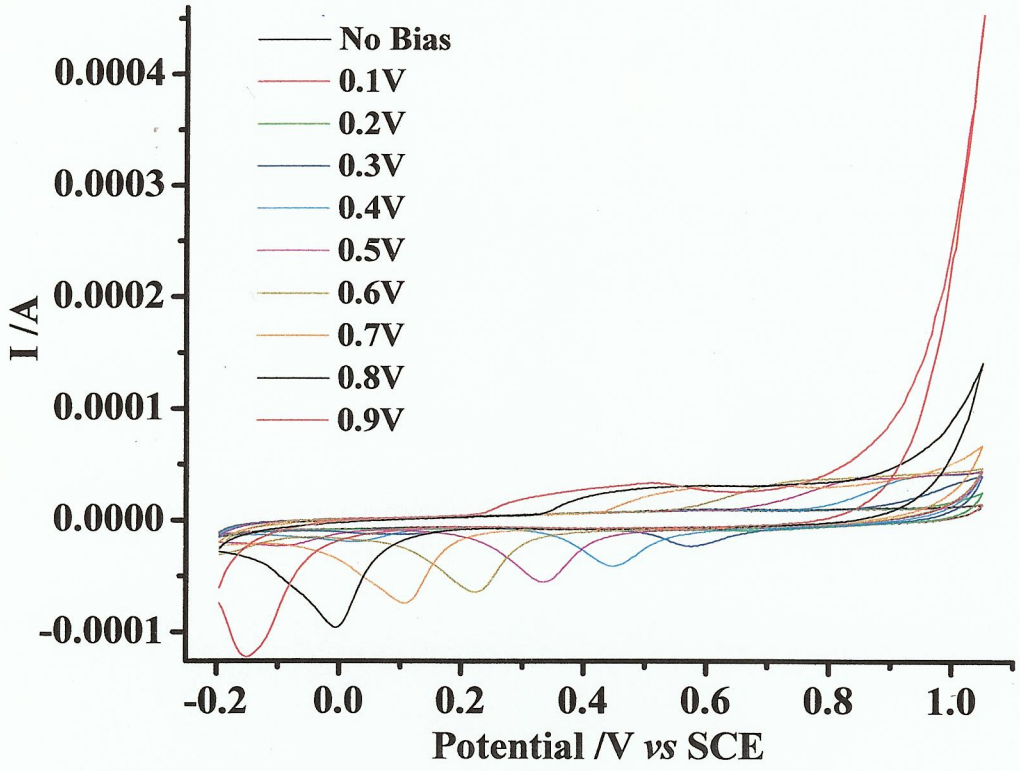
No Bias
0.1V
0.2V
0.3V
0.4V
0.5V
0.6V
0.7V
0.8V
0.9V
0.0004
0.0003
0.0002
0.0001
0.0000
-0.0001
I /A
-0.2
0.0
0.2
0.4
0.6
0.8
1.0
Potential /V vs SCE

(a)

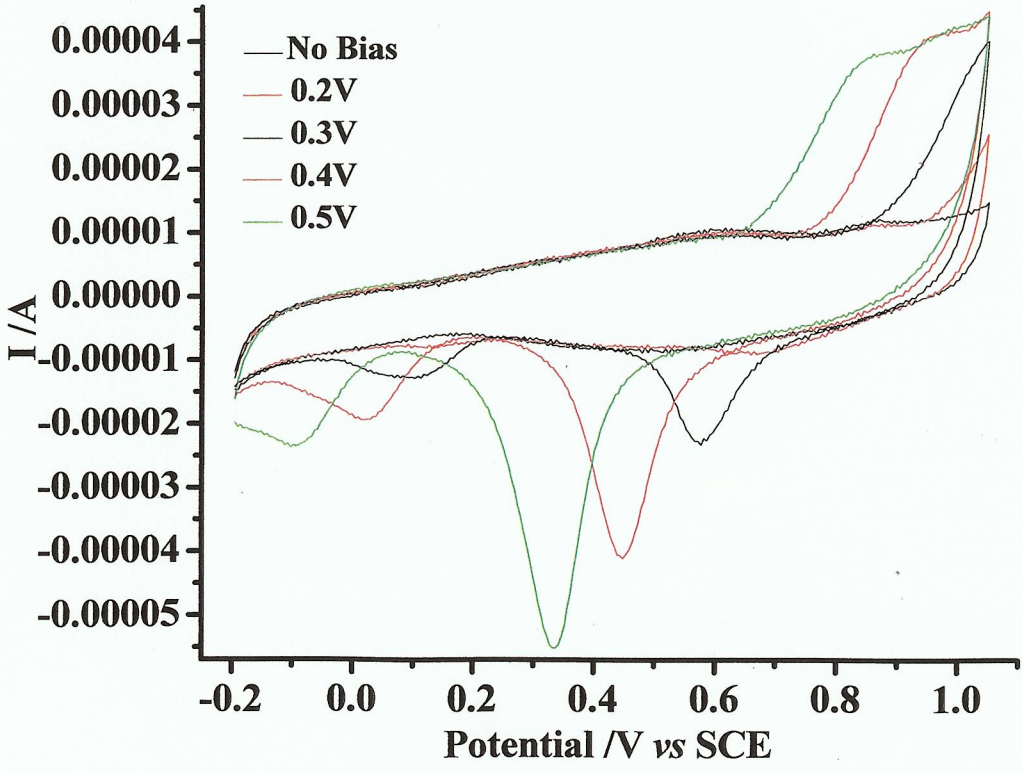
No Bias
0.2V
0.3V
0.4V
0.5V
0.00004
0.00003
0.00002
0.00001
0.00000
-0.00001
-0.00002
-0.00003
-0.00004
-0.00005
I /A
-0.2
0.0
0.2
0.4
0.6
0.8
1.0
Potential /V vs SCE

(b)

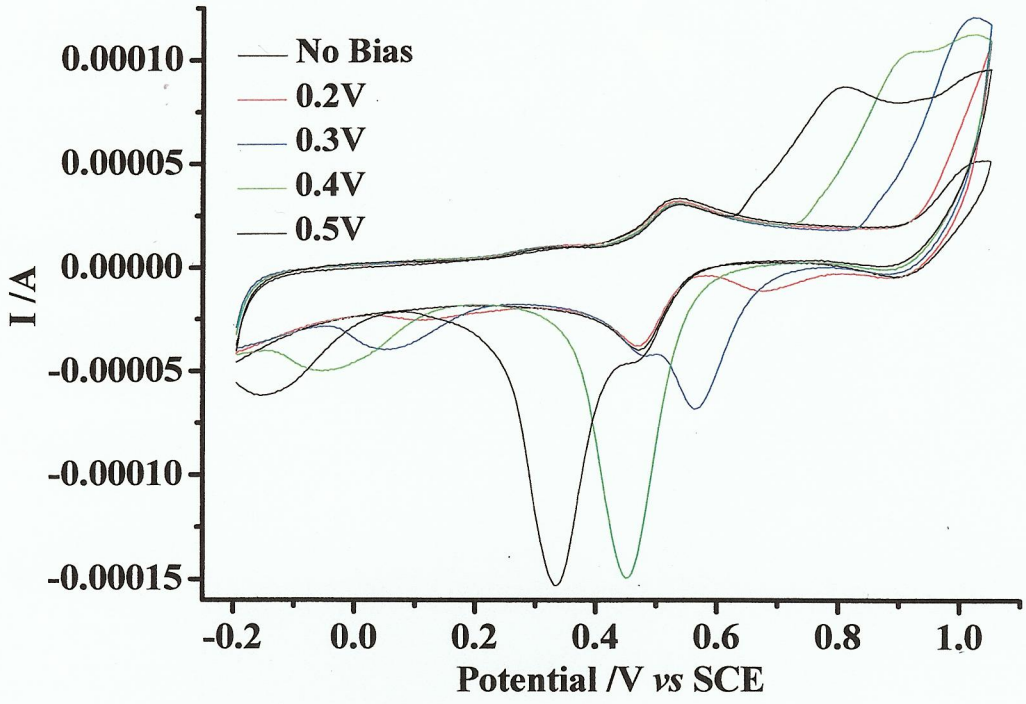
No Bias
0.2V
0.3V
0.4V
0.5V
0.00010
0.00005
0.00000
-0.00005
-0.00010
-0.00015
I /A
-0.2
0.0
0.2
0.4
0.6
0.8
1.0
Potential /V vs SCE

(c)

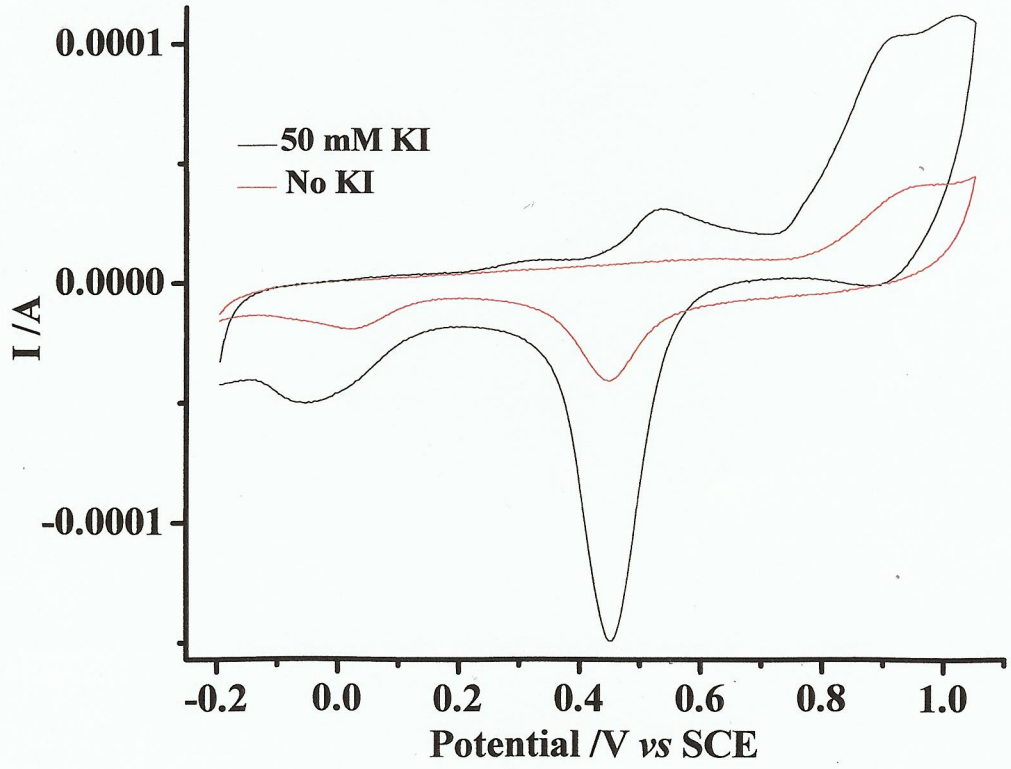
50 mM KI
No KI
0.0001
0.0000
-0.0001
I /A
-0.2
0.0
0.2
0.4
0.6
0.8
1.0
Potential /V vs SCE

(d)

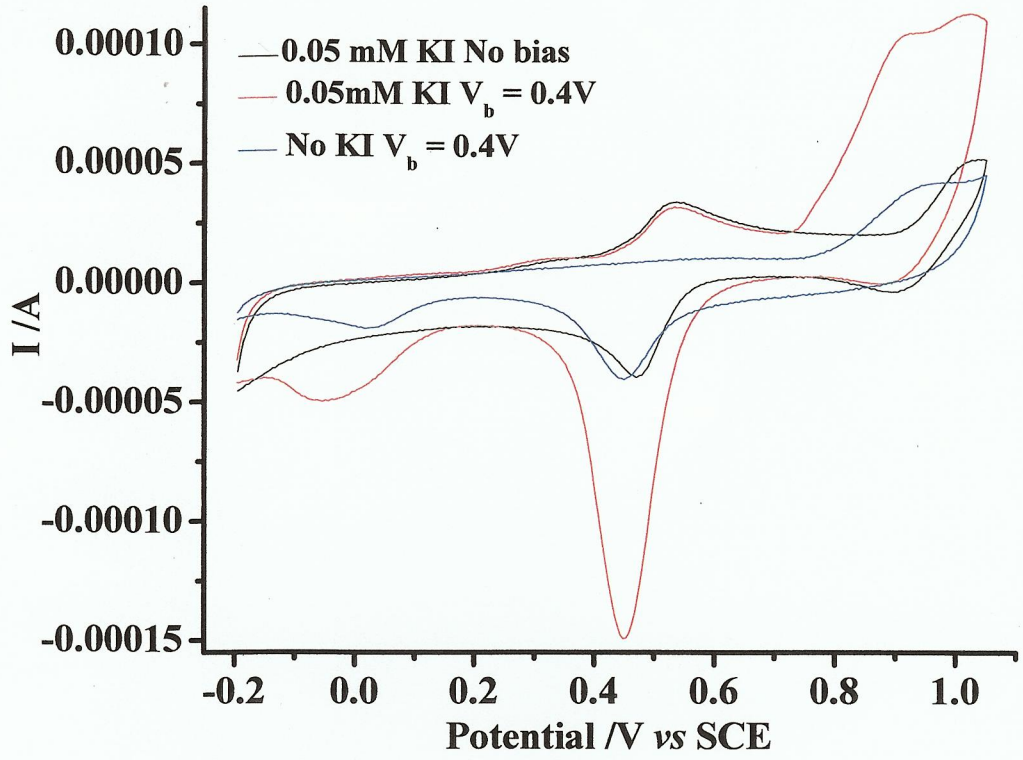

(e)

Figure 7.21. Cyclic voltammograms of (a) Si/TiO_2/Au electrode in 0.5 M H_2SO_4 as function of bias voltage V_b,, (b) CV's collected at V_b = 0.2 V to 0.5 V in (a), (c) CV's collected at V_b = 0.2 V to 0.5 V in 0.5 M H_2SO_4 + 0.05 mM KI, (d) Direct comparison of CV's at V_b =0.4 V from figs, (b) and (c), (e) Enhancement effect of bias voltage in the features of KI redox couple.

7.4. Electrochemical studies at V_b > 1 V

Figure 7.22 shows cyclic voltammograms of a Si/TiO_2/Au electrode in 0.5 M H_2SO_4 at bias voltages between 0.9 V and 2.0 V. As may be seen, at V_b > 1 V, the onset of the 'additional' Faradaic current moves negative, causing the entire voltammogram to 'lift' from the x-axis, with the oxide formation and stripping peaks superimposed upon this current. The situation at V_b > 1 V corresponds to the accessing of surface states on the TiO_2 (see section 7.1.7 and figure 7.6).

There appears to be a linear (Ohmic) dependence of the electrochemical current on the potential at $V_b \leq 1.0$ V. This is confirmed by the plot in fig 7.23, which shows the anodic sweep of the voltammogram collected at zero bias in fig 7.9 subtracted from

that taken at V_b = 1.0 V in fig 7.22, in order to remove the response due to oxide formation.

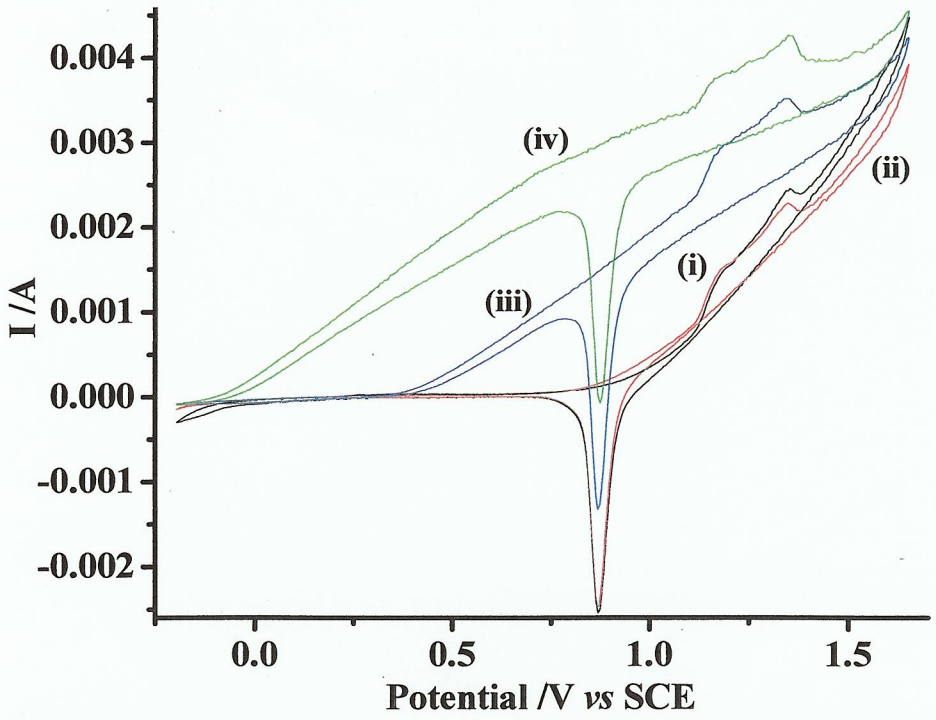

Figure 7.22. Cyclic voltammograms of a Si/TiO_2/Au electrode in 0.5 M H_2SO_4 at a scan rate of 100 mV s^{-1} and V_b = 0.9 V (i); 1.0 V (ii); 1.5 V (iii) and 2.0 V (iv).

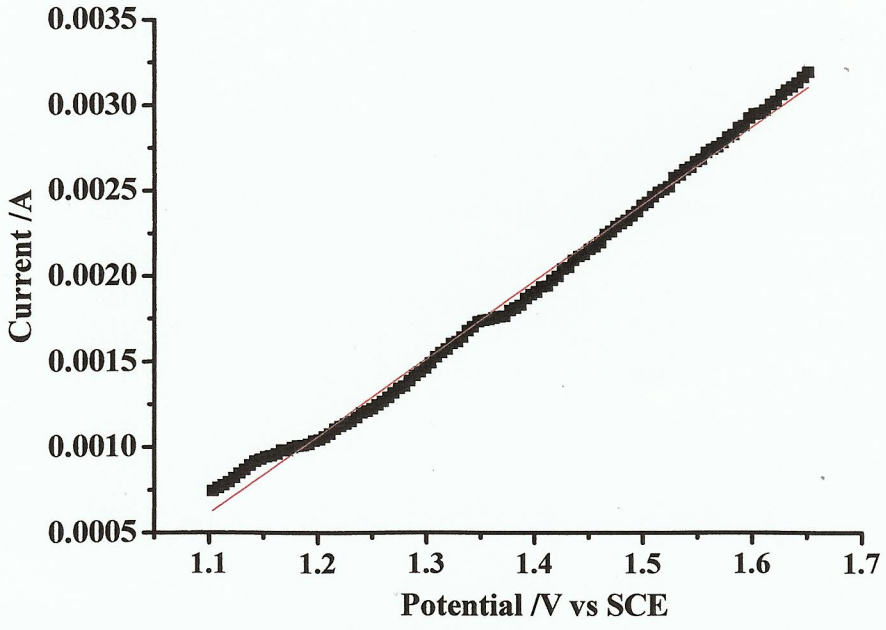

Figure 7.23. Plot of current vs. electrode potential for the experiment at V_b = 1.0V in fig 7.22 in which the corresponding data at V_b = 0 in fig.7.9, were subtracted, see text for details.

As may be seen, the plot is reasonably linear (R^2 = 0.9937) over the region of enhanced current. Further, the plot also shows that the oxide formation features are simply superimposed on the additional current. At higher V_b, i.e. where the model suggests the opening of 'channels' to surface states remote from the Au grid, the current shows a more complicated dependence on potential; over the potential range from 0.4 V to 1.1 V vs. SCE, I^2 appears to be proportional to potential, see fig. 7.24 (R^2 = 0.996); this will be the subject of further investigation.

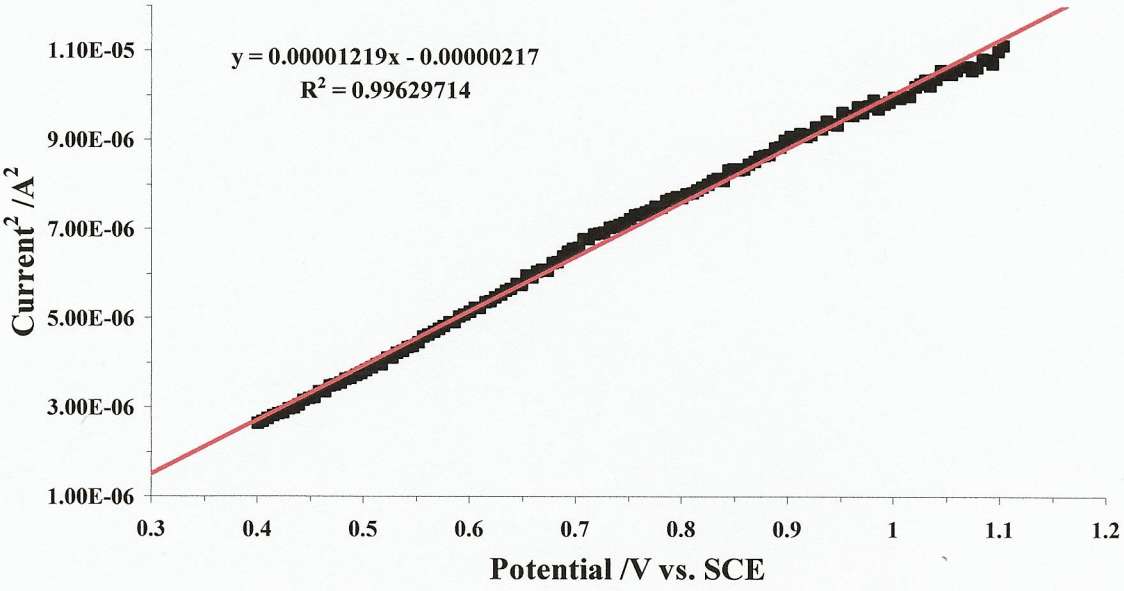

Figure 7.24. Plot of current^2 vs. electrode potential for the experiment at V_b = 2.0 V in fig. 7.22. The corresponding data taken at V_b = 0 were subtracted, see text for details.

7.5. Potential applications

7.5.1. The potential application of composite anodes to fuel cells.

Unfortunately, time and resources (i.e. supply of composite anodes) did not allow the investigation of the potential application of composite anodes to fuel cell technology. Hence, it is appropriate to summarize the preliminary work that sparked the interest in fuel cell applications in more detail than was presented earlier in the chapter; this work was completed prior to my joining Prof. Christensen's group.

The initial studies on the electro-oxidation of methanol were carried out using Au/Si/TiO_2/Au composite anodes, but with platinum electrodeposited on the gold grid, from 2 mM H_2PtCl_6 + 10 mM H_2SO_4 at -0.10 V vs. Ag/AgCl. For comparison, a Pt

foil electrode was also employed upon which Pt was electrodeposited as above. Two composite anodes were investigated: the type A anode was as described in chapter 2 and discussed in this chapter, having a gold grid consisting of linear tracks, see fig. 7.25(a). The type B anode differed only in the structure of the grid which consisted of a gold layer perforated by linear arrays of 360 μm diameter holes, evenly spaced 640 μm centre-to-centre, see fig. 7.25(b).

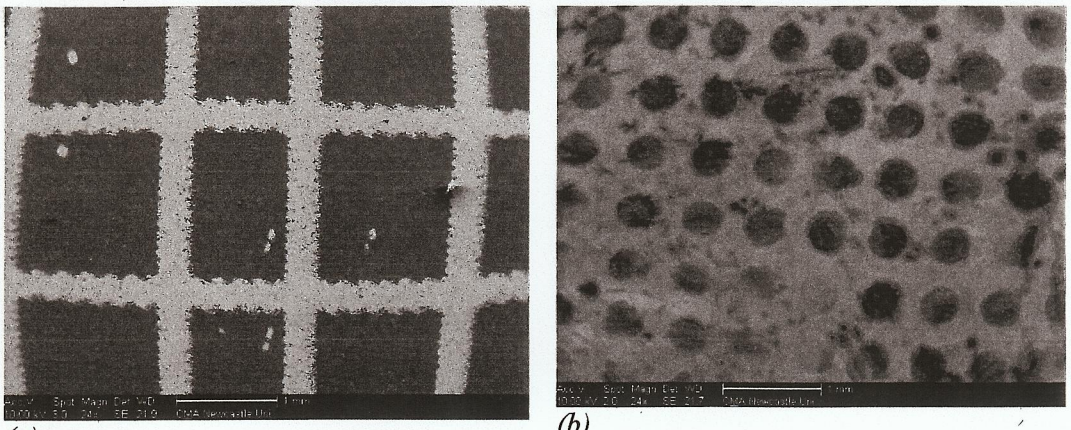

(a) (b)

Figure 7.25 Type (a) A and (b) B gold grid on composite anodes. Bars =1 mm

The areas of the Pt electrodeposits on the foil and type A & B anodes were 37 ± 5 cm^2, calculated from the area under the hydrogen adsorption/desorption peaks and assuming a conversion factor of 220 μC cm^{-2} [52]. The total perimeter length (Au/TiO_2) of the type B anode was 432 cm cff. 218 cm for type A.

Fig. 7.26 shows linear sweep voltammograms of the Pt foil and the type A & B anodes in 0.5 M CH_3OH + 0.5 M H_2SO_4. In acidic methanol solution, taking the electrodeposited Pt on Pt foil electrode and anode A first, with no bias potential applied across the anode, both it and the Pt foil show an onset potential of 350 mV vs. Ag/AgCl, ca. 550 mV vs. RHE, which compares well with the literature value of 560 mV vs. RHE [53]. However, with a 2.0 V bias, anode A shows an onset significantly lower, of 210 mV vs. Ag/AgCl; moreover, the anode shows a markedly higher current density both in the presence and absence of a bias, than the Pt foil. Thus it appears that the application of a bias potential between the Pt and Si of the device results in the predicted enhancement of the electroactivity of the Pt.

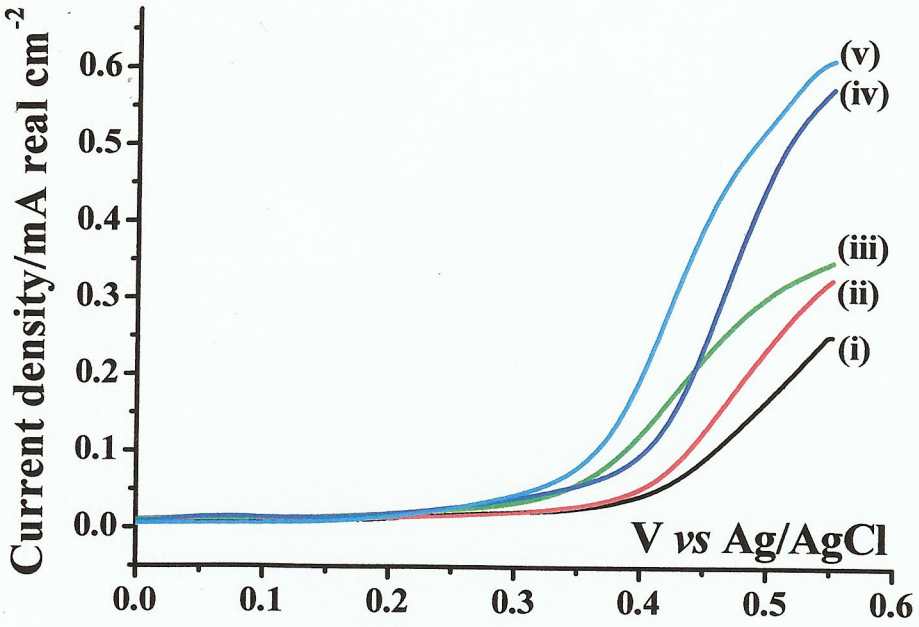

Figure 7.26 Linear sweep voltammograms of (i) the ED Pt/Pt foil, (ii) anode A, (iii) anode A with 2.0 V bias, (iv) anode B and (v) anode B with a 2.0 V bias in N_2-saturated electrolyte containing 0.5 M H_2SO_4 + 0.5 M CH_3OH; scan rate 1 mV s^{-1} room temperature (20 °C). The counter electrode was a 2.5 cm x 2.5 cm Pt mesh.

Anode B has twice the geometric boundary length between the Au underlying the Pt layer and the TiO_2 of anode A, and this is reflected in the significantly higher current density both with and without an applied bias, and the lower onset potential of 0.3 V vs. Ag/AgCl (i.e. the same as that observed at 2.0 V with anode A) even in the absence of the bias. Thus, a key observation from this work was the significantly enhanced activity of anode B than A, characterised by the larger perimeter between the metal layer and the TiO_2, even in the absence of an applied bias voltage.

The Pt and the composite electrodes were employed as the anodes in a simple fuel cell test experiment wherein the anodes and a tubular oxygen cathode (Pt particles/porous carbon on a Ti mesh support, loading was 2.5 mg Pt cm^{-2}) were immersed in a beaker containing 0.5 M H_2SO_4/0.5 M CH_3OH at 20 °C, 400 ml min^{-1} oxygen feed to the centre of the cathode. No membrane was employed to separate the anode from the cathode, hence significant poisoning of the cathode would be expected which, in addition to the low temperature employed, would be expected to result in a poor performance of the fuel cell. Nevertheless, power could be drawn from the fuel cells utilising the three anodes, as can be seen in fig. 7.27.

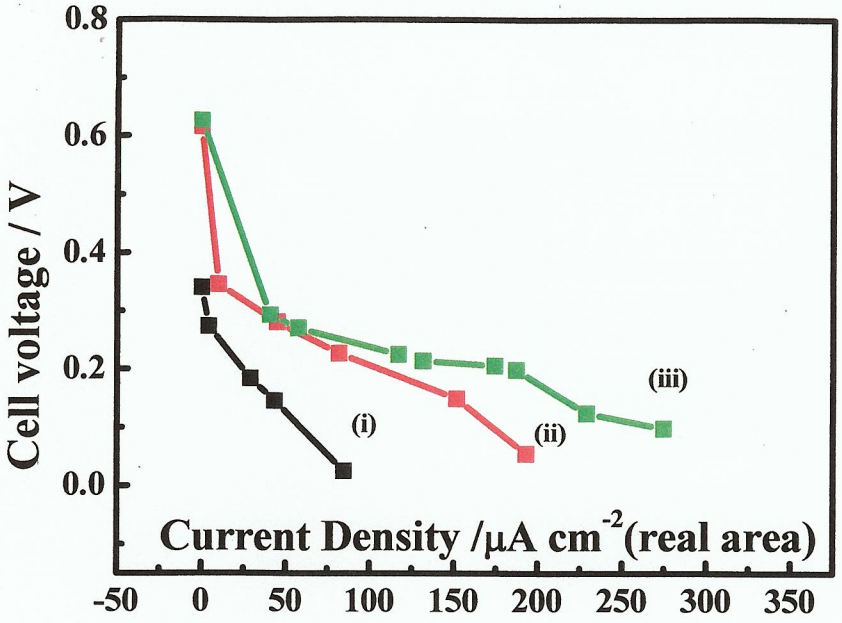

Figure 7.27 The performance of a simple fuel cell employing the (i) Pt foil, (ii) electrode A and (iii) electrode B as the anode, 0.5 M H_2SO_4 + 0.5 M CH_3OH, 20 °C; see text for details. No bias voltage was imposed on either of the composite anodes

The Pt anode was insufficiently active to support current densities > 90 μA cm^{-2}; however, anode A showed a significantly improved performance even in the absence of bias voltage. Anode B showed an even better performance than A at zero bias, strongly supporting the postulate above that the greater activity of anode B is due to the greater perimeter length. Application of a 2.0 V bias (not shown) on the Pt overlayer of anode B increased the performance still more.

7.5.2. Electrofluorination.

Given the potential of the composite anode to deliver very powerfully-oxidising species at the electrode/electrolyte interface, it was decided to explore the potential application of the anodes in electrofluorination.

The unique properties of fluorine has resulted in fluorinated compounds (e.g. ArF, RF, CF_2, CF_3, polyfluoro and perfluoro) finding extensive use in bioactives (pharmaceuticals, agrochemicals), materials applications and also as Positron Emission Tomography (PET) radiopharmaceuticals (fluorine-18 [54-59]).

The PET medical imaging technique is of increasing importance in the personalized diagnosis and management of a diverse range of diseases. Typical radiopharmaceuticals employed in PET are shown in fig. 7.28. (^{18}F) is the reagent of choice for the production of fluorine-18 radiopharmaceuticals as it is available in larger amounts and higher specific activity compared to $(^{18}F)F_2$. The requirement of good manufacturing practice (GMP) grade clinical manufacture coupled with the short half-life of fluorine-18 (110 min) makes the automated, rapid, clean, efficient synthesis and isolation of radioligands paramount [59, 60].

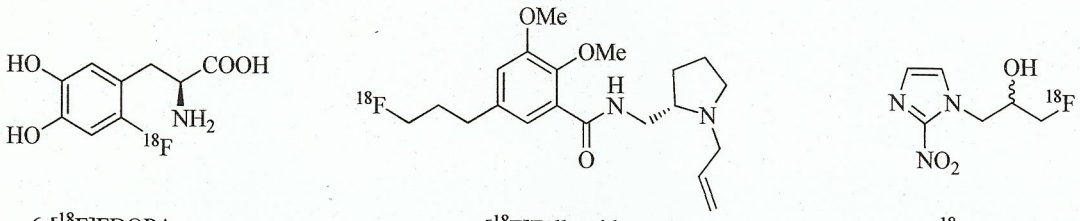

6-[^{18}F]FDOPA [^{18}F]Fallypride [^{18}F]FMISO

Figure 7.28. Typical radiopharmaceuticals used in Positron Emission Tomography.

Electrochemical fluorination (ECF) [61, 62] using fluoride ions, offers potential advantages over conventional synthetic methods in that it provides an opportunity to access both novel and known fluorinated functionality without the need for hazardous and extremely reactive fluorine gas. Surprisingly there have been extremely limited investigations of the technology although the potential for clean, efficient manufacture has resulted in increased interest in the field in recent years [63].

As a first step in determining if the composite electrode could be employed in electrofluorination it was decide to investigate the electrochemical response of a Si/TiO_2/Pt electrode in alkaline solution (pH 9.7) in the presence of F^-. Pt was chosen rather than gold due to the instability of the latter metal to dissolution at anodic potentials in halide-containing electrolytes [64-66]. The alkaline pH was chosen to stabilize any OF^- (hypofluorite) that may be formed from the oxidation of F^-, as OF^- is the electrophilic fluorine which is essential in fluorination reactions [67, 68].

Figures 7.29(a) & (b) show cyclic voltammograms of the Si/TiO_2/Pt composite anode immersed in pH 9.7 0.1 M Na_2SO_4/NaOH in the absence and presence of 0.1 M KF (a) at V_b = 0 V and (b) at V_b = 1.0 V.

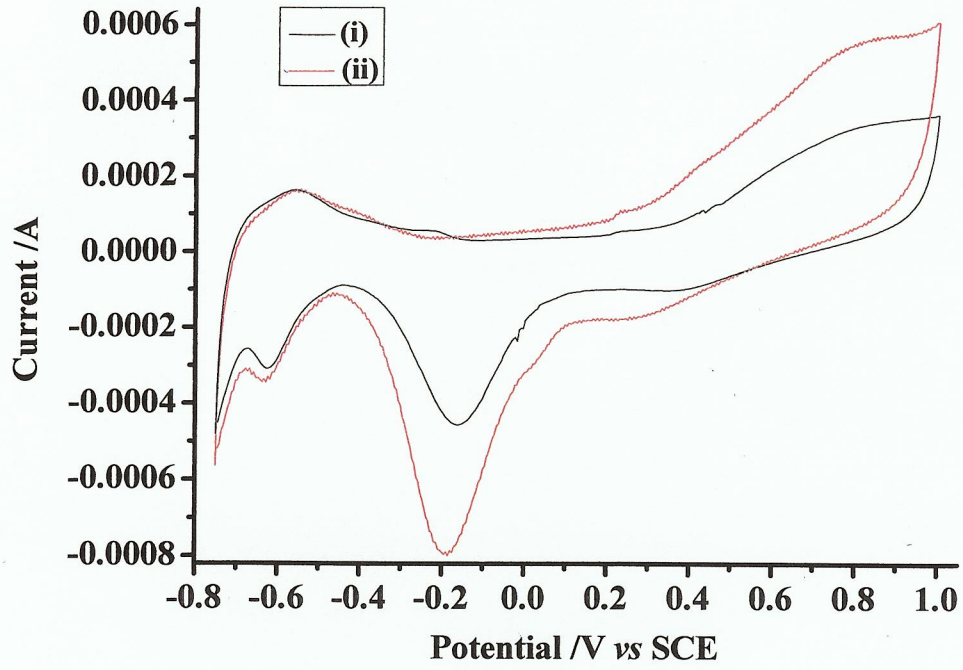

(a)

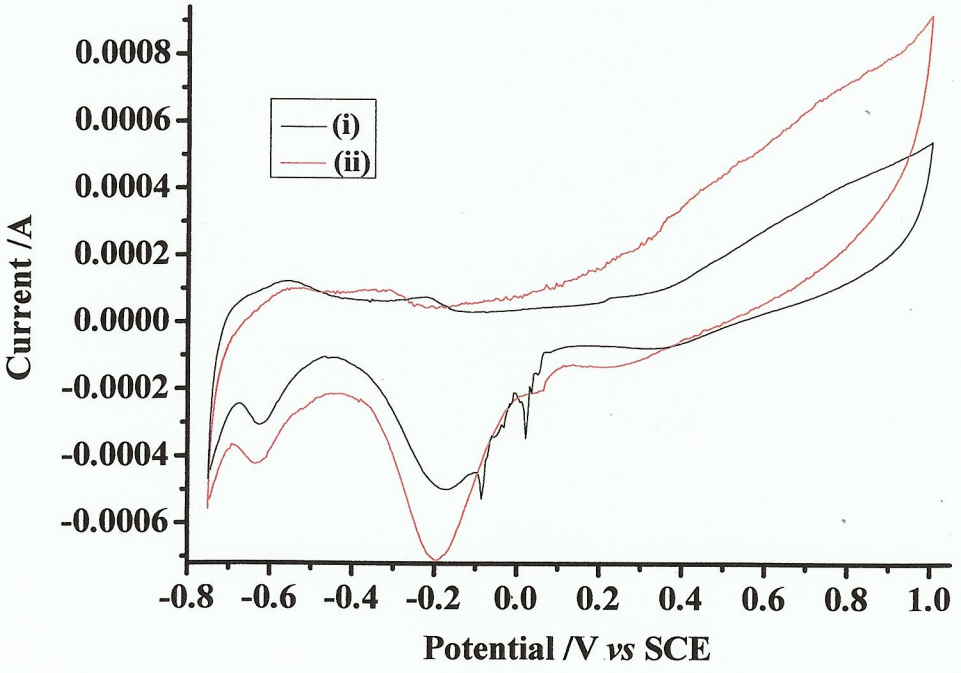

(b)

Figure 7.29. Cyclic voltammograms of the Si/TiO_2/Pt composite anode (Pt grid area ca. 2 cm^2) immersed in pH 9.7 NaOH/0.1 M Na_2SO_4 in the absence (i) and (ii) presence of 0.1 M KF at, (a) V_b = 0 V and (b) V_b =1.0 V. Scan rate 100 mV s^{-1}.

The presence of KF appears to enhance the formation (and subsequent stripping) of the Pt oxide and, at $V_b > 0$, of the underlying formation of oxygen due to the holes at the TiO_2/Pt interface – the latter causing the enhanced cathodic currents at $E < 0.4$ V. This may be due to the displacement of strongly adsorbing sulphate and bisulfate ions from the Pt, and/or the TiO_2, the latter facilitating hole transfer to Pt.

A single, well-defined reduction peak near -0.6 V corresponding (presumably) to:

$$Pt + H_2O \rightarrow Pt\text{-}H + OH^- + e^- \qquad (7.14)$$

may also be observed in fig. 7.29(a) & (b). However, there is no corresponding wave due to the reverse reaction in the anodic sweep; this maybe due to the fact that the reverse process is slow, perhaps due to 'spill-over' of the hydride into the TiO_2 lattice [69, 70], and hence is 'smeared out' over a range of potentials. Reduction of water/H^+ is known to occur at negative potentials at TiO_2 with the insertion of atomic hydrogen into the TiO_2 lattice [71].

There is a major change in the voltammetry between $V_b = 1$ V and $V_b = 2$ V, see fig. 7.30(a), with the appearance of a reversible or quasi-reversible wave centred near -0.45V. The cathodic wave of this feature corresponds in potential to that of the hydride peak discussed above. The quasi-reversible wave may be attributed to the insertion and de-insertion of H into the TiO_2 lattice [71]:

$$TiO_2 + xH_2O + xe^- \text{—} H_xTiO_2 + xOH^- \qquad (7.15)$$

On increasing the bias voltage, see fig. 7.30 (a) & (b), the peak currents associated with the insertion wave increase suggesting that the hole current through the TiO_2 is influencing the electrochemical insertion/de-insertion process: coupled with the coincidence in potential of Pt-H formation and atomic hydrogen formation/insertion into the TiO_2, this suggests that hydride formed on the Pt spills over into the TiO_2:

$$Pt + H_2O + e^- \rightarrow Pt\text{-}H + OH^- \qquad (7.16)$$

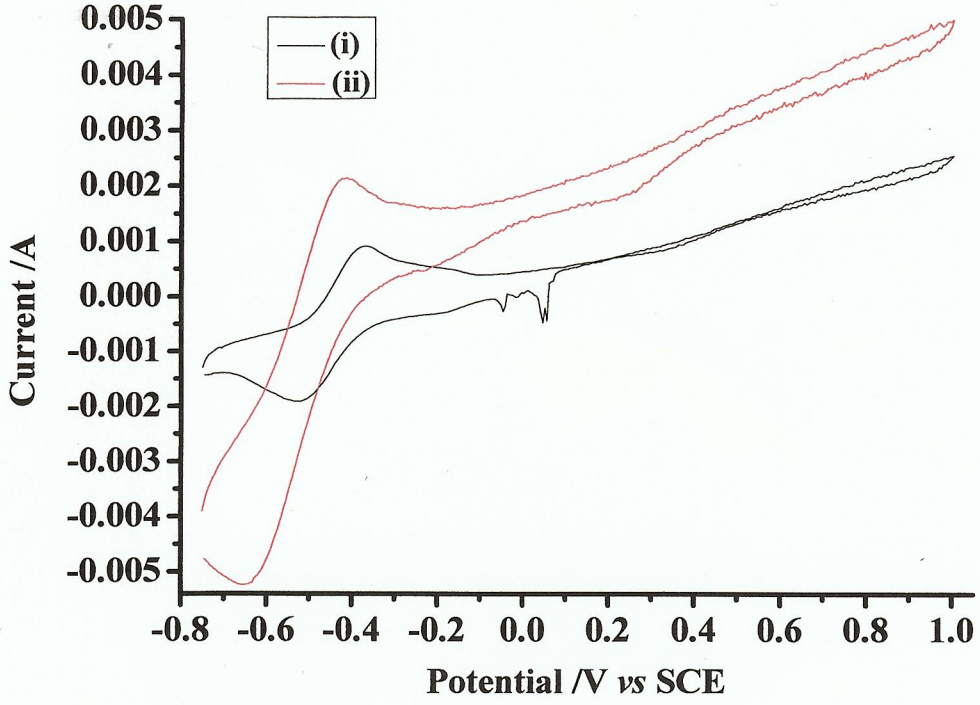

(a)

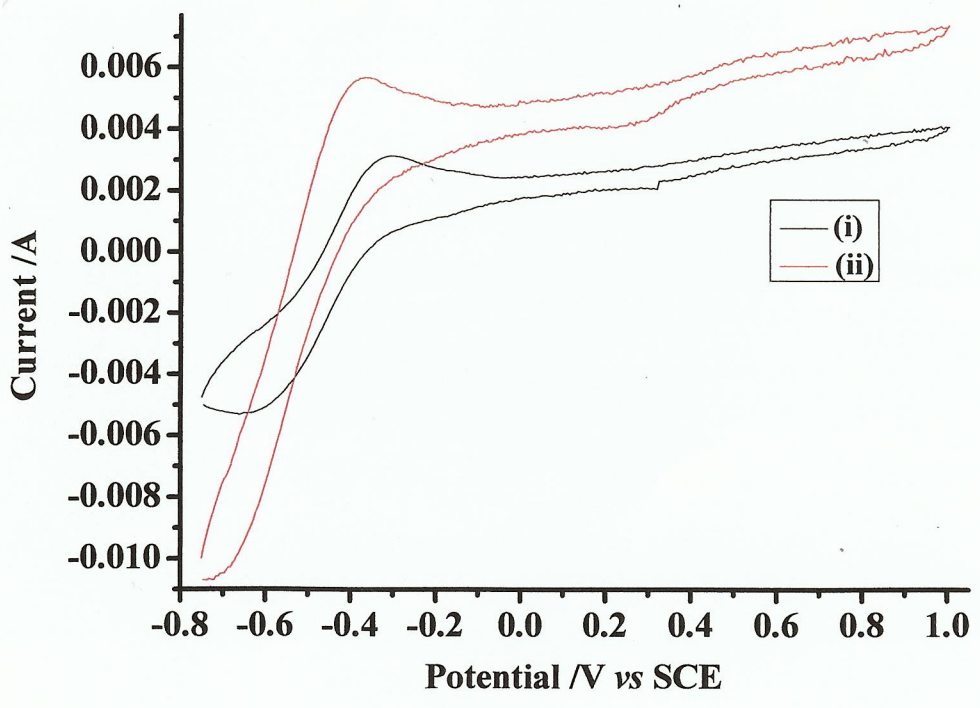

(b)

Figure 7.30. Cyclic voltammograms of the Si/TiO_2/Pt electrode in figs. 7.26(a) & (b) in the (i) absence and (ii) presence of 0.1 M KF at, (a) V_b = 2 V and (b) V_b = 3 V. Scan rate 100 mV s^{-1}

$$xPt\text{-}H + TiO_2 \rightarrow H_xTiO_2 + xPt \quad (7.17)$$

Increasing the bias voltage has no effect upon the TiO_2 until V_b attains values where new channels for the holes are opened up (> 1 V). These holes can oxidise H atoms:

$$h^+ + H_xTiO_2 \rightarrow H_xTiO_2 + H^+ \quad (7.18)$$

and/or recombine with electrons at/near the grid:

$$h^+ + e^- \rightarrow \text{heat} \quad (7.19)$$

Interestingly, as may be seen from figs. 7.30(a) & (b), as well as the insertion/de-insertion peak currents increasing as V_b increases, the separation of the anodic and cathodic waves increases (which would not be expected for a surface process where diffusion in solution is not important). More importantly, the addition of KF has little effect upon the anodic peak potential of this feature, but causes the cathodic peak to move to more negative potentials, suggesting F^- is selectively slowing the insertion process down. It is also clear from figs. 7.30 (a) & (b) that F^- is significantly enhancing both insertion & de-insertion, but the latter ca. 2x the former, and the oxidation current in the anodic sweep. F_2 has the highest E° of 2.87 V, significantly above that of water (1.23 V) and will react rapidly to produce HOF and HF:

$$F_2 + H_2O \rightarrow 2H^+ + {}^-OF + F^- \quad (7.20)$$

HOF is itself unstable and decomposes rapidly to HF and O_2 (in alkaline solution, H_2O_2 in acid):

$$2\,{}^-OF \rightarrow 2F^- + O_2 \quad (7.21)$$

The enhanced electrochemical currents at $V_b > 1$ V in figs 7.30(a) & (b) may thus be due to enhanced water oxidation catalysed by a F-containing intermediate/surface species:

$$4F^- \rightarrow 2F_2 + 4e^- \quad (7.22)$$

$$2F_2 + 2H_2O \rightarrow 4H^+ + 2^-OF + 2F^- \text{ (fast)} \quad (7.23)$$

$$4^-OF \rightarrow 4F^- + 2O_2 \text{ (fast)} \quad (7.24)$$

Overall:

$$2H_2O \rightarrow O_2 + 4H^+ + 4e^- \quad (7.25)$$

At V_b where the new channels for h transfer to the TiO_2 surface open up, the equilibrium (7.18) is dragged over to the left hand side as inserted H is oxidised, increasing the rates of (7.16) and (7.17), but slowing the insertion process.

At the end of the above experiments, the grid has been completely stripped from the TiO_2 surface.

7.6. Conclusions

The electrochemistry of novel composite anodes has been investigated in acidic solution and a model formulated to explain the data so obtained. In the model, hole generated thermally in the silicon near the Si/TiO_2 interface are able to move through the TiO_2, *via* field assisted hopping, to the TiO_2 surface. At bias voltages below 1 V, holes arriving at the TiO_2 surface near the gold grid oxidize the grid which, in turn, oxidizes water, acting as a catalyst (i.e. assuming that such holes oxidise water to produce OH radicals and that these radicals are able to diffuse to the grid). At bias voltages > 1 V, holes generated in region remote from the Au grid are able to access surface states and oxidise water directly. There is evidence to suggest that the powerful oxidising potential of the holes arriving at the surface can be employed to generate "F^+" species, (OF^- and/or F_2), but this is inconclusive.

To my knowledge, the behaviour described in this chapter has not been reported previously and hence any theoretical model will, of necessity be speculative pending in-depth investigation. However it is clear that the model suggests that, instead of having a one dimensional control over the behaviour of an electrode (*via* its electrochemical potential) the composite anodes allow three dimensional control: V_b,

electrochemical potential and visible light intensity. Thus it should be able to 'tune' a composite anode to oxidise a target solution species by selecting a set of parameters corresponding to a suitable point on the 3-dimentional surface represented by V_b, electrochemical potential and visible light intensity. Additional variables are the chemical composition of the metal grid and the ratio of grid area to grid/TiO_2 perimeter length, the latter suggested by the preliminary fuel cell studies.

7.7. References

1. Sun L. and Bolton J.R., (1996). The Journal of Physical Chemistry, 100, 10, pp. 4127-4134.
2. Mills A. and Le Hunte S., (1997). Journal of Photochemistry and Photobiology A: Chemistry, 108, 1, pp. 1-35.
3. Christensen P.A. and Walker G.M. (1996). in ETSU. s/P4/00249/REP.
4. Fujishima A. and Rao T.N., (1998). Pure & Applied Chemistry, 70, 11, pp. 2177-2187.
5. IUPAC, (1985). *Standard Potentials in Aqueous Solution*, 5 ed, ed. A.J. Bard, R. Parsons, and J. Jordan. New York: Marcel Dekker INC. 834.
6. Matsunaga T., Tomoda R., Nakajima T., and Wake H., (1985). FEMS Microbiology Letters, 29, 1-2, pp. 211-214.
7. Christensen P.A., Curtis T.P., Egerton T.A., Kosa S.A.M., and Tinlin J.R., (2003). Applied Catalysis B: Environmental, 41, 4, pp. 371-386.
8. Gautron J., Lemasson P., and Marucco J.-F., (1980). Faraday Discussions of the Chemical Society, 70, pp. 81-91.
9. Hamnett A., Dare-Edwards M.P., Bard A.J., Faulkner L.R., Bockris J.O.M., Khan S.U.M., Uosaki K., Gerischer H., Nozik A.J., Schumacher R., Ellis A.B., Harzion Z., Albery W.J., Davidson R.S., Perone S.P., Richardson J.H., Archer M.D., Gissler W., Pichat P., Ginley D.S., Jarrett H.S., Butler M.A., Armstrong N., Gomes W.P., Peter L.M., Froelicher M., Malati M.A., Lemasson P., Potter R., and Sprunken H.R., (1980). Faraday Discussions of the Chemical Society, 70, pp. 93-132.
10. Butterfield I.M., Christensen P.A., Hamnett A., Shaw K.E., Walker G.M., Walker S.A., and Howarth C.R., (1997). Journal of Applied Electrochemistry, 27, 4, pp. 385-395.
11. Butterfield I.M., Christensen P.A., Curtis T.P., and Gunlazuardi J., (1997). Water Research, 31, 3, pp. 675-677.
12. Harper J.C., Christensen P.A., Egerton T.A., Curtis T.P., and Gunlazuardi J., (2001). Journal of Applied Electrochemistry, 31, 6, pp. 623-628.
13. Hamnett A., (1987). *Semiconductor Electrochemistry*, in: Comprehensive Chemical Kinetics Volume 27 Electrode Kinetics: Reactions, R.G. Compton [Editor], Elsevier, Amsterdam, p. 61-246.
14. Vinodgopal K., Hotchandani S., and Kamat P.V., (1993). The Journal of Physical Chemistry, 97, 35, pp. 9040-9044.
15. Vinodgopal K., Stafford U., Gray K.A., and Kamat P.V., (1984). *Semiconductor particulate films for the photocatalytic degradation of organic contaminants*, in: Proceedings of the symposium on Water Purification by Photocatalytic, Photoelectrochemical, and Electrochemical process., T.L. Rose, O. Murphy, E.

Rudd, and B.E. Conway Editors, The Electrochemical Society New York. p. 332-341.
16. Kim D.H. and Anderson M.A., (1994). Environmental Science & Technology, 28, 3, pp. 479-483.
17. Egerton T.A., Kosa S.A.M., and Christensen P.A., (2006). Physical Chemistry Chemical Physics, 8, 3, pp. 398-406.
18. Christensen P.A., Egerton T., Kosa S., Tinlin J., and Scott K., (2005). Journal of Applied Electrochemistry, 35, 7, pp. 683-692.
19. Rodríguez J., Gómez M., Lindquist S.E., and Granqvist C.G., (2000). Thin Solid Films, 360, 1-2, pp. 250-255.
20. Christensen P.A. (2004). in 55th Annual Meeting of the International Society of Electrochemistry. Thessaloniki, Greece. 19-24.
21. Christensen P.A., Egerton T.A., Lin W.F., Meynet P., Shao Z.G., and Wright N.G., (2006). Chemical Communications, 38, pp. 4022-4023.
22. Christensen P. A., Egerton T.A., and Wright N.G., (2006), ELECTROCHEMICAL DEVICE: Great Britain. Patent W0/2006/024869 PCT/GB2005/003406.
23. Watanabe M. and Motoo S., (1975). Journal of Electroanalytical Chemistry, 60, 3, pp. 275-283.
24. Christensen P.A., Jin J.-M., Lin W.-F., and Hamnett A., (2004). The Journal of Physical Chemistry B, 108, 11, pp. 3391-3394.
25. Christensen P.A., Wright N.G., and Egerton T.A., (2007), METHANOL FUEL CELLS: Great Britain Patent W0/2007/010207 PCT/GB2006/002613.
26. Antolini E. and Gonzalez E.R., (2010). Journal of Power Sources, 195, 11, pp. 3431-3450.
27. Spendelow J.S. and Wieckowski A., (2007). Physical Chemistry Chemical Physics, 9, 21, pp. 2654-2675.
28. McLean G.F., Niet T., Prince-Richard S., and Djilali N., (2002). International Journal of Hydrogen Energy, 27, 5, pp. 507-526.
29. Bidault F., Brett D.J.L., Middleton P.H., and Brandon N.P., (2009). Journal of Power Sources, 187, 1, pp. 39-48.
30. Röppischer H., Bumai Y.A., and Feldmann B., (1995). Journal of The Electrochemical Society, 142, 2, pp. 650-655.
31. Trasatti S., (1980). *The electrode potential*, in: Comprehensive Treatise of Electrochemistry Volume 1: The Double Layer, J.O.M. Bockris, B.E. Conway, and E. Yeager Editors, Plenum Press, New York. p. 45-82.
32. Trasatti S., (1986). Pure & Applied Chemistry, 58, 7, pp. 955-966.
33. Mott N.F. and Davies E.A., (1979). *Electronic Processes in Non-crystalline Materials*, 2 ed. Oxford: Clarendon. 7-37.
34. Poznyak S.K., Pergushov V.I., Kokorin A.I., Kulak A.I., and Schläpfer C.W., (1999). The Journal of Physical Chemistry B, 103, 8, pp. 1308-1315.
35. Kulak A.I., Kokorin A.I., and Sviridov D.V., (2001). Journal of Materials Research, 16, 08, pp. 2357-2361.
36. Mizubayashi W., Yasuda N., Ota H., Hisamatsu H., Tominaga K., Iwamoto K., Yamamoto K., Horikawa T., Nabatame T., and Toriumi A. (2004). in Reliability Physics Symposium Proceedings, 2004. 42nd Annual. 2004 IEEE International. 188-193.
37. Deskins N.A. and Dupuis M., (2008). The Journal of Physical Chemistry C, 113, 1, pp. 346-358.
38. Anderson P.W., (1958). Physical Review, 109, 5, pp. 1492.

39. Miller A. and Abrahams E., (1960). Physical Review, 120, 3, pp. 745.
40. Fox M.A. and Chen C.C., (1981). Journal of the American Chemical Society, 103, 22, pp. 6757-6759.
41. Haick H. and Paz Y., (2001). The Journal of Physical Chemistry B, 105, 15, pp. 3045-3051.
42. Haick H. and Paz Y., (2003). Chemistry Physical Chemistry, 4, 6, pp. 617-620.
43. Kawahara K., Ohko Y., Tatsuma T., and Fujishima A., (2003). Physical Chemistry Chemical Physics, 5, 21, pp. 4764-4766.
44. Salvador P. and Gutierrez C., (1984). The Journal of Physical Chemistry, 88, 16, pp. 3696-3698.
45. Salvador P., (1987). Surface Science, 192, 1, pp. 36-46.
46. Salvador P., (1985). The Journal of Physical Chemistry, 89, 18, pp. 3863-3869.
47. Chongyang L., Yixuan C., and Wenzhao L., (1985). Surface Science, 163, 2-3, pp. 383-390.
48. Laser D. and Gottesfeld S., (1979). Journal of The Electrochemical Society, 126, 3, pp. 475-478.
49. Paulik M.G., Brooksby P.A., Abell A.D., and Downard A.J., (2007). The Journal of Physical Chemistry C, 111, 21, pp. 7808-7815.
50. Chowdhury A.-N., Alam M.T., Okajima T., and Ohsaka T., (2009). Journal of Electroanalytical Chemistry, 634, 1, pp. 35-41.
51. Trasatti S. and Petrii O.A., (1991). Pure & Applied Chemistry, 63, 5, pp. 711-734.
52. Wen-Feng L., Shi-Gang S., and Zhao-Wu T., (1994). Journal of Electroanalytical Chemistry, 364, 1-2, pp. 1-7.
53. Batista E.A., Malpass G.R.P., Motheo A.J., and Iwasita T., (2004). Journal of Electroanalytical Chemistry, 571, 2, pp. 273-282.
54. Bégué J.-P. and Bonnet-Delpon D., (2006). Journal of Fluorine Chemistry, 127, 8, pp. 992-1012.
55. Kirk K.L., (2006). Journal ofFluorine Chemistry, 127, 8, pp. 1013-1029.
56. Kirsch P., (2004). *Modern Fluoroorganic Chemistry. Synthesis, reactivity, Applications*. Darmtadt: WILEY-VCH Verlag GmbH&Co. KGaA. 308.
57. (2007). *Handbook for Reagents in Organic Synthesis. Fluorine Containing Reagents*, 1 ed. Handbook for Reagents in Organic Synthesis, ed. L. Paquette. Chicester/GB: John Wiley and Sons Ltd. 730.
58. Shimizu M. and Hiyama T., (2005). Angewandte Chemie International Edition, 44, 2, pp. 214-231.
59. Cai L., Lu S., and Pike V.W., (2008). European Journal of Organic Chemistry, 17, pp. 2853-2873.
60. Miller P.W., Long N.J., Vilar R., and Gee A.D., (2008). Angewandte Chemie International Edition, 47, 47, pp. 8998-9033.
61. Noel M., Suryanarayanan V., and Chellammal S., (1997). Journal of Fluorine Chemistry, 83, 1, pp. 31-40.
62. Conte L. and Gambaretto G., (2004). Journal of Fluorine Chemistry, 125, 2, pp. 139-144.
63. Molyneux D., Carroll M.A., and Christensen P.A., (Submited 2011). Journal of Fluorine Chemistry.
64. Qi P.H. and Hiskey J.B., (1993). Hydrometallurgy, 32, 2, pp. 161-179.
65. Marsden J.O. and House C.I., (2006). *The Chemistry of Gold Extraction*, 2 ed. Littleton Co, USA: Society for Mining, Metallurgy, and Exploration, inc. (SME). 655.

66. Burke L.D. and Nugent P.F., (1997). Gold Bulletin, 30, 2, pp. 43-53.
67. Purrington S.T., Kagen B.S., and Patrick T.B., (1986). Chemical Reviews, 86, 6, pp. 997-1018.
68. Kirk K.L., (2008). Organic Process Research & Development, 12, 2, pp. 305-321.
69. Roland U., Salzer R., Sümmchen L., and Can Li and Qin X., (1997). *Electronic effects of hydrogen spillover on titania*, in: Studies in Surface Science and Catalysis, Elsevier. p. 339-348.
70. Herrmann J.-M., Guerrero-Ruiz A., and Rodriguez-Ramos I., (2001). *Electronic processes in hydrogen spillover*, in: Studies in Surface Science and Catalysis, Elsevier. p. 189-196.
71. Roland U., Roessner F., and Can Li and Qin X., (1997). *A new model on the nature of spilt-over hydrogen*, in: Studies in Surface Science and Catalysis, Elsevier. p. 191-200.

8. Conclusions / Future work.

The FTIR studies have shown that the oxidation of methanol and ethanol at polycrystalline Pt in alkaline electrolyte proceed *via* oxygen bond intermediates, rather than Pt–CO, as is the case in acid. It is clear that the 'dual path' mechanism involving adsorbed CO as the intermediate species to CO_2 is not applicable in alkaline solution, as adsorbed CO is a spectator in the oxidation of ethanol and methanol, rather than a participant. For C–C cleavage to occur in ethanol, both carbon atoms must form bonds to Pt. This is challenging in acid solution (as may be deduced from the very low typical selectivity towards CO_2 formation) despite chemisorption taking place *via* the stripping of H atoms. In alkaline solution this is simply not possible due to the participation of the –O– atom of the –OH group and it is clear that the other key, active intermediate is the 'reversibly adsorbed' OH_{ads}.

The preliminary work on $Pd_{40}Ni_{60}$ and the SD1 membrane and ionomer are very promising, but significant further studies are required. At the fundamental level, *in-situ* FTIR studies should be carried out to investigate methanol and ethanol oxidation at the catalyst to see if the 'O-intermediate' model developed throughout this thesis remains valid for the $Pd_{40}Ni_{60}$. This will require research into the production of Pd40Ni60 nanoparticles directly onto an inert, reflective anode such as glassy carbon. Attempts to study the catalyst on porous carbon failed due to the poor IR reflectivity of the substrate. The FTIR studies should be supported by standard IVt measurements (rotating disc studies, Tafel slope analysis, etc.), and the optimum catalyst composition Pd_xNi_y, determined.

The preparation of the Membrane Electrode Assemblies employed in the DAAFC studies was not optimised at all; hence the optimum experimental conditions (loading of catalyst, % ionomer, pressing conditions, etc.) should be researched. Only when this has been achieved can the performance of the SD1 membrane and ionomer be assessed and a strategy for its improvement formulated.

The composite anode represent a wholly novel type of electrode to effect oxidative transformation. Unfortunately, time did not allow the assessment of the potential

application of the anodes in fuel cell technology. As a first step, the electrochemistry of the composite anodes should be explored as a function of (1) the grid metal; e.g. using Pt instead of Au, (2) 'the perimeter length' between grid to TiO_2, keeping the overall area of the metal constant, (3) pH and (4) added organic 'fuel', e.g. methanol and ethanol.

The potential application of composite anodes in electrofluorination is very interesting and worthy of further investigation. In order to achieve this, however, stable grid structures need to be researched and developed; perhaps countersinking the grid into the TiO_2 is one strategy. Once such stable anodes are developed, electrofluorination can be explored, initially with $Et_4NF.3HF$, but with the intention of using $Et_4N^+F^-$ (rather than HF) as the source of fluorine.

Appendix I: Lateral diffusion

The basic equation for cylindrical diffusion of a single species is:

$$\frac{\partial c}{\partial t} = D\left(\frac{\partial^2 c}{\partial r^2} + \frac{1}{r}\frac{\partial c}{\partial r}\right) \tag{1}$$

which can be discretised as a dimensionless set of equations following the substitutions $C = c/C^*$, where C^* is the reference concentration of the species (taken here as the concentration of the initial reactant in the bulk of the cell), $R = r/a$ where a is the radius of the cylinder, and $T = Dt/a^2$; given that a may be macroscopic, this may require very long overall time for the simulation.

Rearranging:

$$\frac{\partial C}{\partial T} = D\left(\frac{\partial^2 C}{\partial R^2} + \frac{1}{R}\frac{\partial C}{\partial R}\right) \tag{2}$$

if the lattice points at a distance H apart are such that $R = iH$ then for $i \neq 0$

$$\left(\frac{\partial^2 C}{\partial R^2} + \frac{1}{R}\frac{\partial C}{\partial R}\right) \equiv \frac{1}{2iH^2}\{(2i+1)C(i+1) - 4iC(1) + (2i-1)C(i-1)\} \tag{3}$$

where $C(i)$ is the normalised concentration at the i^{th} point. For $i = 0$, using the Bessel function expansion at small r:

$$\frac{1}{R}\frac{\partial}{\partial R}\left(R\frac{\partial C}{\partial R}\right) = \frac{4}{H^2}(C(1) - C(0)) \tag{4}$$

For the Crank-Nicholson implicit approach [1], and for $i \neq 0$

$$\frac{C'(i)-C(i)}{\delta T} = \frac{1}{4iH^2}\{(2i+1)C(i+1)-4iC(i)+(2i-1)C(i-1)\}$$
$$= \frac{1}{4iH^2}\{(2i+1)C'(i+1)-4iC'(i)+(2i-1)C'(i-1)\} \quad (5)$$

where $C'(i)$ is the concentration at position i at time $t + \delta T$; and $\lambda = \delta T/H^2$ whence

$$\lambda(2i-1)C'(i-1)-4i(\lambda+1)C'(i)+\lambda(2i-1)C'(i+1)=$$
$$-\lambda(2i-1)C(i-1)+4i(\lambda-1)C(i)-\lambda(2i+1)C(i+1) \quad (6)$$

And for $i = 0$:

$$\frac{C'(0)-C(0)}{\delta T} = \frac{2}{H^2}(C'(1)-C'(0))+\frac{2}{H^2}(C(1)-C(0)) \quad (7)$$

whence:

$$-(1+2\lambda)C'(0)-2\lambda C'(1) = -(1-2\lambda)C(0)-2\lambda C(1) \quad (8)$$

whilst for $i = N$ we have, for fixed $C(N+1)$:

$$\lambda(2N-1)C'(N-1)-4N(1+\lambda)C'(N)=$$
$$-(2N-1)\lambda C(N-1)+4N(\lambda-1)C(N)-2(2N+1)\lambda C(N+1) \quad (9)$$

The solution is to use a powerful sparse matrix inverter from the Harwell suite, MA28AD, to solve a set of equations derived from a sparse matrix. The matrix is set up by defining the row and column numbers for each entry, and then running MA28AD. Note that the linear equations to be solved have a dimension (N + 1) and the matrix has the form:

$$M = \begin{bmatrix} -1+2\lambda & 2\lambda & 0 & 0 & 0 & \cdots & 0 \\ \lambda & -8(\lambda+1) & 3\lambda & 0 & 0 & \cdots & 0 \\ 0 & 3\lambda & -12(\lambda+1) & 5\lambda & 0 & \cdots & 0 \\ \vdots & & & & & & \\ 0 & 0 & 0 & \ldots & 0 & (2N-1)\lambda & -4N(\lambda+1) \end{bmatrix}$$

and:

$$Mx\begin{bmatrix} C'(0) \\ C'(1) \\ \vdots \\ C'(N) \end{bmatrix} = \begin{bmatrix} -(1-2\lambda)C(0) - 2\lambda C(1) \\ -\lambda C(i-1) + 4(\lambda-1)C(i) - \lambda 3C(i+1) \\ \vdots \\ -(2N-1)\lambda C(N-1) + 4N(\lambda-1)C(N) - 2(2N+1)\lambda C(N+1) \end{bmatrix}$$

In the geometry found in specular infra-red cells, the cylindrical electrode is pressed against a window that is transparent to infra-red light, leaving a narrow electrolyte gap of about 4 micron width. The electrolyte contains an electro-active material which is assumed to be consumed at a rate proportional to $k_f c$ and, if the cell gap is h, then the pure diffusion equation transforms to:

$$\frac{\partial c}{\partial t} = D\left(\frac{\partial^2 c}{\partial r^2} + \frac{1}{r}\frac{\partial c}{\partial r}\right) - k_f c/h \tag{10}$$

Using the same normalisations as before:

$$\frac{\partial C}{dT} = \left(\frac{\partial^2 C}{\partial R^2} + \frac{1}{R}\frac{\partial C}{\partial R}\right) - \frac{k_f a}{Dh}C$$

form the Crank-Nicholson equations essentially in the same way as above, and save for the end points, results:

$$\begin{aligned} &\lambda(2i-1)C'(i-1) - \left[4i(\lambda+1) + \frac{2k_f c a^2}{DT}\delta T\right]C'(i) + \lambda(2i+1)C'(i+1) \\ &= -\lambda(2i-1)C(i-1) + \left[4i(\lambda-1) + \frac{2k_f a^2}{Dh}\delta T\right]C(i) - \lambda(2i+1)C(i+1). \end{aligned} \tag{11}$$

a

with similar equations for the end points $i = 0$ and $i = N$: More complex equations can be written down in the event of two electroactive species, or if a single electroactive species being converted into a surface-adsorbed species. Whilst the equations become more complex, and the dimension of the matrix M steadily increases, there is nothing fundamentally novel introduced, except in the event that higher-order chemical or electrochemical reactions take place. If the rate of reaction is proportional to the

concentration of two diffusing species, then the rate constant k_f now contains a product term: k_f *c_A *c_B. Thus, if the focus is on the oxidation of small organic molecules in alkaline solution, the rate of the electrochemical reaction will depend on OH^- concentration. This introduces a non-linearity into the equations, and this can be accommodated by using an implicit method as described by Britz [2]: here the product $k\, c_A\, c_B$ is replaced by $\frac{1}{2}\, k\, (c'_A\, c_B + c_A\, c'_B)$.

The method above has been programmed in Fortran 77 and some typical results for a model system, in which an organic molecule is oxidised in the presence of OH^- to a surface-bound species, are shown in the figure AI1.

The pH distribution across the electrode is close to linear after some 10^3 s, varying from 5 up to 13 in the 0.1 M solution investigated. The important point about the figure is that the limitation on the diffusion rate of OH^- leads to a range of pH values being exhibited simultaneously across the electrode, and thus, such a range will be seen in the resultant spectrum. It is, therefore, perfectly possible for the outer part of the electrode to be close to pH 13 but the inner part, near the centre, to be at a much lower pH; all products over the range of pH values will be seen. In the case of oxidation of formate, it is therefore possible to see, simultaneously, CO_3^{2-}, HCO_3^- and CO_2; this is an important point to bear in mind when assignments are being made.

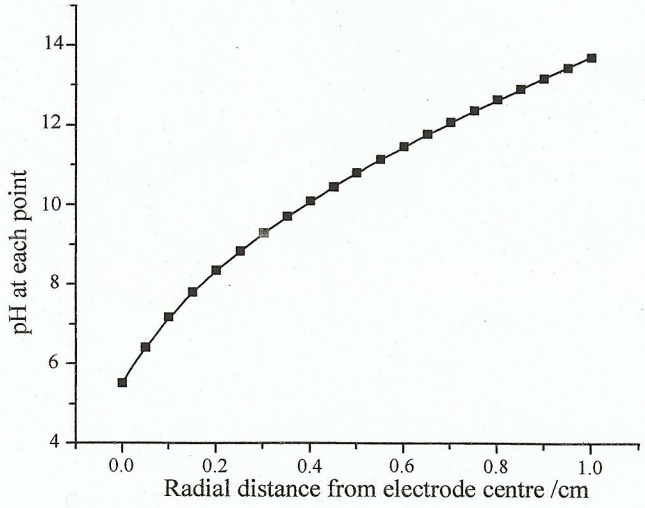

Figure All. pH Variation across electrode surface for a model calculation using the approach discussed above.

References.

1. Crank J., (1975). *The Mathematics of Diffusion*, 2 ed: Oxford science publications. 415.
2. Britz D., (1988). *Digital Simulation in Electrochemistry*, 2 ed. Darmstadt: Springer-Verlag. 229.